



The
University
Of
Sheffield.

**Efficiency Optimised Control of Interior
Permanent Magnet Synchronous Machine
(IPMSM) Drives for Electric Vehicle
Tractions**

By

Tianfu Sun

A thesis submitted in partial fulfilment of the requirements for the degree
of Doctor of Philosophy

The University of Sheffield

Faculty of Engineering

Department of Electronic & Electrical Engineering

March 2016

“The universe has the highest beauty, but it does not speak a single word. Time proceeds in its most admirable manner, but it is silent. All things have their complete and distinctive constitutions, but they say nothing about them. The sages trace out the admirable operations of the universe and time, understand the distinctive constitutions and the rules of the world.”

- Chuang Tzu [369 - 286 BC]

Abstract

The nonlinearity and uncertainty of machine parameters impose great difficulties in accurate modeling and optimal efficiency control of interior permanent magnet synchronous motors (IPMSMs) drives. The goal of this thesis is to propose novel control schemes to achieve accurate and robust optimal efficiency control of IPMSM drives in both constant torque region and field weakening region.

Firstly, this thesis proposes a novel virtual signal injection (VSI) based control method for maximum torque per ampere (MTPA) operation and voltage constraint maximum torque per ampere (VCMTPA) operation of IPMSM drives in constant torque region and field weakening region, respectively. The proposed method injects a small virtual current angle signal mathematically for tracking the MTPA/VCMTPA operating points and automatically generates optimal current commands by utilizing the inherent characteristic of the MTPA/VCMTPA operations.

Secondly, this thesis proposes a novel concept that utilizes rotor synchronous reference (d-q) frame based searching techniques to compensate the MTPA/VCMTPA control errors of control schemes in stator flux linkage synchronous reference (f-t) frame. Without loss of generality, the proposed virtual signal injection control is adopted as an example of searching schemes in the d-q frame and the existing direct flux vector control is adopted in the thesis as an example of f-t frame based control schemes.

Thirdly, this thesis proposes a novel self-learning control (SLC) scheme for MTPA and VCMTPA operations based on the proposed virtual signal injection. This control scheme can be trained online and automatically adapt to machine parameter variations.

Finally, a novel hybrid control concept which combines the conventional field orientated control (FOC) and direct flux vector control (DFVC) is proposed to inherit the advantages of d-q frame based control schemes and f-t frame based control schemes.

This thesis is dedicated to my mother:

Ping Hu

Acknowledgements

First and foremost I would like to thank my supervisor, Prof. Jiabin Wang, for his great contributions of guidance, time and support during my Ph.D. study. I am very grateful for his patience of spending lots of time in reviewing my papers and this thesis. It is my honour to be his Ph.D. student, he not only guides me along my research, but also teaches me how to implement researches rigorously. His inculcations will always have profound influence on me. I also want to thank my second supervisor, Prof. Ziqiang Zhu, for his help during my research and study.

I want to thank Dr. Xiao Chen for his knowledge and Mr. Mikail Koc for his collaboration and discussion. I want to thank Dr. Weiya Wang and Dr. Khoa Dang Hoang for their help in preparing experiments. I want to thank Dr. Vipul Patel and Dr. Bhaskar Sen for their introduction of experiment facilities and help in the lab. I also want to thank the fellow people, Mr. Panagiotis Lazari, Mr. Liang Chen, Mr. Chaohui Liu, Dr. Kalhana Colombage for the happy time we spent together.

I want to thank Mr. Andy Race, Mr. John Wilkinson and Mr. Richard Garraway for their help in setting up experimental test rig.

Last but not the least, I want to thank my mother, Ping Hu, my wife, Xiao Shi, and all my family members. Without their support and help, I can never pursue my dreams.

Table of Contents

Abstract	IV
Acknowledgements	VII
Table of Contents	IX
Nomenclatures	XIV
CHAPTER 1 Introduction	1
1.1 Propulsion Motors for EVs and HEVs.....	1
1.2 Permanent Magnet Synchronous Machines	4
1.2.1 SPMSM.....	4
1.2.2 IPMSM.....	5
1.3 Control of IPMSMs.....	7
1.3.1 d-q Frame Based Control	8
1.3.2 f-t Frame Based Control.....	17
1.4 Overview of Research.....	26
1.5 List of Publications	29
CHAPTER 2 Virtual Signal Injection Based Field Orientated Control	31
2.1 Introduction.....	31
2.2 Virtual Signal Injection Based MTPA Control in d-q Frame	34
2.2.1 Principle of Signal Injection Based MTPA Control	34
2.2.2 Virtual Signal Injection.....	36
2.2.3 Implementation of Virtual Signal Injection	40

2.2.4 Simulation Results	42
2.2.5 Experimental Results	44
2.3 Virtual Signal Injection Aided Field Weakening Control	51
2.3.1 Operational Characteristic of Field Weakening Control.....	51
2.3.2 Virtual Signal Injection Aided Field Weakening Control and Its Implementation	52
2.3.3 Simulation Results	55
2.3.4 Experimental Results	63
2.4 Summary	72
CHAPTER 3 Virtual Signal Injection Based Direct Flux Vector Control.....	73
3.1 Introduction.....	73
3.2 Virtual Signal Injection Based MTPA Control in f-t Frame.....	75
3.2.1 Principle of Proposed Control Scheme	75
3.2.2 Implementation of the Proposed Control Scheme	79
3.2.3 Simulation Studies	81
3.2.4 Experimental Results	85
3.3 Virtual Signal Injection Based Field Weakening Control in f-t Frame	92
3.3.1 Principle of Field Weakening Control of Virtual Signal Injection Based Direct Flux Vector Control	93
3.3.2 Implementation	94
3.3.3 Simulation Results	97
3.3.4 Experimental results.....	100
3.4 Summary	104

CHAPTER 4	Self-learning Control Based on Virtual Signal Injection.....	106
4.1	Introduction.....	106
4.2	Self-learning Control in d-q Frame.....	107
4.2.1	MTPA d-axis Current Generation.....	107
4.2.2	Principle of Proposed Self-learning Control Scheme.....	108
4.2.3	Implementation of the Self-learning Control in d-q Frame.....	110
4.2.4	Simulation Results.....	113
4.2.5	Experimental Results.....	120
4.3	Self-learning Control in f-t Frame.....	126
4.3.1	Relationship between Optimal Stator Flux Amplitude and Torque.....	127
4.3.2	Implementation of the Self-learning Control in f-t Frame.....	128
4.3.3	Simulation Results.....	134
4.3.4	Experimental Result.....	144
4.4	Summary.....	151
CHAPTER 5	Hybrid Control Scheme.....	152
5.1	Introduction.....	152
5.2	Principle of the Proposed Hybrid Control Scheme.....	153
5.2.1	Sensitivity of f-t Frame Based Control Schemes to Errors in Reference Flux Amplitude.....	153
5.2.2	Relationship between d-q Frame Based Control and f-t Frame Based Control.....	154
5.3	Implementation of the Proposed Control Scheme.....	157
5.3.1	FOC at Low Speed.....	158

5.3.2 DFVC at High Speed	159
5.3.3 Transition between FOC and DFVC.....	160
5.4 Simulation Results	161
5.4.1 FOC Performance in DFVC Frame	161
5.4.2 Performance of the Proposed Control Scheme during Speed and Torque Changing	162
5.4.3 Control Performance in Transition Region	163
5.4.4 Comparison between Proposed Control and DFVC	164
5.5 Experimental Results	165
5.5.1 FOC at Low Speed	166
5.5.2 Transition between FOC and DFVC.....	167
5.5.3 DFVC at High Speed	169
5.5.4 Field Weakening Control	170
5.6 Summary	171
CHAPTER 6 Conclusions and Future Work.....	173
6.1 Conclusions.....	173
6.1.1 Proposed Virtual Signal Injection Concept.....	173
6.1.2 Extension of the Virtual Signal Injection Control into Field Weakening Region	174
6.1.3 Applied Virtual Signal Injection Control in f-t Frame.....	175
6.1.4 Proposed Self-learning Control.....	176
6.1.5 Proposed Hybrid Control Concept.....	176
6.2 Future Work	177

6.2.1 Utilization of Virtual Signal Injection Control to Control Other Types of Electric Machine Drives.....	177
6.2.2 Improvement of Self-learning Control.....	177
6.2.3 Improvement of Hybrid Control Scheme.....	178
Bibliography	179
List of Figures	189
List of Tables	202
Appendix A	203
A.1 Inverter Configuration.....	203
A.2 Programming the Inverter	204
Appendix B	208
B.1 Simulink Model of Virtual Signal Injection Control in d-q Frame.....	208
B.2 Simulink Model of Virtual Signal Injection Control in f-t Frame.....	212
B.3 Simulink Model of Self-learning Control in d-q Frame.....	217
B.4 Simulink Model of Self-learning Control in f-t Frame	223
B.5 Simulink Model of Hybrid Control Scheme	230
Appendix C	238
Appendix D	245

Nomenclatures

A	Amplitude of injected signal, rad
B_m	Friction coefficient
β	Angle between current vector and q-axis, rad
β_{MTPA}	Optimal β for MTPA operation, rad
L_d, L_q	d- and q-axis inductances, H
I_a	Amplitude of current vector, A
I_{max}	Maximum amplitude of current vector, A
i_a, i_b, i_c	Three phases currents, A
i_α, i_β	Actual or measured α - and β -axis currents, A
i_d, i_q	Actual or measured d- and q-axis currents, A
i_{dmain}	Nominal reference d-axis current, A
i_d^h, i_q^h	d- and q-axis currents with high frequency component, A
i_{dMTPA}, i_{qMTPA}	Optimal d- and q-axis currents for MTPA operation, A
i_d^*, i_q^*	Reference d- and q-axis currents, A
i_{dFW}^*, i_{qFW}^*	Optimal d- and q-axis currents for field weakening operation, A
\mathbf{i}_{dMTPA}	A vector record of d-axis currents of tracked MTPA points, A
i_{dSLC}	Resultant d-axis current command of self-learning control, A
i_f, i_t	f- and t-axis currents, A
i_f^*, i_t^*	Reference f- and t-axis currents, A
\hat{i}_f, \hat{i}_t	Observed f- and t-axis currents, A
i_{tFOC}^*, i_{tDFVC}^*	Reference t-axis currents for FOC and DFVC, A
$\hat{i}_{tFOC}, \hat{i}_{tDFVC}$	Observed t-axis currents for FOC and DFVC, A
J	Moment of inertia of motor and load, $\text{kg} \cdot \text{m}^2$
K	Gain of band-pass filter at ω_h
k_M	Modulation factor of different modulation techniques
$LPFO$	Signal processing block output
p	Number of pole pairs
P_m	Mechanical power, W
R	Stator per-phase resistance, Ω
\mathbf{T}_{MTPA}	A vector record of reference torques of tracked MTPA points, N·m
$\text{Max}(\mathbf{T}_{MTPA})$	The maximum reference torque in \mathbf{T}_{MTPA} , N·m
T_{max}	Maximum reference torque, N·m

T_e	Electromagnetic torque, N·m
T_L	Load torques, N·m
T_e^h	Electromagnetic torque with high frequency component, N·m
T_e^*	Reference torque, N·m
T_{lim}^*	Maximum reference torque to update \mathbf{T}_{MTPA} and Ψ_{sMTPA} , N·m
\hat{T}_e	Observed torque, N·m
T_s	Sampling period, s
v_{max}	The maximum amplitude of voltage vector, V
v_a	Actual voltage vector amplitude, V
v_a^*	Reference voltage vector amplitude, V
v_α, v_β	α - and β -axis voltages, V
v_α^*, v_β^*	Reference α - and β -axis voltages, V
v_{dc}	dc-link voltage, V
v_d, v_q	d- and q-axis voltages, V
v_d^*, v_q^*	Reference d- and q-axis voltages, V
v_{error}	v_{max} minus v_a , V
v_f, v_t	f- and t-axis voltages, V
v_f^*, v_t^*	Reference f- and t-axis voltages, V
V_0 to V_7	Inverter eight output voltage vectors, V
ξ	Damping ratio of closed loop flux observer
ε	Reference torque change threshold of update SLC output, N·m
ε_T	Torque control signal
ε_ψ	Stator flux control signal
μ	Reference voltage amplitude threshold of stop training, V
δ	Actual angle between d-axis and f-axis, rad
$\hat{\delta}$	Observed angle between d-axis and f-axis, rad
$\hat{\delta}_{FOC}$	Observed angle between d-axis and f-axis for FOC, rad
$\hat{\delta}_{DFVC}$	Observed angle between d-axis and f-axis for DFVC, rad
$\Delta\beta$	Injected current angle perturbation signal, rad
Δi_d	d-axis current error compensator, A
Δi_d^*	Reference d-axis error, A
$\Delta\Psi_s$	Flux amplitude error compensator, Wb
$\Delta\Psi_s^*$	Reference flux amplitude error, Wb
ΔT_e^*	Reference torque change, N·m
ω_e	Rotor electrical angular speed, rad/s

ω_h	Angular frequency of injected signal, rad/s
ω_m	Rotor angular speed, rad/s
ω_0	Crossover frequency of closed loop flux observer, rad/s
Ψ_m	Flux linkage due to permanent magnets, Wb
Ψ_α, Ψ_β	α - and β -axis flux amplitudes, Wb
$\hat{\Psi}_\alpha, \hat{\Psi}_\beta$	Observed α - and β -axis flux amplitudes, Wb
Ψ_d, Ψ_q	d- and q-axis flux amplitudes, Wb
Ψ_d^*, Ψ_q^*	Reference d- and q-axis flux amplitudes, Wb
$\hat{\Psi}_d, \hat{\Psi}_q$	Observed d- and q-axis flux amplitudes, Wb
$\Psi_{dMTPA}, \Psi_{qMTPA}$	Optimal d- and q-axis flux amplitudes for MTPA operation, Wb
Ψ_s	Actual flux amplitude, Wb
Ψ_s^*	Reference flux amplitude, Wb
$\hat{\Psi}_s$	Observed flux amplitude, Wb
$\hat{\Psi}_{s_c}$	Flux vector estimated by current model based flux observer, Wb
Ψ_{SLC}	Resultant flux amplitude command of self-learning control, Wb
$\Psi_{sFOC}^*, \Psi_{sDFVC}^*$	Reference flux amplitudes for FOC and DFVC, Wb
$\hat{\Psi}_{sFOC}, \hat{\Psi}_{sDFVC}$	Observed flux amplitudes for FOC and DFVC, Wb
Ψ_{smain}	Nominal reference flux amplitude, Wb
Ψ_{sMTPA}	Optimal flux amplitude for MTPA operation, Wb
Ψ_{sFW}	Optimal flux amplitude for field weakening operation, Wb
Ψ_{sMTPA}	A vector record of flux amplitude of tracked MTPA points, Wb
θ_e	Angle between α - axis and d-axis, rad
θ_s	Angle between α - axis and f-axis, rad
$\hat{\theta}_s$	Observed angle between α - axis and f-axis, rad

CHAPTER 1 Introduction

1.1 Propulsion Motors for EVs and HEVs

The limited petroleum resource is increasingly difficult to support the growing huge energy consumption. Meanwhile, the environmental issues, such as smog, air pollution, greenhouse effect, acid rain, etc., became the main factors that impact human health and economic growth. New energy vehicles, especially the electric vehicles (EV) and hybrid electric vehicles (HEV), are desirable for substitution of traditional internal-combustion engine vehicles. The electric vehicles and hybrid electric vehicles are not only environmental-friendly, but also have very high energy efficient. As reported in [1], for urban traffic, the efficiency range of internal combust engine (ICE) in traditional vehicles is only about 13% - 20%, while the overall efficiency of Tesla Roadster is about 88% [1]. In the circumstance that the governments around the world have made their ambitious goals to reduce greenhouse gas emissions, new energy vehicles increasingly attract worldwide attentions. U.S. has released policies to encourage the development of new energy vehicles. It plans 1.5 million zero-emission vehicles on California roadways by 2025 [2]. Meanwhile, Europe and China also have made their plans to stimulate the development of new energy vehicles. It is reported that from 2004 to 2012, in 8 years, the HEV market increased from 165000 to more than 1.5 million vehicles sold [3]. Huge sales increase will also be achieved for EVs [4].

The core technologies of new energy vehicles include chassis and body technology, propulsion technology, energy storage technology [5]. According to the method for propulsion, the new energy vehicles can be classified into EV and HEV. Further, the EV can also be classified into battery electric vehicles (BEVs), fuel-cell electric vehicles (FCEVs) according to the method of energy storage. The characteristics of different types of new energy vehicles are given in Table 1-1.

As shown in Table 1-1, electric motor drives are essential propulsive components for all of the three types of new energy vehicles, therefore, the improvements of electric motor drives will have significant contributions to the development of new energy vehicles.

Table 1-1
Characteristics of three types of new energy vehicles

Type of vehicle	BEV	HEV	FCEV
Propulsion	electric motor drives	internal combust engine	electric motor drives
		electric motor drives	
Energy system	battery	battery	fuel cells
		ICE generating unit	
Characteristics	zero emission	low emission	zero emission
	independence on crude oil	dependence on crude oil	independence on crude oil
	relatively short driving range	long driving range	long driving range
		complex/high cost	currently high cost
Issues	relatively small battery capacity	integration/managing of multiple energy sources	fuel cell cost
	long charging time	long charging time	fuel generation
	battery safety	battery safety	

Currently, the types of motors adopted by new energy vehicles are mainly induction machines (IMs), permanent magnet synchronous machines (PMSMs), and switched reluctance machines (SRMs). The characteristics of the three types of motors are given in Table 1-2 and the IMs and PMSMs are the main machines adopted by automotive industry.

Table 1-2
Characteristics of three types of motors

Type of motor	IM	PMSM	SRM
Advantage	Low cost	High efficiency	Low cost
	Robust	Mature	Robust
	Mature	High torque/power density	Simple control Wide speed range
Disadvantage	Low efficiency	High cost	High acoustic noise
	Low torque/power density		Low torque/power density
	Difficult cooling		Not mature
Application	Tesla Roadster	Toyota Prius	John Deere 944K
	BMW X5	Honda Insight	Holden ECommodore

As can be seen from Table 1-2, all of the three types of motors have their own advantages and disadvantages, therefore, selection of traction motors for new power vehicles is a very important step that requires special attentions [6].

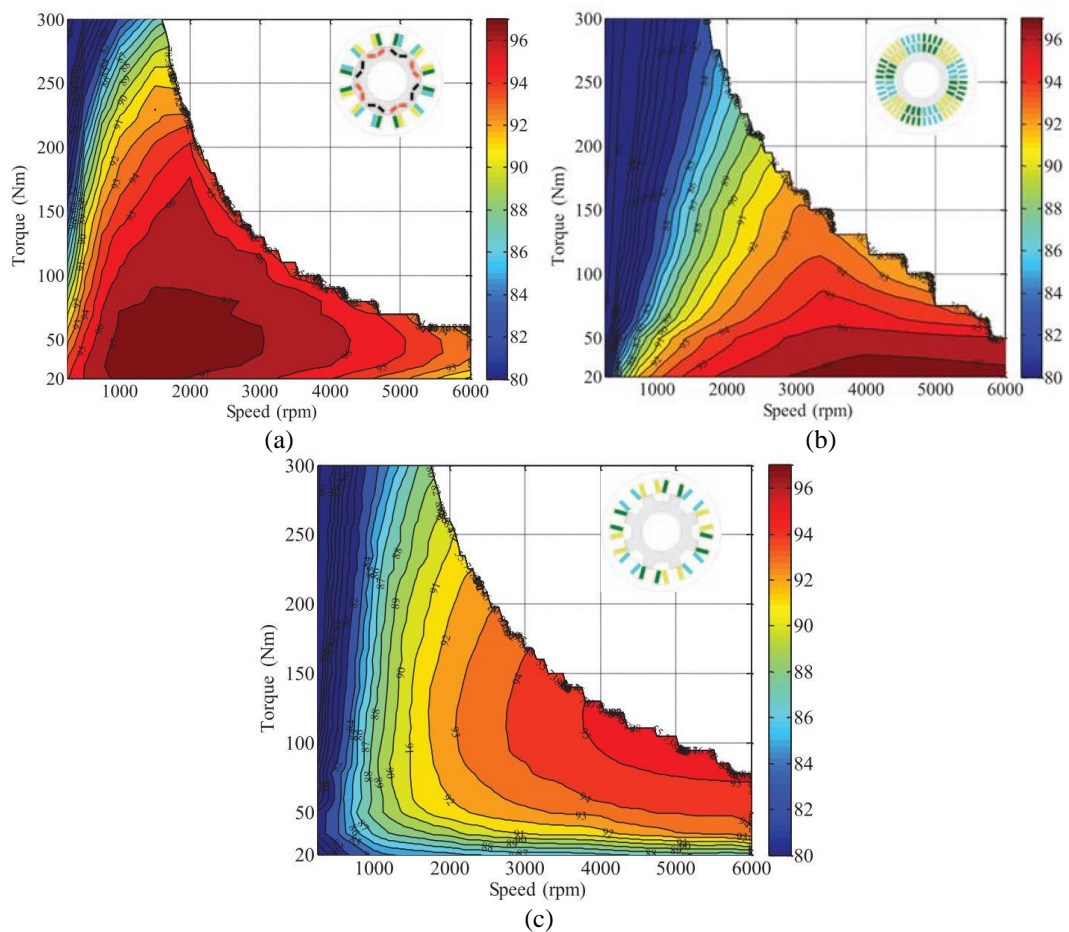


Fig. 1-1. Efficiency map of: (a) IPMSM. (b) IM. (c) SRM. [7]

Comparative studies of the different types of motors have been performed in the literature. Reference [8] reported a survey on experts' opinion on the three types of motors. References [5] and [6] provide general overviews of characteristics associated with different motor types and comparative evaluation methods based on main requirements for HEV propulsion are also discussed. References [9] and [10] compared dynamic operation performances of IM and PMSM propulsion systems based on the energy consumed in drive-cycles, respectively. In [7] and [11], efficiency maps, as shown in Fig. 1-1, of IM, PMSM and SRM related to the steady-state operation are compared. According to [7], PMSMs offer higher efficiency than IMs and SRMs between low- and medium-speed range. However, at high speed, the efficiency of PMSMs will decrease due to increase in iron loss and the PM eddy current losses. While IM delivers the highest efficiency at high speed but has the widest low efficiency region at low speed due to high copper loss [7]. The low efficiency region of SRMs is smaller than that of IMs but larger than that of PMSMs, and the high efficiency region of SRMs is smaller than both of that of the IMs and PMSMs. Moreover, SRMs have more severe vibration deformation than

that of PMSMs [7], which means higher acoustic noise and vibration which poses challenges for noise, vibration and harshness (NVH) qualification.

The energy density of batteries is much lower than that of gasoline while the charging time of batteries is much longer than that of gasoline refuelling. For the purpose of obtaining the maximum mileage per charge and to reduce the greenhouse gas emission, high efficiency motor and minimal loss control methods are required. As the most frequent operation of EVs and HEVs lies between low- and medium-speed ranges, therefore, as discussed above, PMSMs are favoured for EV and HEV applications for the overall power train energy efficiency and longer mileage. This thesis will focus on high efficiency control schemes for one of the most commonly used PMSMs, i.e., the interior permanent magnet synchronous motor (IPMSM), in EV and HEV tractions.

1.2 Permanent Magnet Synchronous Machines

Currently, PMSMs are playing more and more important role in automotive industry and other applications due to their high torque/power density and high efficiency. Based on their rotor topologies, PMSMs can be broadly classified into two main types, i.e., the surface-mounted permanent magnet synchronous motor (SPMSM) and interior permanent magnet synchronous motor (IPMSM). The two types of PMSMs are briefly illustrated below.

1.2.1 SPMSM

The schematic of an SPMSM is shown in Fig. 1-2. The permanent magnets of the SPMSM are mounted on the rotor surface. Since the magnetic permeability of ceramic and rare-earth magnet materials is nearly that of free space [12], the permanent magnet can be considered as a part of air-gap. Therefore, the effective air-gap of a SPMSM seen by the stator winding is equal to the sum of the permanent magnet thickness and the air-gap [13]. Due to the air-gap thickness of the SPMSM around rotor is uniform, the winding inductance is virtually independent of rotor position. Therefore, SPMSMs only have the alignment torque component which is generated from the interaction between the armature reaction and permanent magnet fields. However, due to absence of the

reluctance torque component, SPMSMs tend to consume relatively large amount of permanent magnets and it is not easy to achieve field weakening control. Moreover, since the permanent magnet is mounted on the rotor surface, the mechanical containment of the magnets at high speed has to be carefully addressed.

To ensure safety at high speed when the inverter which drives the SPMSM fails, the maximum induced back electromotive force (emf) has to be limited. This requirement is in conflict with the need for high torque because both back-emf and torque in an SPMSM are proportional to the permanent magnet flux linkage. This conflict can only be resolved by increase in the inverter voltage-ampere (VA) rating, which leads to large inverter size and cost.

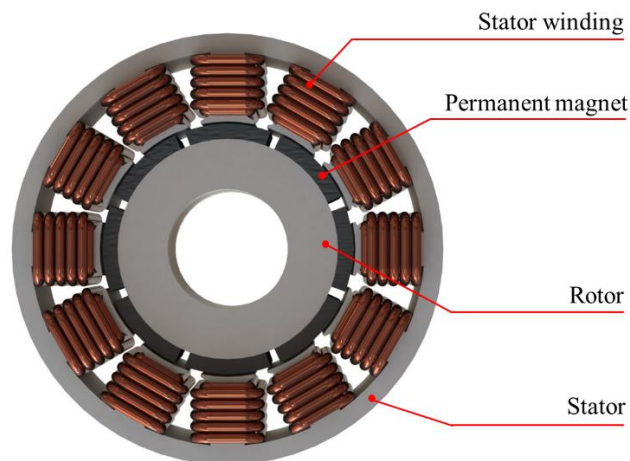


Fig. 1-2. Schematic of SPMSM.

1.2.2 IPMSM

The schematic of an IPMSM is shown in Fig. 1-3. A few typical IPMSM rotor topologies are shown in Fig. 1-4, i.e., internal magnets (I-PMSM), radially arranged internal magnets (RI-PMSM), V-shaped internal magnets (VI-PMSM), respectively [14]. Different from SPMSMs, the permanent magnets of IPMSMs are buried inside the steel rotor core and this difference brings many advantages. First, the permanent magnets are physically contained and protected by the steel rotor core, therefore, the mechanical robustness of IPMSMs is improved, which makes IPMSMs more suitable for high torque, high speed operations. Secondly, since the magnetic permeability of permanent magnet

is different from that of the steel rotor core, the winding inductance varies with rotor position, which generates reluctance torque and improves the field weakening capability. Thirdly, the reluctance torque also decreases the usage of permanent magnets and increases the torque density. Moreover, the IPMSMs also have a very good overload capability over entire speed range [15].

Since the PM flux-linkage contributes a portion of the motor torque, the back-emf of the IPM machine at high speed is much lower compared to an SPMSM counterpart. Therefore, the maximum back-emf in an IPMSM can be easily limited with increase in inverter VA rating.

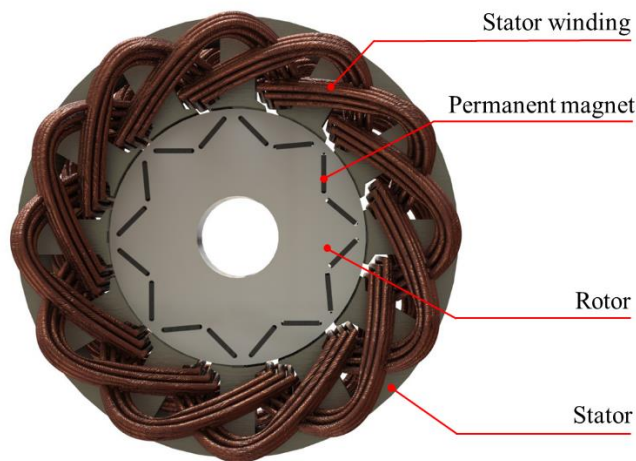


Fig. 1-3. Schematic of IPMSM.

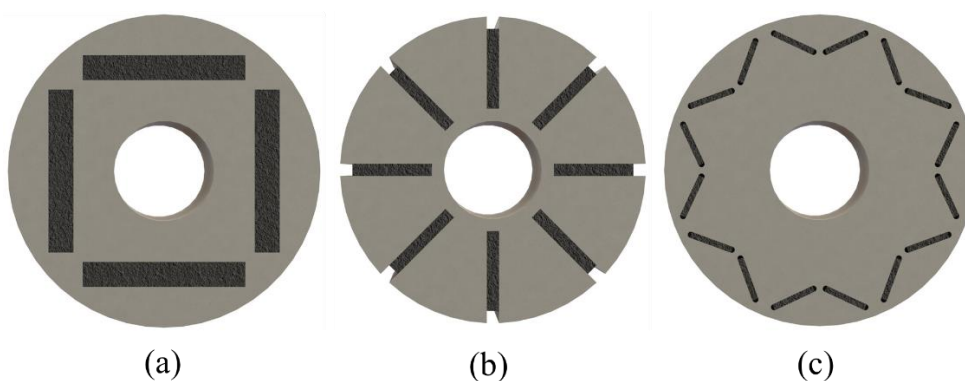


Fig. 1-4. Different IPMSM rotor topologies: (a) I-PMSM. (b) RI-PMSM. (c) VI-PMSM.

1.3 Control of IPMSMs

Due to the advantages of IPMSMs, the IPMSM are increasingly being used in automotive tractions and a variety of applications. To control the IPMSMs, either field oriented control (FOC) in the rotor synchronous reference (d-q) frame [16]–[19] or direct torque control (DTC) [20]–[24] and direct flux vector control (DFVC) [25]–[27] in the stator flux linkage synchronous reference (f-t) frame can be adopted. The relationship between the d-q frame and the f-t reference frame is illustrated in Fig. 1-5. In the d-q frame, the d-axis is aligned with the rotor permanent magnet flux axis and q-axis leads the d-axis by 90 degrees. While for the f-t frame, the f-axis is aligned with the stator flux vector while the t-axis leads the f-axis by 90 degrees. Both the d-q frame and f-t frame rotate in synchronism with the rotor and their angular displacements with respect to the stationary α -axis are θ_e and $\theta_s = \theta_e + \delta$, respectively, where δ is the angular displacement between the d-axis and the f-axis. I_a represents stator current amplitude. i_d , i_q represent the d- and q-axis current components, respectively. i_t , i_f represent the t- and f-axis current components, respectively. Ψ_s is the flux amplitude. β is the current angle between current vector and the q-axis. Control schemes in different reference frames will be reviewed and discussed in the following parts of this chapter.

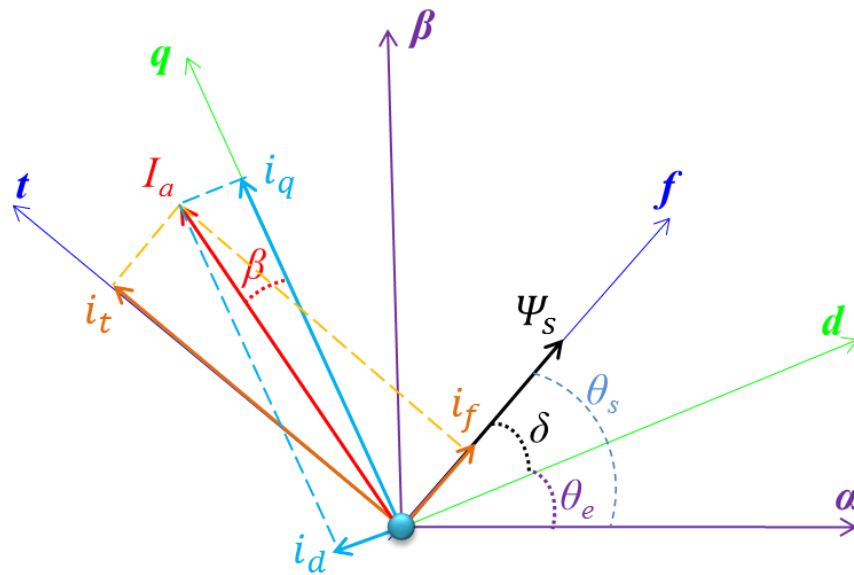


Fig. 1-5. α - β reference frame, f-t reference frame and d-q reference frame.

1.3.1 d-q Frame Based Control

1.3.1.1 Mathematical Model in d-q Frame

The mathematical model of an IPMSM in the d-q reference frame can be expressed as in (1-1) to (1-9) when high order space harmonics are neglected [28], where L_d and L_q are the d- and q-axis inductances, v_d and v_q are the d- and q-axis voltages, respectively. Ψ_m is the flux linkage due to permanent magnets, R is the stator resistance, p is the number of pole pairs, T_e and T_L are the electromagnetic and load torques, respectively. ω_m is rotor angular speed, ω_e is rotor electrical angular speed. B_m is the friction coefficient of the motor and J is the moment of inertia of the motor and load. The current amplitude I_a , expressed in (1-5), should be limited to the maximum permissible current amplitude I_{max} . Similarly, voltage amplitude v_a , expressed in (1-8), should be below the maximum voltage amplitude v_{max} .

$$v_q = L_q \frac{di_q}{dt} + Ri_q + p\omega_m L_d i_d + p\omega_m \Psi_m \quad (1-1)$$

$$v_d = L_d \frac{di_d}{dt} + Ri_d - p\omega_m L_q i_q \quad (1-2)$$

$$T_e = \frac{3p}{2} [\Psi_m i_q + (L_d - L_q) i_q i_d] \quad (1-3)$$

$$T_e = T_L + B_m \omega_m + J \frac{d\omega_m}{dt} \quad (1-4)$$

$$I_a = \sqrt{i_d^2 + i_q^2} \leq I_{max} \quad (1-5)$$

$$i_d = -I_a \sin(\beta) \quad (1-6)$$

$$i_q = I_a \cos(\beta) \quad (1-7)$$

$$v_a = \sqrt{v_d^2 + v_q^2} \leq v_{max} \quad (1-8)$$

$$\omega_e = p\omega_m \quad (1-9)$$

Due to magnetic saturation often present in an IPMSM, the PM flux-linkage and d-q axis inductances are dependent on d-q axis currents. Further, the stator resistance and the PM flux-linkage also vary with temperature, which in turn influences the d-q axis inductances through non-linear magnetic characteristics. Therefore, the parameters of the

machine are largely dependent on operating conditions.

1.3.1.2 MTPA Control of IPMSM in d-q Frame

As can be seen from (1-3), the torque is contributed by the alignment torque component as the result of the interaction of the permanent magnet flux linkage with the q-axis current, and the reluctance torque component due to the difference in the d- and q-axis inductances. According to (1-3), each T_e corresponds to various combinations of d- and q-axis currents. Therefore, to choose an optimal d- and q-axis current combination for minimum loss becomes the main issue of IPMSM drive control.

In order to control the d- and q-axis current, field oriented control (FOC) is adopted [18], [29]–[31]. The schematic of the FOC is shown in Fig. 1-6, where the errors between the reference currents, i_d^* , i_q^* , and the measured currents, i_d , i_q , are fed to two proportional and integral controllers (PI controllers). The reference d- and q-axis voltages, v_d^* , v_q^* , are equal to the sums of the outputs of PI controllers and the decoupling terms. The decoupling terms are introduced to minimize the cross-coupling effect between the d- and q-axis control loops, and hence improve dynamic performance of the drive, particularly at high speed.

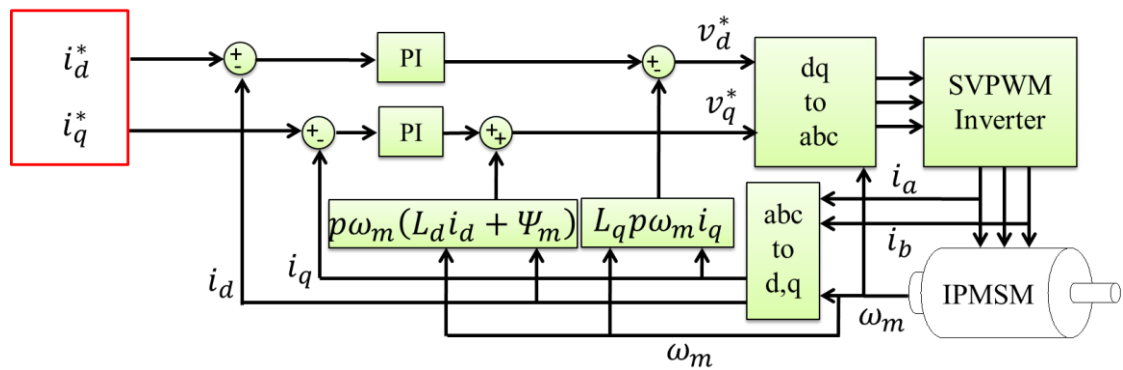


Fig. 1-6. Schematic of FOC.

For field oriented control scheme, as shown in Fig. 1-6, the d- and q-axis currents can be accurately controlled based on the two current feedback loops. At early stages of IPMSM drive development, IPMSMs were controlled by ‘ $i_d=0$ control’ scheme. The ‘ $i_d=0$ control’ is to control the d-axis component of the armature current to zero. The advantage of this control scheme is that the torque is proportional to the armature current

and the demagnetization of permanent magnet materials can be avoided [32]. However, as many permanent magnet materials have large coercive force, there is no need to control PM machines in such a conservative way [31]. The unity power factor control was then proposed to control the power factor always as equal to one. In this way, the current vector is in the same direction as the voltage vector. Beside the unity power factor control, constant flux-linkage control method was proposed to control the phase current such that the flux-linkage and induced electromotive force are kept constant at any load. A comparative study of the three control methods mentioned above was conducted by Shigeo Morimoto and his colleagues in [31].

For EV/HEV traction applications, due to the limited battery capacity, high efficiency IPMSM operations are desired. Since the copper loss is the dominant loss in constant torque region, in order to obtain the maximum torque and reduce the copper loss, the maximum torque per ampere control (MTPA) has been proposed [12], [33]–[35]. The schematic of constant current loci and constant torque loci in the d-q frame are shown in Fig. 1-7. As can be seen in Fig. 1-7, given that the current amplitude is calculated from (1-5), the constant current amplitude loci for different current amplitudes are circles, therefore, the constant current amplitude loci are also named as current circles [36]–[39]. An MTPA point is the point at which a current circle is tangential to a constant torque locus. In other words, MTPA points are the intersection between the constant torque locus and the current circles with minimum magnitude of the current vector, and the MTPA point trajectory is also shown in Fig. 1-7.

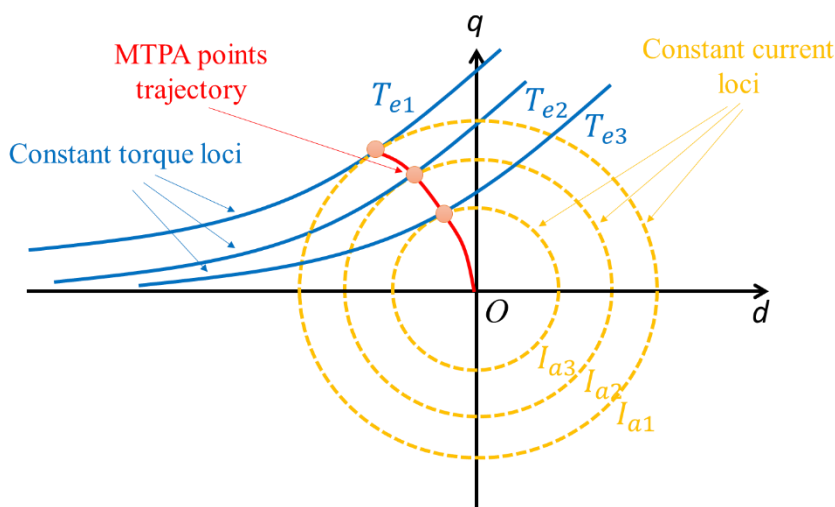


Fig. 1-7. Constant current loci, constant torque loci, and MTPA trajectory.

Since an MTPA point is at the tangent point between a constant torque locus and a current circle, the optimal current angle, β_{MTPA} , for MTPA operation with a given current magnitude I_a can be derived by letting the derivative of torque with respect to the current angle ($\partial T_e / \partial \beta$) to zero. Substituting (1-6), (1-7) into (1-3) and let $\partial T_e / \partial \beta = 0$, the optimal current angle for MTPA operation is expressed in (1-10) [40]:

$$\beta_{MTPA} = \sin^{-1} \frac{-\Psi_m + \sqrt{\Psi_m^2 + 8(L_q - L_d)^2 I_a^2}}{4(L_q - L_d)I_a} \quad (1-10)$$

The optimal d- and q-axis reference currents, i_{dMTPA} , i_{qMTPA} , for MTPA operation can be obtained by substituting (1-10) into (1-6) and (1-7), respectively. It is evident from (1-10) that the current angle for MTPA operation is dependent on the motor parameters, e.g., L_d, L_q and Ψ_m . However, IPMSMs are well-known for their nonlinear machine parameters because of magnetic saturation and cross-coupling effects [40] as shown in Fig. 1-8 for an IPMSM designed for electric vehicle (EV) traction.

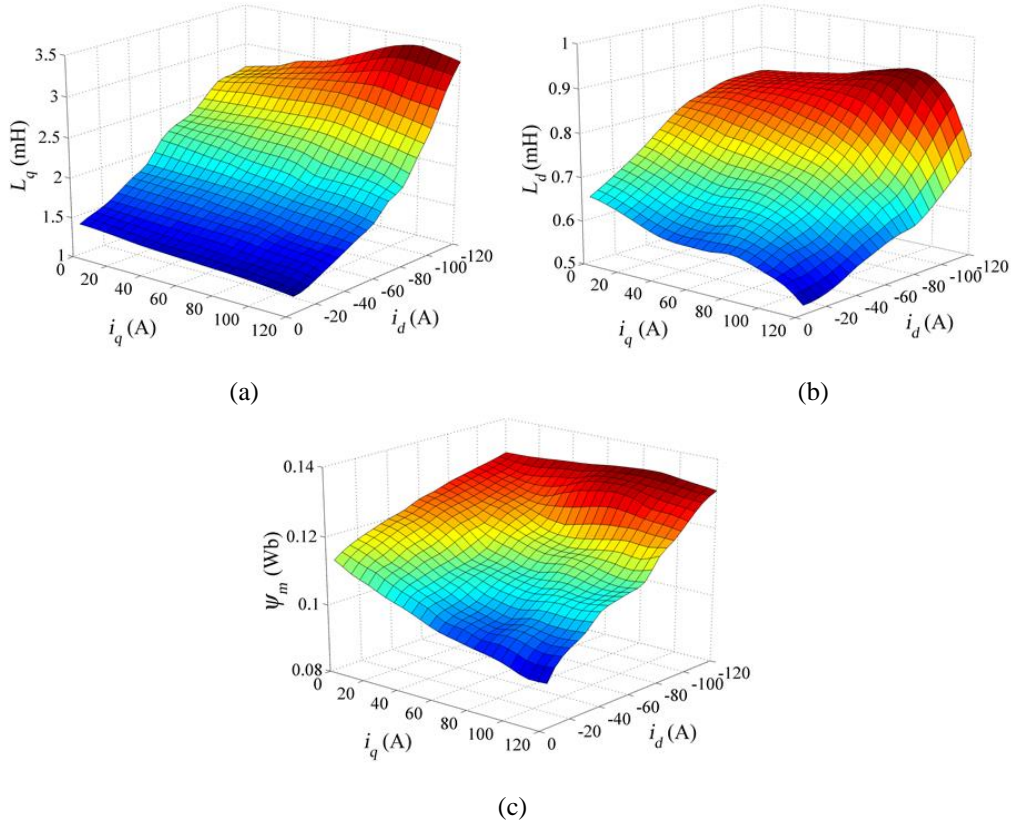


Fig. 1-8. Nonlinear IPMSM machine parameters. (a): L_d as a function of d- and q-axis currents. (b): L_q as a function of d- and q- axis currents. (c): Ψ_m as a function of d- and q-axis currents [41]. The results apply to the machine used throughout this thesis and the data will be given in Chapter 2.

The machine with the parameters shown in Fig. 1-8 will be used throughout this thesis and the data will be given in Chapter 2. Further, since the remanence of permanent magnets varies with temperature, the permanent magnet flux linkage, Ψ_m , is also dependent on temperature and so are L_d, L_q due to cross coupling through magnetic saturation. The nonlinearity and uncertainty of the IPMSM machine parameters imposes a great challenge for realization of the MTPA operation in real-world applications.

In order to achieve MTPA control, many control schemes have been proposed in the literature. In [12], [33]–[35], [42], [43] the MTPA points were calculated assuming that the motor parameters are constant. In order to take the machine parameter nonlinearity into account, d- and q-axis inductances as functions of currents have been proposed in [44]–[46]. While in [36], [40], [47]–[49], look-up tables (LUTs) are utilized to facilitate the MTPA control with nonlinear machine parameters. The LUT data may be obtained from the numerical analysis of electromagnetic field of the machine or from a set of experiments. However, these control schemes highly rely on the prior knowledge of machine parameters or the data stored in look-up tables. As machine parameters vary under influence of magnetic saturation, cross-coupling and temperature [50], [51], the performance of these control schemes cannot be guaranteed.

To achieve machine parameter independent MTPA operation, search algorithms are proposed in [52]–[54] to adjust the current vector until the resultant current amplitude is minimized for a given load torque. These control schemes do not require prior knowledge on motor parameters but exhibits low torque control accuracy under the influence of torque disturbance and current/voltage harmonics. These control schemes also suffer from the relatively poor dynamic performance [29] due to slow converging rate.

Recently, new methods for the MTPA operation by injecting high-frequency current signal into the motor have been proposed. By injecting high-frequency current signals into motor, the resultant torque contains a variable component. Due to the fact that at a MTPA point the variation in torque caused by the variation in the current angle is zero, that is $\partial T_e / \partial \beta = 0$, the MTPA point can be detected and tracked. Since it is less convenient to measure the torque and its variation, variation in speed was utilized in [55]–[57] instead of torque variation. The convergence properties as well as stability of this method were analyzed in [58]. In [59] variation in mechanical power was utilized instead of torque variation. However, these signal injection based control schemes may be affected by harmonics in terminal voltage and current. Moreover, the frequency of

injected signal is limited by hardware and the injected signal results in additional power losses.

In Chapter 2 of this thesis, a novel virtual signal injection control (VSIC) method is proposed. This method is parameter independent in tracking the MTPA point as well as robust to current and voltage harmonics and parameter variations. Moreover, it does not inject any real signal into the motor, and hence the problems associated with real-signal injection such as deterioration in control performance, sensitivity to harmonics, resonant problems and additional power losses are avoided.

1.3.1.3 Field Weakening Control of IPMSM in d-q Frame

According to (1-1), (1-2) and (1-8), the voltage amplitude, v_a , is dependent on rotor speed, ω_m . In real application, v_a should be smaller than v_{max} which is determined by modulation techniques and inverter dc-link voltage. v_{max} can be calculated from (1-11) [50].

$$v_{max} = k_M v_{dc} \quad (1-11)$$

where v_{dc} is the inverter dc-link voltage. k_M , given in Table 1-3, is modulation factor associated with different modulation techniques.

Table 1-3
Characteristics of three types of motors

Modulation technique	Sinusoidal PWM (SPWM)	Third-harmonics injection PWM (THIPWM)	Space vector PWM (SVPWM)	Six-step PWM
k_M	$\frac{1}{2}$	$\frac{1}{\sqrt{3}}$	$\frac{1}{\sqrt{3}}$	$\frac{2}{\pi}$

From (1-1), (1-2), and (1-9), when motor is operated at steady state, (1-8) can be expressed in (1-12).

$$(Ri_d - \omega_e L_q i_q)^2 + (Ri_q + \omega_e L_d i_d + \omega_e \Psi_m)^2 \leq v_{max}^2 \quad (1-12)$$

As the voltage drop across stator resistance is relatively small compared with v_{max} , the voltage drop across stator resistance can be ignored. (1-12) can be expressed in (1-13). The resultant current vector loci for different angular frequencies are also known as voltage ellipse or voltage limit ellipse [16], [34], [36], [60].

$$(L_q i_q)^2 + (L_d i_d + \Psi_m)^2 \leq \frac{v_{max}^2}{\omega_e^2} \quad (1-13)$$

The maximum current circle, voltage ellipses, constant torque loci, and MTPA trajectory are shown in Fig. 1-9. As shown in Fig. 1-9, when ω_e increases, i.e., from ω_{ea} to ω_{ee} , the corresponding voltage ellipse shrinks. When the rotor speed is beyond ω_{eb} , part or whole of the MTPA trajectory will be outside the corresponding voltage ellipse and the MTPA operation at the MTPA points outside the voltage ellipse will not be possible due to the voltage limit. In order to fully utilize the dc-link voltage, field weakening control is needed. As can be seen from Fig. 1-9, points B , C , D are all on the constant torque locus of T_{e1} . When rotor speed is equal to ω_{ed} , the point B , a MTPA point, is outside the voltage ellipse of ω_{ed} . To maintain T_{e1} , the motor can be operated at point C by increasing d-axis current amplitude while decreasing q-axis current amplitude, as shown in Fig. 1-9. Similarly, when rotor speed is equal to ω_{ee} , the motor can be operated at point D . Since the d-axis is aligned with the rotor permanent magnet flux axis, increase of the magnitude of negative d-axis current will increase the component of reaction flux which is opposite to the flux excited by rotor permanent magnets and the resultant flux will be weakened. Therefore, such control scheme is called flux weakening or field weakening control [19], [38], [61].

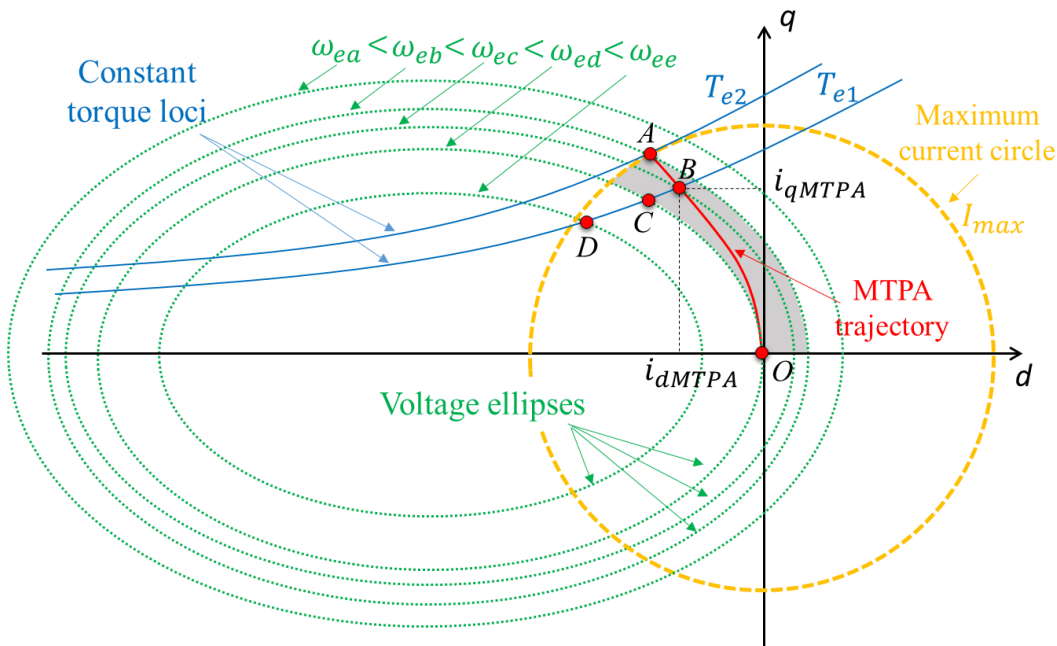


Fig. 1-9. Maximum current circle, voltage ellipses, constant torque loci, and MTPA trajectory of IPMSM in d-q axes coordinate.

Fig. 1-10 shows the variations of torque and voltage amplitude with d-axis current for a given current amplitude, I_a , when the required voltage for the MTPA operation is greater than the voltage limit. If the d-axis current magnitude decreases towards the MTPA point, the torque and v_a will increase. Therefore, when voltage amplitude is equal to the voltage limit, the motor can produce the maximum torque with the given current amplitude, and this condition is independent of iron loss because it is uniquely determined by the voltage limit and current amplitude. Such operation points are named as voltage constrained maximum torque per Ampere (VCMTPA) points [62].

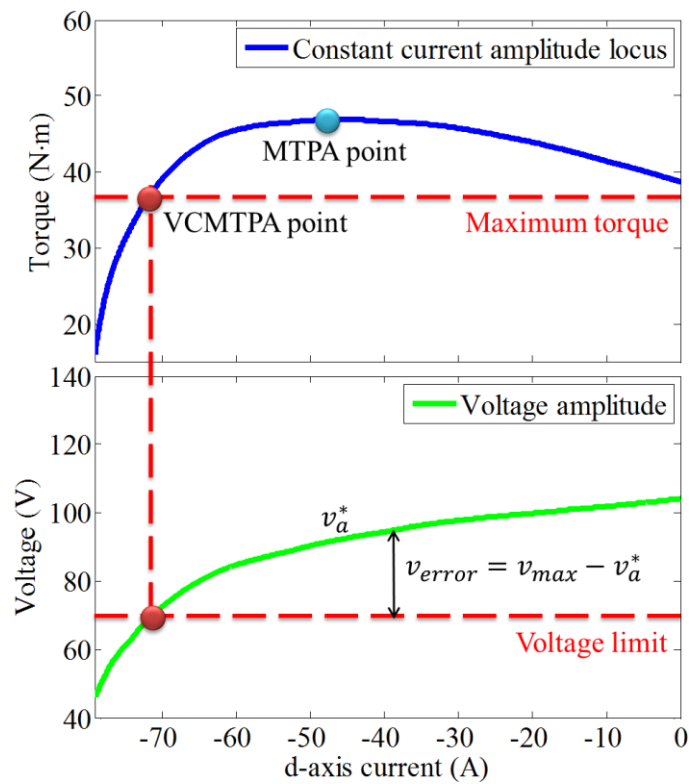


Fig. 1-10. Variations of torque and voltage amplitude with d-axis current for given current amplitude I_a .

According to (1-13), the VCMTPA reference d-axis current, i_{dFW}^* , for field weakening control is expressed in (1-14).

$$i_{dFW}^* = -\frac{\Psi_m}{L_d} + \frac{1}{L_d} \sqrt{\frac{(v_{max})^2}{\omega_e^2} - L_q^2 i_q^2} \quad (1-14)$$

As mentioned above, in order to expand the speed operating range, field-weakening control is needed. In general, there are two kinds of field-weakening controls in the d-q frame. One is feed forward [42], and the other is feedback field-weakening control [63]. The feed forward field weakening control is based on PMSMs mathematical model [64].

When motor is operated in field weakening region, if the reference d-axis current for field weakening control is insufficient, the current control loop will saturate and the corresponding v_a^* will be larger than v_{max} , which causes v_{error} to be negative. The negative v_{error} will drive the Δi_d to increase in the negative direction, and as a result, the amplitude of the d-axis reference current, i_d^* , increases until $v_{error} = 0$. Thus, Δi_d will compensate for insufficient d-axis current to prevent the current regulators from saturation by decreasing v_a until it equals to v_{max} . The compensation is parameter independent.

However, when the amplitude of the reference d-axis current is larger than the amplitude of the VCMTPA d-axis current due to the inaccurate machine parameters, according to Fig. 1-10, v_a^* is smaller than v_{max} . Therefore, Δi_d will be kept equal to zero and the voltage feedback loop is no longer in action and hence the VCMTPA control in the field weakening region cannot be achieved.

In order to avoid the disadvantages of the conventional feed forward and feedback field weakening control, in this thesis, a novel field weakening control scheme that combines virtual signal injection control (VSIC) together with voltage feedback based field weakening control is proposed in Chapter 2. The proposed novel field weakening control scheme also exploits the advantages of feed forward field weakening control method so that it not only has fast response to torque demand but also is parameter independent in searching the minimal current amplitude points, i.e., the MTPA in constant torque region and VCMTPA points in field weakening region.

1.3.2 f-t Frame Based Control

1.3.2.1 Direct Torque Control

The IPMSM motor drives can also be controlled in the f-t frame which is shown in Fig. 1-5. Compared with the d-q frame based control, the f-t frame based control can regulate the stator flux amplitude directly and can manage motor voltage limit in field weakening region without look-up tables of current or flux references [65]. Therefore, the f-t frame based control scheme can easily cope with voltage saturation and has better performance in field weakening region [66], [24].

In order to control motors in the f-t frame, direct torque control (DTC) was firstly proposed by Takahashi and Noguchi [67] for induction motor drives. Since then, the DTC became another important control scheme beside the FOC. In the literature, conventional DTC is mainly achieved by controlling the stator flux magnitude and electromagnetic torque through hysteresis regulators based on switching tables [68]–[70].

The principle of the conventional DTC operation is shown in Fig. 1-12. For a two-level inverter, there are eight output voltage vectors, i.e., 6 active vectors V_1 to V_6 and two zero voltage vectors V_0 and V_7 [71], [72]. Due to the trajectory of stator flux vector $\bar{\Psi}_s$ moves in the direction of the inverter output voltage vector [67], the stator flux vector and torque can be controlled through voltage vectors directly. For example, as shown in Fig. 1-12, the f-axis is aligned with $\bar{\Psi}_s$, while the t-axis leads the f-axis by 90 degrees. If a voltage vector with positive f-axis component, i.e., V_2 or V_6 , is applied to the stator winding, the amplitude of $\bar{\Psi}_s$ increases, otherwise, if V_3 or V_5 is applied, the amplitude of $\bar{\Psi}_s$ decreases. Similarly, if a voltage vector with positive t-axis component, i.e., V_2 or V_3 , is applied to stator winding, the resultant torque increases, otherwise, if V_5 or V_6 is applied, the torque decreases. In this way, the trajectory of $\bar{\Psi}_s$ can be controlled within the hysteresis band shown in Fig. 1-12.

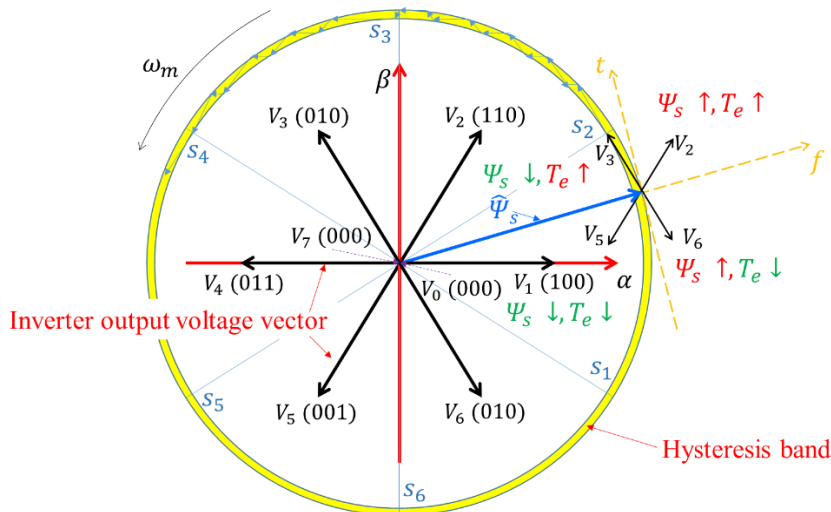


Fig. 1-12. Principle of DTC operation.

In order to properly select the optimal voltage vectors, the α - β plane is divided into six sectors, i.e., S_1 to S_6 . The torque and stator flux control signals ε_T and ε_ψ from the hysteresis comparators are defined in (1-18) and (1-19), respectively.

$$\varepsilon_T = \begin{cases} 1 & \text{increase } T_e \\ -1 & \text{decrease } T_e \end{cases} \quad (1-18)$$

$$\varepsilon_\psi = \begin{cases} 1 & \text{increase } \Psi_s \\ -1 & \text{decrease } \Psi_s \end{cases} \quad (1-19)$$

The optimal switching table for appropriate selection of the voltage vectors is given in Table 1-4.

Table 1-4
Optimal switching table

Sector	S_1	$(\varepsilon_T, \varepsilon_\psi)$	$(-1,-1)$	$(-1,1)$	$(1,-1)$	$(1,1)$
		Voltage vector	V_5	V_6	V_3	V_2
	S_2	$(\varepsilon_T, \varepsilon_\psi)$	$(-1,-1)$	$(-1,1)$	$(1,-1)$	$(1,1)$
		Voltage vector	V_6	V_1	V_4	V_3
	S_3	$(\varepsilon_T, \varepsilon_\psi)$	$(-1,-1)$	$(-1,1)$	$(1,-1)$	$(1,1)$
		Voltage vector	V_1	V_2	V_5	V_4
	S_4	$(\varepsilon_T, \varepsilon_\psi)$	$(-1,-1)$	$(-1,1)$	$(1,-1)$	$(1,1)$
		Voltage vector	V_2	V_3	V_6	V_5
	S_5	$(\varepsilon_T, \varepsilon_\psi)$	$(-1,-1)$	$(-1,1)$	$(1,-1)$	$(1,1)$
		Voltage vector	V_3	V_4	V_1	V_6
	S_6	$(\varepsilon_T, \varepsilon_\psi)$	$(-1,-1)$	$(-1,1)$	$(1,-1)$	$(1,1)$
		Voltage vector	V_4	V_5	V_2	V_1

The block diagram of the DTC is shown in Fig. 1-13. The torque regulator and flux regulator are two hysteresis comparators. The inputs of the torque regulator is the error between reference torque, T_e^* , and observed torque, \hat{T}_e . The output of the torque regulator is torque control signal, ε_T . While the input of the flux regulator is the error between reference flux amplitude, Ψ_s^* , and observed flux amplitude, $\hat{\Psi}_s$. The output of the flux regulator is flux control signal, ε_ψ . Then the resultant ε_T and ε_ψ are input into the switching table in Table 1-4 and the voltage vectors can be selected.

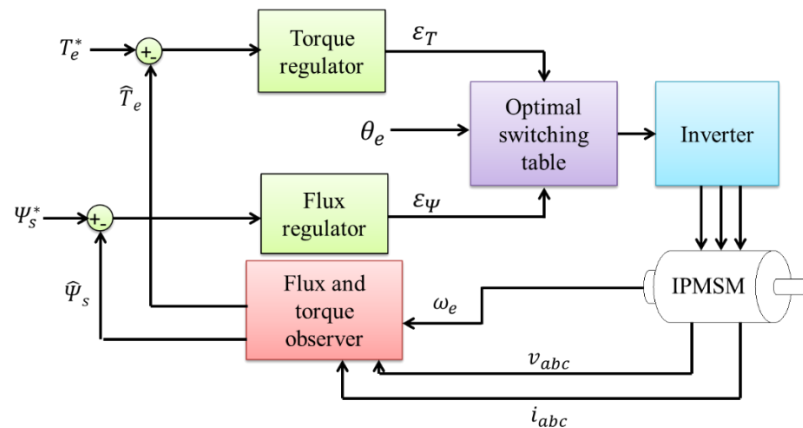


Fig. 1-13. Block diagram of DTC scheme

Compared with the FOC, the conventional DTC does not need integral regulators, therefore, the DTC has an arguably faster torque response than FOC [21]. Moreover, since the DTC directly controls stator flux magnitude, it can easily achieve field weakening control by directly limiting the flux magnitude. However, in real applications, due to time delay caused by the fixed sampling rate of a controller, the stator flux and torque will exceed the predefined hysteresis bands, which causes relative large flux chattering and torque ripples. And the hysteresis band also causes undesired steady-state torque control error [69], [70] as well as variable switching frequency.

1.3.2.2 Improved Direct Torque Control

To solve the issues of the conventional DTC, in [20], [73], space vector pulse width modulation (SVPWM) is integrated in the DTC and the torque ripple is significantly reduced. The block diagram of the improved DTC by means of space vector modulation is shown in Fig. 1-14.

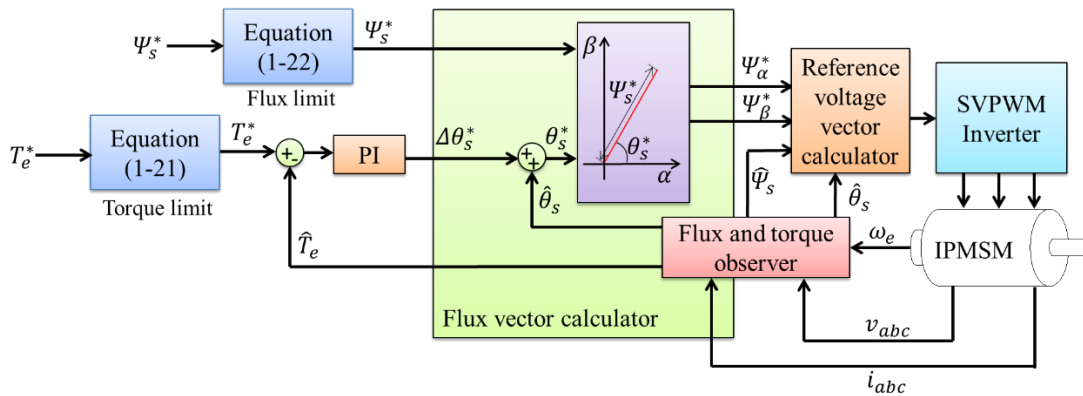


Fig. 1-14. Block diagram of improved DTC

As shown in Fig. 1-14, instead of the hysteresis controllers and switching table, the flux vector of the improved DTC is directly determined by reference flux amplitude, Ψ_s^* , and reference flux linkage position, θ_s^* . A proportional and integral (PI) controller is utilized to obtain the change of flux linkage position, $\Delta\theta_s^*$, within each sample time through torque error. The θ_s^* is equal to the observed flux linkage position, $\hat{\theta}_s$, plus $\Delta\theta_s^*$. The reference voltage vector can be calculated by the reference voltage vector calculator based on (1-20), where \vec{v}_a^* is reference voltage vector, $\vec{\Psi}_s^*$ is reference flux vector, $\hat{\vec{\Psi}}_s$ is observed flux vector, T_s is sampling period.

$$\vec{v}_a^* = \frac{\vec{\Psi}_s^* - \widehat{\vec{\Psi}}_s}{T_s} \quad (1-20)$$

The reference torque is limited by the maximum torque, T_{max} , which can be calculated from (1-21), where i_f is the f-axis current.

$$T_e \leq T_{max} = \frac{3}{2} p \widehat{\Psi}_s \sqrt{I_{max}^2 - i_f^2} \quad (1-21)$$

In field weakening region, in order to maintain the voltage amplitude, v_a , within the maximum voltage amplitude, v_{max} , the flux amplitude is limited by (1-22), where ω_e is rotor electrical angular speed, R is the stator armature resistance, i_t is t-axis current component.

$$\Psi_s \leq \frac{1}{\omega_e} \left[\sqrt{v_{max}^2 - (Ri_f)^2} - Ri_t \right] \quad (1-22)$$

The improved DTC retains the advantages of conventional DTC, e.g., independence of machine parameters in field weakening region, no current control loop, etc., [20]. Moreover, due to the integration of SVPWM, the torque ripple is effectively reduced.

1.3.2.3 Direct Flux Vector Control

Direct flux vector control (DFVC) [25]-[27] is another kind of control scheme in the f-t frame. This control scheme directly controls flux amplitude and t-axis current based on the mathematical model of IPMSM in the f-t frame. The mathematical model is expressed in (1-23) to (1-26).

$$v_f = Ri_f + \frac{d\Psi_s}{dt} \quad (1-23)$$

$$v_t = Ri_t + \Psi_s \left(p\omega_m + \frac{d\delta}{dt} \right) \quad (1-24)$$

$$T_e = \frac{3}{2} p \Psi_s i_t \quad (1-25)$$

$$i_t \leq \sqrt{I_{max}^2 - i_f^2} \quad (1-26)$$

The block diagram of the direct flux vector control is shown in Fig. 1-15. To ensure the IPMSM drive operates within the current and voltage limits, the reference torque, T_e^* , is limited by (1-21). The reference flux amplitude, Ψ_s^* , is limited by (1-22), i.e., for field weakening control. The t-axis reference current, i_t^* , is generated from (1-25) and limited

by (1-26). The observed flux amplitude and t-axis current are denoted by $\hat{\Psi}_s$ and \hat{i}_t respectively. As proposed in [25], the stator flux linkage is directly regulated by the f-axis voltage while the t-axis current is regulated by the t-axis voltage. Compared with the DTC, the advantage of DFVC is that the stator current amplitude can be effectively limited since the t-axis current in DFVC is controlled in closed loop [25]. More details for the DFVC can be found in [25].

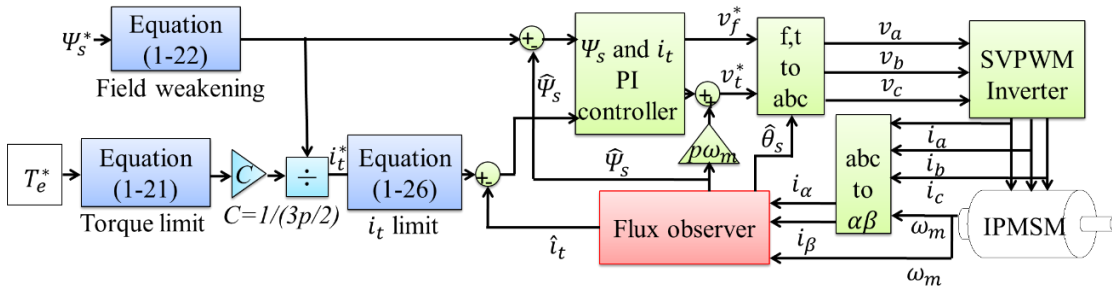


Fig. 1-15. Block diagram of direct flux vector control.

1.3.2.4 Flux Observer

For the f-t reference frame based control, a flux observer is needed. The flux vector can either be estimated from voltage model given in (1-27) or from current model given in (1-28). Here $\hat{\Psi}_\alpha$ and $\hat{\Psi}_\beta$ are the observed α - and β -axis flux components. v_α^* and v_β^* are the α - and β -axis reference voltages, i_α and i_β are the measured α - and β -axis currents. $\hat{\Psi}_d$ and $\hat{\Psi}_q$ are the observed d- and q-axis flux components.

$$\begin{bmatrix} \hat{\Psi}_\alpha \\ \hat{\Psi}_\beta \end{bmatrix} = \begin{bmatrix} \int (v_\alpha^* - Ri_\alpha) dt \\ \int (v_\beta^* - Ri_\beta) dt \end{bmatrix} \quad (1-27)$$

$$\begin{bmatrix} \hat{\Psi}_d \\ \hat{\Psi}_q \end{bmatrix} = \begin{bmatrix} L_d i_d + \Psi_m \\ L_q i_q \end{bmatrix} \quad (1-28)$$

The block diagrams of voltage model based flux observer and current model based flux observer are given in Fig. 1-16 and Fig. 1-17, respectively.

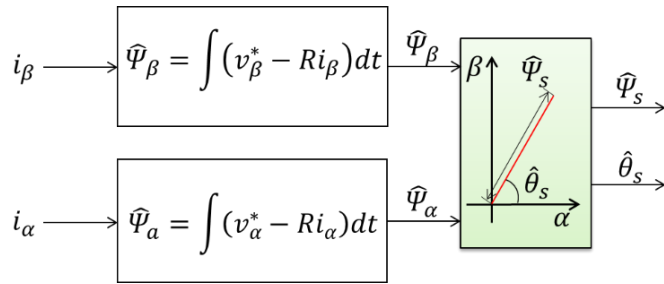


Fig. 1-16. Block diagram of voltage model based flux observer.

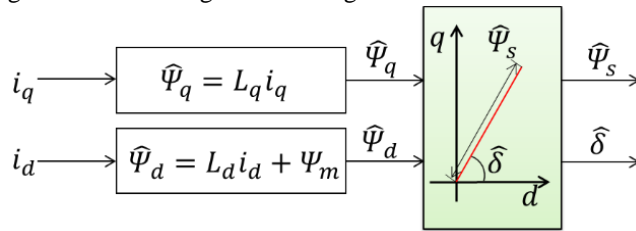


Fig. 1-17. Block diagram of voltage model based flux observer.

As can be seen from Fig. 1-16, voltage model based flux observer is independent from machine parameters except stator resistance. Since at high speed the voltage drops on the stator resistant and inverter are relatively small compared with voltage amplitude, the stator resistance can be assumed as its nominal value and the flux vector can be estimated by voltage model based flux observer with relatively high accuracy [74].

In practice, since the voltage model based flux observer is based on integration of the induced voltage, voltage model based flux observer may suffer from drifting problem. In order to avoid the drifting issue, closed loop flux observer was proposed. The simplified block diagram of closed loop flux observers is illustrated in Fig. 1-18. The $\widehat{\psi}_{s_c}$ in Fig. 1-18 is the flux vector estimated by current model based flux observer, and $\widehat{\psi}_s$ is the output of the closed loop flux observer. \vec{v}_a and \vec{i}_a are voltage and current vectors, respectively. As can be seen from Fig. 1-18, the difference between $\widehat{\psi}_{s_c}$ and $\widehat{\psi}_s$ is input into a proportional and integral (PI) controller to correct the voltage model based flux observer.

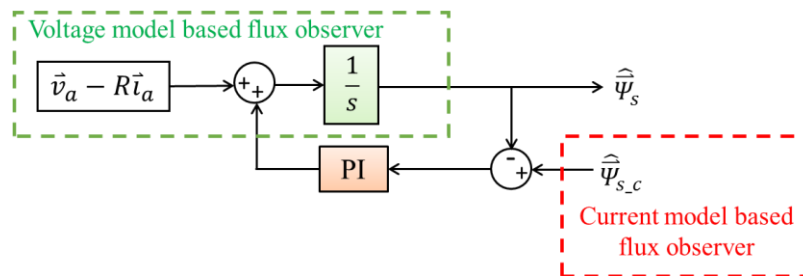


Fig. 1-18. Simplified block diagram of closed loop flux observers.

At low speed, since the voltage amplitude is relatively small, the stator resistance and inverter voltage drop may have significant effect on voltage model based flux observer. Therefore, at low speed, current model based flux observer is preferred although the current model based flux observer relies on machine parameters as shown in Fig. 1-17, and inaccurate machine parameters may affect the accuracy of current model based flux observer.

In order to take the advantages of current model based flux observer at low speed and voltage model based flux observer at high speed, the PI controller in closed loop flux observer is tuned for the best combination of the two model based flux observers. The block diagram of the conventional closed loop flux observer is shown in Fig. 1-19. ξ and ω_0 of the PI controller in Fig. 1-19 are the damping ratio and crossover frequency, respectively, associated with the combination of the two outputs. As discussed in [75], the voltage model will be dominant above the predefined crossover frequency while the current model will be dominant below the crossover frequency.

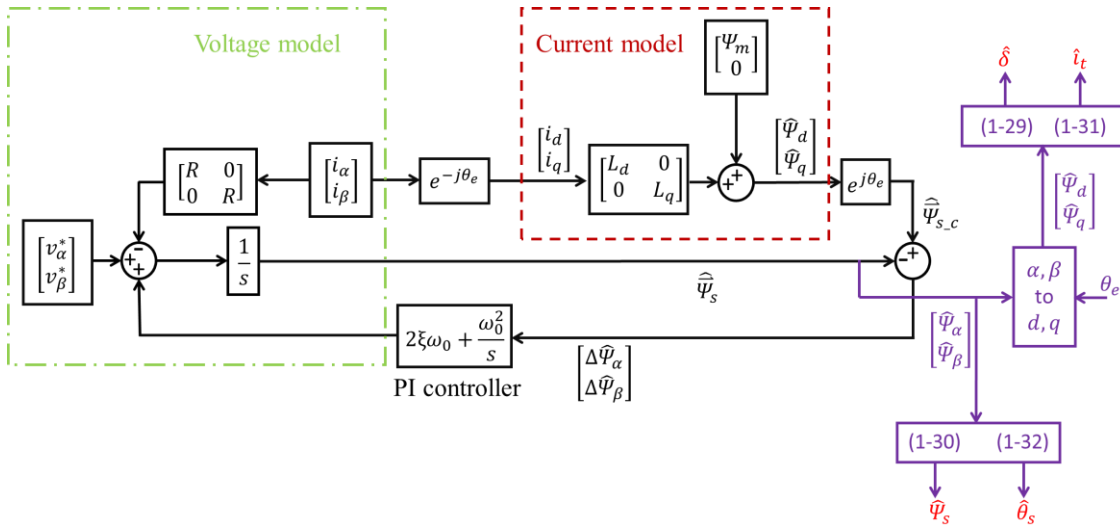


Fig. 1-19. Block diagram of flux observer.

The observed d- and q-axis fluxes, $\hat{\Psi}_d$ and $\hat{\Psi}_q$, can be obtained through $\hat{\Psi}_\alpha$, $\hat{\Psi}_\beta$ and θ_e , as shown in Fig. 1-5. The estimated angle between the f-axis and the d-axis, $\hat{\delta}$, can be calculated from (1-29):

$$\hat{\delta} = \tan^{-1} \frac{\hat{\Psi}_q}{\hat{\Psi}_d} \quad (1-29)$$

The observed flux amplitude $\hat{\Psi}_s$ can be calculated from (1-30):

$$\hat{\Psi}_s = \sqrt{\hat{\Psi}_\alpha^2 + \hat{\Psi}_\beta^2} \quad (1-30)$$

The observed t-axis current, \hat{i}_t , can be generated from (1-31) with the measured d- and q-axis currents, i_d and i_q .

$$\hat{i}_t = i_q \cos \hat{\delta} - i_d \sin \hat{\delta} \quad (1-31)$$

The estimated angle between f-axis and α -axis, $\hat{\theta}_s$, can be calculated from (1-32).

$$\hat{\theta}_s = \tan^{-1} \frac{\hat{\Psi}_\beta}{\hat{\Psi}_\alpha} \quad (1-32)$$

The closed loop flux observer shown in Fig. 1-19 is adopted in this thesis.

1.3.2.5 MTPA Control in f-t Frame

As mentioned above, the f-t frame based control schemes can easily cope with the field weakening control by directly limiting the reference flux amplitude. However, due to the machine parameter uncertainty and nonlinearity, MTPA operation in the f-t frame is also challenging.

Currently, MTPA operations for f-t frame based control schemes are mainly achieved by controlling the reference flux amplitude. The optimal reference flux amplitude can be generated through mathematical model [76] or pre-defined look-up tables which are obtained from experiments or numerical machine model [41]. However, the f-t frame based MTPA control schemes are affected not only by the error in the reference flux amplitude due to the machine parameter uncertainty and nonlinearity, but also by the flux observer error in the flux control loop [77]. Thus, compared with d-q frame based MTPA control schemes, f-t frame based control schemes are vulnerable to flux errors in the reference and observer [62].

In order to reduce the dependency on motor parameters for MTPA operations with the f-t frame based control of IPMSM drives, search algorithms were, therefore, proposed in [78]. Although this scheme does not depend on the knowledge of machine parameters, its accuracy was affected by voltage and current harmonics and load torque disturbance. In [79], a signal injection based MTPA point tracking scheme was proposed based on the principle of extremum seeking control (ESC) [80], [58]. The MTPA tracking is based on the fact that the rate of change of current amplitude with respect to injected reference flux perturbation at MTPA points is zero. Instead of injecting sinusoidal signal at fixed

frequency [55], [58], [59], this control method injects a random signal into the reference flux amplitude to avoid the residual torque harmonic at the injected signal frequency. However, as a result of the injected signal, this method causes additional copper/iron loss and additional torque ripple. Moreover, the errors in flux observer may also deteriorate the MTPA control quality.

In Chapter 3 of this thesis, a novel MTPA control scheme in the f-t frame is proposed. This control scheme adopts a novel concept that utilizes d-q frame based searching techniques to compensate the MTPA control errors of the f-t frame based control schemes. In this way, the proposed f-t frame based control will be independent from flux observer errors. Moreover, by using the d-q frame based searching schemes to compensate the error of reference flux amplitude, the MTPA control accuracy and the robustness of the f-t frame based control scheme can be significantly increased.

1.4 Overview of Research

The main objective of the research described in the thesis is to address the difficulty of accurate MTPA operation and VCMTPA operation of IPMSMs due to the nonlinear machine parameters and machine parameter variations. The thesis contains 6 chapters and the content of each chapter is briefly summarized below.

Chapter 1 introduces the global trend of new energy vehicles and compares different types of motors adopted by new energy vehicles. Chapter 1 also introduces the state of the art of MTPA operation and field weakening operation for IPMSMs in the d-q frame or f-t frame and compares the advantages and disadvantages of each control scheme. The technical challenges for realising MTPA and VCMTPA operations over a wide torque speed range with varying temperature and battery voltage are highlighted, and limitations of the current state-of-the art in addressing these challenges are also described.

Chapter 2 proposes a novel virtual signal injection control (VSIC) method for MTPA operation and field weakening operation of IPMSM drives in the d-q frame. The proposed method injects a small virtual current angle signal mathematically for tracking the MTPA or VCMTPA operating point and generating d-axis current command by utilizing the inherent characteristic of the MTPA and VCMTPA operation. This method is parameter independent in tracking the MTPA/VCMTPA points and it does not inject any real signal

to current or voltage command. Consequently, the problems associated with real high-frequency signal injection, such as increases in copper and iron loss can be avoided. Moreover, it is robust to current/voltage harmonics and motor torque disturbances. The proposed method is verified by simulations and experiments under various operating conditions on a prototype IPMSM drive system.

Chapter 3 proposes a novel concept that utilizes d-q frame based searching techniques to compensate the MTPA control errors of the f-t frame based control schemes. Without loss of generality, the direct flux vector control is adopted in Chapter 3 as an example of the f-t frame based control scheme and the virtual signal injection control (VSIC) is adopted as an example of searching scheme in the d-q frame. The proposed method virtually injects a small high frequency current angle signal for tracking the optimal flux amplitude of MTPA operation in constant torque region. A control method that can achieve smooth transition between constant torque region and field weakening region is also proposed in Chapter 3. The proposed control scheme in Chapter 3 is not affected by the accuracy of flux observer and is independent of machine parameters in tracking the MTPA points and will not cause additional iron loss, copper loss and torque ripple as a result of real signal injection. Moreover, by employing a band-pass filter with a narrow frequency range the proposed control scheme is also robust to current and voltage harmonics, and load torque disturbances. The proposed method is verified by simulations and experiments under various operating conditions on a prototype IPMSM drive system.

Chapter 4 proposes novel self-learning control schemes for IPMSM drives to achieve MTPA operation in constant torque region and VCMTPA operation in field weakening region with fast response. The proposed self-learning control schemes (SLC) are based on the virtual signal injection control proposed in Chapter 2 and 3. Initially the reference d-axis currents or reference flux amplitudes for MTPA operation are tracked by virtual signal injection, and the data are used by the proposed control scheme to train the reference d-axis current map or reference flux map. After training, the proposed control scheme generates the optimal reference d-axis current or reference flux amplitude with fast dynamic response. The proposed control scheme can achieve MTPA or VCMTPA control fast and accurately without accurate prior knowledge of machine parameters and can adapt to machine parameter changes during operation. The proposed control scheme is verified by simulations and experiments under various operation conditions.

Chapter 5 proposes a novel hybrid control scheme for IPMSM drives. The proposed control scheme combines conventional field orientated control (FOC) with direct flux vector control (DFVC). At low speeds, the machine drive is controlled through d- and q-axis currents, while at high speeds the direct flux vector control is adopted. A shape function is utilized by the proposed control scheme to achieve smooth transition between the two control schemes. Therefore, the proposed control scheme inherits the advantages of both the direct flux vector control and field orientated control while avoiding their disadvantages. The proposed control scheme is verified by simulations and experiments under various operation conditions on a prototype IPMSM drive.

Chapter 6 presents the conclusion and suggestion for future work.

Finally, at the end of this thesis, the configuration of the inverter adopted for the experiments in this thesis and the introduction of programming the inverter is provided in Appendix A. The key blocks in Simulink models of the proposed control schemes in this thesis is given in Appendix B. The error analysis of virtual signal injection is given in Appendix C. Appendix D introduces the high fidelity machine model adopted by the thesis.

1.5 List of Publications

Journal Papers:

1. **T. Sun**, J. Wang, M. Koc, “Virtual Signal Injection Based Direct Flux Vector Control of IPMSM Drives”, *IEEE Transactions on Industrial Electronics.*, accepted.
2. **T. Sun**, J. Wang, M. Koc, X. Chen, “Self-Learning MTPA Control of Interior Permanent Magnet Synchronous Machine Drives Based on Virtual Signal Injection”, *IEEE Transactions on Industrial Applications.*, in press.
3. **T. Sun**, J. Wang, “ Extension of Virtual Signal Injection Based MTPA Control for Interior Permanent Magnet Synchronous Machine Drives into Field Weakening Region”, *IEEE Transactions on Industrial Electronics.*, vol. 62, no. 11, pp. 6809–6817, 2015.
4. **T. Sun**, J. Wang, X. Chen, “ Maximum Torque per Ampere (MTPA) Control for Interior Permanent Magnet Synchronous Machine Drives Based on Virtual Signal Injection”, *IEEE Transactions on Power Electronics.*, vol. 30, no. 9, pp. 5036–5045, 2015.

Conference Papers:

1. **T. Sun**, J. Wang, M. Koc, X. Chen, “Self-Learning MTPA Control of Interior Permanent Magnet Synchronous Machine Drives Based on Virtual Signal Injection”, in *Proc. IEEE International Electric Machines & Drives Conference (IEMDC2015), Coeur d'Alene, 2015*.
2. M. Koc, **T. Sun**, J. Wang, “A linear combination of current and voltage based flux observers for direct torque controlled IPM drives”, in *Proc. The 8th IET int. Conf. on Power Electronics, Machines and Drives (PEMD), Glasgow, 2016*.
3. M. Koc, J. Wang, **T. Sun**, “Stator flux oriented control for high performance interior permanent magnet synchronous machine drives”, in *Proc. The 8th IET int. Conf. on Power Electronics, Machines and Drives (PEMD), Glasgow, 2016*.

CHAPTER 2 Virtual Signal Injection Based Field Orientated Control

2.1 Introduction

As has been described in Chapter 1, the interior permanent magnet synchronous motors (IPMSM) are increasingly being used in a variety of applications [81] due to their high efficiency, high power density, high reliability, and good field-weakening performance [31], [60], [82], [83].

In constant torque region, in order to achieve optimal efficiency of an IPMSM drive, the maximum torque per ampere (MTPA) operation is often necessary by controlling the current vector according to load conditions [12], [33], [42]. However, due to the magnetic saturation, cross-coupling effects, manufacturing tolerance, material property variation and temperature variation, the parameters of IPMSMs are highly nonlinear and uncertain [40]. This imposes a great challenge for realization of the MTPA operation in real-world applications.

As proposed in [12], [33]–[35], [42], [43], the MTPA points were calculated assuming that the motor parameters are constant. However, real MTPA operation will not be possible due to parameter variations under influence of magnetic saturation, cross-coupling and temperature [50], [51]. To take into account the effects of magnetic saturation and cross-coupling, flux linkage due to permanent magnets and d- and q-axis inductances as functions of current have been considered in [44]–[46]. However, it is difficult to derive accurate and computationally efficient models for these parameters as functions of currents.

In [36], [40], [47]–[49], look-up tables (LUTs) are employed to facilitate the MTPA control. The LUT data may be obtained from the numerical analysis of electromagnetic field of the machine. However, the accuracy will be dependent on manufacturing tolerance, material property variations and temperature. It is also possible to extract LUT data by performing a set of experiments, however experimental approaches are rather time consuming and require considerably more resources while the variability due to manufacture, materials and temperature may not be accounted fully by testing a few

representative samples. These factors greatly limit the performance and scope of the LUT based approaches for the MTPA operation.

In [52]–[54], search algorithms are employed to adjusting the current vector so that the MTPA condition is met for a given load torque. These techniques do not require prior knowledge on motor parameters but have relatively poor dynamic performance [29] due to slow converging rate of the search algorithms. The search algorithms based control schemes also exhibit low torque control accuracy as well as large torque ripple under the influence of torque disturbance and current/voltage harmonics.

Recently, novel methods for the MTPA operation by injecting high-frequency current signal into the motor have been proposed. They are based on the principle of the extremum seeking control (ESC) [80]. Because of the injected high-frequency current signal, the resultant torque contains a variable component. By utilizing the fact that at a MTPA point the variation in torque caused by the variation in the current angle is zero, the MTPA point can be detected and tracked. Since it is less convenient to measure the torque and its variation, in [79] signal was injected into the reference flux amplitude and torque variation was estimated from the reference flux amplitude and measured current. In [55]–[57] variation in speed was utilized instead of torque variation. The convergence properties as well as stability of this method were analyzed in [58]. Unfortunately, the performance of this method was limited by the hardware such as the resolution of position/speed sensor [59]. The high frequency current injected into the motor drive for the MTPA tracking also gives rise to speed ripple that deteriorates control performance and incurs additional power losses in the drive system. In [59] variation in mechanical power was utilized instead of torque variation. However, this method requires a careful selection of the frequency and amplitude of the injected signal according to motor speed to avoid resonant problems. Because the input power calculation was based on terminal voltage and current, the signal processing may be affected by harmonics in terminal voltage and current. Similar to other signal injection based control schemes, the injected signal also results in additional power losses. Moreover, the extremum seeking based control schemes are only effective in constant torque region. In field weakening region, due to voltage saturation, the MTPA points cannot be reached. Consequently, the variation in torque caused by the variation in the current angle will not equal zero when the voltage is constrained to its maximum value and the extremum seeking based control schemes will no longer be effective.

To operate IPMSM drives at high speed, field weakening control is needed. The nonlinear and uncertain machine parameters of IPMSMs pose similar challenges to effective field weakening control. In order to achieve good performance in field weakening region, extensive studies have been carried out on control of IPMSM drives. The early researches in [84]–[86] were focused on the IPMSM torque capability in field weakening operation. Model based field weakening control schemes [34], [42]–[44], [87]–[90] and Look-up tables (LUTs) based field weakening control schemes [50], [91]–[93] were proposed. The advantage of these control schemes is their fast response. However, the performance of these control schemes for IPMSM drives may be significantly affected by parameter variations and inaccuracies [94]. In order to address this problem, several parameter-independent control strategies were proposed.

In [95], voltage amplitude feedback was utilized by a PI controller to generate reference d-axis current in field weakening region. Although this control scheme was not parameter sensitive, its response was slow. Single current regulator and voltage angle control were used in [96], [97] to adjust the phase angle of the voltage vector whose amplitude was limited according to the DC link voltage. However, this method also suffered from slow response. Moreover, field weakening control scheme for signal injection based control mentioned above has not been reported yet.

In this chapter, a novel virtual signal injection control (VSIC) method based on field orientated control is proposed. In constant torque region, this method is parameter independent in tracking the MTPA point as well as robust to current and voltage harmonics and machine parameter variations. Moreover, it does not inject any real signal into the motor, and hence the problems associated with real-signal injection such as deterioration in control performance, resonant problems and additional power losses are avoided.

Further, in field weakening region, a novel field weakening control scheme that combines virtual signal injection control together with voltage feedback based field weakening control is proposed. The proposed novel field weakening control scheme also exploits the advantages of model based field weakening control methods so that it not only has fast response to torque demand but also is parameter independent in searching the minimal current amplitude points, i.e., the MTPA and voltage constrained maximum torque per Ampere (VCMTPA) points, in constant torque region and in field weakening region, respectively.

2.2 Virtual Signal Injection Based MTPA Control in d-q Frame

2.2.1 Principle of Signal Injection Based MTPA Control

Fig. 2-1 shows the constant torque loci and constant current magnitude locus for IPMSMs in d-q frame. The MTPA point M is the point at which the constant current magnitude locus is tangential to a constant torque locus. In other words, M is the intersection between the constant torque locus and the constant current locus with minimum magnitude of the current vector.

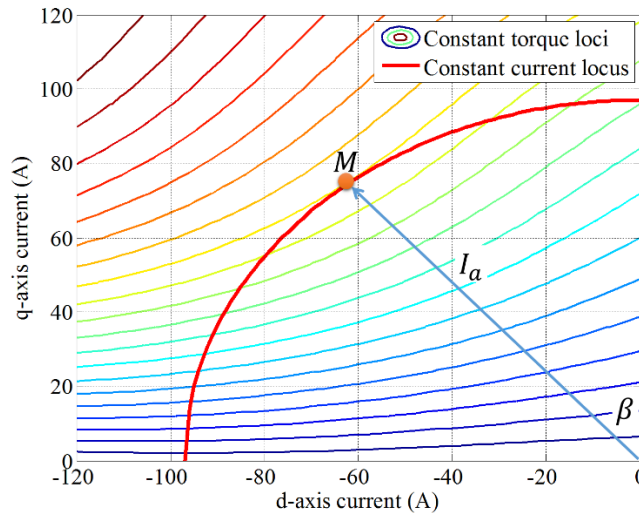


Fig. 2-1. The MTPA point, constant current locus and constant torque locus.

The relationship between current angle β and electromagnetic torque for a fixed current vector magnitude is illustrated in Fig. 2-2. If a small sinusoidal signal, $\Delta\beta = A \sin(\omega_h t)$, is injected into the current angle β , the resultant torque will contain variable components as shown in (2-1) derived from the Taylor's series expansion:

$$\begin{aligned}
 & T_e(\beta + A \sin(\omega_h t)) \\
 &= T_e(\beta) + \frac{\partial T_e}{\partial \beta} A \sin(\omega_h t) + \frac{1}{2} \frac{\partial}{\partial \beta} \left(\frac{\partial T_e}{\partial \beta} \right) A^2 \sin^2(\omega_h t) + \dots \quad (2-1)
 \end{aligned}$$

As the amplitude, A , of the injected signal is very small, the first order term is the dominant component and the influence of other higher order terms, including the second-

order term, on the torque variation is relatively small.

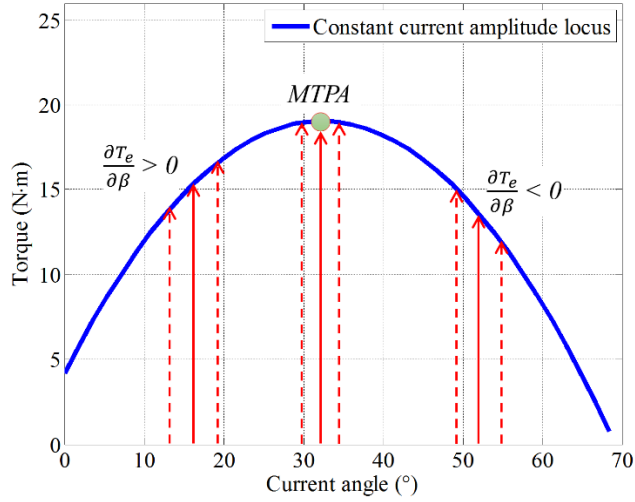


Fig. 2-2. The relationship between current angle and torque of fixed current vector amplitude.

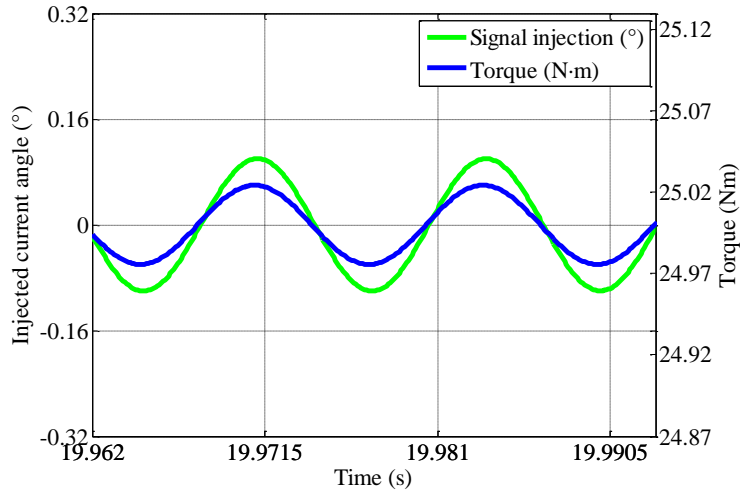
As shown in Fig. 2-2, when the current angle is smaller than the MTPA current angle, the torque increases or decreases with increase or decrease in $\Delta\beta$. Thus, $\partial T_e/\partial\beta$ is positive, therefore the variation of the dominant first order term in (2-1) has the same phase and frequency as the injected current angle signal. The waveforms of torque and injected current angle signal are shown in Fig. 2-3(a).

When the current angle is equal to the MTPA current angle, the derivative of torque with respect to the current angle $\partial T_e/\partial\beta$ is equal to zero. Therefore the torque variation due to the injected signal is dominated by the second-order term which can be expressed as:

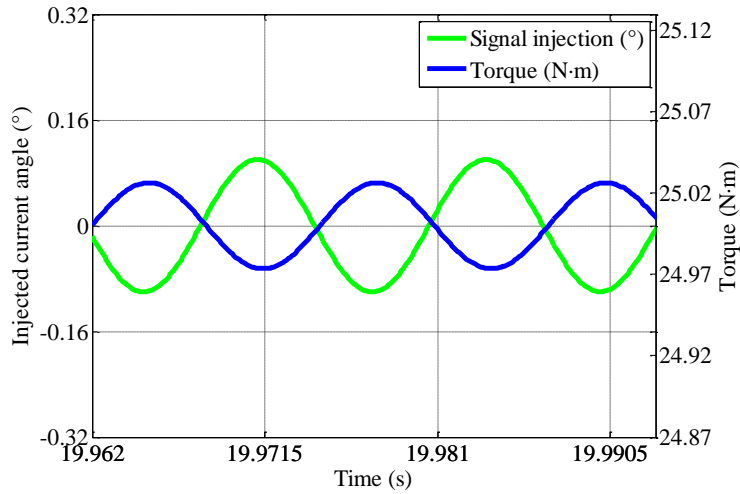
$$\frac{\partial}{\partial\beta} \left(\frac{\partial T_e}{\partial\beta} \right) A^2 \sin^2(\omega_h t) = \frac{1}{2} \frac{\partial}{\partial\beta} \left(\frac{\partial T_e}{\partial\beta} \right) A^2 [1 - \cos(2\omega_h t)] \quad (2-2)$$

As shown in (2-2), the second-order term can be divided into a constant term and a high frequency term whose frequency is twice of the injected signal frequency.

When the current angle is larger than the MTPA current angle, as it is shown in Fig. 2-2, the torque decreases or increases with increase or decrease in $\Delta\beta$, and $\partial T_e/\partial\beta$ is negative. Therefore the variation of the dominant first-order term has the same frequency as the injected current angle signal but opposite phase as shown in Fig. 2-3(b). These characteristic features can be employed to design virtual signal injection based MTPA tracking control.



(a)



(b)

Fig. 2-3. The waveform of injected signal and torque fluctuation.

2.2.2 Virtual Signal Injection

2.2.2.1 Method to Obtain Torque Variation Information

In the steady stage, the mechanical power can be expressed as in (2-3), and the relationship between torque and power can be expressed as in (2-4) if the iron loss is neglected in the total input power.

$$P_m = \frac{3}{2} [(v_d - Ri_d)i_d + (v_q - Ri_q)i_q] = \frac{3}{2} \left[(v_q - Ri_q) + \frac{(v_d - Ri_d)}{i_q} i_d \right] i_q \quad (2-3)$$

$$\frac{P_m}{\omega_m} = T_e = \frac{3}{2} [\Psi_m p + p(L_d - L_q) i_d] i_q \quad (2-4)$$

To assess the validity of neglecting iron loss in (2-3), extensive simulations with a representative iron loss model in [98], [99] were performed. By way of example, Fig. 2-4 shows torque variations with current angle with and without iron loss being considered when the current magnitude is kept constant. It is evident that the influence of iron loss on MTPA points is, indeed, negligible in the constant torque region [59].

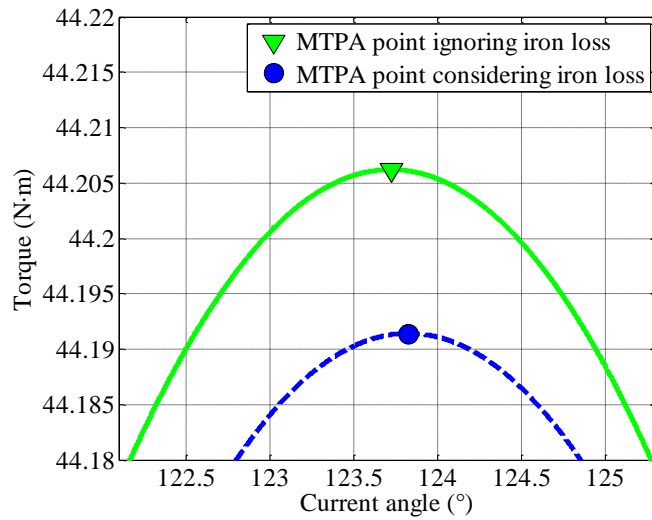


Fig. 2-4. The influence of iron loss on MTPA point at speed of 1000 r/min.

As described previously, if a small sinusoidal signal $\Delta\beta$ is injected into the stator current angle, according to (1-6) and (1-7), the corresponding d- and q-axis currents with high frequency component can be expressed in (2-6) and (2-7), respectively.

$$\Delta\beta = A \sin(\omega_h t) \quad (2-5)$$

$$i_d^h = -I_a \sin(\beta + \Delta\beta) \quad (2-6)$$

$$i_q^h = I_a \cos(\beta + \Delta\beta) \quad (2-7)$$

Combining (2-3) and (2-4) yields:

$$\frac{P_m}{\omega_m} = T_e = \frac{3}{2} \left[\frac{(v_q - R i_q)}{\omega_m} + \frac{(v_d - R i_d)}{i_q \omega_m} i_d \right] i_q \quad (2-8)$$

It is worth noting that although $(v_q - R i_q)/\omega_m$ and $(v_d - R i_d)/(i_q \omega_m)$ in (2-8) vary with operating conditions, they can be considered as constants over the very short period of the injected signal, $\Delta\beta$. Similarly, $p\Psi_m$ and $p(L_d - L_q)$ in (2-4) can be also considered as constants over the very short period of the injected signal despite of their changes with

respect to d- and q- axis currents and temperature. Since the torque is contributed by the alignment torque component, $\Psi_m i_q$, and the reluctance torque component due to the difference in the d- and q-axis inductances, $(L_d - L_q)$, the relationship between torque and d- and q-axis currents can be approximated by a polynomial in the form of (2-9):

$$T_e = (a + bi_d)i_q \quad (2-9)$$

According to (2-8) and (2-9), assume:

$$a = \frac{(v_q - Ri_q)}{p\omega_m} \quad (2-10)$$

$$b = \frac{(v_d - Ri_d)}{p\omega_m i_q} \quad (2-11)$$

Substituting (2-6), (2-7), (2-10) and (2-11) into (2-9):

$$T_e^h = \frac{3}{2} \left[\frac{(v_q - Ri_q)}{\omega_m} + \frac{(v_d - Ri_d)}{i_q \omega_m} i_d^h \right] i_q^h \quad (2-12)$$

It should be noticed that the (2-10), (2-11) are approximations, the error analysis of the virtual signal injection will be detailed in Appendix C.

Equation (2-12) represents the sum of the torque variations in (2-1) due to $\Delta\beta$ and can be obtained from measured q-axis current, motor speed, and d- and q-axis command voltages as well as the d- and q-axis current with high frequency component given by (2-6) and (2-7). This implies that it is not necessary to inject real signals into the motor current in order to extract the high frequency component of the torque variation. In other word, the proposed virtual signal injection method replaces the $p\Psi_m$ and $(L_d - L_q)p$ in (2-4) with $(v_q - Ri_q)/\omega_m$ and $(v_d - Ri_d)/(i_q \omega_m)$. In this way the difficulties in obtaining accurate PM flux linkage and d- and q-axis inductances can be avoided.

The proposed technique is therefore called virtual signal injection. Moreover, as the resistance R in (2-12) has very little influence on tracking the MTPA point [100], it can be assumed as its nominal value or even be neglected. In essence, the above derivation shows that torque variation with β angle can be obtained through signal processing rather than real signal injection.

2.2.2.2 Signal Processing for Extraction of $\partial T_e / \partial \beta$

According to Taylor's series expansion, the left hand side of (2-12) can be expressed with (2-13).

$$T_e^h = T_e(\beta) + \frac{\partial T_e}{\partial \beta} A \sin(\omega_h t) + \frac{1}{2} \frac{\partial}{\partial \beta} \left(\frac{\partial T_e}{\partial \beta} \right) A^2 \sin^2(\omega_h t) + \dots \quad (2-13)$$

It can be shown that the partial derivative of torque with respect to the current angle, $\partial T_e / \partial \beta$, is indicative of the MTPA operation as mentioned in section 2.2.1. This information can be extracted from T_e^h with the signal processing scheme shown in Fig. 2-5. The low-pass filter output in Fig. 2-5 is denoted as *LPFO* which is proportional to $\partial T_e / \partial \beta$. The cut-off frequency of the low-pass filter should be below the virtually injected signal frequency ω_h .

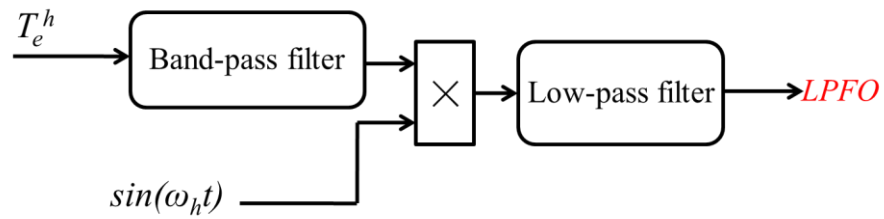


Fig. 2-5. Schematic of signal processing block to extract $\partial T_e / \partial \beta$.

Since (2-12) and (2-13) are equivalent, T_e^h can be obtained from the d- and q-axis reference voltages, (v_d, v_q) , the measured speed, ω_m , and the measured d- and q-axis currents, (i_d, i_q) together with the virtually injected signals, (i_d^h, i_q^h) , according to (2-12).

As shown in Fig. 2-5, if T_e^h obtained from (2-12) is processed first by a band-pass filter whose centre frequency is equal to the frequency of the virtually injected signal, ω_h , the output of the band-pass filter will be proportional to the first order term in (2-13). The output of the band-pass filter is further multiplied by $\sin(\omega_h t)$; the result can be expressed as:

$$\begin{aligned} K \frac{\partial T_e}{\partial \beta} A \sin^2(\omega_h t) &= K \frac{\partial T_e}{\partial \beta} A \left\{ \frac{1}{2} [\cos(0) - \cos(2\omega_h t)] \right\} \\ &= \frac{1}{2} KA \frac{\partial T_e}{\partial \beta} - \frac{\partial T_e}{\partial \beta} KA \cos(2\omega_h t) \end{aligned} \quad (2-14)$$

where K is the gain of the band-pass filter at ω_h . The right hand side of (2-14) will be filtered by a 1st order low-pass filter whose cut-off frequency is below the virtually injected signal frequency ω_h . The output of the low-pass filter in Fig. 2-5 will be proportional to $\partial T_e / \partial \beta$.

In this way, the information of $\partial T_e / \partial \beta$ can be extracted. It follows that if the current angle is equal to the MTPA current angle, the output of the low-pass filter is essentially

equal to zero. This condition will be used by an integrator to generate the d-axis current reference for maintaining the MTPA operation.

2.2.3 Implementation of Virtual Signal Injection

Fig. 2-6 shows the schematic of the IPMSM drive control system employing the proposed virtual signal injection method, and Fig. 2-7 shows the details of the virtual signal injection and signal processing blocks.

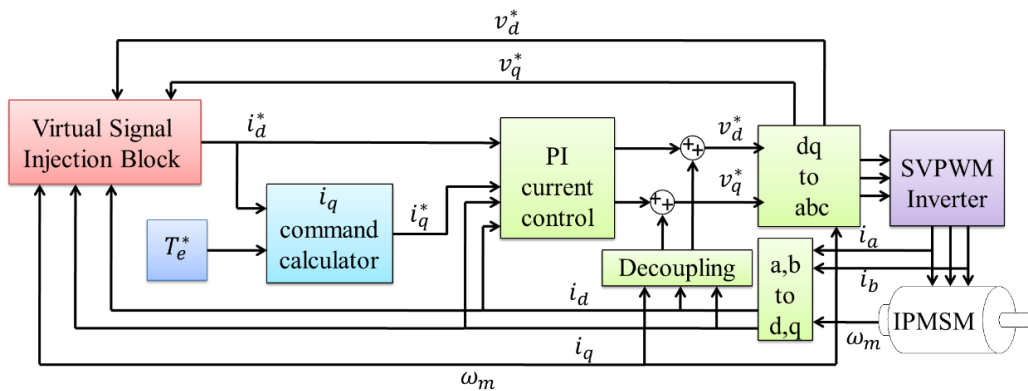


Fig. 2-6. IPMSM drive control system with virtual signal injection method.

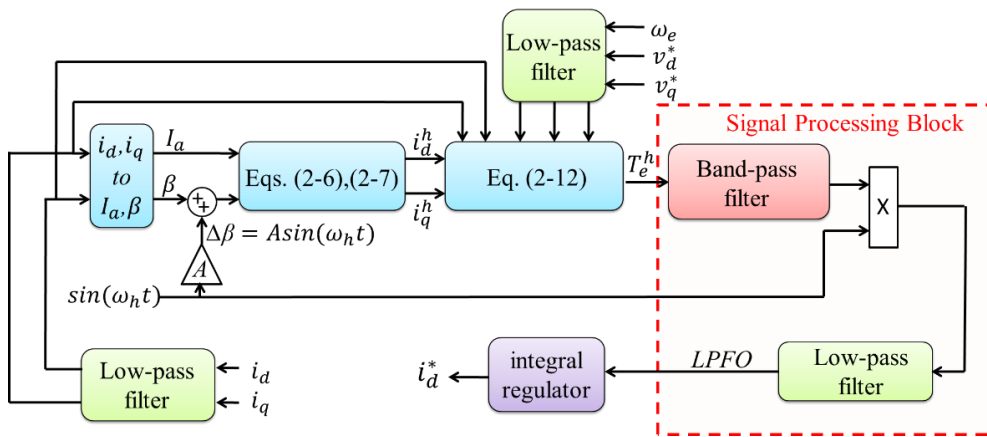


Fig. 2-7. Schematic of virtual signal injection block of Fig. 2-6.

The measured d- and q-axis currents are conditioned by a low pass-pass filter to eliminate noise due to PWM switching. The filtered currents, i_d and i_q , are transformed into the polar coordinate system to obtain the amplitude I_a and angle β . The high frequency virtual signal, i.e., $\Delta\beta = A \sin(\omega_h t)$, is injected into the estimated current angle β mathematically and the high frequency d- and q-axis current perturbations, i_d^h and i_q^h , are obtained from (2-6) and (2-7). The amplitude of $\Delta\beta$ is adjusted by the gain A

as shown in Fig. 2-7. The resultant torque variation is calculated using (2-12) with the filtered d- and q-axis currents, the virtually injected perturbation currents, i_d^h and i_q^h , the measured motor speed and the d- and q-axis command voltages.

Both the speed and voltages are low-pass filtered to attenuate undesirable noise. The torque perturbation is subsequently fed into the signal processing block shown in Fig. 2-5 and, as described in section 2.2.2.2, the output of the signal processing block is proportional to $\partial T_e / \partial \beta$. This signal is fed into the integrator in Fig. 2-7 and its output is used to adjust the d-axis current reference i_d^* in such a way that $\partial T_e / \partial \beta$ becomes zero, i.e., reaching the MPTA operation.

Any other controller, such as a PI controller, capable of zero control error in steady state, may also be used in Fig. 2-7 to track the d-axis current reference for the MTPA control and with a PI controller the dynamic response of the virtual signal injection control scheme may be increased.

The q-axis current command, i_q^* , is calculated from the d-axis current command, i_d^* and the torque command, T_e^* , by the following equation:

$$i_q^* = \frac{T_e^*}{\frac{3}{2}p[\Psi_m + (L_d - L_q)i_d^*]} \quad (2-15)$$

In (2-15), the motor parameters L_d , L_q , Ψ_m can be assumed as their nominal values or obtained from pre-defined lookup-tables. As it is shown in (2-12), the torque variation information is obtained independently from motor parameters. Therefore, even if the motor parameters are chosen inaccurately, the virtual signal injection method can still obtain the $\partial T_e / \partial \beta$ information accurately and track the MTPA point accurately. Inaccurate motor parameters used in (2-15) may cause torque error, but this error will be eliminated by a speed feedback control loop. If the drive only requires torque control, such as for EV traction, pre-defined parameter look-up tables obtained from finite element (FE) analysis are often sufficient for good dynamic torque response as accurate torque control is not necessary.

As it is shown in Fig. 2-7, the measured d- and q-axis currents and d- and q-axis command voltages as well as measured speed are processed by the low-pass filters to eliminate the influence of their harmonics. If the frequency of injected signal is sufficiently high, the low-pass filter with a corner frequency 3~4 times lower can effectively eliminate all harmonics whose frequencies are close to the injected signal.

Consequently, the proposed VSIC scheme is very robust to voltage and current harmonics, and other electric noise. The integral regulator adjusts the d-axis current command until the output of signal processing block is zero, i.e. the MTPA point.

It should be noted that, as the speed approaches zero, (2-12) should not become undetermined in a noise-free environment since it is derived from (2-8) which are independent of the speed. Significant deviations may occur due to noise at very low speeds. Therefore, the currents, speed and command voltages in (2-12) should be conditioned by low-pass filters to minimize the effect of noise. In order to avoid being divided by zero, the speed should be set to a small value when the measured speed is below a minimum threshold.

The robustness of the proposed VSIC at low speeds which is further studied by simulation and experiments will be discussed in section 2.2.4 and section 2.2.5.

2.2.4 Simulation Results

Table 2-1
IPMSM parameters

Number of pole-pairs	3
Phase resistance	51.2 m Ω
Continuous/Maximum current (Peak values)	58.5/118 A
Peak power below base speed	10 kW
DC link voltage	120 V
Base/maximum speed	1350/4500 r/min
Continuous/peak torque	35.5/70 N·m
Peak power at maximum speed	7 kW

The virtual signal injection control scheme has been extensively simulated against a prototype IPMSM drive system [13]. The motor specification is given in Table 2-1 and the FE predicted variations of d- and q-axis inductances and permanent magnet flux linkage with d- and q-axis currents are shown in Fig. 1-8. The simulations were performed based on this machine model with nonlinear machine parameters.

In order to study the influence of stator resistance on the virtual signal injection based MTPA tracking performance, simulations with the measured resistance of the motor phase winding at room temperature of 20 °C and simulations which ignore the resistance in (2-12) were performed. Fig. 2-8 shows the simulation results of torque command variations from 10 N·m to 45 N·m in steps of 5 N·m at the speed of 1000 r/min when stator resistance in (2-12) was considered or ignored.

The circles represent the actual MTPA points of different operation conditions. The triangles represent the simulation results obtained from the virtual signal injection control with the accurate resistance value in (2-12) while the squares represent the results when the effect of the winding resistance in (2-12) is ignored in the virtual signal injection control. The simulation results show that the virtual signal injection method can track the MTPA points accurately and the influence of resistance on tracking MTPA points is negligible.

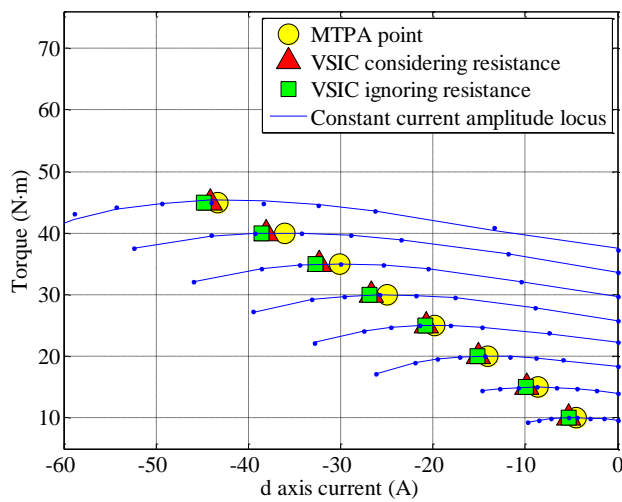


Fig. 2-8. The MTPA points and virtual signal injection MTPA tracking simulation result.

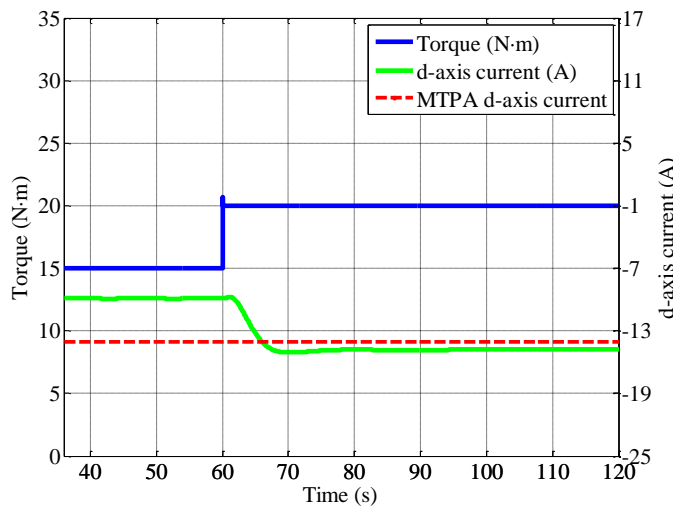


Fig. 2-9. d-axis current tracking response to step change in torque at speed of 1 r/min.

Simulations have also been performed at low speeds. Fig. 2-9 shows the simulation results of the torque and d-axis current responses when a step change in torque from 15 N·m to 20 N·m is applied at the speed of 1 r/min. The dashed line in Fig. 2-9 is the ideal

MTPA d-axis current for 20 N·m torque. As it is shown in Fig. 2-9, although the speed is equal to 1 r/min, the proposed VSIC can still track the MPTA point accurately.

2.2.5 Experimental Results

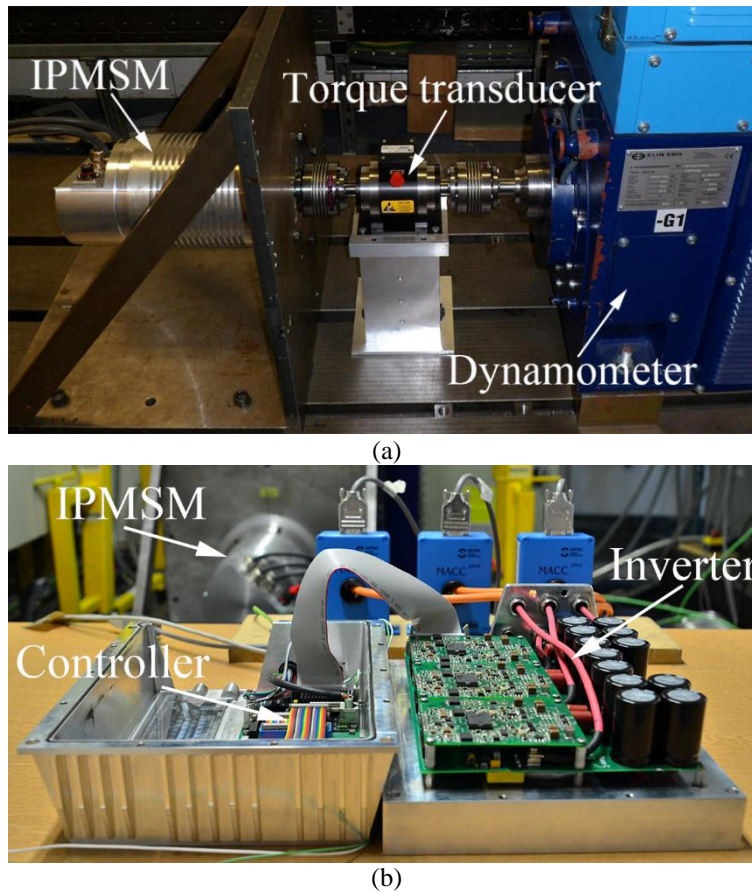


Fig. 2-10. Experimental test-rig. (a): IPMSM, torque transducer, dynamometer. (b): controller and inverter.

In order to verify the proposed virtual signal injection method, a test-rig as shown in Fig. 2-10 has been set up. The 10 kW IPMSM is designed for traction applications for a wide constant power operation. The motor is controlled in torque control mode and loaded by the dynamometer in speed control mode. The inductance and PM flux linkage parameters as shown in Fig. 1-8 of the machine are highly nonlinear and its torque and speed ratings are provided in Table 2-1. The motor torque is measured by a high precision torque transducer. The input and output powers of the drive were measured by Yokogawa WT3000 power analyser with high bandwidth, high precision voltage and current transducers. All the experiments in this thesis are based on this test rig and motor.

Because the signal is injected virtually, the maximum frequency of the injected signal is only limited by the sample rate of the controller. In this experiment, the controller sampling rate is 8 kHz and the frequency of injected signal is set to 1 kHz. Thus, 8 samples of the injected sinusoidal signal $\sin(\omega_h t)$ shown in Fig. 2-7 are required over one signal period. The waveform represented by the 8 discrete samples contains the fundamental component of the injected signal and higher frequency harmonics due to discretisation. These higher frequency harmonics and other undesirable harmonics, e.g., the high-order terms in (2-1), will be eliminated by the band-pass filter shown in Fig. 2-7. Therefore, they will not affect the MTPA tracking performance.

In the experiments, a 4th order band pass filter with a bandwidth of 1 Hz at the centre frequency of the virtually injected signal is utilized to process the torque signal in Fig. 2-5. The above settings apply to all the subsequent test as well.

2.2.5.1 MTPA Points Tracking Test

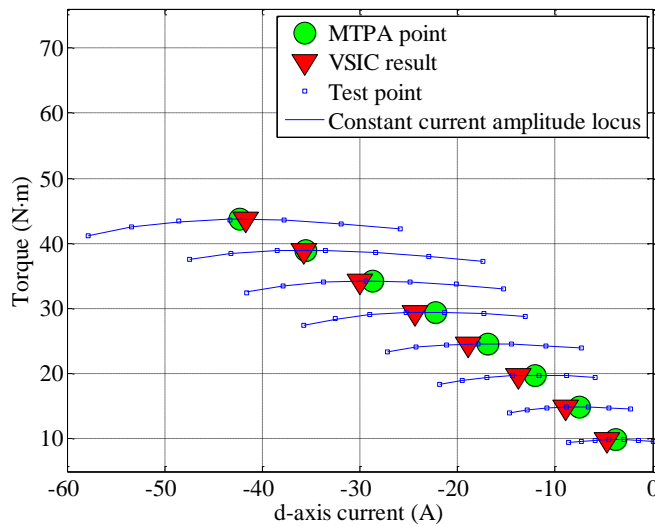


Fig. 2-11. The exact MTPA points and virtual signal injection MTPA tracking experimental result at speed of 400 r/min.

The first set of tests was performed with torque command variations from 10 N·m to 45 N·m in steps of 5 N·m at the speed of 400 r/min. The MTPA points tracking results of the proposed virtual signal injection method at the different torque commands are represented by triangles in Fig. 2-11. For a given torque command, tests were also

performed by varying the current vector angle while its magnitude was kept constant. The results are shown in the curve marked by the squares. The exact MTPA points can be obtained using curve-fitting of the constant current amplitude locus, denoted by curves in Fig. 2-11, for the different torque commands. These exact MTPA points are denoted by the circles.

The test results shown in Fig. 2-11 demonstrate that the proposed virtual signal injection method can track the MTPA points accurately. The comparison between the resultant torque of the proposed virtual signal injection control and the torque of the actual MTPA points is shown in Table 2-2.

Table 2-2
Comparison between the resultant torque of VSIC and the torque of MTPA points at speed of 400 r/min

Torque reference	Current amplitude	Torque generated by VSIC	MTPA torque	Torque error
10 N·m	17.26 A	9.88 N·m	9.90 N·m	0.20%
15 N·m	25.65 A	14.83 N·m	14.86 N·m	0.20%
20 N·m	34.00 A	19.73 N·m	19.76 N·m	0.15%
25 N·m	42.29 A	24.56 N·m	24.60 N·m	0.16%
30 N·m	50.56 A	29.42 N·m	29.44 N·m	0.07%
35 N·m	58.86 A	34.21 N·m	34.22 N·m	0.03%
40 N·m	67.15 A	38.94 N·m	38.94 N·m	0.00%
45 N·m	75.54 A	43.67 N·m	43.67 N·m	0.00%

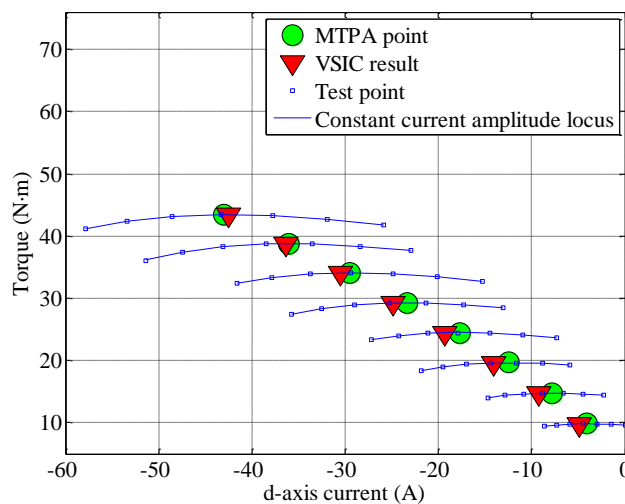


Fig. 2-12. The exact MTPA points and virtual signal injection MTPA tracking experimental result at speed of 1000 r/min.

The motor drive was also tested at 1000 r/min with torque command variations from 10 N·m to 45 N·m in steps of 5 N·m. The comparison between the resultant torque of the

virtual signal injection control and the torque at the experimentally measured MTPA points is shown in Fig. 2-12 and Table 2-3.

The error between the resultant torque of the proposed virtual signal injection method and the torque of actual MTPA points is less than 0.2%.

Table 2-3
Comparison between the resultant torque of VSIC and the torque of MTPA points at speed of 1000 r/min

Torque reference	Current amplitude	Torque generated by VSIC	MTPA torque	Torque error
10 N·m	17.26 A	9.83 N·m	9.84 N·m	0.10%
15 N·m	25.66 A	14.75 N·m	14.78 N·m	0.20%
20 N·m	34.02 A	19.63 N·m	19.66 N·m	0.15%
25 N·m	42.30 A	24.45 N·m	24.48 N·m	0.12%
30 N·m	50.57 A	29.26 N·m	29.28 N·m	0.07%
35 N·m	58.86 A	34.03 N·m	34.04 N·m	0.03%
40 N·m	67.12 A	38.74 N·m	38.74 N·m	0.00%
45 N·m	75.49 A	43.41 N·m	43.41 N·m	0.00%

The waveforms of three-phase voltages applied to the motor and the phase currents at 45 N·m, 400 r/min and 1000 r/min are shown in Fig. 2-13(a) and Fig. 2-13(b), respectively.

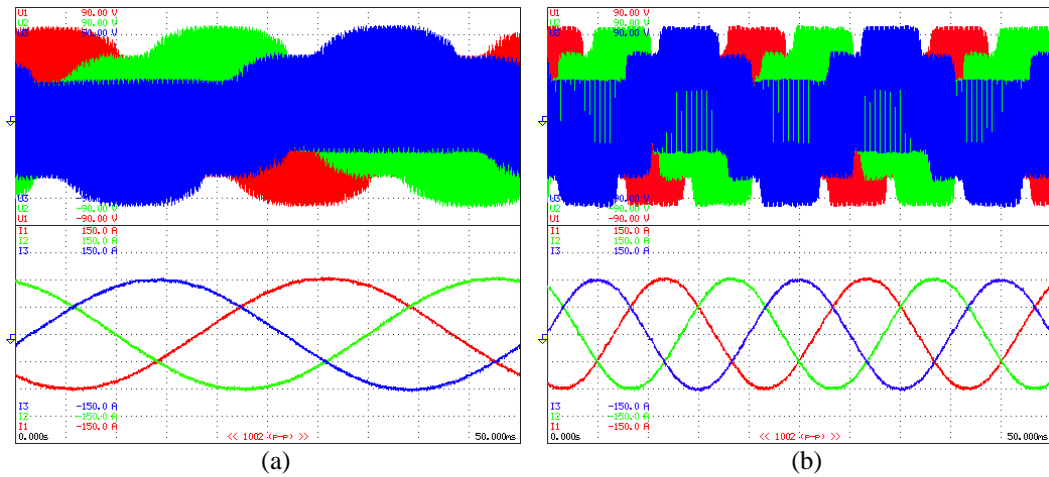


Fig. 2-13. Measured results of proposed VSIC method for IPMSM control under MTPA operation. (a): Voltage and current waveform at 400 r/min speed and 45 N·m torque. (b): Voltage and current waveform at 1000 r/min speed and 45 N·m torque.

2.2.5.2 Performance of Virtual Signal Injection Control during Payload Torque Change

Fig. 2-14 shows experimental result of the MTPA tracking performance when the reference torque is varied from 45 N·m to 0 N·m in steps of 5 N·m at the speed of 1000 r/min and the proposed VSIC method keeps adjusting the d- axis current to track the

MTPA points during the process.

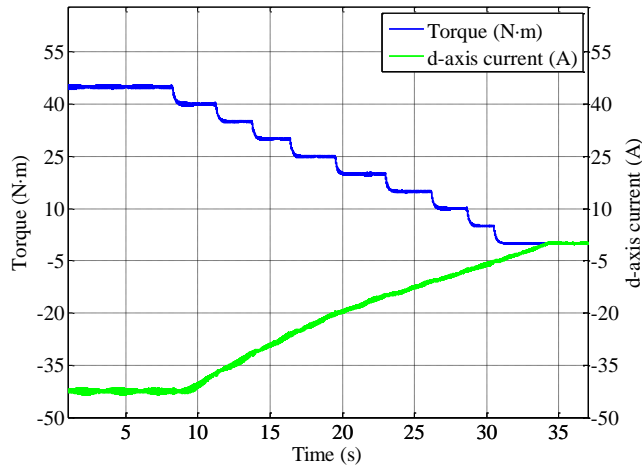


Fig. 2-14. Experimental result of MTPA tracking performance during torque changing.

Fig. 2-15 shows the d-axis current responses and the estimated torque based on the measured d/q-axis currents and machine parameters used in (2-15) when a step change in reference torque from 40 N·m to 45 N·m is applied at the speed of 1000 r/min. The dashed line in Fig. 2-15 is the theoretical MTPA d-axis current of 45 N·m at speed of 1000 r/min.

It can be seen that the torque responded quickly while the d-axis current tracks the MTPA point gradually. The experiment results in Fig. 2-14 and Fig. 2-15 also illustrate the robustness of the proposed control scheme to torque disturbances.

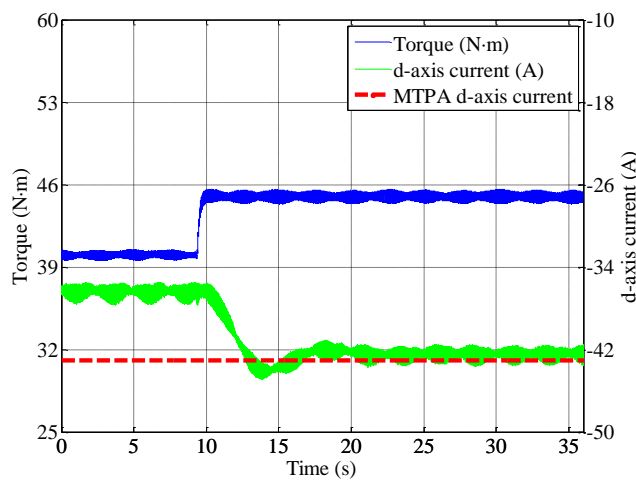


Fig. 2-15. Experimental result of torque step response at speed of 1000 r/min.

The measured torque, estimated torque, reference torque for a step change in torque from 40 N·m to 45 N·m at 1000 r/min are shown in Fig. 2-16. It can be seen that the torque

responds fast and the small error between the reference and measurement may be caused by the combined effect of the friction torque which is not accounted in the reference torque, iron loss, and the errors of machine parameters in (2-15).

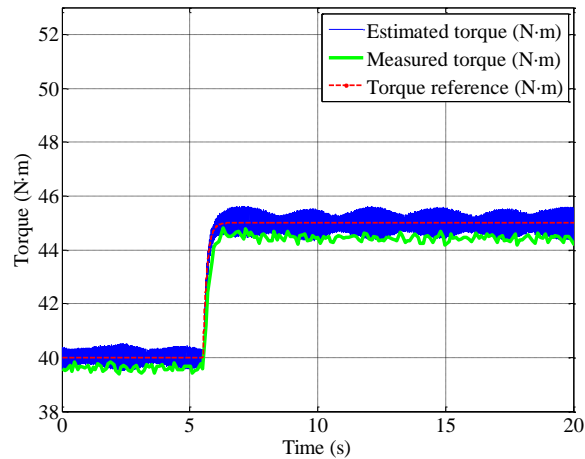


Fig. 2-16. Measured torque, estimated torque, reference torque of a step change in torque from 40 N·m to 45 N·m at 1000 r/min.

Fig. 2-17 compares the theoretical MTPA current angle and VSIC current angle tracking response when a step change in torque from 40 N·m to 45 N·m is applied at the speed of 1000 r/min.

Due to the increase in the q-axis current in response to the step increase in torque, the current angle initially decreases. However, the VSIC adjusts the current angle until it reaches the MTPA angle of the new operation condition. It is evident that the proposed VSIC can track the MTPA current angle accurately.

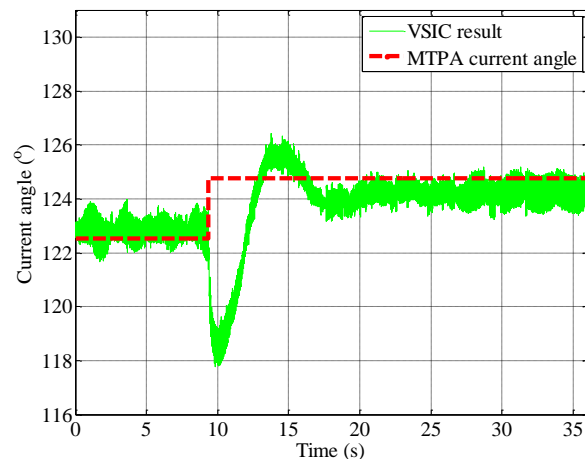


Fig. 2-17. Theoretical MTPA current angle and VSIC tracking current angle in response to a step load torque change.

Fig. 2-18 shows the motor current amplitude and estimated torque responses to the step change in torque. As can be seen, the current amplitude is larger initially and decreases gradually until it reaches the minimal value of the MTPA operation.

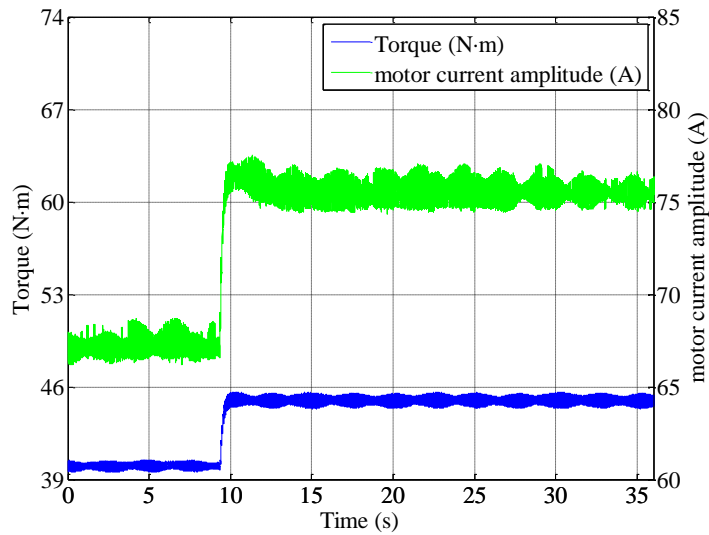


Fig. 2-18. Measured current amplitude and torque responses to a step load torque change.

2.2.5.3 Performance of Virtual Signal Injection Control at Low Speeds

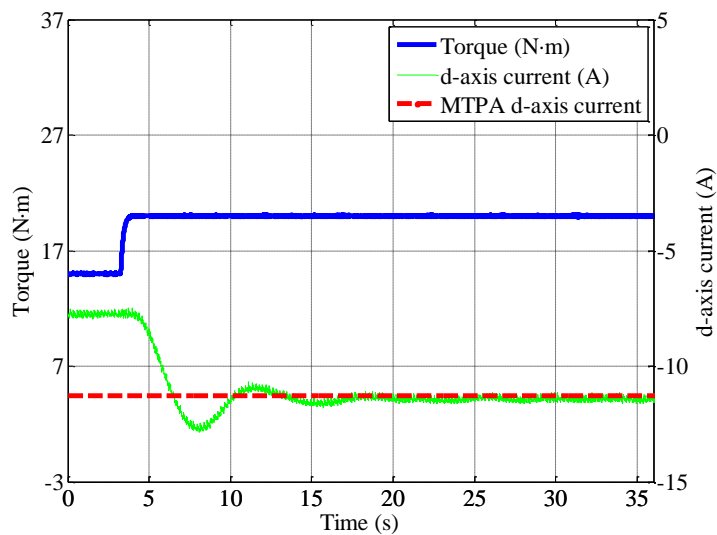


Fig. 2-19. Experimental result of torque step response at speed of 15 r/min.

Fig. 2-19 shows the measured torque and d-axis current responses when a step change in torque from 15 N·m to 20 N·m is applied at the speed of 15 r/min. The dashed line in

Fig. 2-19 is the theoretical MTPA d-axis current of 20 N·m at 15 r/min. It is shown in Fig. 2-19 that the proposed VSIC can still track the MPTA point accurately at low speeds.

Significant speed fluctuation was observed in the dynamometer when operating at speeds below 15 r/min. It was not, therefore, possible to perform experiments at lower speeds. In practice, pre-calculated look-up tables for d- and q-axis current references obtained from FE analysis may be used when speed is below a pre-defined threshold.

2.3 Virtual Signal Injection Aided Field Weakening Control

As discussed in section 2.2, the proposed virtual signal injection control has several advantages over the current state-of-the-art approaches to control of permanent magnet synchronous motors for maximum torque per ampere (MTPA) operations, such as high accuracy, parameter independence, robustness to electromotive force (emf) and tooth ripple harmonics, and no additional iron and copper loss due to real signal injection, etc.

However, the VSIC is not effective under voltage saturation. In order to expand the speed operating region, an additional control scheme for field weakening operation will be proposed below.

2.3.1 Operational Characteristic of Field Weakening Control

Fig. 2-20 shows the variations of torque and voltage amplitude with d-axis current for a given current amplitude, I_a , when the required voltage for the MTPA operation is greater than the voltage limit.

The voltage amplitude and voltage error in Fig. 2-20 are defined in (2-16) and (2-17), respectively. If the d-axis current magnitude decreases towards the MTPA point, the torque and v_a^* will increase. Therefore, the voltage constrained MTPA point, VCMTPA, is the point at which the voltage amplitude is equal to the voltage limit, and this condition is independent of iron loss.

$$v_a^* = \sqrt{(v_d^*)^2 + (v_q^*)^2} \quad (2-16)$$

$$v_{error} = v_{max} - v_a^* \tag{2-17}$$

Because of the voltage limit, the motor cannot reach the MTPA point shown in Fig. 2-20. It is evident from Fig. 2-20 that at the VCMTPA point, the partial derivative of torque with respect to the current angle is smaller than zero, i.e., $-\partial T_e / \partial \beta > 0$. This implies that the output of the low-pass filter in Fig. 2-5 will tend to adjust the d-axis current toward the MTPA point until $-\partial T_e / \partial \beta = 0$. This may cause the voltage amplitude to go beyond the maximum voltage and consequently the current regulators saturate. Therefore, if the voltage amplitude reaches or exceeds the voltage limit, the virtual signal injection control should be suspended. Effective field weakening control may therefore be realised by conditioning the VISC with the voltage error in (2-17).

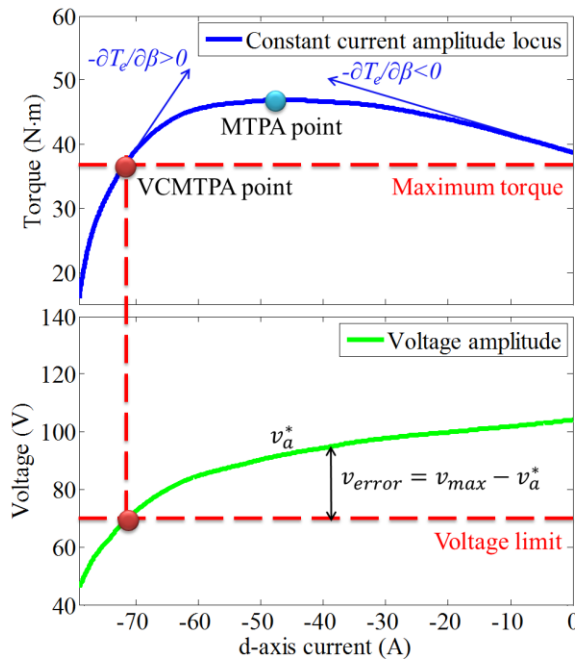


Fig. 2-20. Variations of torque and voltage amplitude with d-axis current for given current amplitude.

2.3.2 Virtual Signal Injection Aided Field Weakening Control and Its Implementation

As discussed in section 2.3.1, since the MTPA operating condition is only valid when the drive voltage is below the voltage limit, the virtual signal injection control is only effective in constant torque region.

To expand the drive operation into field weakening region, an additional voltage feedback loop is incorporated into the virtual signal injection based control. This control scheme is named as virtual signal injection aided field weakening control (VSIAFWC). Moreover, the proposed virtual signal injection aided field weakening control also incorporates conventional model based MTPA and field weakening control scheme for fast response.

Fig. 2-21 shows the schematic of the virtual signal injection aided field weakening control for IPMSM drives. It consists of three parts in addition to the classic d-q axis current control loop with decoupling compensation. Part I in Fig. 2-21 is a model-based reference d-axis current generator. It provides a nominal reference d-axis current, i_{dmain} , with fast response. i_{dmain} can be obtained from look-up tables or calculated from (1-6) and (1-10) or (1-14) with the nominal PM flux linkage, and d- and q-axis inductances. Under the assistance of i_{dmain} , the MTPA points can be tracked quickly and accurately through virtual signal injection.

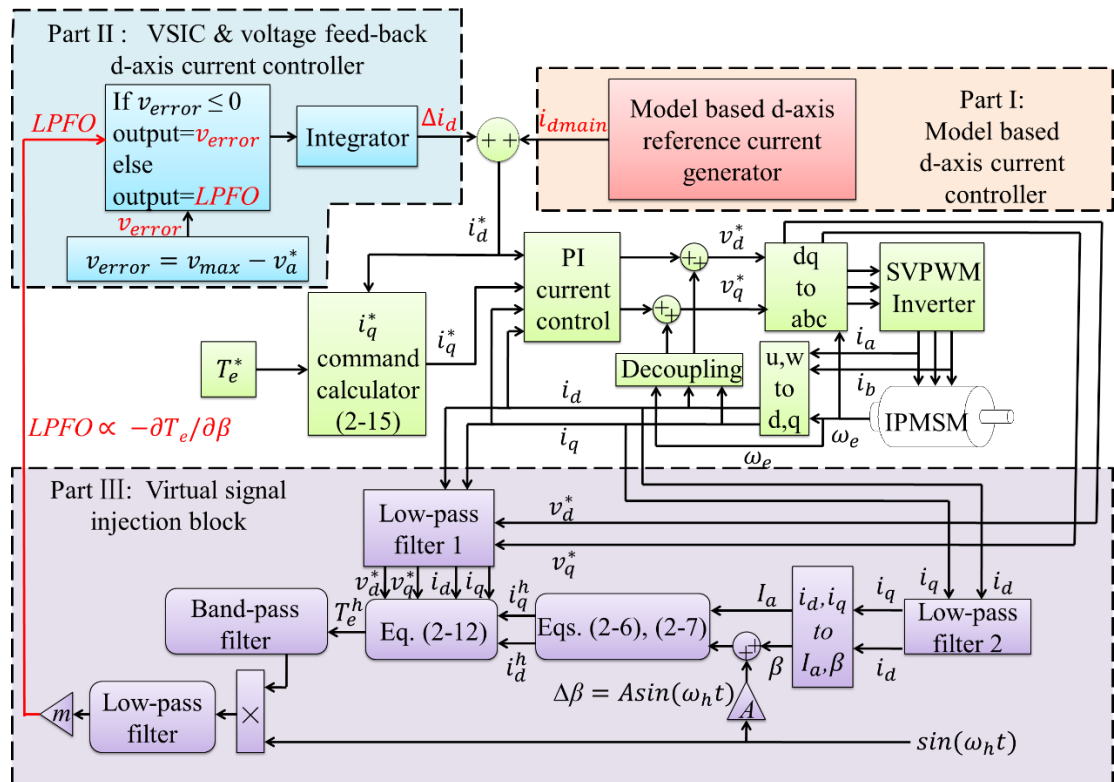


Fig. 2-21. The diagram of virtual signal injection aided field weakening control.

However, due to parameter inaccuracies, the reference d-axis current generated in Part I may not be equal to the optimal reference d-axis current for MTPA or VCMTA control. In order to compensate for the error of i_{dmain} , the virtual signal injection control

combined with the voltage feedback d-axis current controller is introduced in Part II of Fig. 2-21. The output of Part II, denoted as Δi_d , is utilized to compensate the error of i_{dmain} .

The *LPFO* signal input to Part II is generated from the virtual signal injection block, shown in Part III, as described in section 2.2.2.2, and it is proportional to $-\partial T_e / \partial \beta$. Whether this signal will be fed to the integrator in Part II will depend on the voltage error v_{error} defined in (2-17). Therefore, the proposed field weakening control scheme uses v_{error} to identify the onset of the voltage saturation (or the need for field weakening). The operations against the voltage error are described as follows.

2.3.2.1 If $v_{error} \leq 0$

Under this condition, the amplitude of the reference voltage is greater than the voltage limit, which implies that the reference d-axis current generated by the virtual signal injection control in Part III will cause voltage saturation in the current control loops and, hence, insufficient voltage for field weakening control. v_{error} will be fed into the integrator in Part II and the *LPFO* signal (the output of Part III) will be suspended. The negative v_{error} will cause the integral regulator output, denoted by Δi_d , to increase in the negative direction, and as a result, the d-axis reference current, i_d^* , moves toward the VCMTPA point as shown in Fig. 2-20. Thus, Δi_d will compensate for insufficient d-axis current to prevent the current regulators from saturation by decreasing v_a until it equals v_{max} .

2.3.2.2 If $v_{error} > 0$

Under this condition, the integrator input in Part II is the *LPFO* signal from the output of Part III which is proportional to $-\partial T_e / \partial \beta$. As shown in Fig. 2-20, if the voltage amplitude v_a^* is lower than v_{max} , the motor operates on the left side of the VCMTPA point. Δi_d will be adjusted such that the d-axis current tends toward the MTPA point until $-\partial T_e / \partial \beta = 0$ or $v_{error} = 0$, i.e., when either the MTPA or VCMTPA point is reached.

It follows that the Δi_d can be utilized to ensure efficient operation of IPMSM drives in the field weakening regions. In conventional feedback based field weakening control

without the VSIC, if $|i_{dmain}|$ is larger than the d-axis current amplitude of the VCMTPA point due to inaccurate parameters, the voltage feedback loop is no longer in action and hence the VCMTPA control in the field weakening region may not be achievable.

However, as described above, the MTPA control in constant torque region and VCMTPA control in field weakening region can always be guaranteed by the proposed virtual signal injection aided field weakening control scheme.

2.3.2.3 Reference q-axis Current Generation

The reference q-axis current i_q^* in Fig. 2-21 is also calculated from (2-15). The machine parameters, L_d , L_q , Ψ_m , can be obtained from pre-defined look-up tables or their nominal values.

Since T_e^h in (2-12) and the voltage error are independent of the motor parameters, even if the motor parameters in (2-15) are inaccurate, the proposed method can still extract $-\partial T_e / \partial \beta$ and v_{error} information, which are used in the manner described previously to track the MTPA point or VCMTPA point of the actual torque accurately.

However, the inaccurate motor parameters in (2-15) may cause torque error. For speed control mode, the error is compensated by the speed loop, while in EV traction the loop is closed by the vehicle driver. It is worth noting that due to inaccurate parameters, the q-axis reference current calculated from (2-15) may result in the actual torque being greater or less than the reference torque. When the reference torque reaches the predefined limit, the inaccurate reference q-axis current implies that the actual motor torque may be greater or less than the maximum torque limit.

2.3.3 Simulation Results

Simulations of the virtual signal injection aided field weakening control were performed based on the prototype IPMSM drive system. The motor model used in the drive system simulation is described in section 2.2.4.

2.3.3.1 Relationship between LPFO Signal and Reference Voltage Amplitude

The relationship between the virtual signal processing block output, i.e., the LPFO signal in Fig. 2-21, and the reference voltage amplitude was studied by simulations when speed gradually increases. Simulation was first performed when the motor is controlled by the virtual signal injection control illustrated in Fig. 2-6 without the proposed field weakening control scheme. The resultant reference voltage amplitude and LPFO signal are shown in Fig. 2-22. As can be seen, when $t < 16.2$ s, the reference voltage amplitude is below the voltage limit and the LPFO signal is zero, implying the MTPA is realized. However, when $t > 16.2$ s, the motor is entering field weakening region, and the reference voltage amplitude will reach the voltage limit.

Due to $-\partial T_e / \partial \beta > 0$ (shown in Fig. 2-20), the LPFO signal will keep driving the d-axis current toward the MTPA point in Fig. 2-20, resulting in a deeper saturation of the current controllers; this will further increase the reference voltage amplitude. Since T_e^h used in the virtual signal injection is obtained with the reference voltage, the LPFO signal increases significantly when the voltage saturation in the current controllers occurs, as is observed in Fig. 2-22. Therefore, in the field weakening region, the virtual signal injection should be suspended.

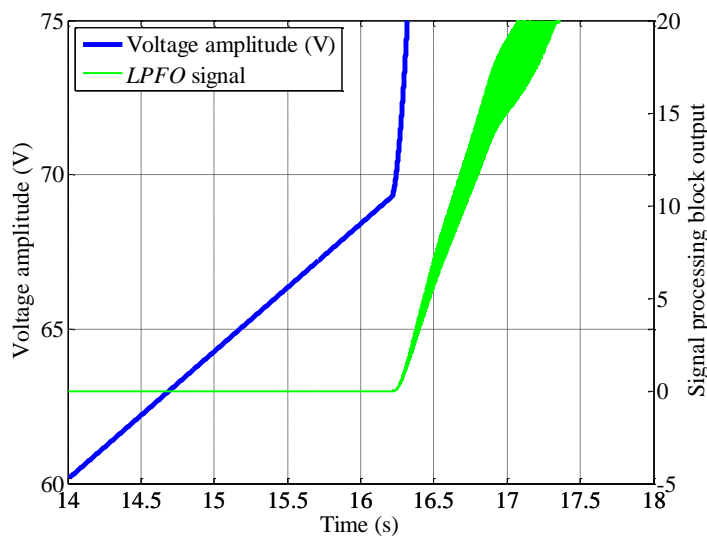


Fig. 2-22. The reference voltage amplitude and LPFO signal without field weakening control (from constant torque region to field weakening region).

Simulation was repeated when the motor was controlled by the proposed field weakening control scheme and the results are shown in Fig. 2-23. If the motor enters the field weakening region, the *LPFO* signal will be suspended and v_{error} calculated by (2-17) is used to operate the motor at the VCMTPA point by increasing the d-axis current amplitude, and consequently the voltage reference amplitude will be kept to the voltage limit as it is shown in Fig. 2-23.

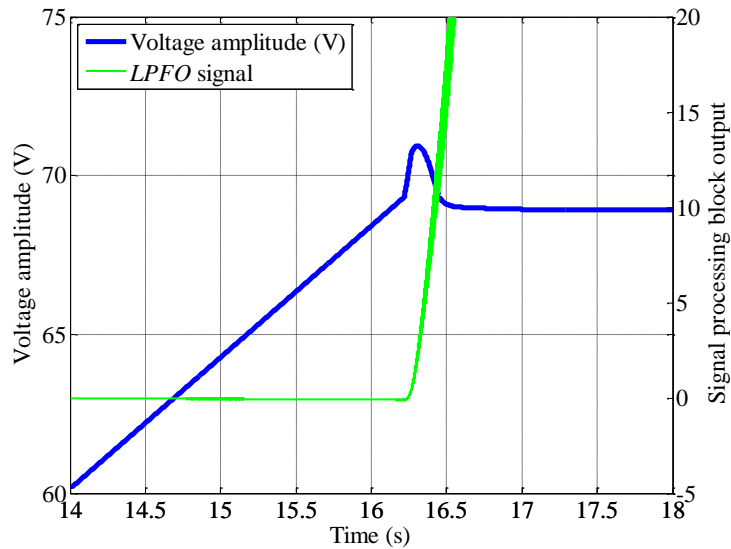


Fig. 2-23. The reference voltage amplitude and *LPFO* signal with proposed field weakening control (from constant torque region to field weakening region)

Due to the increase in the d-axis current amplitude, the operating point shown in Fig. 2-20 will move to the left side of the MTPA point shown Fig. 2-20 where $-\partial T_e / \partial \beta > 0$. Hence, virtual signal injection will tend to increase (decrease in magnitude) the d-axis current toward the MTPA point in Fig. 2-20. This implies, as evident in Fig. 2-22 and Fig. 2-23, that in the field weakening region the output of virtual signal injection block, i.e., the *LPFO* signal, is always larger than zero regardless of whether the current controllers are saturated or not. Therefore, the virtual signal injection action will always tend to move the operating point to the right. It follows that under the combined actions of v_{error} and *LPFO*, the operation points of the machine will always be kept at the VCMTPA point where $v_{error} = 0$.

Fig. 2-24 shows the variations of the reference voltage and virtual signal injection block output when the drive initially operates in the field weakening region while the speed is reduced gradually. When the speed decreases, the operating point moves to the right and

$-\partial T_e / \partial \beta$ as well as the *LPFO* signal decrease. When the motor enters the constant torque region from field weakening region, the reference voltage amplitude will be below the voltage limit and the virtual signal injection control will be activated to adjust the d-axis current toward the MTPA point. When the motor reaches the MTPA point, the output of VSIC will be zero as it is shown in Fig. 2-24.

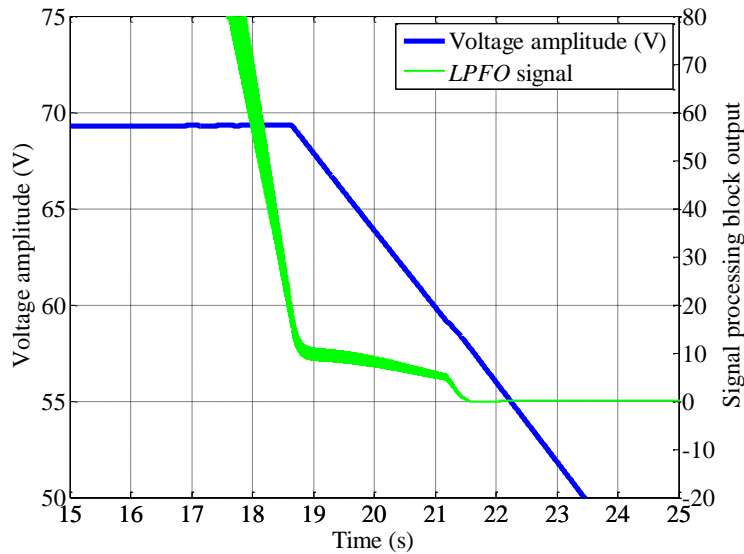


Fig. 2-24. The reference voltage amplitude and *LPFO* signal output with proposed field weakening control (from field weakening region to constant torque region).

2.3.3.2 VCMTPA Point Tracking

Fig. 2-25 shows the simulation result of the proposed field weakening control of the IPMSM drive when it was operated at 3000 r/min and 10 N·m in the field weakening region. The ideal d-axis current for the VCMTPA operation was -66 A. As it is shown in Fig. 2-25, the value of i_{dmain} obtained from Fig. 2-21 was initially equal to -56 A which was larger than the ideal value due to inaccurate machine parameters. The reference d-axis current, i_d^* , generated by the proposed field weakening control scheme gradually converged to the VCMTPA operation under the proposed control.

To illustrate another possible condition in which the magnitude of i_{dmain} may be greater than that of the ideal d-axis current, the nominal parameters of the machine were varied at $t = 20$ s such that i_{dmain} became -76 A. Again, the d-axis current reference tracked the ideal value and the difference was compensated by the proposed control automatically.

It should be noticed that the iron loss causes the MTPA point tracked by the VSIC to deviate slightly from the maximum efficiency operating point. However the deviation is negligible for most IPMSMs due to the fact that in the constant torque region when speed is low, the loss is dominated by the copper loss.

In the field weakening region when the iron loss is more significant, the VCMTPA is usually uniquely determined by the payload torque and voltage limit, as shown in Fig. 2-20, and hence independent of the iron loss.

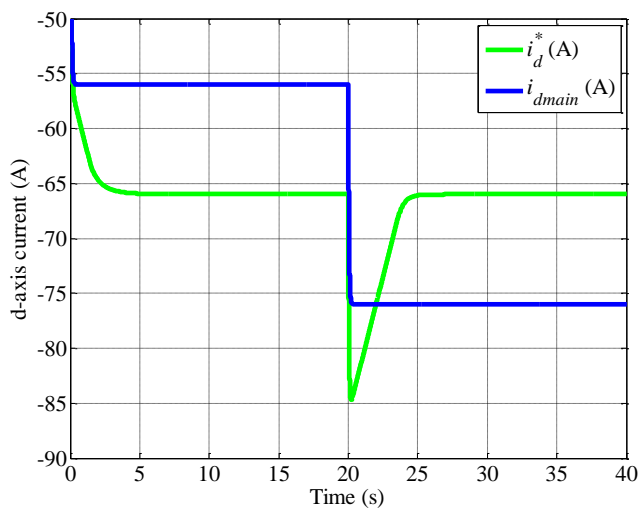


Fig. 2-25. d-axis current responses of proposed field weakening control.

2.3.3.3 Fast Transition from Constant Torque Region to Field Weakening Region

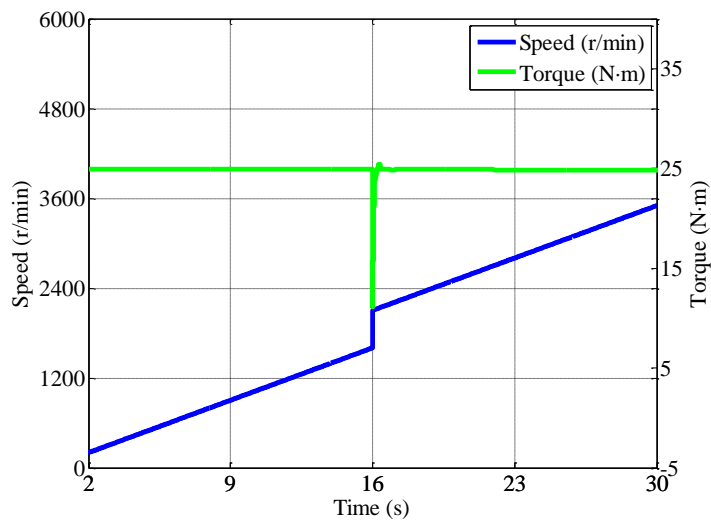


Fig. 2-26. Fast transition of the motor operation from constant torque region to field weakening region through a 500 r/min speed step.

Fig. 2-26 shows the simulated torque response to a step change of 500 r/min in speed when the drive operating condition changed from the constant torque region to the field weakening region.

It can be seen that the proposed control exhibits stable and fast transition from the constant torque region to the field weakening region in response to the step change in speed. However, in real applications, electric vehicle traction in particular, a step change in speed cannot occur due to drive system inertia or large mass. Therefore, conditions which are worse than that illustrated in Fig. 2-26 will not occur practically.

2.3.3.4 Peak Torque for Full Speed Range Operation

To verify the performance of the proposed control scheme in full speed range at peak torque, simulations were performed employing a high fidelity non-linear IPMSM machine model which represents the real electromagnetic behaviours of IPMSMs. The high fidelity model is flux linkage-based and captures all non-linear effects and high order space harmonics as described in [13]. The machine specifications are listed in Table 2-1. The motor was controlled in torque control mode when the speed is increased from 0 r/min to the maximum speed, i.e., 4500 r/min, within 15 s.

The reference torque was set to the peak torque according to the peak torque profile. The q-axis reference current was calculated based on (2-15) and the machine parameters in (2-15) were obtained from the predefined look-up tables as functions of d- and q- axis currents. The i_{dmain} in Fig. 2-21 was obtained from a pre-defined look-up table with reference torque and rotor speed as its inputs.

In order to compare performances with the conventional field weakening control scheme, simulations were performed with the virtual signal injection aided field weakening control as shown in Fig. 2-21 and with the conventional field weakening control when the virtual signal injection in Fig. 2-21 was disabled, but the d-axis current for field weakening was obtained from the model (the look-up table) and adjusted by the voltage error feedback loop.

Fig. 2-27 shows the resultant reference voltages throughout the speed ramp obtained from the two control schemes. As can be seen from Fig. 2-27, for the field weakening operation which is assisted by the virtual signal injection, in field weakening region, the resultant reference voltage amplitude is always equal to the maximum voltage amplitude limit, which indicates the motor is operated at the VCMTA points.

However, for the field weakening control which is not assisted by the virtual signal injection, the resultant reference voltage amplitude is smaller than the maximum voltage amplitude limit. This is because the absolute value of the reference d-axis current in the conventional field weakening control was larger than the optimal d-axis current amplitude in the field weakening operation. Under this condition, the voltage feedback loop of the conventional scheme is no longer able to keep the operation at the VCMTPA points.

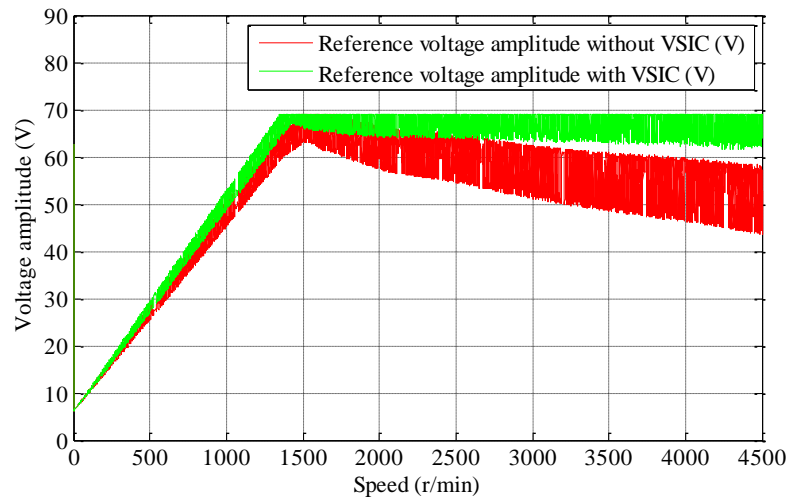


Fig. 2-27. Reference voltage amplitude for different speed with and without virtual signal injection.

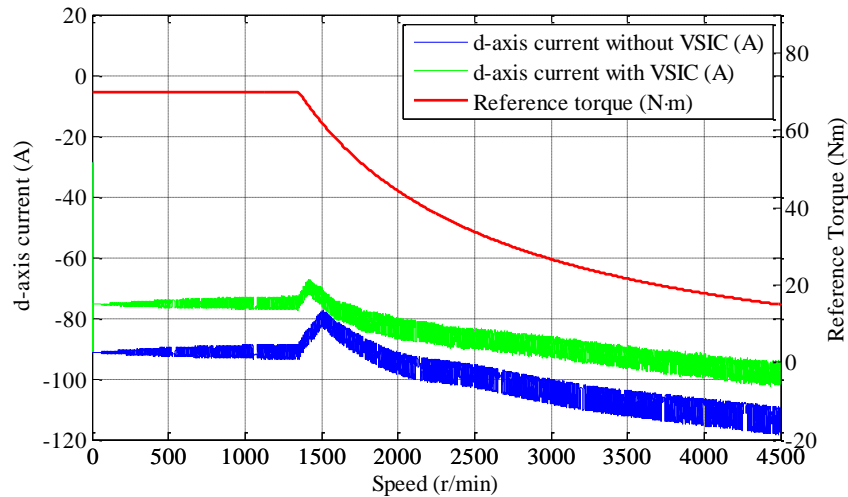


Fig. 2-28. Reference torque and d-axis currents.

The resultant d-axis currents of the conventional and proposed control schemes are shown in Fig. 2-28. As shown in Fig. 2-28, in the constant torque region, the virtual signal injection aided control scheme automatically compensates the error of i_{dmain} . In the field weakening region, the amplitude of the resultant d-axis current generated by the proposed control scheme is smaller than that of the conventional control scheme. This is due to the

fact that the error between i_{dmain} and the optimal d-axis current was compensated by the virtual signal injection and the motor is controlled on the VCMTPA points.

It should be noticed that when the motor just enters the field weakening region, at speed ≈ 1400 r/min in Fig. 2-28, the d-axis current initially increases then decreases. This is due to the combined effect of the reference torque decrease and d-axis current amplitude increases as a result of field weakening operation.

Fig. 2-29 shows the reference torque and the resultant q-axis currents of the conventional field weakening control and the virtual signal injection aided field weakening control. Again, the error of the conventional control scheme is compensated by the proposed control scheme.

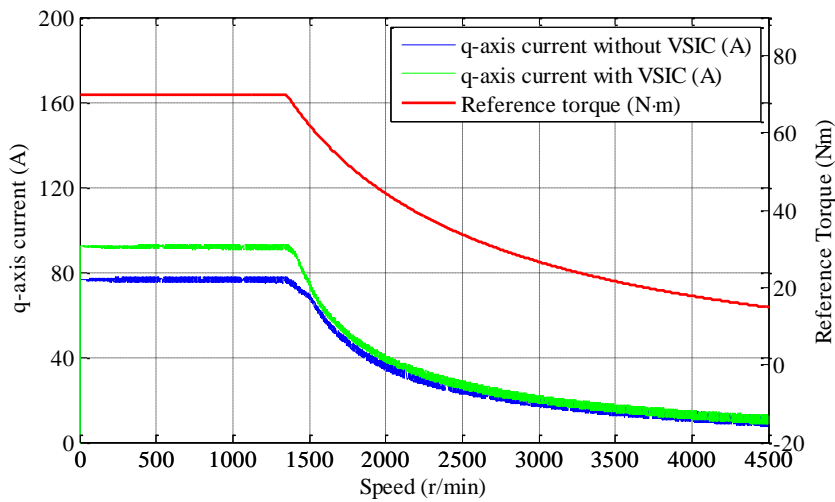


Fig. 2-29. Reference torque and q-axis currents.

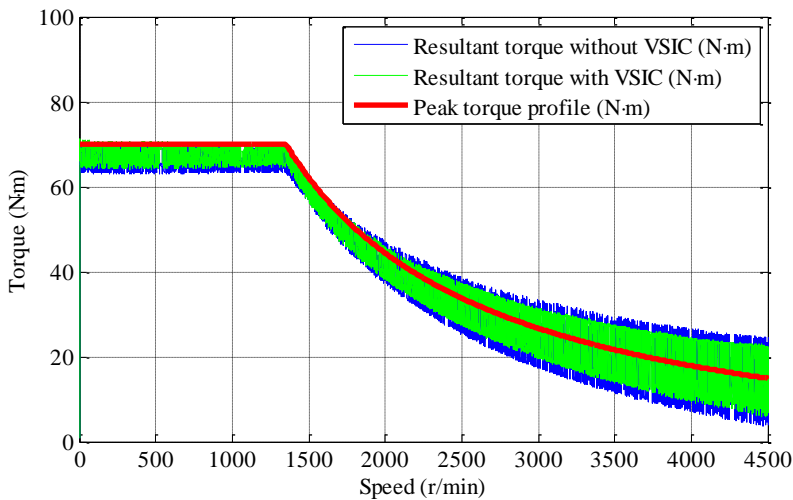


Fig. 2-30. Peak torque profile and resultant torques against the speed.

Fig. 2-30 illustrates the peak torque profile and resultant torques of the two control schemes. Since the IPMSM model utilized in simulations considered all non-linear effects and high order space harmonics as described in [13], large ripples in resultant torque can be observed. This is due to the interaction of large d-axis current in the field weakening region with the position dependent saliency. The detail for the cause of the large torque ripple is given in [13].

Because the virtual signal injection aided field weakening control scheme can always keep the d-axis current at the optimal value, the resultant torque ripple shown in Fig. 2-30 is also smaller than that of the conventional control scheme.

2.3.4 Experimental Results

The proposed field weakening control which incorporates the VSIC was implemented in the IPMSM drive, whose specification is given in Table 2-1. The drive was tested on the test rig shown in Fig. 2-10.

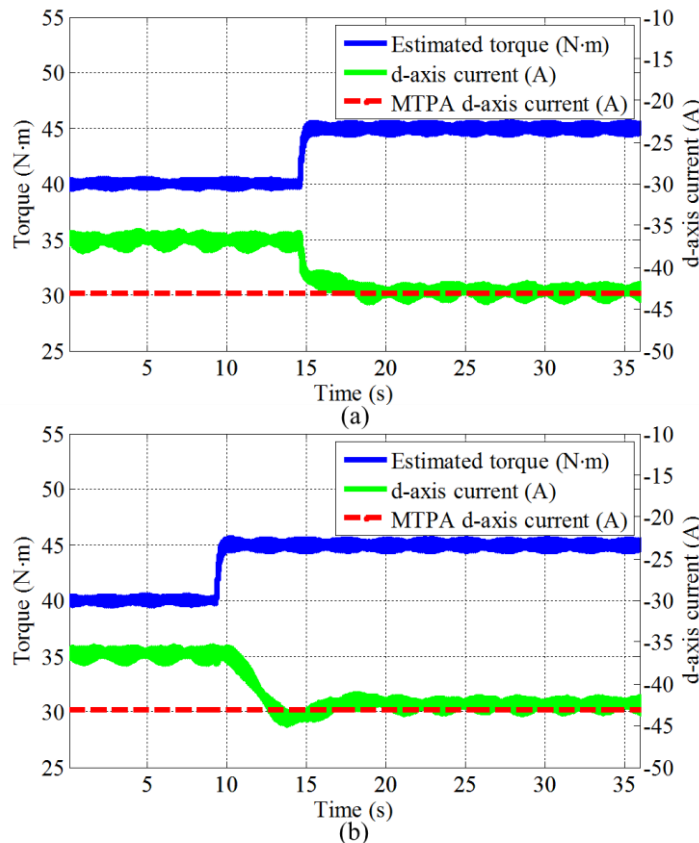


Fig. 2-31. d-axis current responses to step change in torque from 40 N·m to 45 N·m at 1000 r/min.

2.3.4.1 VSIC Performance in Constant Torque Region

Tests were first performed in constant torque region to verify the MTPA tracking performance of the combination of conventional model based control scheme and the virtual signal injection control. The measured d-axis current together with estimated torque based on the measured d- and q-axis currents and the nonlinear machine model in the form of look-up tables are shown in Fig. 2-31(a) in responses to a step change in torque demand from 40 N·m to 45 N·m at speed of 1000 r/min. The dotted lines in Fig. 2-31 are the theoretical MTPA d-axis current of 45 N·m at the speed of 1000 r/min.

It can be seen in Fig. 2-31(a) that the d-axis current firstly experiences a step change due to i_{dmain} then tracks the MTPA point gradually under assistance of VSIC.

Fig. 2-31 (b) shows the MTPA point tracking performance of the virtual signal injection control without the assistance of i_{dmain} . By comparing Fig. 2-31 (a) and (b), it is evident that the combination of the model based control scheme with the virtual signal injection control can track the MTPA point quickly.

Fig. 2-32 compares the measured torque and reference torque in response to a step change in the reference torque at the same operating condition of Fig. 2-31. A small error of ~0.4 N·m between the measured torque and reference torque is due to the same reasons detailed before. It should be noted that measured ripple is much less than the estimation due to the presence of a low pass filter in the torque measurement.

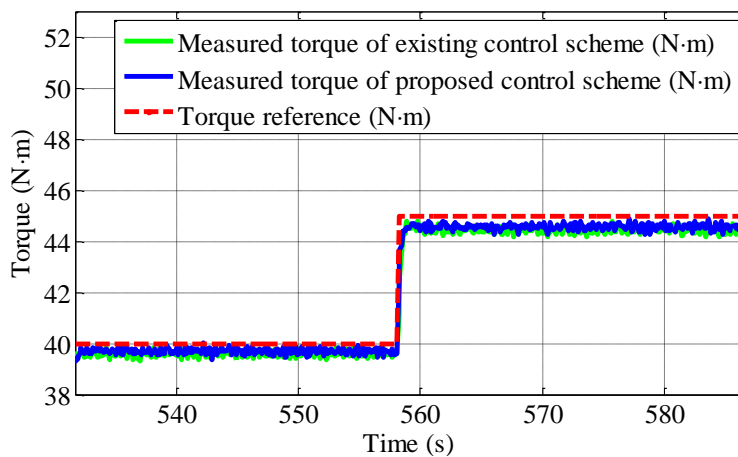


Fig. 2-32. The comparison between the measured torques and torque reference.

The variation of measured drive system efficiency (including the inverter and IPMSM) with d-axis current for a given current amplitude (75.5 A) is illustrated in Fig. 2-33. As can be seen, the maximum system efficiency coincides with that tracked by the VSIC.

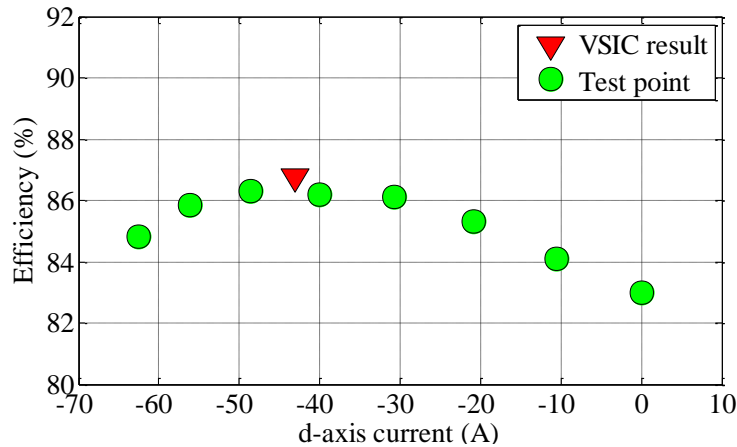


Fig. 2-33. Variation of measured drive system efficiency with d-axis current for a given current amplitude (75.5 A, 1000 r/min, 45 N·m).

2.3.4.2 d-axis Current Response to Step Change in Torque Demand in Deep Field Weakening Region

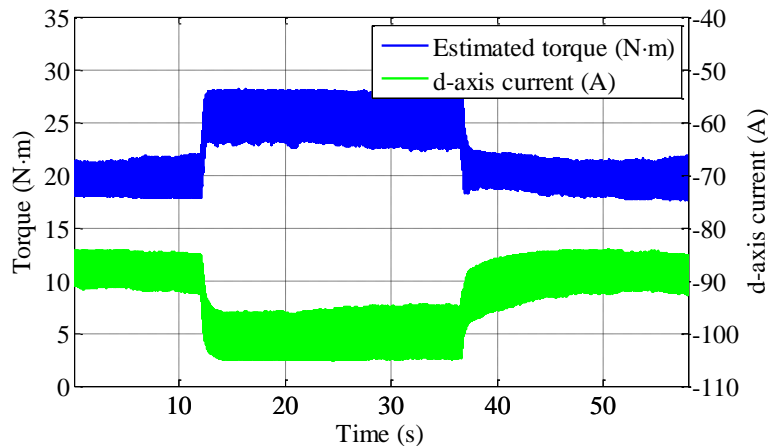


Fig. 2-34. d-axis current and estimated torque response to step changes in torque demand from 20 N·m to 25 N·m and back to 20 N·m at 3000 r/min.

Fig. 2-34 shows the measured d-axis current response when the torque demand increases in step from 20 N·m to 25 N·m at 12 s and decreases in step from 25 N·m to 20 N·m at 36.5 s at 3000 r/min when the drive operated in deep field weakening region. The estimated torque based on the measured d- and q-axis currents and nonlinear machine model is also illustrated in Fig. 2-34.

When the reference torque has a step change from 25 N·m to 20 N·m, the amplitude of d-axis current exhibits an immediate step change associated with i_{dmain} . It subsequently converges to the optimal value under the influence of Δi_d .

To illustrate the torque control accuracy in the field weakening region, the measured torque is compared in Fig. 2-35 with the reference torque at 3000 r/min when step changes in reference from 20 N·m to 25 N·m and back to 20 N·m take place. A small torque error of $\sim 0.8\text{N}\cdot\text{m}$ is caused by the same reasons detailed before.

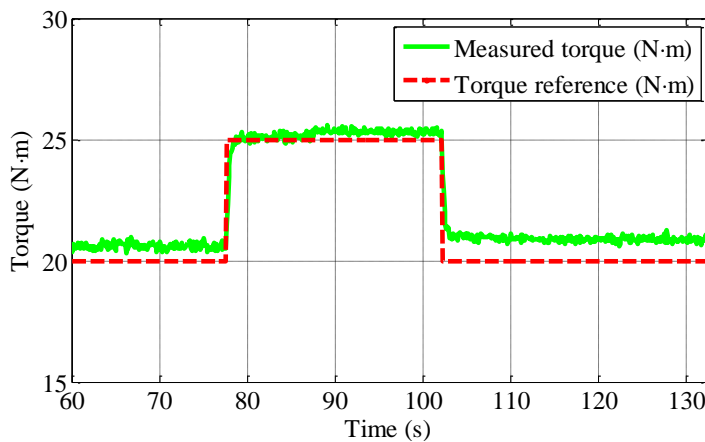


Fig. 2-35. Measured torque and reference torque at 3000 r/min.

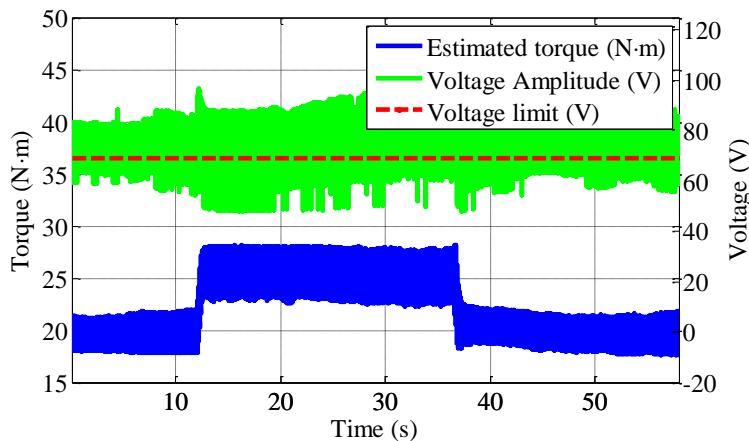


Fig. 2-36. Reference voltage amplitude and estimated torque responses during step change in torque demand.

The reference voltage amplitude during the torque reference step is shown in Fig. 2-36 where the dotted line represents the voltage amplitude limit of the inscribed circle of the voltage hexagon. As is evident, the voltage amplitude is essentially kept at the limit during the torque step changes. The high frequency voltage ripple is caused by spatial harmonics

[13] and the over-modulation technique employed to fully utilize the voltage boundary at the hexagon.

It can also be seen that a fast torque response has been achieved with the proposed control albeit high frequency estimated torque ripple is clearly visible. This is due to the combined effect of PWM switching and the distortion in phase currents as well as the distortion in the flux linkage.

The current angle variation during torque step is shown in Fig. 2-37. The efficiency of the drive system was 0.878 at 20 N·m, 3000 r/min and 0.866 at 25 N·m, 3000 r/min.

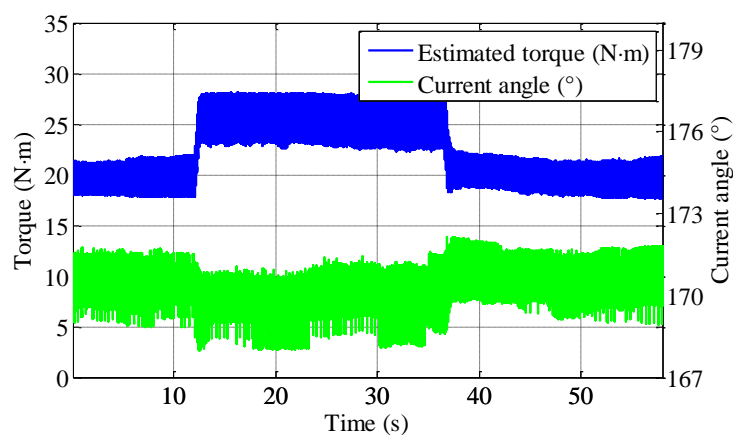


Fig. 2-37. The current angle variation during torque step.

The waveforms of three-phase voltages applied to the motor and the phase currents at 20 N·m, 3000r/min are shown in Fig. 2-38.

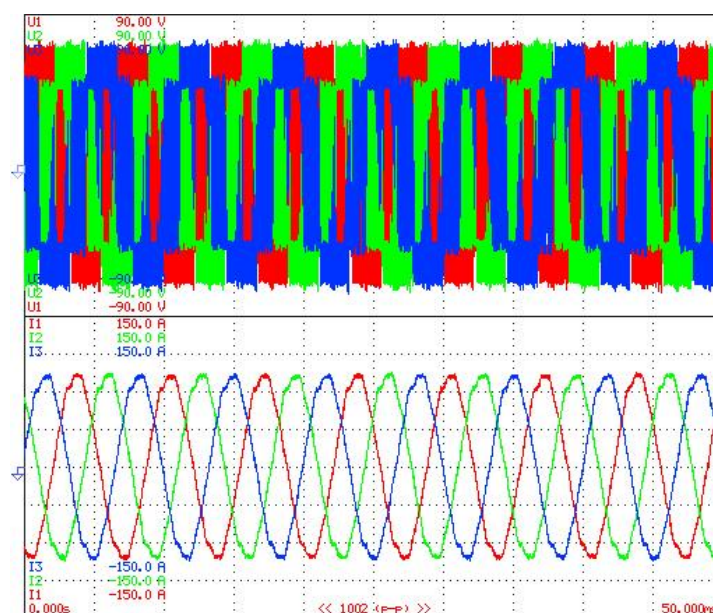


Fig. 2-38. Voltage and current waveform at 3000 r/min speed and 20 N·m torque.

2.3.4.3 Transition between Constant Torque Region and Field Weakening Region

To demonstrate seamless transitions between the constant torque and field weakening regions with the proposed control, 20 N·m torque was applied to the drive while its speed was varied from 1620 r/min to 1453 r/min. Fig. 2-39 shows the speed variation and the measured d-axis current response. When the speed is at 1620 r/min, the motor operated in the field weakening region. As the speed decreases, the amplitude of d-axis current also decreases. At the speed below 1520 r/min, the motor enters the constant torque region, and consequently, the d-axis current reaches its optimal value under the MTPA operation. A smooth transition from the field weakening region to the constant torque region can be observed.

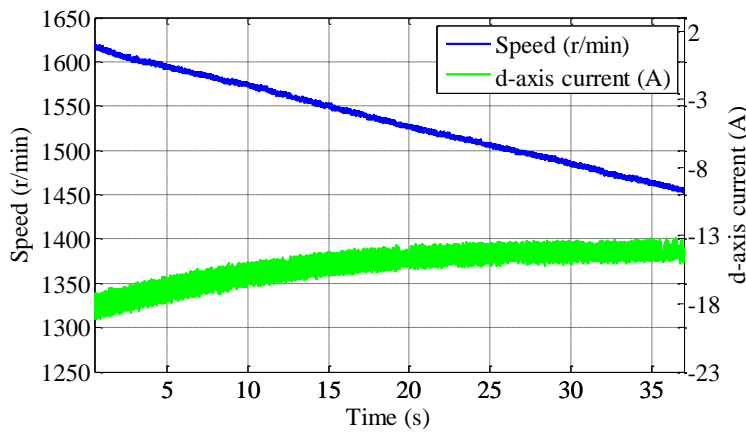


Fig. 2-39. Variations of speed and d-axis current during transition from field weakening region to constant torque region.

A similar test was performed when the load torque was kept at 20 N·m and the speed was increased from 1551 r/min to 1713 r/min. The measured d-axis current response is shown in Fig. 2-40. When the speed is below 1630 r/min, the motor operates in the constant torque region and the d-axis current is kept constant as the speed is increased. The amplitude of the d-axis current begins to increase when the motor enters the field weakening region.

The small hysteresis band of 110 r/min between the constant torque and field weakening operations is due to the delay and transient error of the integral regulator in Fig. 2-21, when the speed varied continuously during the test. This hysteresis band is useful in that it provides smooth transitions between the constant torque region and the field weakening region.

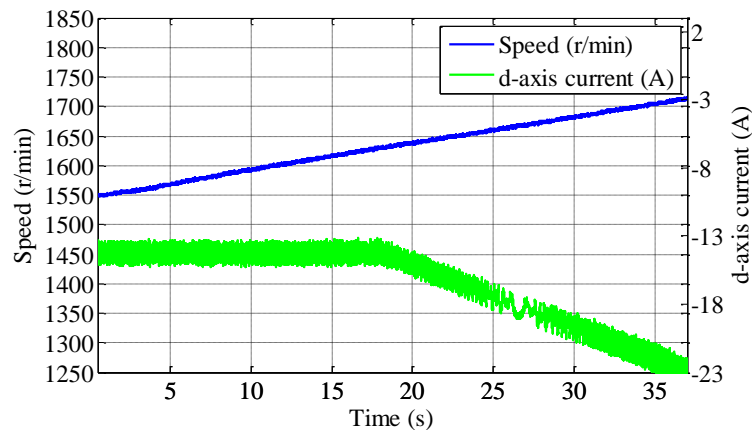


Fig. 2-40. Variations of speed and d-axis current during transition from constant torque region to field weakening region.

A further test was carried out in which the speed of the drive was kept at 1600 r/min and the reference torque was varied from 0 to 30 N·m in steps of 5 N·m. The reference torque and reference voltage amplitude are shown in Fig. 2-41. Again, the dotted line illustrates the voltage limit.

When the load torque is below 10 N·m, the motor operates in the constant torque region and the resultant voltage amplitude increases with increase in load torque, but is below the limit in average sense. As the torque is increased above 10 N·m, the voltage amplitude reaches the limit and the motor enters field weakening operation. As shown in Fig. 2-41, when the machine enters the field weakening region, the voltage amplitude is essentially kept at the limit during the torque step changes, which again indicates the proposed control scheme can always keep motor operating at the VCMTPA points.

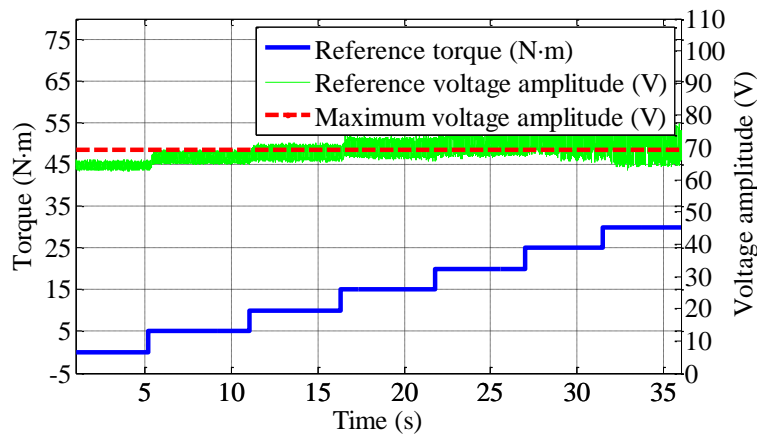


Fig. 2-41. Reference torque and reference voltage amplitude when reference torque varies from 0 N·m to 30 N·m at 1600 r/min.

To illustrate the d- and q-axis currents control performance of the proposed control scheme, the measured d- and q-axis currents under the same operation conditions as Fig. 2-41 are shown in Fig. 2-42. It is evident that the resultant d- and q-axis currents follow the reference d- and q-axis currents accurately.

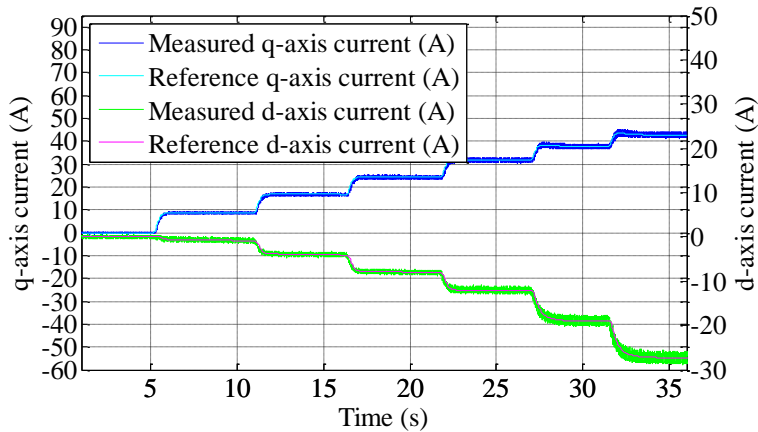


Fig. 2-42. Measured d- and q-axis currents when reference torque was varied from 0 to 30 N·m in steps of 5 N·m.

The reference torque was also varied from 30 to 0 N·m in steps of 5 N·m at 1600 r/min to test the control performance of the transition from field weakening region to constant torque region. The reference torque and reference voltage amplitude are shown in Fig. 2-43. As shown in Fig. 2-43, when the load torque is above 10 N·m, the reference voltage amplitude is maintained at the voltage limit, i.e., the VCMTPA points. Whereas when the load torque steps below 10 N·m, the motor enters constant torque region, and the reference voltage amplitude decreases.

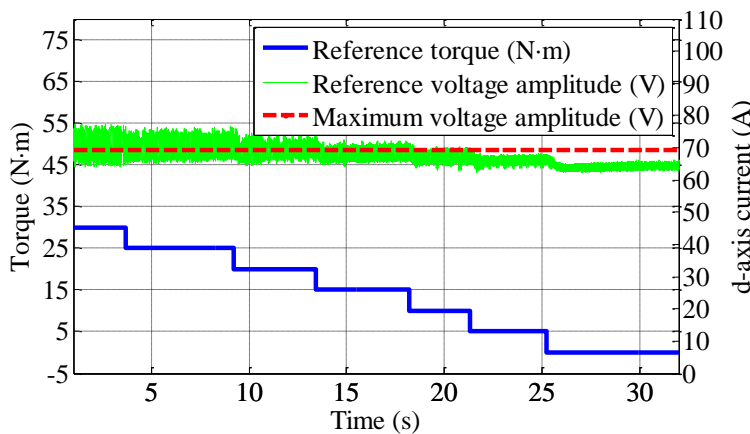


Fig. 2-43. Reference torque and reference voltage amplitude when reference torque varies from 30 N·m to 0 N·m at 1600 r/min.

The measured d- and q-axis currents under the same operation conditions as Fig. 2-43 are shown in Fig. 2-44. As can be seen, when the reference torque steps, the amplitude of d-axis current exhibits an immediate step change associated with i_{dmain} . It subsequently converges to the optimal value under the influence of Δi_d .

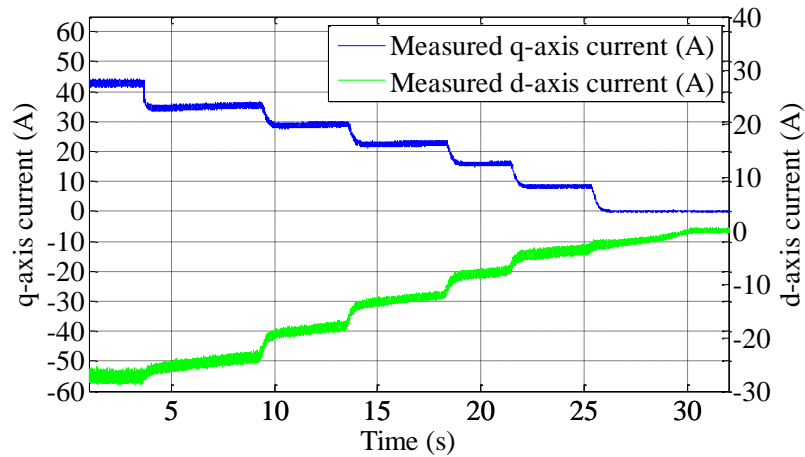


Fig. 2-44. Measured d- and q-axis currents when reference torque was varied from 30 to 0 N·m in steps of 5 N·m.

The measured torque and reference torque at 1660 r/min when the reference torque varies from 0 N·m to 30 N·m in a step of 5 N·m and from 30 N·m back to 0 N·m in the same step are shown in Fig. 2-45. The smooth transitions between the two operating regions can be inferred from the good torque response and the voltage amplitude variation.

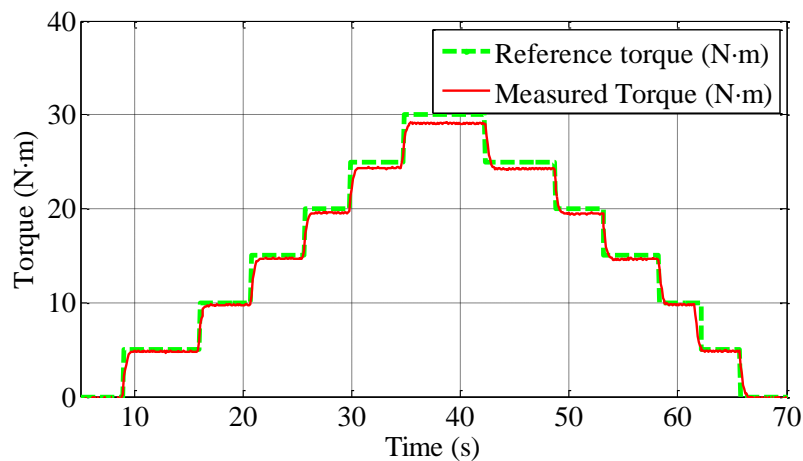


Fig. 2-45. Measured torque and reference torque when reference torque was varied from 0 N·m to 30 N·m in a step of 5 N·m and from 30 N·m back to 0 N·m in the same step.

2.4 Summary

In this chapter, virtual signal injection control is proposed and achieved in the d-q frame. The virtual signal injection method utilizes the fact that at an MTPA point the torque variation with the current angle is zero. It is shown that this variation can be obtained mathematically from the measured speed, currents, and the command voltage applied to an IPMSM through a virtual signal injected into current angle instead of real signals injected into current. In this way, the proposed method is much more robust with respect to current and voltage harmonics which are always present in a practical IPMSM. It also avoids any torque ripple and resonant problem due to the current ripple in the real signal injection methods, and will not cause additional power loss as a result of real signal injection. Both the simulation and experimental results demonstrate that the proposed control scheme is very accurate in tracking the MTPA points without prior knowledge of motor parameters and is robust with respect to torque variations.

The virtual signal injection aided field weakening control scheme expands the virtual signal injection control into field weakening region. It combines conventional model based field weakening control and virtual signal injection control with voltage feedback. The virtual signal injection aided field weakening control scheme realizes maximum torque per ampere operation in constant torque region and voltage constrained maximum torque per ampere operation in field weakening region and achieves seamless transitions between the two regions. The proposed control scheme not only has fast torque response but also can track the MTPA points in constant torque and VCMTPA in field weakening regions without knowledge of accurate machine parameters.

CHAPTER 3 Virtual Signal Injection Based Direct Flux Vector Control

3.1 Introduction

In Chapter 2, the virtual signal injection based field orientated control in the rotor synchronous (d-q) frame has been developed to control IPMSM drives in both constant torque region and field weakening region. Alternatively IPMSM drives can also be controlled in the stator flux linkage synchronous (f-t) frame through direct torque control [20]–[24] or direct flux vector control [25]–[27].

Compared with d-q frame based control schemes, f-t frame based control scheme not only can manage motor voltage in field weakening region without look-up tables of currents or reference flux [65] but also has better performance in field weakening [66], fast torque response [24], and higher torque control accuracy.

In order to operate IPMSM in constant torque region effectively, maximum torque per ampere (MTPA) control is necessary. The MTPA control results in minimum current amplitude for a given torque, and hence minimum copper loss which is dominant in constant torque region. In literature, MTPA strategies for d-q frame based control schemes have been well studied. However, MTPA control strategies for f-t frame based control schemes have not been comprehensively reported. Different from d-q frame based MTPA control schemes, the performances of f-t frame based MTPA control schemes are not only dependent on the accuracy of commands generated by the MTPA control schemes, but also on the accuracy of flux observer. This implies that, compared with d-q frame based MTPA control schemes, f-t frame based MTPA control schemes are more vulnerable to command and flux observer errors. Therefore, studies of MTPA control in f-t frame based control schemes for IPMSM drives are necessary.

Currently, the MTPA operation for f-t frame based control schemes are mainly achieved by controlling the reference flux amplitude. The reference flux amplitude for MTPA operation can either be calculated based on mathematical model [76] or generated from pre-defined look-up tables which are obtained from numerical machine model or experiments [26]. However, in real applications, due to magnetic saturation, cross-

coupling effects, manufacturing tolerance, material property variation, and temperature variation, the parameters of an IPMSM are highly nonlinear and uncertain. Therefore, it is almost impossible to obtain accurate reference flux amplitude according to predefined look-up tables or mathematical models. On the other hand, it is difficult to obtain the predefined reference flux from experimental data. Further, the factors that influence the MTPA operations such as temperature, manufacture tolerances and material property variations may also vary in individual machines [41]. In order to reduce the dependency on motor parameters, search algorithms were, therefore, proposed in [78]. This scheme did not rely on the knowledge of motor parameters for MTPA operations. However, due to slow converging rate, the dynamic performance of this search algorithm was unsatisfactory and the torque control accuracy was affected by load torque disturbance as well as voltage and current harmonics in a practical machine.

Recently, new methods based on the principle of extremum seeking control (ESC) [58], [59], [80] for tracking the MTPA points by injecting high-frequency current signal into machines have been reported. In [79], a signal injection based MTPA point tracking scheme in f-t frame is proposed. In order to avoid the residual torque harmonic at the frequency of the injected signal, a random signal was injected into reference flux amplitude instead of the pure sinusoidal signal injection. And the MTPA points were tracked based on the fact that the current amplitude variation with respect to injected reference flux amplitude perturbation on MTPA points is zero [79]. However, this method may induce additional iron/copper loss as well as additional torque ripple as a result of the injected signal. Moreover similar to other f-t frame based control techniques described previously, this method did not consider the influence of flux observer error on MTPA operations. Consequently, quality of MTPA operations may be significantly affected.

In this chapter, an f-t frame based control scheme employing the virtual signal injection [41], [62], described in Chapter 2, is proposed for realization of MTPA operation of IPMSM drives in constant torque region and voltage constraint MTPA (VCMTPA) operation in field weakening region. Without loss of generality, the direct flux vector control scheme is selected to demonstrate the proposed control scheme. The proposed control scheme retains the advantages of the f-t frame based control schemes but eliminates any problem associated with real signal injection. Moreover, the proposed control scheme is robust to flux observer error and motor parameters inaccuracy in

tracking MTPA points in constant torque region and voltage constraint MTPA points in field weakening region.

The rest of this chapter is organized as follows: section 3.2 outlines the mathematic model of IPMSM drives in the f-t reference frame and briefly describes the principle of virtual signal injection. The implementation of the proposed control scheme in constant torque region is also illustrated in section 3.2 and the proposed control scheme was verified by simulations and experiments. Section 3.3 illustrates the implementation of field weakening control based on the proposed control scheme. Simulations and experiments were performed to verify the proposed control scheme in field weakening region. Section 3.4 draws conclusion from the work.

3.2 Virtual Signal Injection Based MTPA Control in f-t Frame

3.2.1 Principle of Proposed Control Scheme

Control schemes of IPMSM drive can be achieved based on the flux and torque (f-t) reference frame whose relationship with respect to the classic (d-q) frame is illustrated in Fig. 1-5. The mathematical model of an IPMSM in the f-t reference frame is given in (1-23) to (1-26) and the limit of torque is expressed with (1-22).

An f-t frame based control scheme can be formulated by controlling the stator flux amplitude, Ψ_s , and the t-axis component, i_t , of the stator current, when the stator flux is estimated by a flux observer. The flux linkage references for MTPA operations may be generated from the numerical model of the IPMSM and the data is stored in the controller in a look-up table. However, the reference flux may deviate from the MTPA value when the flux map of the actual machine differs from the model because of temperature variation and other modeling errors. Although this problem may partly be circumvented by the signal injection control proposed in [79], the flux observer error may bring additional control error which affects MTPA operations. Further, in the field oriented control, a deviation of d-axis current from its true MTPA point only affects the second term in (1-3). Hence the resulting torque control error is relatively small. With the f-t

frame based control, errors in Ψ_s , whether it is generated from the reference or from the observer, will cause larger torque deviation as is evident from (1-25). Therefore, the MTPA operation in the f-t frame is more sensitive to flux errors and the accuracy of MTPA control is more difficult to be guaranteed.

3.2.1.1 Relationship Between Ψ_{sMTPA} and β_{MTPA}

For a given current amplitude in (3-1), the relationship between electromagnetic torque, T_e , and the current angle, β , defined in (3-2), can be expressed in (3-3).

$$I_a = \sqrt{i_d^2 + i_q^2} \quad (3-1)$$

$$\beta = \arccos\left(\frac{i_q}{I_a}\right) \quad (3-2)$$

$$T_e = \frac{3p}{2} \left[\Psi_m I_a \cos(\beta) - \frac{1}{2} (L_d - L_q) I_a^2 \sin(2\beta) \right] \quad (3-3)$$

Let β_{MTPA} denote the optimal stator current angle for MTPA operation. The d- and q-axis currents for MTPA operation can be expressed in (3-4), (3-5) according to (3-1) and (3-2):

$$i_{dMTPA} = -I_a \sin(\beta_{MTPA}) \quad (3-4)$$

$$i_{qMTPA} = I_a \cos(\beta_{MTPA}) \quad (3-5)$$

The d- and q-axis fluxes can be expressed in (3-6) and (3-7), respectively.

$$\Psi_d = \Psi_m + L_d i_d \quad (3-6)$$

$$\Psi_q = L_q i_q \quad (3-7)$$

Substituting (3-4) and (3-5) into (3-6) and (3-7), the optimal d- and q-axis fluxes for the MTPA operation can be expressed with (3-8) and (3-9), respectively.

$$\Psi_{dMTPA} = \Psi_m - L_d I_a \sin(\beta_{MTPA}) \quad (3-8)$$

$$\Psi_{qMTPA} = L_q I_a \cos(\beta_{MTPA}) \quad (3-9)$$

The flux amplitude can be expressed with:

$$\Psi_s = \sqrt{\Psi_d^2 + \Psi_q^2} \quad (3-10)$$

Substituting (3-8) and (3-9) into (3-10) yields the optimal flux amplitude for MTPA operation:

$$\Psi_{SMTPA} = \sqrt{[\Psi_m - I_a L_d \sin(\beta_{MTPA})]^2 + [I_a L_q \cos(\beta_{MTPA})]^2} \quad (3-11)$$

Moreover, under MTPA operation $\partial T_e / \partial \beta = 0$, and according to (3-3), the relationship between β_{MTPA} and I_a can be expressed as [40]:

$$\beta_{MTPA} = \sin^{-1} \frac{-\Psi_m + \sqrt{\Psi_m^2 + 8(L_q - L_d)^2 I_a^2}}{4(L_q - L_d)I_a} \quad (3-12)$$

(3-12) can also be written as:

$$I_a = \frac{\Psi_m \sin(\beta_{MTPA})}{(L_q - L_d)[1 - 2 \sin^2(\beta_{MTPA})]} \quad (3-13)$$

Substituting (3-13) into (3-11), the flux amplitude that corresponds to β_{MTPA} , i.e., the optimal flux amplitude Ψ_{SMTPA} for MTPA operation, can be expressed as:

$$\Psi_{SMTPA} = \sqrt{a^2 + b} \quad (3-14)$$

Where

$$a = \Psi_m - \frac{\Psi_m L_d \sin^2(\beta_{MTPA})}{(L_d - L_q)[2 \sin^2(\beta_{MTPA}) - 1]} \quad (3-15)$$

$$b = \frac{\Psi_m^2 L_q^2 \cos^2(\beta_{MTPA}) \sin^2(\beta_{MTPA})}{(L_d - L_q)^2 [2 \sin^2(\beta_{MTPA}) - 1]^2} \quad (3-16)$$

It follows from (3-12) and (3-14) that for given current amplitude I_a there is a unique relationship between the optimal stator flux amplitude, Ψ_{SMTPA} , and the optimal current angle β_{MTPA} . Therefore, Ψ_{SMTPA} can be obtained through adjusting the current angle β to its optimal value and vice versa.

By way of example, Fig. 3-1 (a) and (b) show the variation of the stator current angle β and the variation of the electromagnetic torque with the amplitude of the stator flux, respectively, for a prototype IPMSM whose specification is given in Table 2-1.

As it is shown in Fig. 3-1 (b), when the flux amplitude increases, the resultant torque initially increases and reaches a maximum before decreasing. This maximum condition corresponds to MTPA operation. It is also evident from Fig. 3-1 (a) that the optimal flux for MTPA operation can be found by adjusting the current angle such that $\partial T_e / \partial \beta = 0$.

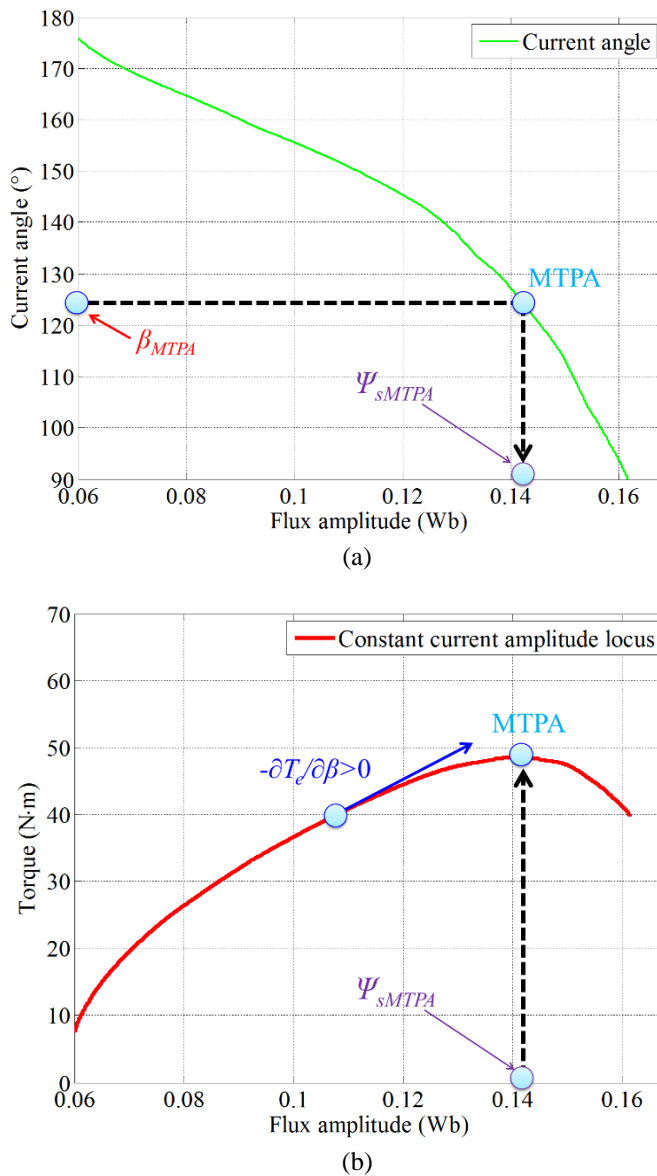


Fig. 3-1. (a) Relationship between flux amplitude and current angle. (b) Relationship between flux amplitude and resultant torque.

From Fig. 3-1 (a) and (b), $\partial T_e / \partial \beta$ will be negative when the stator flux amplitude is smaller than Ψ_{sMTPA} , and vice versa. This characteristic of $\partial T_e / \partial \beta$ is utilized by the proposed control scheme to track the MTPA point.

3.2.1.2 Virtual Signal Injection

The concept and implementation of the virtual signal injection are proposed in Chapter 2. The torque fluctuation given by (2-12) as a result of the virtual signal injection forms the basis for extracting $\partial T_e / \partial \beta$. The $\partial T_e / \partial \beta$ information can be extracted by signal

processing blocks in Chapter 2. It is worth noting that the reason for injecting high frequency signal into the current angle is that it can be easily and accurately obtained from measured d- and q-axis currents and it is independent from flux observer errors. When the output of the signal processing unit is equal to zero, the MTPA operation can be inferred. Otherwise the information of $\partial T_e / \partial \beta$ can be utilized to adjust the stator reference flux amplitude until it reaches the optimal value. Details about this adjustment will be given in section 3.2.2.

3.2.2 Implementation of the Proposed Control Scheme

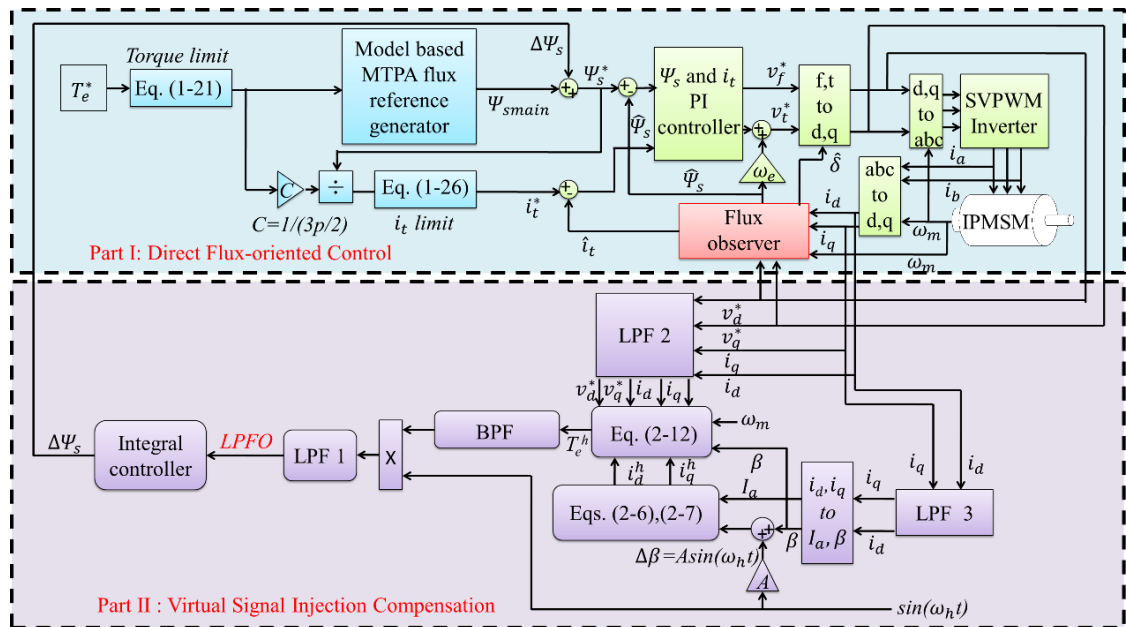


Fig. 3-2. Schematic of the proposed control scheme.

In this section, the details for implementing the proposed control scheme are described. The proposed control scheme can be divided into two parts, as shown in Fig. 3-2. The first part is a conventional direct flux vector control scheme proposed in [26] which is utilized to generate nominal reference flux linkage (Ψ_{smain}^*) and reference t-axis current for MTPA operation with fast response. The second part of the proposed control scheme is a compensation loop based on the virtual signal injection to correct the errors of the reference flux Ψ_{smain}^* and the observed flux.

3.2.2.1 Direct Flux Vector Control

The direct flux vector control scheme [25]–[27] is adopted by the proposed control scheme as an example of an f-t frame based control scheme shown in Part I of Fig. 3-2. To ensure an IPMSM drive operates within the current and voltage limits, the reference torque is limited by (1-21). The nominal reference flux amplitude Ψ_{smain} is generated from a predefined look-up table which produces the nominal optimal reference flux amplitude from the limited reference torque as its input. The table is computed off-line from a high fidelity nonlinear IPMSM machine model based on FE analysis [13]. The reference t-axis current is generated according to (1-25) and limited by (1-26). As proposed in [25], the stator flux linkage is directly regulated by the f-axis voltage while the t-axis current is regulated by the t-axis voltage. More details for the direct flux vector control can be found in [25].

However, due to machine parameter variations and uncertainty, the accuracy of Ψ_{smain} generated from the look-up table cannot be guaranteed. Moreover, due to errors in the flux observer, the observed i_t , Ψ_s and δ may not equal their actual values, which will also affect the MTPA control performance significantly. In order to compensate these errors, an error compensation term $\Delta\Psi_s$ for the reference flux amplitude which is generated from the virtual signal injection is proposed.

3.2.2.2 Reference Flux Amplitude Error Compensation

The reference flux amplitude compensation term $\Delta\Psi_s$ is generated from Part II of Fig. 3-2 according to the virtual signal injection and $\partial T_e / \partial \beta$ information extraction described in section 3.2.1.2.

As shown in Part II of Fig. 3-2, the measured d- and q-axis currents are filtered by a low-pass filter denoted as LPF 3 to eliminate high order harmonics. The filtered d- and q-axis currents are transformed into the polar coordinate system by (3-1) and (3-2) to obtain β and I_α . The d- and q-axis current perturbations with the injected high frequency signal are calculated from (2-6) and (2-7). The resultant torque variation T_e^h is obtained from (2-12) based on i_d^h, i_q^h , the d- and q-axis reference voltages, the measured d- and q-axis currents, and the measured speed. Both the reference voltages and measured currents

are filtered by a low-pass filter denoted as LPF 2 to attenuate undesirable noise. The torque perturbation T_e^h is filtered by a band-pass filter (BPF) to extract the first order term of (2-13). The output of the BPF is further multiplied by $\sin(\omega_h t)$ before being fed to the low-pass filter denoted as LPF 1 to obtain the signal proportional to $\partial T_e / \partial \beta$.

The output of the LPF 1 is used by an integral controller to produce $\Delta \Psi_s$. The gains of the integral controller are negative since when the stator flux amplitude is smaller than Ψ_{sMTPA} as shown in Fig. 3-1 (b), $-\partial T_e / \partial \beta > 0$ and vice versa. Thus, the integral controller will adjust the reference flux amplitude such that when lower than Ψ_{sMTPA} , it will be increased, or otherwise decreased until $\partial T_e / \partial \beta = 0$, i.e., the MTPA point is reached. In this way, the errors of Ψ_{smain} and the flux observer are compensated by $\Delta \Psi_s$.

It is worth noting that the voltages and currents in (2-12) are in d- and q-axis coordinates, therefore, the virtual signal injection based feedback loop will not be affected by the inaccuracies in the observed quantities, such as f- and t-axis currents, flux amplitude and the angle δ . Therefore, while flux observer error may cause torque control error, the accuracy of the proposed control scheme in tracking MTPA operation of actual torque will not be affected. This property will be demonstrated by simulations and experiments in sections 3.2.3 and 3.2.4.

3.2.2.3 Flux observer

For the f-t reference frame based control, a flux observer is needed. In this Chapter, the conventional closed loop flux observer introduced in [75] is adopted. The schematic of the flux observer is illustrated in Fig. 1-19 and more details can be found in Chapter 1. However, other kinds of observer are also possible for the proposed control scheme.

3.2.3 Simulation Studies

Simulations were performed based on a prototype IPMSM drive system whose motor specification is given in Table 2-1. The d- and q-axis inductances and the permanent magnet flux linkage of the machine are highly non-linear and vary significantly with currents because of magnetic saturation. ξ in the conventional closed loop flux observer introduced in Fig. 1-19 is set to 0.707 while the ω_0 is set to 50π rad/s since the 50π rad/s

corresponds to 500 r/min rotor speed and the accuracy of the voltage model based observer is satisfactory above this speed. Ψ_{smain} is generated from a predefined look-up table.

The influences of the amplitude and angle errors of the flux observer on the proposed control scheme and on the conventional look-up table based direct flux vector control scheme are studied by simulation when the drive operates in the constant torque region with 45 N·m reference torque at 1000 r/min. A high fidelity IPMSM model with due account of temperature effects on phase resistance and permanent magnet flux linkage is employed to represent more realistic machine behavior in the simulation. Variations of the PM flux linkage and the d- and q-axis inductances at room temperature of 20 °C with currents are mapped in the flux observer and the inverter is assumed to be ideal. While the real motor temperature will be different from the room temperature, this assumption is used for the purpose of simulation studies. Thus, the observer will be accurate in steady-state if the phase resistance, d- and q-axis inductances and the PM flux linkage used in the observer are the same as those in the machine model. However, observer errors can be deliberately injected in the simulations. Fig. 3-3 shows simulated torque variations with stator flux amplitude when the flux observer is accurate, when the observed flux amplitude is 5% and 10% lower but the observed angle of the flux vector is accurate.

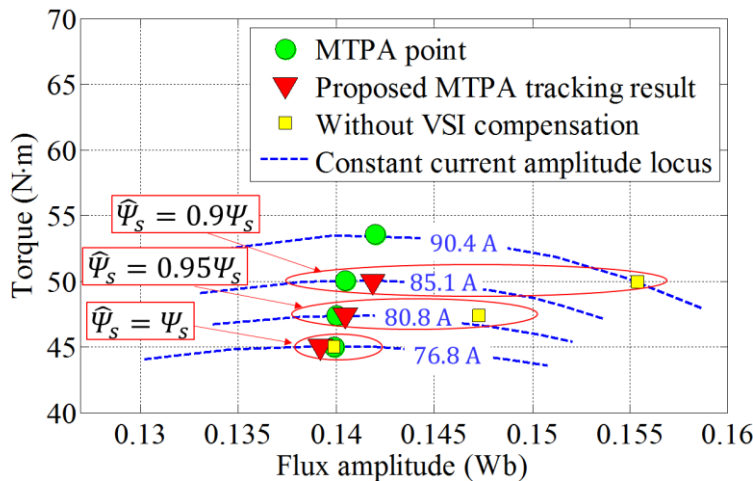


Fig. 3-3. Influence of observed flux amplitude error on MTPA tracking of proposed and conventional direct flux vector control schemes.

In each case, simulations are first performed by disabling the MTPA reference flux generation table and the VSI based flux correction loop, and repeated for different values of the stator reference flux amplitude while the current amplitude is kept constant when

the reference flux amplitude varies. The constant current loci obtained from the simulations are used to predict torque control accuracy and the MTPA points associated with each case as shown in Fig. 3-3.

The simulations are performed subsequently for the proposed and conventional direct flux vector control schemes for each case, and the resultant stator flux amplitudes of the two control schemes are also shown in Fig. 3-3. The actual MTPA points obtained from curve fitting of the simulation data are denoted by cycles, the MTPA points tracked by the proposed control scheme are denoted by triangles and the control result of the conventional look-up table based scheme are denoted by squares. As can be seen, when the flux observer is accurate, both control schemes operate on the MTPA point and the output torque equals to the reference torque. Torque control errors occur when the observed flux deviates from the true value. For example, when the observed flux amplitude is 10% lower, the torque is greater than the reference of 45 N·m because the reference t-axis current generated by (1-25) is greater than what is required. However, the proposed control scheme is still capable of tracking the reference flux amplitudes to the actual MTPA flux amplitude despite of large torque errors. In contrast, the observer magnitude error results in a significant deviation from the MTPA point with the conventional look-up table based control scheme, which will increase copper loss.

Fig. 3-4 shows simulated torque variations with stator flux amplitude when the flux observer is accurate, when the observed angle of the flux vector is 10% and 20% lower but the observed flux amplitude is accurate. Same as Fig. 3-3, the actual MTPA points obtained from curve fitting of the simulation data are denoted by cycles, the MTPA points tracked by the proposed control scheme are denoted by triangles and the control result of the conventional look-up table based scheme are denoted by squares. As shown in Fig. 3-4, when the magnitudes of the flux amplitude and t-axis current are equal to their optimal values but the flux vector angle is inaccurate, the net torque production component is reduced and hence the output torque is lower than the reference. However, as can be seen from Fig. 3-3 and Fig. 3-4, the differences between optimal flux amplitudes of different MTPA points are relatively small. Therefore, although the resultant torque is reduced due to the angle error, its corresponding optimal flux amplitude does not deviate much from the optimal flux amplitude of the reference torque. Therefore, according to Fig. 3-3 and Fig. 3-4, the MTPA operation of direct flux vector control is not sensitive to the error of observed flux vector angle but is very sensitive to the error of observed flux

amplitude. However, the proposed control scheme can always track the MTPA points accurately.

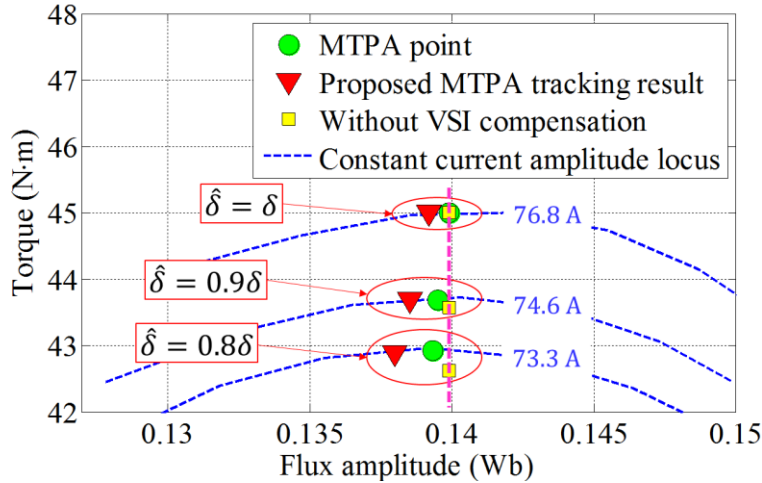


Fig. 3-4. Influence of observed flux vector angle error on MTPA tracking of proposed and conventional direct flux vector control schemes.

It should be noted that torque control error is inevitable when the flux observer is not accurate. However, the torque error can be corrected by the speed feedback loop in a speed servo drive. For EV tractions, the feedback correction will be performed by a human driver.

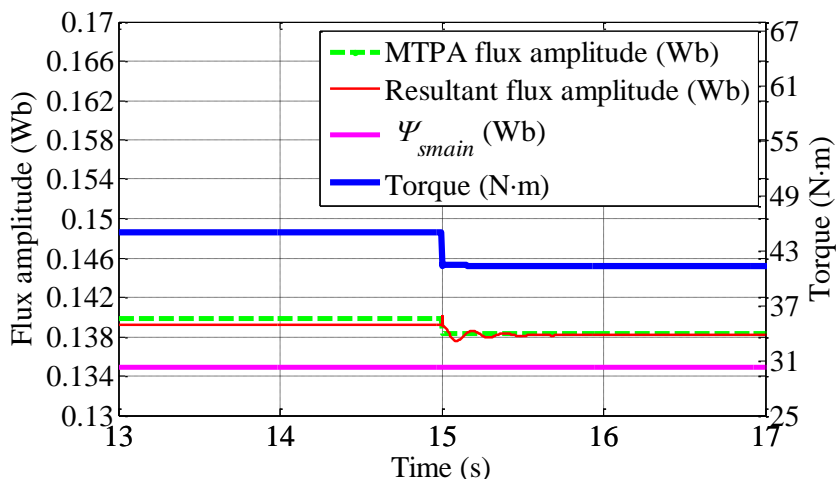


Fig. 3-5. MTPA point tracking performance when temperature changes.

The temperature influence on the proposed control scheme has also been studied by employing a temperature dependent machine model. From the design data of the prototype machine, the stator resistance increases 39% per 100 °C temperature rise and the remanence of the permanent magnets decreases 12% per 100 °C temperature rise.

However, the model used in simulations for the observer and for generating reference flux amplitude and current assumes a constant temperature of 20 °C. The simulation result of the influence of temperature on MTPA point tracking performance of the proposed control scheme is shown in Fig. 3-5 where the stator temperature in the machine model is changed from 20 °C to 120 °C at $t=15$ s. As can be seen, due to the machine parameter variations with temperature, the flux observer is no longer accurate. Consequently, the torque decreases when the temperature is increased. However, the new reference flux amplitude which results with the proposed control scheme follows closely the optimal MTPA flux amplitude of the new machine parameters by the virtual signal injection based correction loop although the change of the optimal flux amplitude is small. It follows from the simulation results shown in Fig. 3-4 and Fig. 3-5 that the proposed control scheme is robust to flux observer errors.

3.2.4 Experimental Results

The proposed direct flux vector control scheme has been tested on the same prototype IPMSM drive using the same test-rig as shown in Fig. 2-10. L_d , L_q , Ψ_m in the current model based flux observer are set to their nominal values, i.e., 0.64 mH, 1.84 mH and 0.1132 Wb, respectively. The PI gains of the observer shown in Fig. 1-19 are set to the same values used in the simulation. Ψ_{smain} is generated from a predefined look-up table.

3.2.4.1 Validation of Machine Parameters Independent MTPA Control

For the conventional look-up table based direct flux vector control, i.e., Part I in Fig. 3-2, the accuracy of MTPA operation is highly depend on the reference flux amplitude, Ψ_{smain} , and the accuracy of the flux observer.

However, the proposed virtual signal injection based direct flux vector control can automatically and accurately track the MTPA points without knowing machine parameters except for the nominal machine parameters in the flux observer expressed in (1-28).

In order to verify the MTPA tracking performance of the proposed control scheme, experiments were first performed by setting Ψ_{smain} as a constant value, i.e., $\Psi_{smain} =$

0.1 Wb. The drive was tested at 1000 r/min and torque varied from 5 N·m to 35 N·m. Since the actual flux amplitude is difficult to measure, the measured d-axis current is utilized instead of flux amplitude to illustrate the MTPA tracking performance of the proposed control scheme. As shown in Fig. 3-6, the drive is enabled with 5 N·m reference torque at $t=4$ s. At the beginning, due to the inaccurate Ψ_{smain} , the resultant d-axis current is quite large, about -30 A. However, $\Delta\Psi_s$ in Fig. 3-2 automatically compensates the error in the reference flux amplitude until the MTPA point is reached. Moreover, as shown in Fig. 3-6, for each torque step, the proposed control scheme always tracks the MTPA points accurately although a small overshoot can be observed in the measured d-axis current. The response of the proposed control scheme can be improved by a more accurate Ψ_{smain} .

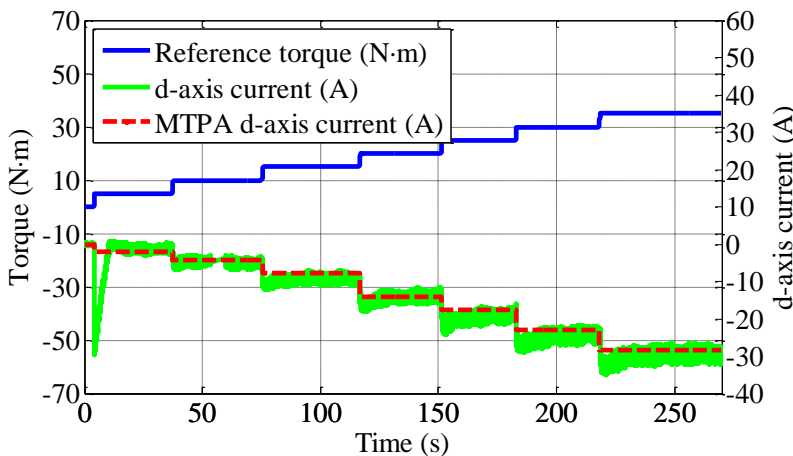


Fig. 3-6. Measured d-axis current, MTPA d-axis current, and reference torque

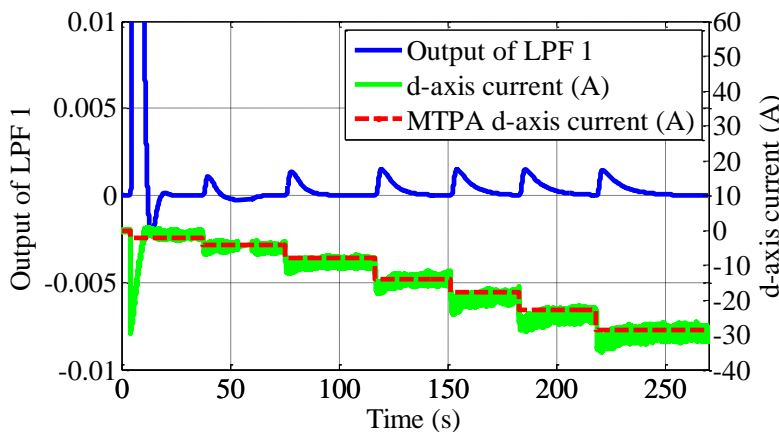


Fig. 3-7. The output of LPF 1 and measured d-axis current.

Fig. 3-7 shows the variation of d-axis current with the output of LPF 1 which is proportional to $-\partial T_e / \partial \beta$ and utilized to generate $\Delta\Psi_s$. As is seen, at each torque step, the

output of LPF 1 is initially large and then decreases to zero, which indicates that the MTPA point is tracked gradually, until $-\partial T_e/\partial\beta = 0$.

3.2.4.2 Independence of Flux Observer Error in MTPA Operation

Since the virtual signal injection compensation is based on measured currents in the d-q frame, the flux observer error does not affect the MTPA tracking performance of the proposed control scheme. In order to verify the independence of flux observer error, the proposed control scheme and conventional control scheme, i.e., the control scheme in Fig. 3-2 Part I without $\Delta\Psi_s$ compensation, were tested at 400 r/min when the reference torque was stepped from 0 N·m to 5 N·m. The reference flux amplitude, Ψ_{smain} , in both control schemes was generated by the same pre-defined look-up table which is obtained from a high fidelity nonlinear IPMSM machine model [13]. The high fidelity IPMSM machine model was generated from numerical analysis of electromagnetic field based on finite element analysis.

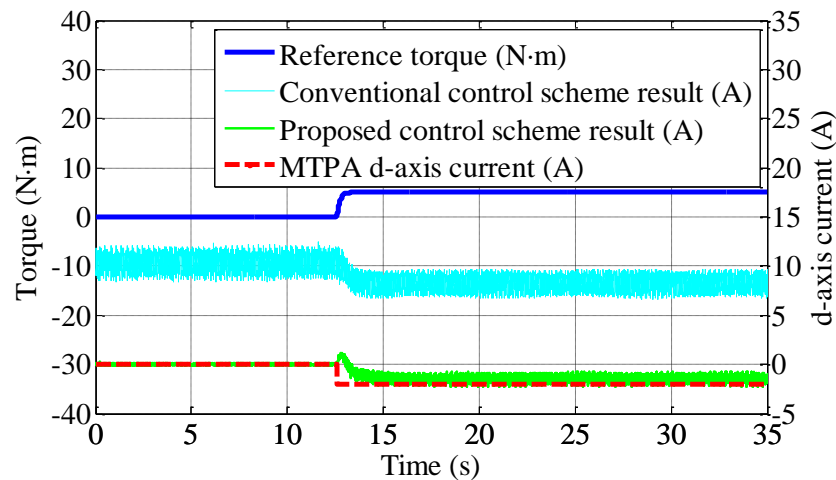


Fig. 3-8. Comparison between proposed control scheme and conventional control scheme at 400 r/min when reference torque steps from 0 N·m to 5 N·m.

Because of inverter nonlinearity and voltage drop, the flux observer illustrated in Fig. 1-19 may have large error at low reference torque and low speed, i.e., low current amplitude and low voltage amplitude. The comparison between proposed control scheme and conventional look-up table based control scheme is shown in Fig. 3-8. As can be seen, when the reference torque is 0 N·m, the resultant d-axis current of the proposed control scheme is 0 A, being the same as the MTPA d-axis current. However, the resultant d-axis current of the conventional model based control scheme is about -10 A which is caused

by the errors in both the flux observer and Ψ_{smain} . This will lead to larger copper loss and inefficient operation.

When reference torque steps to 5 N·m, the resultant d-axis current of the proposed control scheme follows the MTPA d-axis current accurately, however, the error between the resultant d-axis current of the conventional control scheme and the MTPA d-axis current remains large. The high MTPA tracking accuracy of the proposed control scheme is due to the fact that $\Delta\Psi_s$ in Fig. 3-2 automatically compensates the errors in both Ψ_{smain} and flux observer.

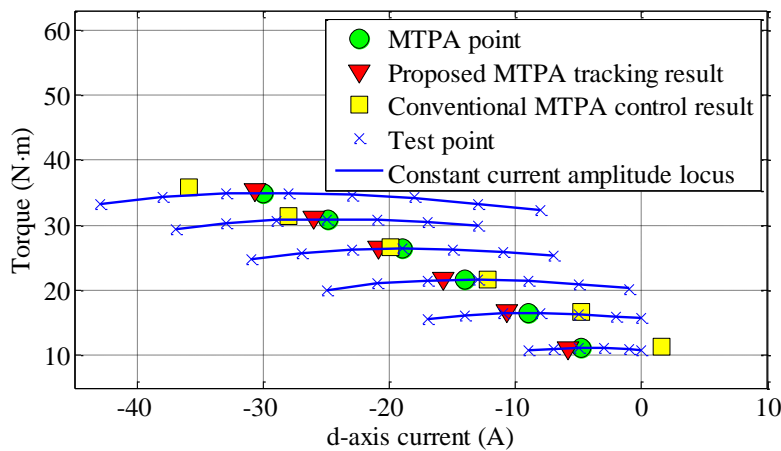


Fig. 3-9. Comparison of MTPA tracking performances of proposed and conventional control scheme at 400 r/min.

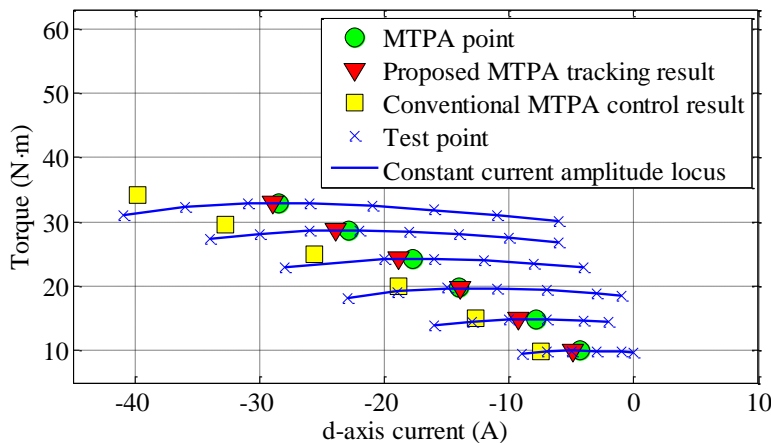


Fig. 3-10. Comparison of MTPA tracking performances of proposed and conventional control schemes at 1000 r/min.

The MTPA tracking performance of the proposed control scheme was also tested at various speeds and reference torques in steady state. Fig. 3-9 and Fig. 3-10 show the MTPA control performance of the conventional control scheme and the proposed control scheme when the motor drive operates at 400 r/min and 1000 r/min, respectively. At both

speeds, the motor drive was tested by varying the reference torque from 10 N·m to 35 N·m in steps of 5 N·m. Again, Ψ_{smain} in both the control schemes was generated by the same pre-defined look-up table as described previously.

The MTPA tracking results of the proposed control scheme are denoted by triangles in Fig. 3-9 and Fig. 3-10, whereas the control results of the conventional direct flux vector control scheme are denoted by squares. Tests were also performed by varying the current vector angle while its magnitude was kept constant. The results are shown in the curve marked by the crosses. The exact MTPA points, denoted by the circles, can be obtained using curve-fitting of the constant current amplitude loci for the different reference torques.

Comparing Fig. 3-9 and Fig. 3-10, it can be seen that the MTPA tracking errors of the conventional control scheme are dependent on both torque and speed. Since the nominal flux reference Ψ_{smain} generated from the look-up table for a given reference torque in constant torque region is independent of speed, the deviations of the control results must be caused by observer errors. However, although the reference flux amplitude Ψ_{smain} and the flux observer in the proposed control scheme are the same as those in the conventional control scheme under test, the proposed control scheme can track the MTPA points accurately and consistently. Therefore, the flux observer independence of the proposed control scheme in tracking MTPA points can be verified.

To illustrate the quality of MTPA tracking of the proposed control scheme, the measured torque-per-Ampere variations with load torque at 1000 r/min obtained from the proposed and conventional control schemes are compared with the MTPA points in Fig. 3-11. Again, the good MTPA tracking of the proposed control scheme can be observed.

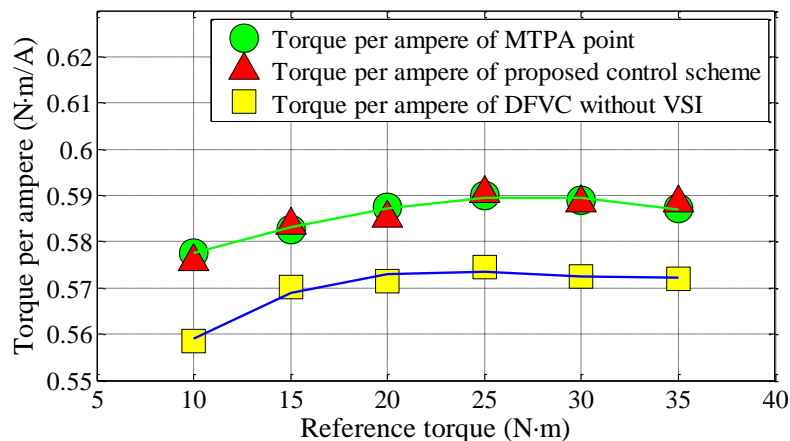


Fig. 3-11. Comparison of torque per ampere variations of proposed and conventional control schemes at 1000 r/min.

It is worth noting that the MTPA tracking performance of the conventional control scheme is mainly dependent on the accuracy of Ψ_{smain} . An inaccurate Ψ_{smain} may cause large deviation from the MTPA point as shown in Fig. 3-6 at $t=4$ s. Hence, due to the nonlinearity and uncertainty of the machine parameters, the MTPA control performance of the conventional control scheme is difficult to guarantee. However, the MTPA control accuracy can always be guaranteed by the proposed control scheme.

3.2.4.3 Performance of Proposed Control Scheme during Payload Torque Change

The MTPA tracking performance of the proposed control scheme during payload torque changes is shown in Fig. 3-12. The motor was operated at 1000 r/min and a step change in reference torque from 30 N·m to 35 N·m was applied. The reference torque is filtered by a low-pass filter to limit the torque variation rate. The dashed line represents the ideal MTPA d-axis current at 30 N·m and 35 N·m at 1000 r/min. It can be seen that the corresponding d-axis current generated by the proposed control scheme is very close to the ideal d-axis current during the torque step change.

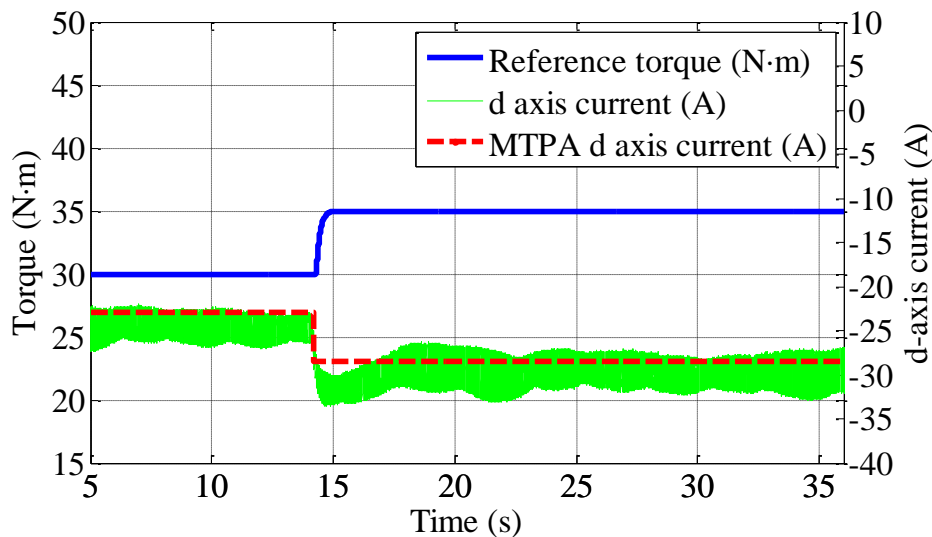


Fig. 3-12. MTPA tracking response of proposed control scheme to step change in reference torque at speed of 1000 r/min.

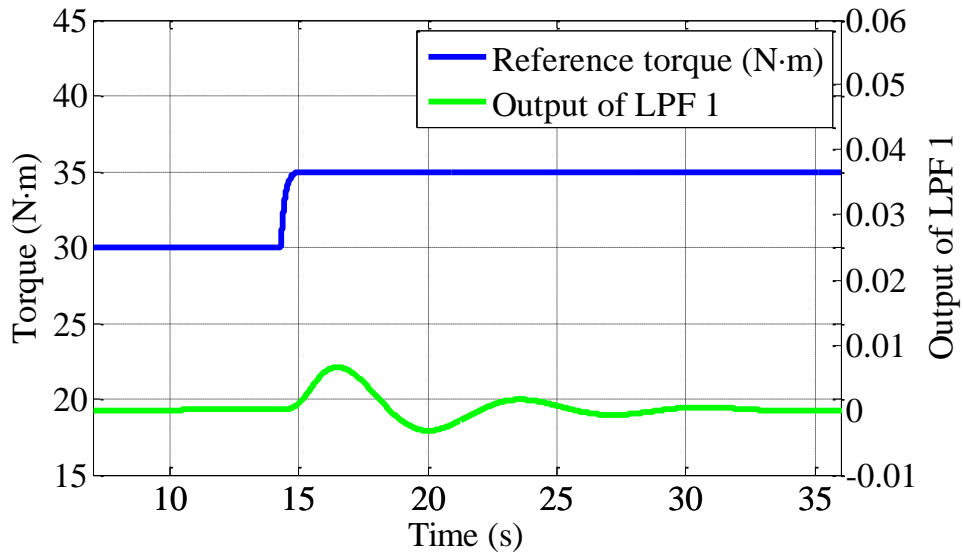


Fig. 3-13. Response of LPF 1 output to torque step change at 1000 r/min.

Fig. 3-13 shows the response of the LPF 1 output which is proportional to $\partial T_e / \partial \beta$ as is shown in Fig. 3-2. Since the torque change results in deviation from the MTPA operation, therefore, $\partial T_e / \partial \beta$ is no longer zero when torque changes. But it is used to adjust the reference flux amplitude until $\partial T_e / \partial \beta$ becomes zero again, i.e., reaching the new MTPA point.

Fig. 3-14 shows the measured and estimated torque responses to the step change in reference torque. The estimated torque is calculated from the machine parameters stored in look-up tables with the measured d- and q-axis currents.

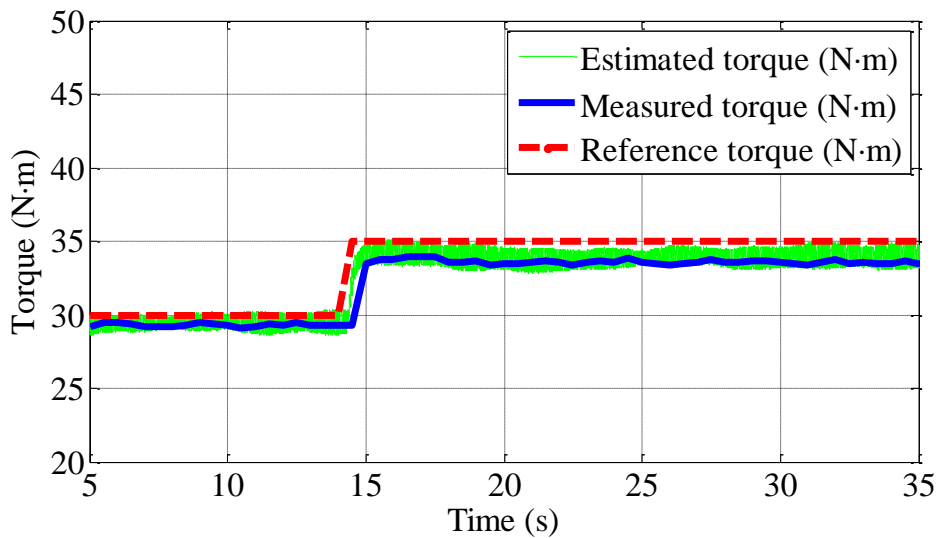


Fig. 3-14. Measured torque and reference torque at 1000 r/min.

3.2.4.4 Performance of Proposed Control Scheme at Low Speed

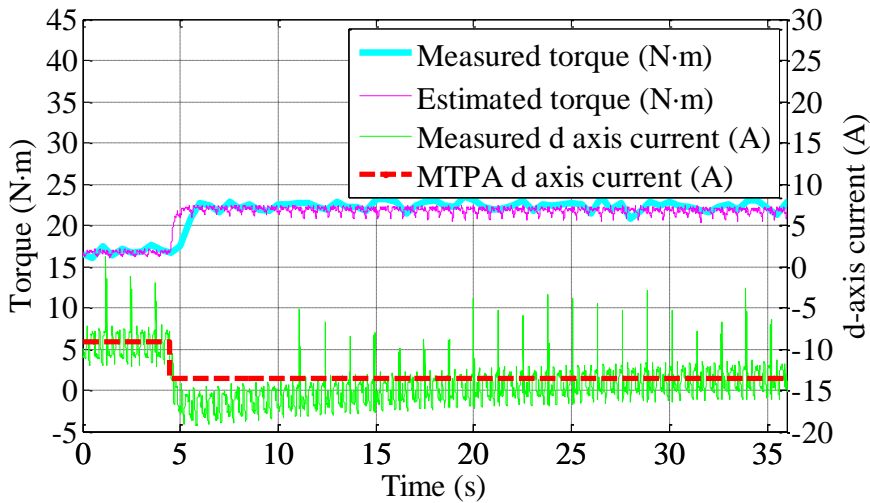


Fig. 3-15. MTPA tracking response of proposed control scheme to step change in reference torque at 15 r/min.

In order to verify the performance of the proposed control scheme at low speed when the d- and q-axis voltages are small, the motor drive was tested at 15 r/min. The estimated torque and measured d-axis current responses to the step change of reference torque from 15 N·m to 20 N·m at 15 r/min are shown in Fig. 3-15. Again, the dashed line in Fig. 3-15 indicates the actual MTPA d-axis current associated with 15 N·m and 20 N·m at 15 r/min. It can be seen that the proposed control scheme can still track the MTPA point accurately although the torque error and ripple is noticeable. In order to avoid dividing by zero at very low speeds when processing the right hand side of (2-12), the $\Delta\Psi_s$ term can be suspended when the measured speed is below a minimum threshold.

3.3 Virtual Signal Injection Based Field Weakening Control in f-t Frame

Compared with the d-q frame based field weakening control schemes, f-t frame based control schemes have many merits. The f-t frame based field weakening control scheme can directly regulate the flux amplitude without knowledge of machine parameters except for stator resistance which can be considered as its nominal value. It is also robust to variable dc-link voltage. Therefore the problems of field weakening control caused by

inaccurate machine parameters as discussed in Chapter 1 can be avoided. Moreover, since the dc-link voltage is one of the key factors for field weakening control, the variation of dc-link voltage always causes great difficulties in controlling the battery-powered system, such as electrical vehicle, in d-q frame. However, the difficulty can be easily solved by f-t frame based field weakening control schemes.

As illustrated in Chapter 2, the virtual signal injection control is not effective in field weakening region. In order to extend the virtual signal injection control scheme into field weakening region, additional control scheme is needed, which will be discussed in the rest of this chapter.

3.3.1 Principle of Field Weakening Control of Virtual Signal Injection Based Direct Flux Vector Control

As discussed in section 3.2, the direct flux vector control scheme controls the stator flux amplitude and the t-axis current through f- and t-axis voltages. The relationship between the stator flux amplitude and the maximum voltage amplitude is expressed in (1-22) and the voltage amplitude is given with:

$$v_a^* = \sqrt{(v_f^*)^2 + (v_t^*)^2} \quad (3-17)$$

From (1-23), (1-24) and (3-17), when speed increases, the voltage amplitude also increases. Since the voltage amplitude is limited by the maximum voltage, at high speed the stator flux amplitude should be decreased to guarantee that the resultant voltage amplitude is not larger than the maximum voltage, i.e., the field weakening control is needed.

When the motor drive is operating in the field weakening region, the stator voltage is constrained by the maximum voltage. Fig. 3-16 shows the variations of torque and voltage amplitudes with stator flux amplitude for a given current amplitude when the required voltage for the MTPA operation is larger than the voltage limit. As the flux amplitude increases towards the MTPA point, the resultant torque and voltage amplitude, v_a , will increase. Therefore, the voltage constrained maximum torque per ampere (VCMTPA) operation is the point at which the voltage amplitude is equal to the voltage limit [77] and on the VCMTPA point, the maximum torque is achieved for the given current amplitude

and voltage limit. Moreover, as illustrated in Fig. 3-16, on the VCMTPA point $-\partial T_e/\partial\beta > 0$, which implies that the *LPFO* signal from Part II of Fig. 3-2 will tend to adjust the flux amplitude toward the MTPA point until $-\partial T_e/\partial\beta = 0$. This may cause the voltage amplitude to increase beyond the maximum voltage. Therefore, if the voltage amplitude reaches or exceeds the voltage limit, the virtual signal injection control should be suspended.

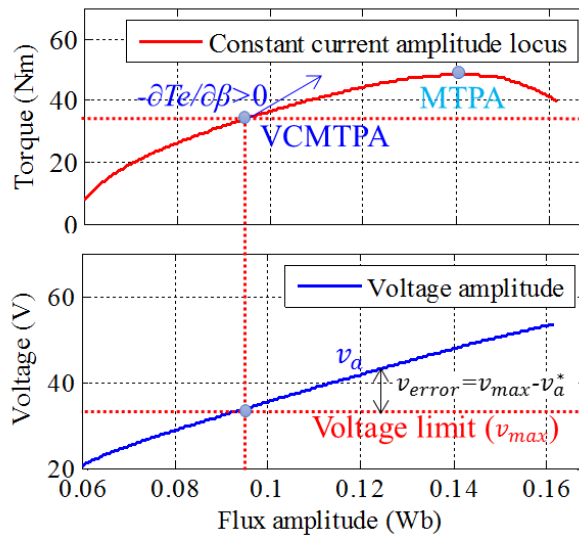


Fig. 3-16. Torque and voltage amplitude variations according to flux amplitude variation for a given current amplitude.

According to (1-22), the maximum flux amplitude under the voltage constraint is parameter-independent except for the phase resistance. However, the voltage drop across the resistance is relatively small compared with the voltage limit and the resistance can be assumed as its nominal value. Therefore, by assuming the nominal value of the phase resistance at a representative temperature, the optimal flux amplitude for VCMTPA operations, Ψ_{sFW} , can be obtained by (1-22).

3.3.2 Implementation

The proposed virtual signal injection based direct flux vector control utilizes (1-22) to set the limit of the reference flux amplitude for field weakening control. The schematic of the proposed control scheme is shown in Fig. 3-17. It consists of three parts. Part I is the conventional direct flux vector control as proposed in [26]. Part II in Fig. 3-17 is a

virtual signal injection block which generates the *LPFO* signal proportional to $\partial T_e / \partial \beta$ as described in section 3.2.2 based on the virtual signal injection. Part III is the field weakening error compensation block to achieve seamless combination of the virtual signal injection control and voltage feedback field weakening control.

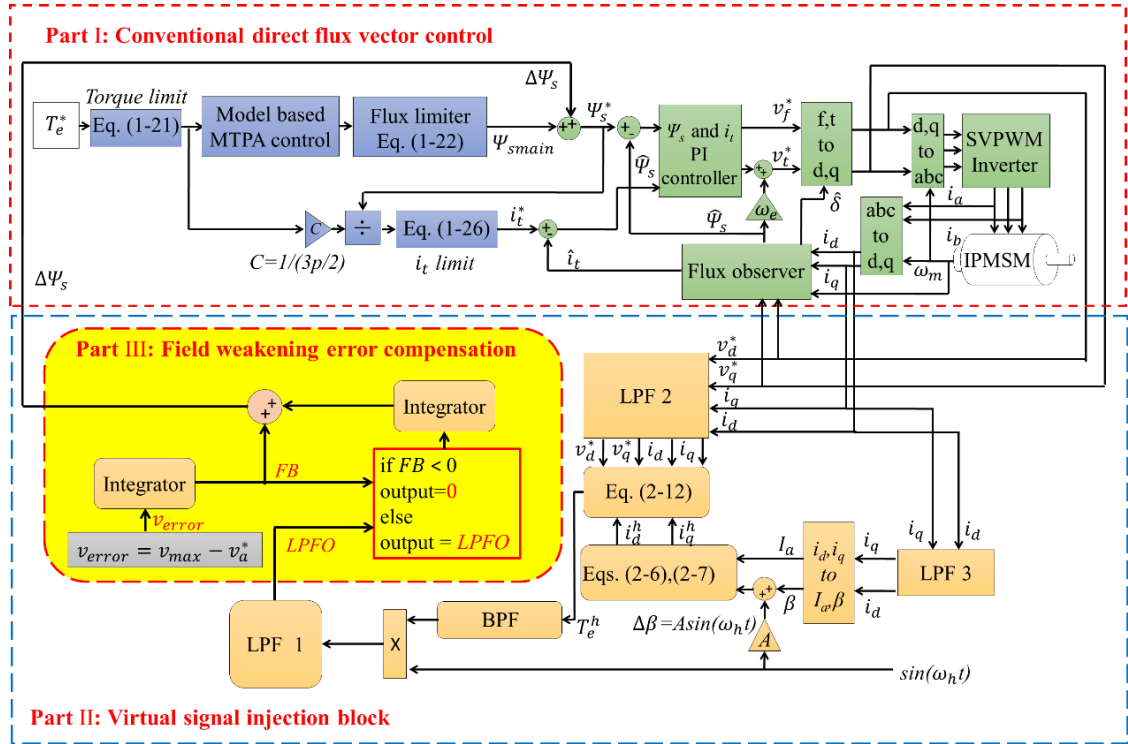


Fig. 3-17. Schematic of the proposed control scheme.

As shown in Fig. 3-17 Part I, Ψ_{smain} is limited by (1-22). However, due to the parameter inaccuracies and flux observer error, the nominal reference flux amplitude, Ψ_{smain} , may not equal its optimal value. In order to compensate for the errors in Ψ_{smain} and in the flux observer, the virtual signal injection combined with the voltage feedback field weakening control is employed in Part III of Fig. 3-17 to generate the reference flux amplitude compensation term $\Delta\Psi_s$. The voltage error v_{error} in Fig. 3-17 is calculated from (3-18) and the reference voltage amplitude v_a^* in (3-18) is obtained from (3-17).

$$v_{error} = v_{max} - v_a^* \quad (3-18)$$

Whether the low-pass filter output, i.e., the *LPFO* signal, or v_{error} is fed to the integrator in Part III of Fig. 3-17 depends on the sign of v_{error} . The operations with regard to the voltage error are described as follows.

3.3.2.1 $v_{error} \leq 0$

Under this condition, the amplitude of the reference voltage is greater than the voltage limit, which implies that Ψ_{smain} is larger than Ψ_{sFW} and will cause voltage saturation. Hence, the reference flux amplitude, Ψ_s^* , should decrease. v_{error} will be fed into the integrator in Part III and the *LPFO* signal (the output of LPF 1) will be suspended. The negative v_{error} will cause the integral regulator output, $\Delta\Psi_s$, to decrease, and as a result, the reference flux amplitude moves toward the VCMTPA point. Thus, $\Delta\Psi_s$ will compensate the error in Ψ_{smain} as well as in flux observer to prevent the voltage saturation by decreasing v_a^* until it equals v_{max} .

3.3.2.2 $v_{error} > 0$

Under this condition, the integrator input in Part III is the *LPFO* signal which is proportional to $-\partial T_e / \partial \beta$. As shown in Fig. 3-16, if the reference voltage amplitude v_a^* is lower than v_{max} , the motor operates on the left side of the VCMTPA point. $\Delta\Psi_s$ will be adjusted such that flux amplitude tends toward the MTPA point until $-\partial T_e / \partial \beta = 0$ or $v_{error} = 0$, i.e., when either the MTPA or VCMTPA point is reached.

It follows that the $\Delta\Psi_s$ can be utilized to ensure efficient operation of IPMSM drives in the field weakening region. In conventional feedback based field weakening control without the virtual signal injection compensation, if the observed flux amplitude is larger than the actual flux amplitude due to flux observer error, the generated flux amplitude in stator will be lower than the optimal flux amplitude and the voltage feedback loop is no longer in action and hence the VCMTPA control in the field weakening region may not be achievable.

However, as described above, the MTPA control in constant torque region and the VCMTPA control in field weakening region can always be guaranteed by the proposed control scheme.

3.3.3 Simulation Results

Simulations of the virtual signal injection aided direct flux vector control for field weakening operation were performed based on a prototype IPMSM drive system. The motor model in the drive system is the same as that described in section 3.2.3.

3.3.3.1 VCMTPA tracking performance

Fig. 3-18 shows the simulation result of the proposed field weakening control of the IPMSM drive when it is operated at 3000 r/min and 25 N·m in the field weakening region. The ideal flux amplitude for the VCMTPA operation is 0.069 Wb. As shown in Fig. 3-18, the value of Ψ_{smain} obtained from (1-22) is initially equal to 0.072 Wb which is larger than the ideal value due to inaccurate machine parameters. However, the reference flux amplitude, Ψ_s^* , generated by the proposed control scheme compensates for the error in Ψ_{smain} and maintains the motor operating on the VCMTPA point.

To illustrate another possible condition in which the Ψ_{smain} may be smaller than the ideal flux amplitude, at $t = 25$ s, Ψ_{smain} becomes equal to 0.066 Wb. Again, the reference flux amplitude tracks the ideal value and the difference is compensated by the proposed control automatically.

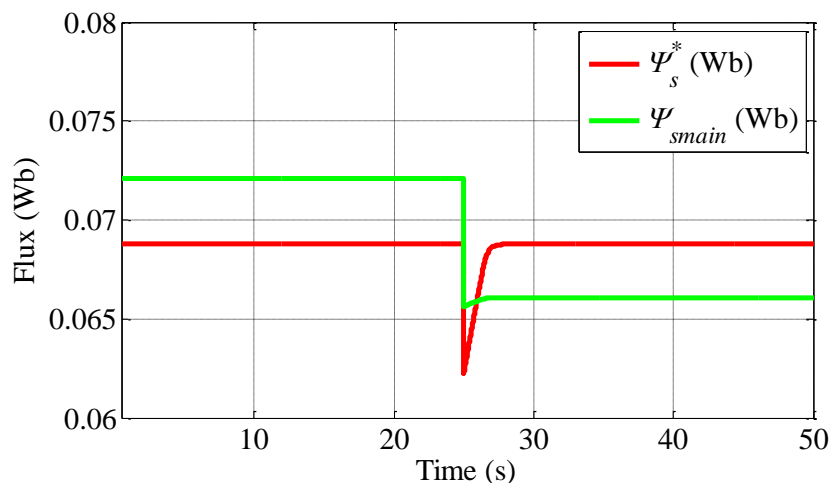


Fig. 3-18. Reference flux responses of proposed field weakening control.

The resultant voltage amplitude and reference flux amplitude under the same operation conditions are shown in Fig. 3-19. As can be seen, the resultant voltage amplitude is

always kept at the maximum voltage amplitude, which indicates the VCMTPA operation can be guaranteed by the proposed control scheme although Ψ_{smain} is inaccurate and a larger disturbance is applied to the reference flux at $t=25$ s.

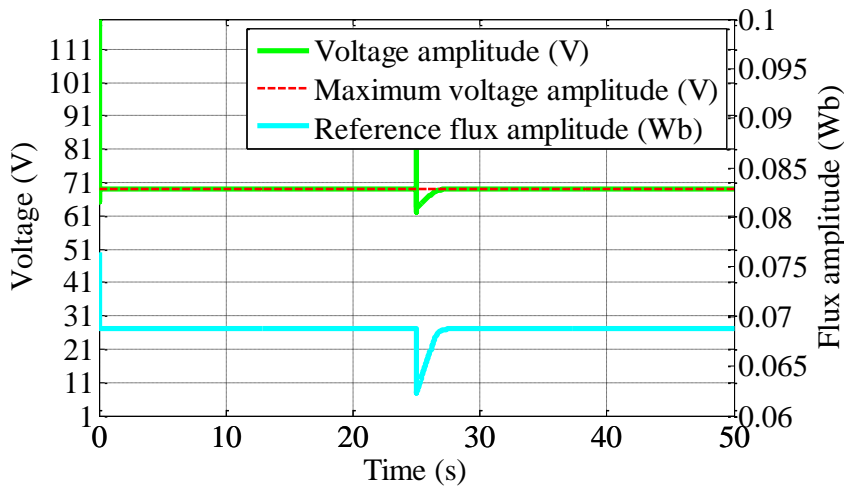


Fig. 3-19. Resultant voltage amplitude and reference flux amplitude under same operation conditions of Fig. 3-18.

3.3.3.2 Robustness to Speed Change in Field Weakening Region

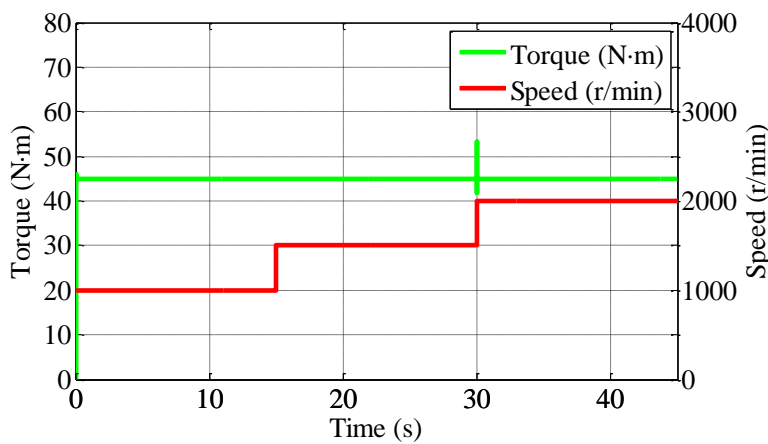


Fig. 3-20. Fast transition of motor operation from constant torque region to field weakening region and large speed step in field weakening region.

In order to demonstrate robustness of the proposed control scheme to step changes in speed, the torque response to step changes of 500 r/min in speed is shown in Fig. 3-20. The reference torque is set to 45 N·m and speed varies from 1000 r/min to 1500 r/min at $t=15$ s and varies from 1500 r/min to 2000 r/min at $t=30$ s. It can be seen that the proposed control achieves stable and fast response to the speed step changes. However, for electric vehicle traction and other applications, a step change in speed cannot occur due to large

mass and inertia of a drive system. Therefore, the condition illustrated in Fig. 3-20 can be considered as the worst condition which may occur practically.

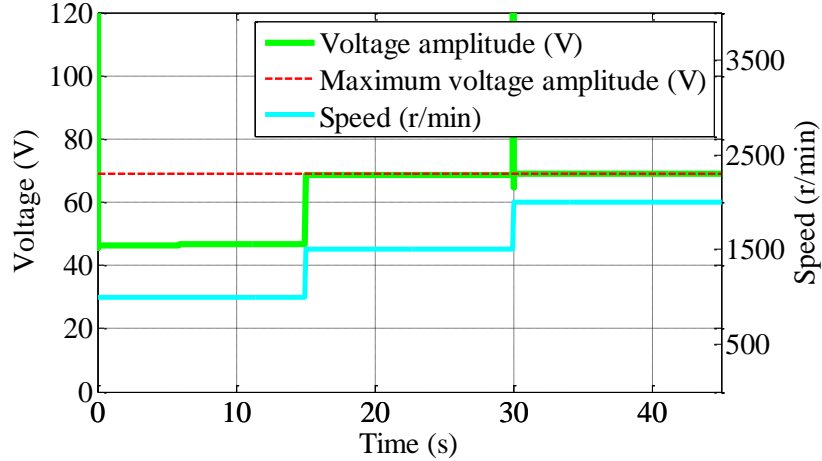


Fig. 3-21. Resultant voltage amplitude during speed step.

Fig. 3-21 shows the resultant voltage amplitude and motor speed under the same operation conditions as Fig. 3-20. As shown in Fig. 3-21, when the motor is operating at 1000 r/min in the constant torque region, the voltage amplitude is below the maximum voltage amplitude. However, when the motor speed steps to 1500 r/min, the voltage amplitude reaches the maximum voltage amplitude, and the VCMTPA is achieved. The fast and smooth transition from the constant torque region to the field weakening region can be inferred. When the speed steps from 1500 r/min to 2000 r/min, the resultant voltage amplitude is always kept at the maximum voltage amplitude and the robustness of the VCMTPA control to speed change can be verified.

3.3.3.3 Influence of Flux Observer Error

The influence of flux observer error on proposed control scheme in field weakening region was also simulated. Fig. 3-22 shows the simulation result of the proposed control scheme when the drive operates at 3000 r/min and 20 N·m in field weakening region. Initially the observer was ideal. At $t=15$ s, the observed angle, δ , became 0.5 times of its accurate value and at $t=25$ s the observed flux amplitude became 1.1 times of its accurate value. However, under all of these conditions, the proposed control scheme can always keep the voltage amplitude equal to v_{max} except for transient deviations. Therefore, the proposed control scheme can always guarantee the drive operating on the VCMTPA points in the field weakening region.

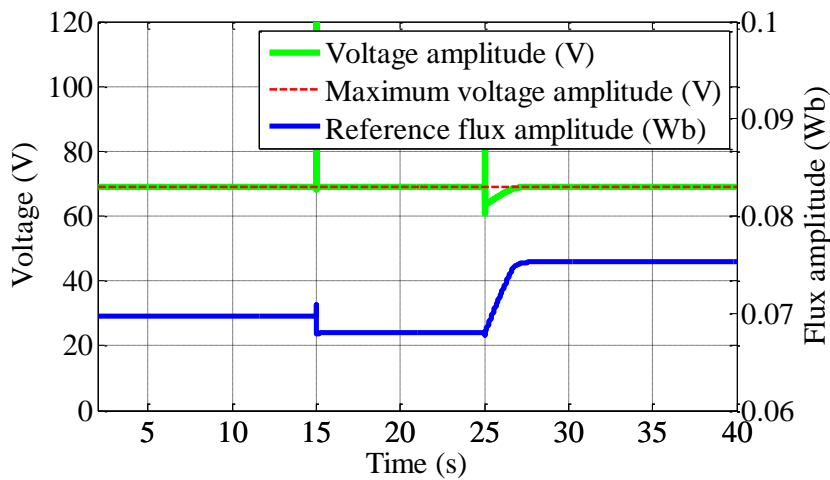


Fig. 3-22. Reference flux and voltage amplitude response to observer error in field weakening region.

3.3.4 Experimental results

The proposed field weakening control in the f - t frame, which incorporates the VSIC, was implemented in the IPMSM drive. The parameters of the virtual signal injection block employed in the experiments have been described in section 3.2.4.

3.3.4.1 Transition between Constant Torque Region and Field Weakening Region

Since the MTPA operation performance of the virtual signal injection based direct flux vector control has been verified by experiments in section 3.2.4, in this section, experimental results that verify seamless transitions between the constant torque region and field weakening region are presented. As the actual flux amplitude is difficult to measure, the measured d -axis current is utilized instead of flux amplitude to illustrate the performance of the proposed control scheme.

As shown in Fig. 3-23, the test of transition from the field weakening region to the constant torque region is first performed. The speed is decreased from 1750 r/min to 1520 r/min with reference torque equal to 20 N·m. When speed is 1750 r/min, the motor operates in the field weakening. As the speed decreases, the amplitude of d -axis current also decreases. At the speed below 1640 r/min, the motor enters the constant torque region, and consequently, the d -axis current reaches its optimal value under the MTPA operation. A smooth transition from the field weakening region to the constant torque region can be observed.

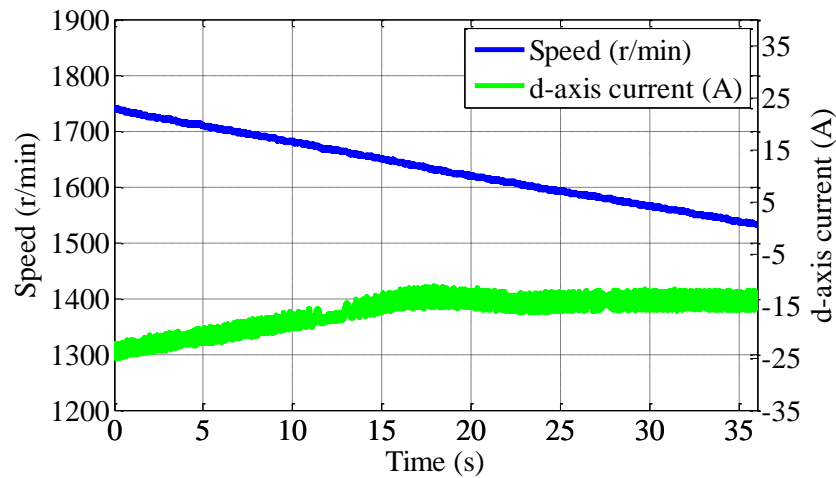


Fig. 3-23. Variations of speed and d-axis current during transition from field weakening region to constant torque region.

The reference voltage amplitude and d-axis current under the same operation conditions as Fig. 3-23 are shown in Fig. 3-24. From Fig. 3-24, it can be seen that before the motor enters the constant torque region, the voltage amplitude is kept at the maximum voltage limit, i.e., the motor operates on the VCMTPA point. However, when motor enters constant torque region, i.e., the d-axis current becomes constant, the voltage amplitude decreases as the speed decreases. A smooth transition from the field weakening region to the constant torque region can be observed.

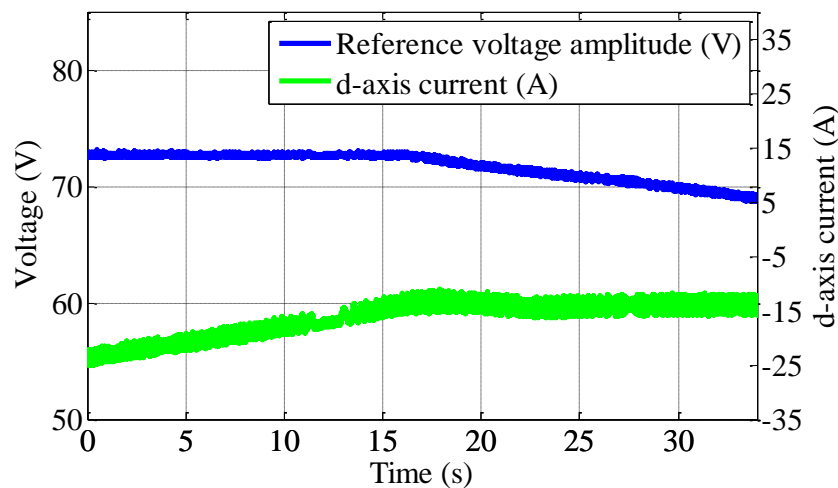


Fig. 3-24. Reference voltage amplitude and d-axis current during transition from field weakening region to constant torque region.

A similar test was performed when the load torque was kept at 20 N·m and the speed was increased from 1550 r/min to 1720 r/min. The rotor speed and measured d-axis

current response are shown in Fig. 3-25. When the speed is below 1630 r/min, the motor operates in the constant torque region and the d-axis current is kept constant as the speed increases. The amplitude of the d-axis current begins to increase when the motor enters the field weakening region.

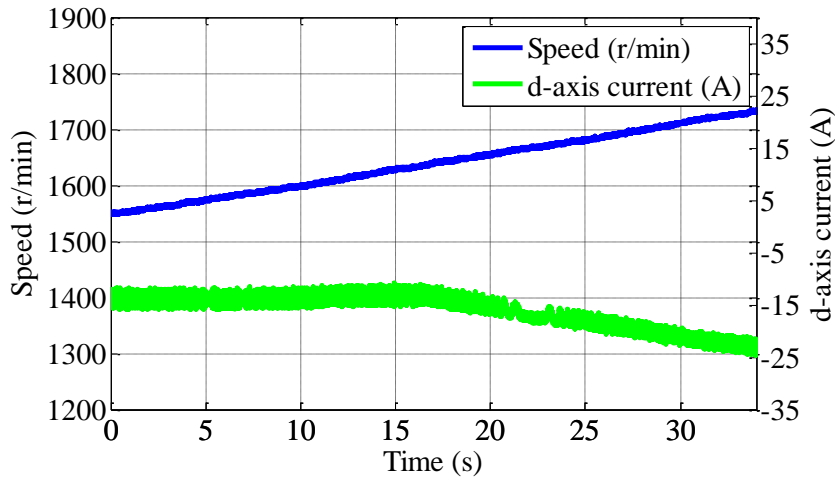


Fig. 3-25. Variations of speed and d-axis current during transition from constant torque region to field weakening region.

The reference voltage amplitude and d-axis current under the same operation conditions as Fig. 3-25 are shown in Fig. 3-26. From Fig. 3-26, it can be seen that before the motor enters the field weakening region, the d-axis current is constant while the voltage increases as the speed increases. However, when motor enters the field weakening region, the voltage amplitude is kept at the maximum voltage amplitude. Again, a smooth transition from the constant torque region to field weakening region can be observed.

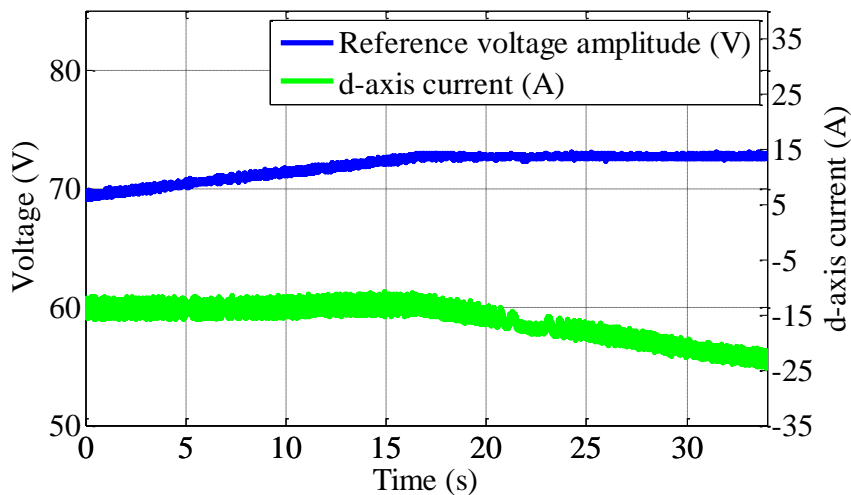


Fig. 3-26. Reference voltage amplitude and motor speed during transition from constant torque region to field weakening region.

3.3.4.2 Performance of the Proposed Control Scheme in Deep Field Weakening Region

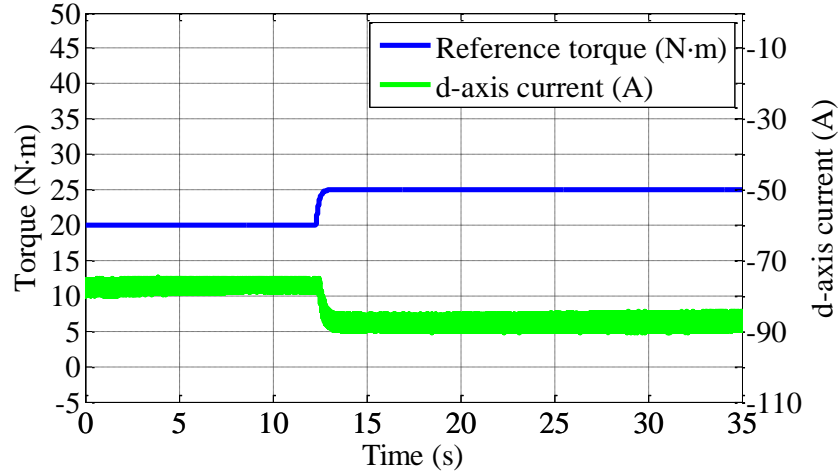


Fig. 3-27. Measured d-axis current and reference torque when reference torque steps from 10 N·m to 15 N·m at 3000 r/min.

In the field weakening region, the fast dynamic response of the reference flux amplitude can be achieved by (1-22) directly, and the errors in Ψ_{smain} and flux observer can be compensated by $\Delta\Psi_s$ automatically. Fig. 3-27 shows the measured d-axis current and reference torque when the reference torque steps from 20 N·m to 25 N·m at 3000 r/min (more than two times the base speed). As shown in Fig. 3-27, the fast response of the d-axis current can be observed.

The reference voltage amplitude and reference torque under the same operation conditions as Fig. 3-27 are shown in Fig. 3-28. As can be seen, the reference voltage from the proposed control is essentially equal to the maximum voltage even during the reference torque change, which illustrates that the motor is controlled on the VCMTPA point. The small error between the reference voltage and the maximum voltage is due to the combination effect of the flux observer error and voltage drop in the inverter.

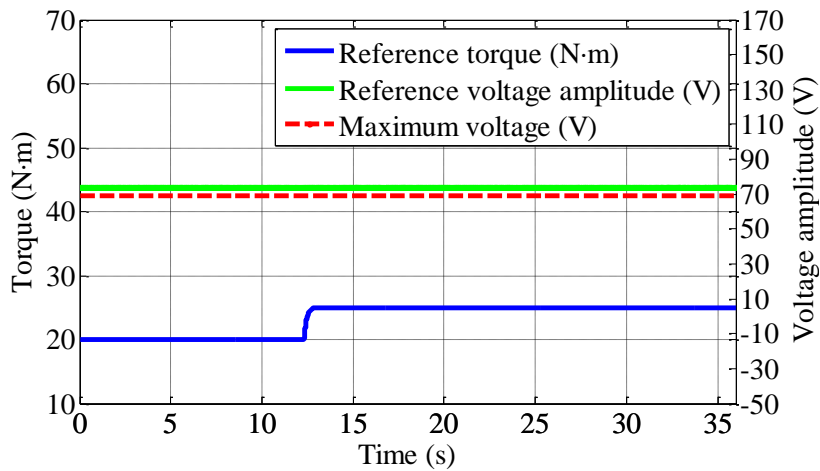


Fig. 3-28. Reference voltage amplitude and reference torque when reference torque steps from 20 N·m to 25 N·m at 3000 r/min.

The comparison between reference torque and measured torque when the reference torque increased from 20 N·m to 25 N·m at 3000 r/min is shown in Fig. 3-29. The measured torque response is fast and the gap between the reference and measured torques is due to the flux observer error, iron loss and the frictional torque of the motor.

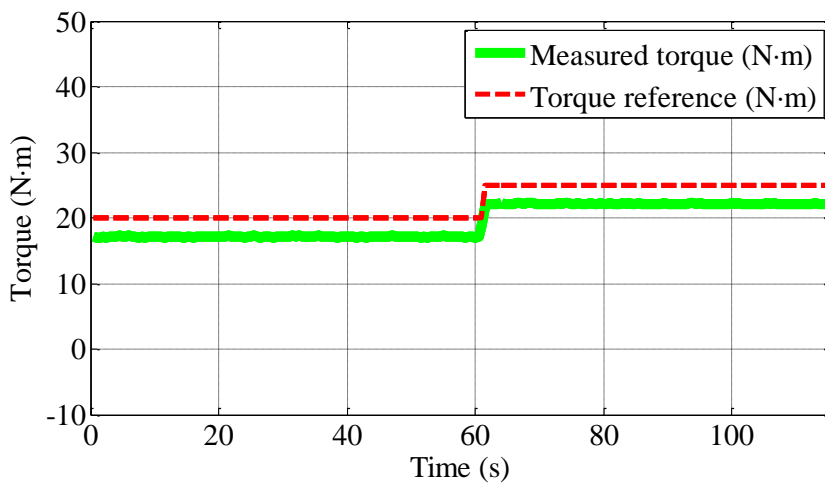


Fig. 3-29. Comparison between reference torque and measured torque when reference torque increased from 20 N·m to 25 N·m at 3000 r/min.

3.4 Summary

The proposed virtual signal injection based direct flux vector control scheme provides a parameter independent and observer error insensitive method to achieve accurate control of IPMSM drives in the f-t frame. Because high frequency signal is injected virtually, the proposed method does not cause any additional iron/copper loss and is very

robust to voltage and current harmonics. The proposed method also avoids any torque or speed ripple and resonant problems caused by current ripple associated with real signal injection. Because the signal injection is based on d- and q-axis quantities, the proposed control scheme is not affected by the observer's error in tracking optimal efficiency operation points. Moreover, in order to achieve accurate voltage constraint MTPA control in field weakening region, a voltage feedback loop is incorporated into the proposed virtual signal injection based direct flux vector control.

Both simulation results and experiment results demonstrate that the proposed method can track the MTPA points in constant torque region and voltage constraint MTPA points in field weakening region accurately and automatically.

CHAPTER 4 Self-learning Control Based on Virtual Signal Injection

4.1 Introduction

In Chapter 2 and Chapter 3, virtual signal injection control schemes based on the principle of extremum seeking control (ESC) [80] were proposed to control IPMSM drives in the d-q frame and the f-t frame, respectively. These control schemes are not affected by parameter uncertainty and lead to relatively accurate MTPA operations. However, similar to all search algorithm based control schemes, they still suffer from the slow dynamic response as it takes time for the search based schemes to converge to MTPA operating points.

In order to increase the dynamic response of the search algorithm based control schemes, in [101] fuzzy logic is utilized to increase the converging rate of the search algorithms. The output of the fuzzy logic controller in steady state is the change in reference d-axis current and the inputs are the output of the fuzzy logic controller in the previous step and the change in power loss. Although the fuzzy logic controller can increase convergence rate, the control scheme is sensitive to current and voltage harmonics and causes torque ripple as a result of d-axis current perturbation.

Another potential solution for improving the convergence rate is to equip these controllers with self-learning or intelligence. Artificial intelligence based on neural network and fuzzy logic may serve this purpose. However, neural network or fuzzy logic based control schemes in literature [102]–[110] are primarily concerned with speed or position tracking rather than MTPA operations.

On the other hand, if MTPA points can be tracked by parameter independent MTPA control schemes accurately, the tracked MTPA points can be utilized to improve the accuracy and dynamic response of the generations of the optimal reference d-axis current or reference flux amplitude through on-line training. However, study of seamless integration of on-line training with signal injection based control for MTPA operations have not been reported to date.

In this chapter, novel curve fitting based self-learning control (SLC) schemes are proposed for control of IPMSM drives in the d-q frame and f-t frame employing virtual signal injection for MTPA and field weakening operations. The training data of the self-learning controls are based on the virtual signal injection control described in Chapter 2 and Chapter 3 as it tracks the MTPA points with high precision and is robust to voltage and current harmonics. The virtual signal injection control is utilized to generate the optimal reference d-axis current or optimal reference flux amplitude for MTPA operation and the proposed SLC schemes are trained on-line by the tracked MTPA points. After a period of on-line training, the SLC generates the optimal reference d-axis current or optimal reference flux amplitude for MTPA operation with fast response. In this way, the proposed control scheme not only retains the advantages of virtual signal injection control, such as parameter independence, high accuracy in tracking the MTPA points, and robustness to voltage and current harmonics but also has a fast dynamic response. Further the on-line training of the SLC does not affect the MTPA or field weakening operations of the IPMSM drive.

4.2 Self-learning Control in d-q Frame

4.2.1 MTPA d-axis Current Generation

The MTPA d-axis current generation of the proposed control scheme is achieved by virtual signal injection. The principle and implementation of virtual signal injection control has been described in Chapter 2 and Chapter 3. According to previous discussions, the information of $\partial T_e / \partial \beta$ can be extracted from signal processing block as shown in Fig. 2-5. The low-pass filter output, defined as signal *LPFO*, is proportional to $\partial T_e / \partial \beta$. As proposed in Chapter 2, in the d-q frame, the optimal d-axis current for MTPA operation can be adjusted by signal *LPFO* through an integral regulator until $\partial T_e / \partial \beta = 0$. The *LPFO* signal can also be utilized to indicate MTPA operation for a given torque command. If the absolute value of signal *LPFO* is close to zero, the motor can be considered operating close to the MTPA point. Therefore, signal *LPFO* can be defined as a MTPA quality indicator. When the motor is running on the MTPA point, the corresponding

reference d-axis current and reference torque will be recorded as a tracked MTPA point on the MTPA trajectory shown in Fig. 4-1.

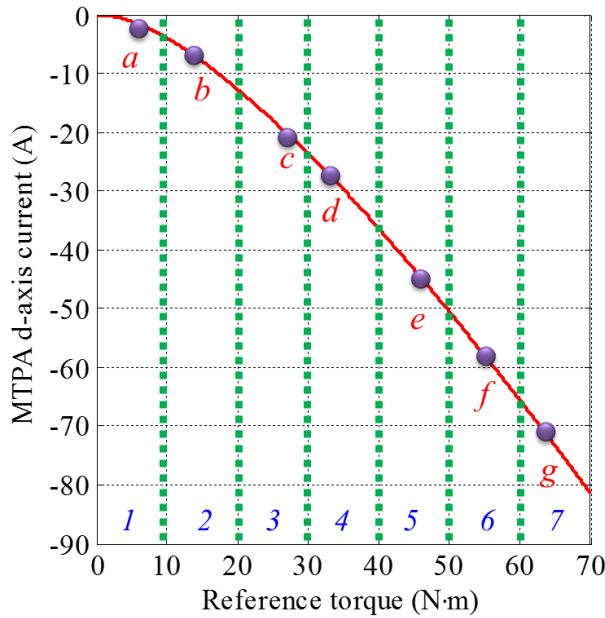


Fig. 4-1. d-axis current vs. torque for MTPA operation.

It should be noted that MTPA operation is only valid in steady state sense. Thus, the *LPFO* signal is masked during d- and q-axis current transients for a small period of 3 times of the current loop time constant.

4.2.2 Principle of Proposed Self-learning Control Scheme

Fig. 4-1 shows the relationship between reference torque and corresponding optimal d-axis current for MTPA operation. For a given reference torque there is a unique optimal d-axis current for MTPA operation. If a sufficient number of MTPA points on the curve, *a* to *g* in Fig. 4-1, are known, other points on the curve can be approximated by interpolations among these known points. The proposed self-learning control scheme is based on this idea.

As shown in Fig. 4-1, in order to have an even distribution of recorded MTPA points, the applicable reference torque range of a machine is divided into *n* sections and each section records one tracked MTPA point. By way of example, seven sections are shown in Fig. 4-1. The reference torques and their corresponding d-axis currents of tracked MTPA points are recorded as column vectors \mathbf{T}_{MTPA} and \mathbf{i}_{dMTPA} . If a new MTPA point is

identified in section m , the m^{th} element of \mathbf{T}_{MTPA} and \mathbf{i}_{dMTPA} will be replaced by the corresponding value of the new MTPA point. This process repeats during the SLC operation.

Since MTPA points on the curve can be tracked by virtual signal injection control accurately, the training process is performed under virtual signal injection operation. The schematic of the proposed self-learning control scheme is shown in Fig. 4-2.

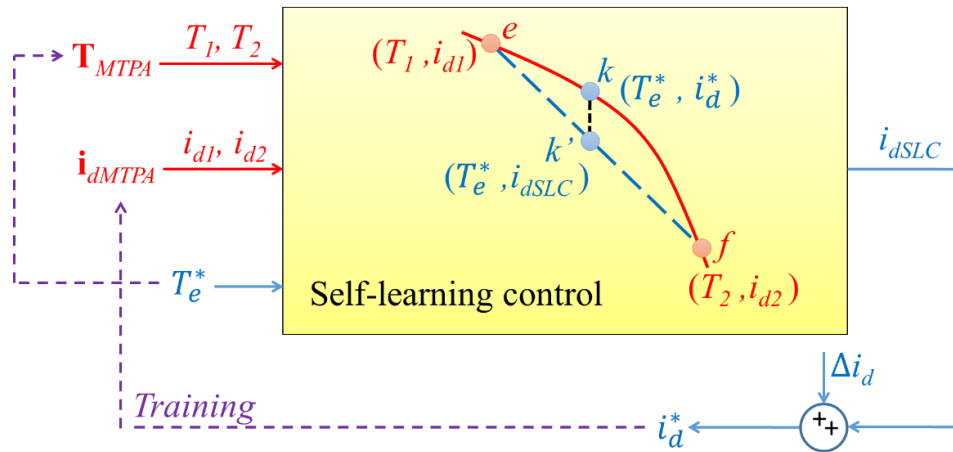


Fig. 4-2 Schematic of the proposed self-learning control scheme.

Each newly tracked MTPA d-axis current (i_{dMTPA}) by virtual signal injection control and the corresponding reference torque (T_{MTPA}) are recorded in the column vectors \mathbf{i}_{dMTPA} and \mathbf{T}_{MTPA} , respectively. The two vectors which form the MTPA curve are updated continuously by tracked MTPA points obtained from the virtual signal injection. The recorded data can be used to generate reference d-axis current instantly. For a given torque demand T_e^* , the corresponding d-axis current at the MTPA point k in Fig. 4-2 can be approximated by k' through linear interpolation between the two adjacent MTPA points recorded in \mathbf{T}_{MTPA} and \mathbf{i}_{dMTPA} , i.e., points e and f in Fig. 4-2, according to (4-1).

$$i_{dSLC} = \frac{T_e^* - T_2}{T_1 - T_2} (i_{d1} - i_{d2}) + i_{d2} \quad (4-1)$$

where T_1 and T_2 are the reference torques of e and f in \mathbf{T}_{MTPA} , respectively, and i_{d1} and i_{d2} are the recorded optimal d-axis currents of e and f in \mathbf{i}_{dMTPA} . i_{dSLC} is the output of the self-learning control.

Once the control scheme is fully trained, the output of SLC (i_{dSLC}) should approximate the optimal d-axis current of MTPA operation. If the number of sections is sufficient, the error between the MTPA d-axis current and the SLC output will be very small. The final

reference d-axis current will be a combination of i_{dSLC} and an error compensation component, Δi_d , generated from the virtual signal injection control.

4.2.3 Implementation of the Self-learning Control in d-q Frame

The schematic of the proposed self-learning control scheme for MTPA operation is shown in Fig. 4-3. It consists of conventional PI current control loops for tracking the reference d-axis and q-axis currents, a virtual signal injection (VSI) processing unit, and a self-learning controller. The output of the VSI processing unit is fed to an integrator. The output of the integrator is fed to a summing junction. The reference d-axis current, i_d^* , is the sum of the SLC output, i_{dSLC} , and the integrated output.

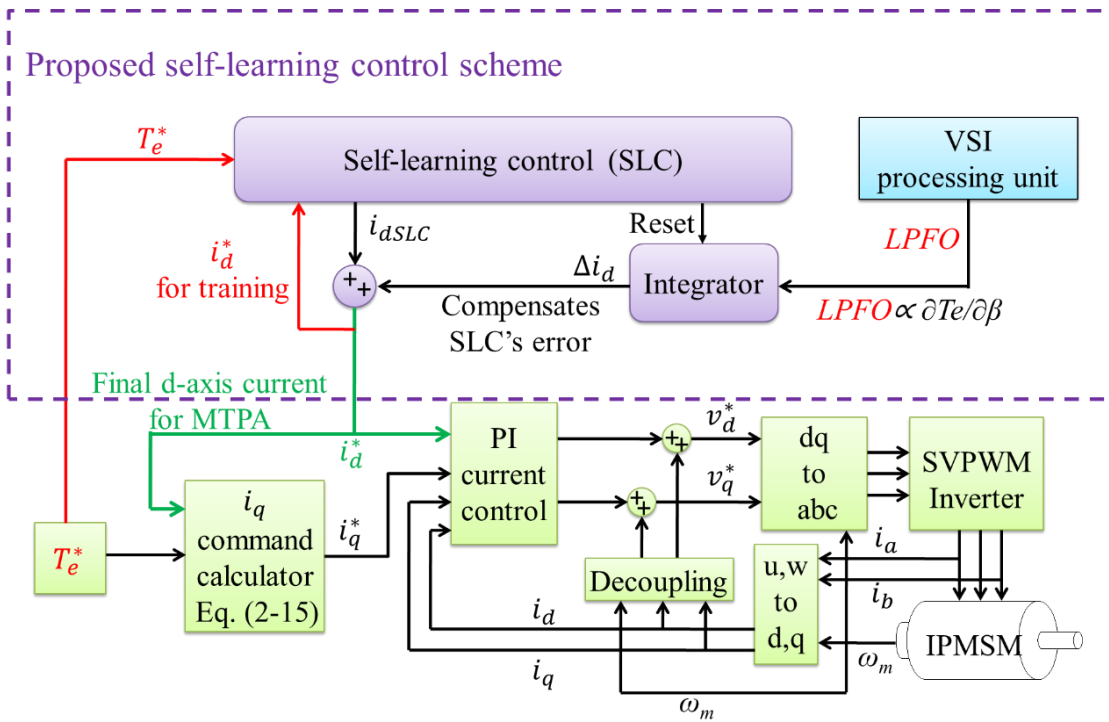


Fig. 4-3. Schematic of proposed self-learning MTPA control for IPMSM drives.

The flowchart of the proposed self-learning control is illustrated in Fig. 4-4. Before training, \mathbf{T}_{MTPA} and \mathbf{i}_{dMTPA} are zero vectors initially, or they may contain the data associated with the MTPA curve generated off-line using nominal motor parameters. To make use of as much available stored or trained data as possible for fast response, the following process is adopted. If a torque demand, T_e^* in Fig. 4-3, is larger than the maximum value in vector \mathbf{T}_{MTPA} , i.e., the $\max(\mathbf{T}_{MTPA})$ in Fig. 4-4, the output, i_{dSLC} , of

the self-learning control will be limited to the element in vector \mathbf{i}_{dMTPA} which corresponds to the $\max(\mathbf{T}_{MTPA})$. If T_e^* is located between two elements of \mathbf{T}_{MTPA} , as shown in Fig. 4-2, i_{dSLC} can be obtained through linear interpolation of the two recorded MTPA points according to (4-1). Before the SLC controller is fully trained, its output may deviate from the MTPA point by a large margin. However, any error will be adjusted by the integrator output until the output, *LPFO*, of the VSI processing block is approximately zero, i.e., the MTPA operation is realized [41].

Since the integrator in Fig. 4-3 will accumulate value, in order to increase d-axis current response, at each time when the absolute value of torque step is larger than a pre-defined threshold, ε , the integrator will be reset. Meanwhile i_{dSLC} will be updated according to new reference torque based on the data recorded in \mathbf{T}_{MTPA} and \mathbf{i}_{dMTPA} when the integrator is reset. For the condition that the torque step is smaller than the threshold, because the corresponding change in reference d-axis current should be small too, the i_{dSLC} will not update and the small error will be compensated by virtual signal injection in short time. \mathbf{T}_{MTPA} and \mathbf{i}_{dMTPA} will be updated continuously by the reference torque and resultant d-axis current. The exact value of the predefined threshold ε is not important, as it only affects slightly the MTPA tracking response.

When a torque step is larger than the threshold, *LPFO* signal will be masked for a small period of time. After this period, the virtual signal injection will drive the resultant d-axis current toward the MTPA point and the \mathbf{T}_{MTPA} and \mathbf{i}_{dMTPA} will be updated continuously by the reference torque and the resultant d-axis current. Since the virtual signal injection adjusts the d-axis current towards the MTPA point, the resultant d-axis current can be considered as the optimal i_{dMTPA} and the newly recorded d-axis current in \mathbf{i}_{dMTPA} should be closer to the actual MTPA point than the previously recorded in \mathbf{i}_{dMTPA} . Therefore, the accuracy of SLC output will continuously be improved. Moreover, a more accurate SLC output will also accelerate the convergent rate of the d-axis current to the actual MTPA point. Therefore, although the MTPA d-axis currents recorded in \mathbf{i}_{dMTPA} may initially have large errors, they will eventually approach the ideal MTPA d-axis currents. Consequently, the proposed SLC can be trained on-line, and the training of the SLC will not affect the MTPA operation.

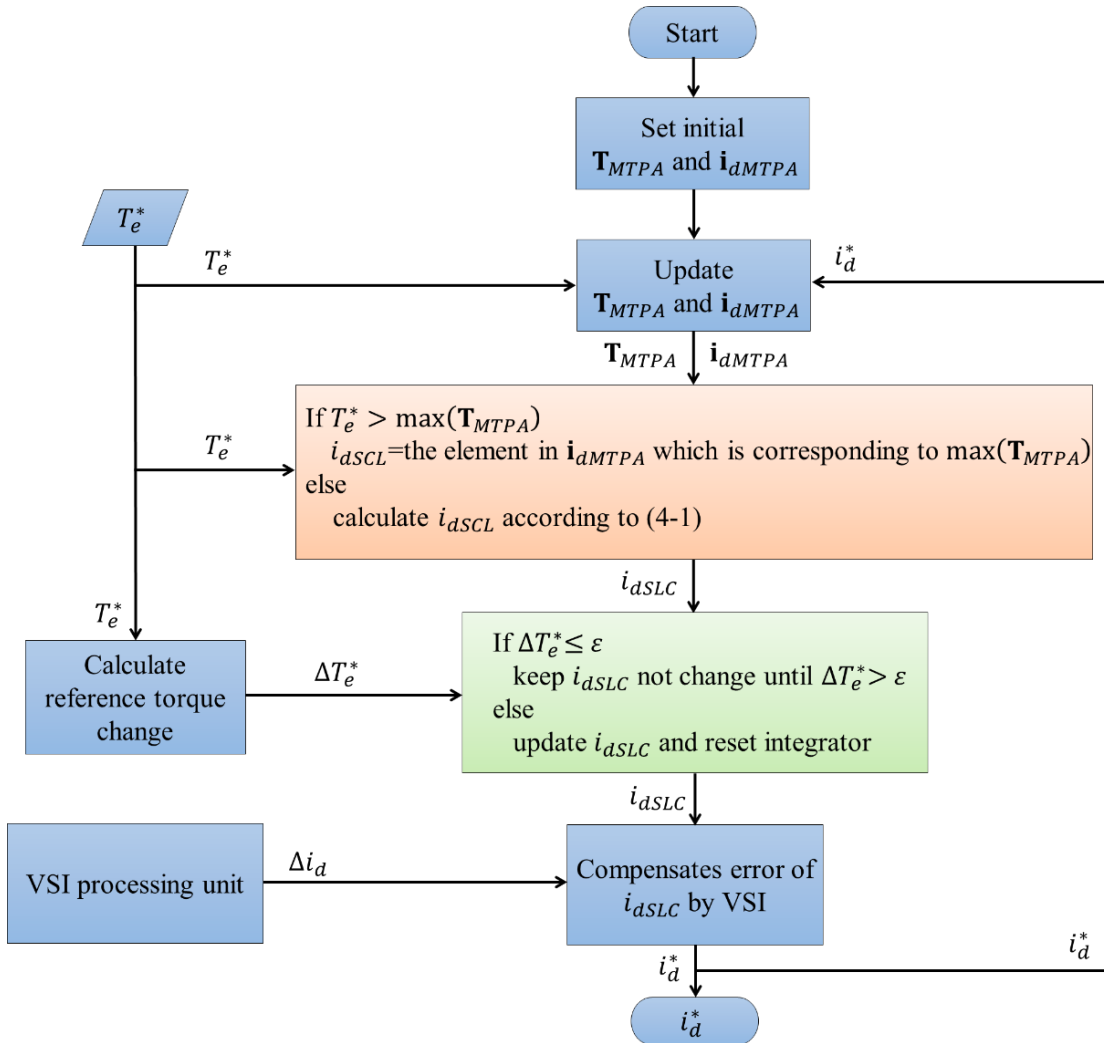


Fig. 4-4. Flowchart of proposed self-learning MTPA control for IPMSM drives

The reference q-axis current in Fig. 4-3 is generated from (2-15) based on the reference torque and reference d-axis current. The machine parameters employed in (2-15) can either be the nominal machine parameters or obtained from look-up tables as functions of d- and q-axis currents. It should be noted that if the parameters in (2-15) are inaccurate, the q-axis current will not yield the exact reference torque, and there will be torque control error. However, since the signal T_e^h in (2-12) which corrects the d-axis current is independent from these parameters, the resultant d-axis current will be corrected by the VSI and still ensure that the motor operates on the MTPA points for the actual torque. The gap in the reference and actual torque can be corrected by the speed feedback loop in a speed servo drive. For EV tractions however, the feedback correction will be performed by a human driver. Of course, if high fidelity model parameters are stored in a look-up table, the torque control accuracy can be improved.

4.2.4 Simulation Results

To verify the performance of the proposed self-learning control scheme, simulations were performed employing again the high fidelity non-linear IPMSM machine model which represents the real electromagnetic behaviors of the IPMSM. The applicable reference torque range of a machine is divided into 35 sections. The reference q-axis current was calculated based on (2-15) and the machine parameters in (2-15) were obtained from predefined look-up tables as functions of d- and q- axis currents. The torque step threshold, ε , in this chapter is defined as 2 N·m. Initially \mathbf{T}_{MTPA} and \mathbf{i}_{dMTPA} are set to zero.

4.2.4.1 Reference Torque Step Larger Than the Threshold

Fig. 4-5 shows the variations of the resultant torque and reference d-axis current together with the SLC output when the torque varied between 9 N·m and 68 N·m in steps periodically.

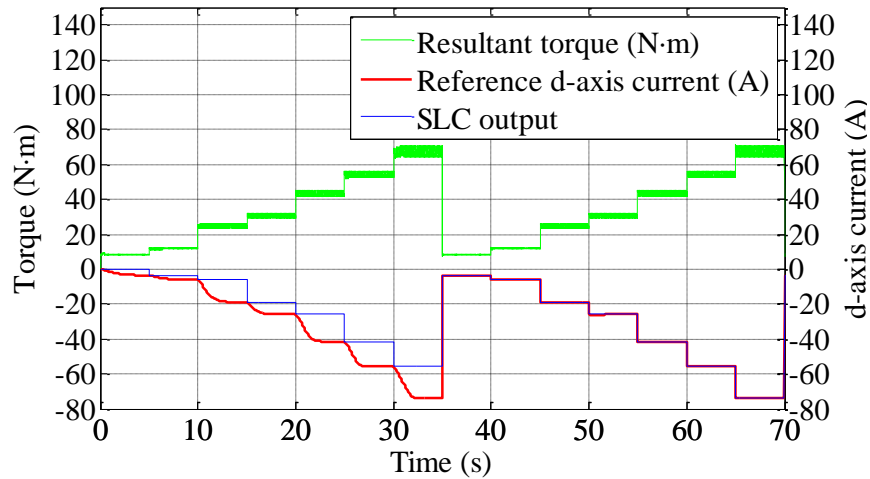


Fig. 4-5. Variations of resultant torque, reference d-axis current and output of SLC.

When $t < 35$ s, the SLC is not trained and its output is equal to the reference d-axis current recorded in \mathbf{i}_{dMTPA} corresponding to the maximum reference torque in \mathbf{T}_{MTPA} through each torque step. The error between actual MTPA d-axis current for the reference torque T_e^* and the SLC output is compensated by the virtual signal injection control, albeit its response is slow. However, when the proposed self-learning control scheme is trained,

i.e., when $t > 35$ s, the SLC output approximates the actual MTPA d-axis current and the approximation error is small. This error is still compensated by the virtual signal injection control in short time. The speed of tracking response of the proposed control has been significantly increased.

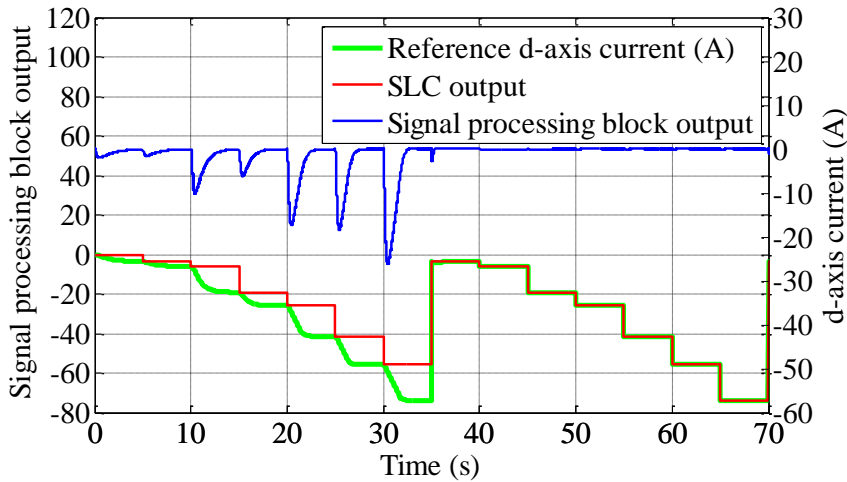


Fig. 4-6. Signal processing block output and reference d-axis current generation.

The simulation results of the signal processing block output, *LPFO*, SLC output and reference d-axis current generated from the proposed self-learning control scheme under the same operating conditions as Fig. 4-5 are shown in Fig. 4-6. It can be seen from Fig. 4-6, before the proposed self-learning control scheme is trained, i.e., $t < 35$ s, at each reference torque step, the output of the signal processing block, *LPFO*, is initially large and then converges to zero gradually. This is because the large error of untrained SLC output and the tracking of the MTPA reference d-axis currents by the virtual signal injection have relatively slow converging rate. After the proposed self-learning control scheme has been trained, the output of the signal processing block becomes small and the d-axis reference current responds quickly to the torque change. Moreover, *LPFO* always converges to zero, which implies that the d-axis current converges to the MTPA point and the training of the proposed self-learning control scheme based on the virtual signal injection control is accurate.

The resultant torque and reference q-axis current under the same operation condition of Fig. 4-5 are shown in Fig. 4-7. When $t < 35$ s, the SLC is not fully trained and large overshoots in reference q-axis current can be observed. This is due to the inaccurate SLC output. However, after training, $t > 35$ s, the overshoots in the reference q-axis current are

eliminated and the response of the proposed control scheme has been significantly improved.

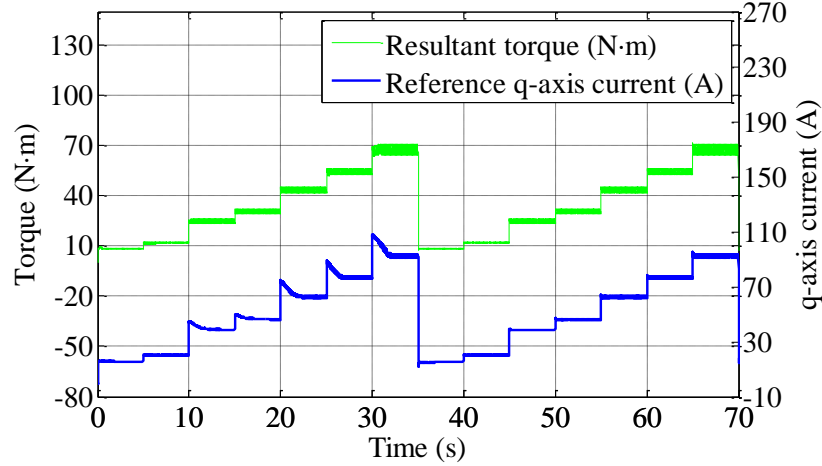


Fig. 4-7. The simulation result of resultant torque and reference q-axis current.

4.2.4.2 Automatical Adaptation to Machine Parameter Change

Simulations were also performed with significant change in the permanent magnet flux. At $t=70$ s, the permanent magnet (PM) flux linkage in the machine model is reduced to 80 percent of its original value while the parameters in (2-15) used to compute the reference q-axis current were not changed. This may represent the combined effect of temperature increase and partial demagnetization of the machine. The change in the PM flux linkage caused the new MTPA points to deviate from the original MTPA points obtained in the previous training. However, the virtual signal injection compensated the deviations. Meanwhile T_{MTPA} and i_{dMTPA} are updated according to newly identified MTPA points.

It can be seen from Fig. 4-8 that in the first cycle after the parameter changed (from $t=70$ s to $t=105$ s), the reference d-axis current is obtained from the sum of the SLC output and virtual signal injection with relatively slow response. During this period, the proposed SLC was trained by the newly tracked MTPA reference d-axis currents.

In the second cycle after the machine parameter changed ($t>105$ s), the proposed SLC has adapted itself to the new machine parameters and the output of the SLC reaches the MTPA reference d-axis current tracked by the virtual signal injection of the new operation condition with fast response. The training of the SLC does not affect MTPA operation of

the IPMSM drive, albeit the torque control error increases due to inaccurate machine parameters in (2-15).

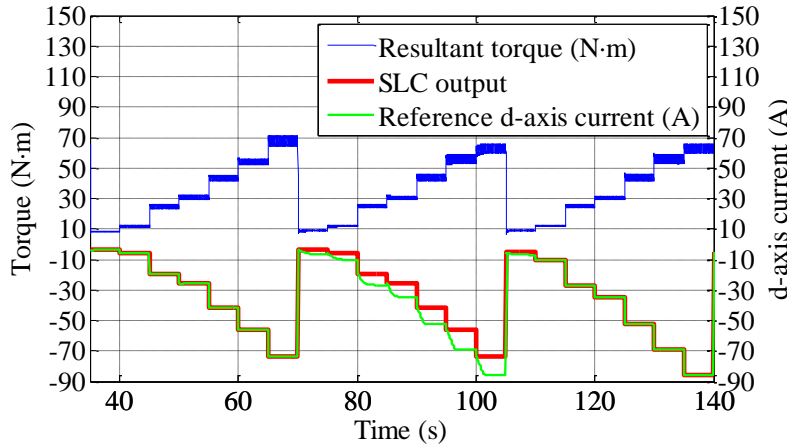


Fig. 4-8. SLC behavior after machine parameter changes.

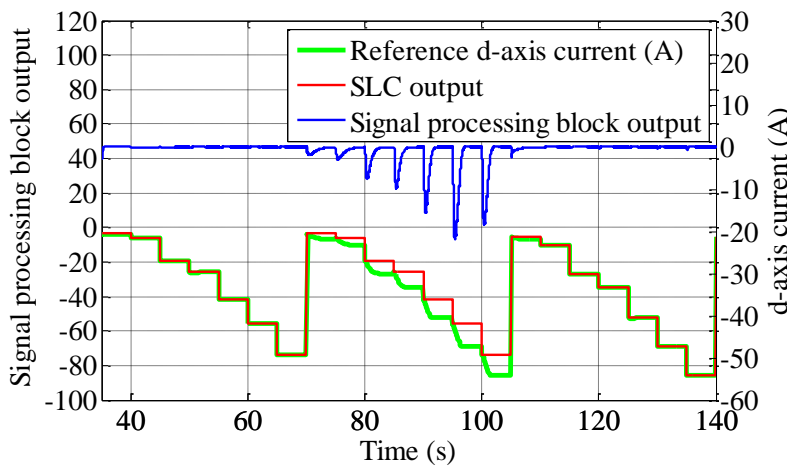


Fig. 4-9. The simulation result of *LPFO*, reference d-axis current generation and SLC output after machine parameter changes.

The simulation results of the SLC output, signal processing block output, i.e., *LPFO*, and reference d-axis current generated from the proposed self-learning control scheme under the same operating conditions as Fig. 4-8 are shown in Fig. 4-9. It can be seen from Fig. 4-9 that before the machine parameter is changed, i.e., $t < 70$ s, at each reference torque step, the output of the signal processing block is almost zero. This is because the SLC output is close to the actual MTPA d-axis currents. However, in the first cycle after the machine parameters changed (from $t = 70$ s to $t = 105$ s), at each reference torque step, the output of the signal processing block is initially large and then converges to zero gradually. This is due to the large error between the actual MTPA points corresponding to the new machine parameters and the SLC output based on the previous training. After $t = 105$ s, the proposed SLC has adapted itself to the new machine parameters and the output of the

signal processing block becomes small and the d-axis reference current responds quickly to the torque change.

The simulation results of the reference torque, resultant torque and q-axis current responses under the same operating conditions as Fig. 4-8 are shown in Fig. 4-10. Due to the change in the PM flux linkage, the torque error becomes significant.

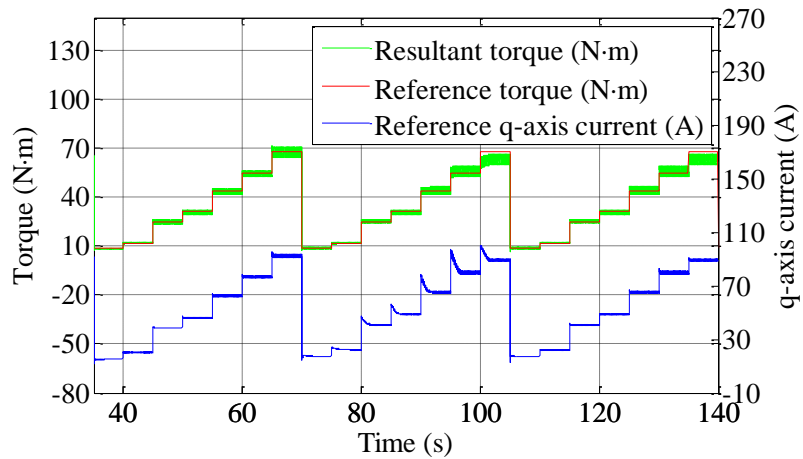


Fig. 4-10. Simulation results of reference torque, resultant torque as well as q-axis current.

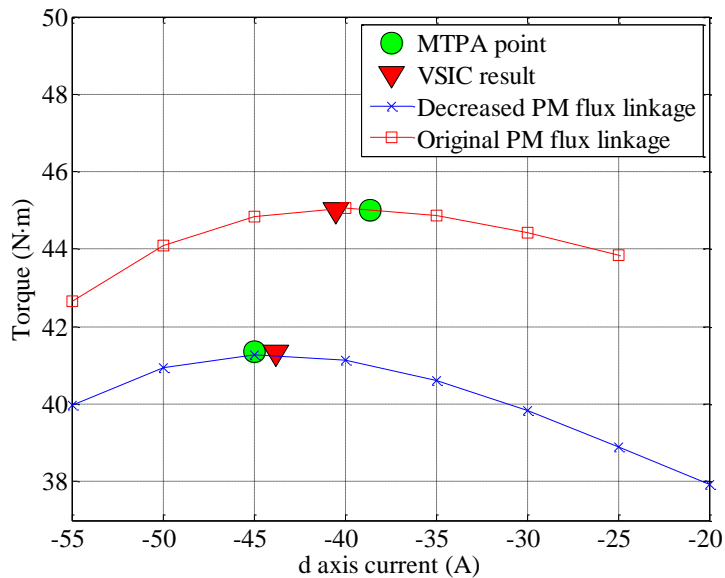


Fig. 4-11. Constant current amplitude loci and the control performance of the proposed control scheme with inaccurate q-axis current.

Fig. 4-11 illustrates constant current loci of the two current amplitudes which correspond to the original and reduced PM flux linkages, respectively. The simulation results obtained from the original PM flux linkage and reduced PM flux linkage for the reference torque of 45 N·m are also shown in Fig. 4-11. It can be seen from Fig. 4-11 that although the machine parameter in (2-15) was not accurate and the resultant torque was

not equal to the reference torque, the proposed control scheme can still track the MTPA point accurately.

4.2.4.3 Reference Torque Step is Smaller than the Threshold

Fig. 4-12 shows the simulation results when the reference torque step is smaller than the threshold. As shown in Fig. 4-12, when $t < 35$ s, the proposed control scheme is not trained, and the reference torque is slowly increased with a $2 \text{ N}\cdot\text{m/s}$ gradient. Under this condition, the integrator in Fig. 4-3 will not be reset and i_{dSLC} will not be updated. The reference d-axis current is generated from the combination of initial i_{dSLC} and the integrator output based on virtual signal injection. However, T_{MTPA} and i_{dMTPA} are updated regularly and the proposed control scheme is still trained. When $t > 35$ s the reference torque steps are larger than $2 \text{ N}\cdot\text{m}$; hence the optimal d-axis current is approximated by SLC directly with fast response.

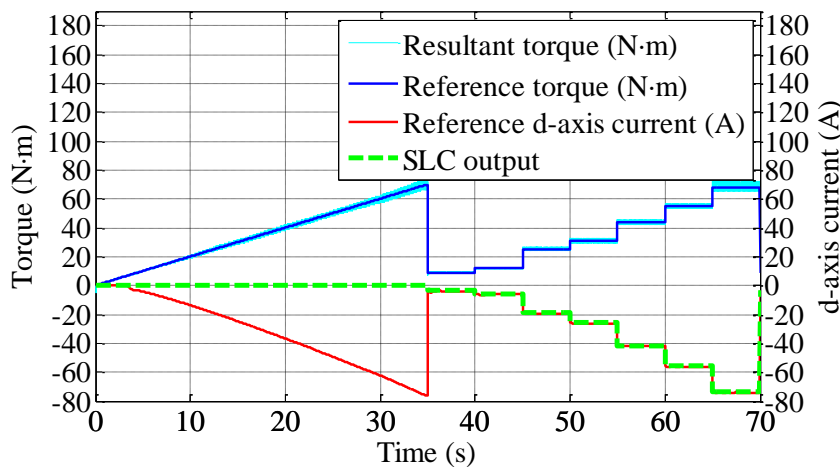


Fig. 4-12. Reference torque slowly changes.

The simulation results of the integrator output, reference d-axis current and the reference torque under the same operating conditions as Fig. 4-12 are shown in Fig. 4-13. As can be seen, when $t < 35$ s, the proposed control scheme is not trained and the error between the optimal d-axis current and i_{dSLC} is compensated by the VSIC integrator output, Δi_d , in Fig. 4-3. After $t = 35$ s, the reference torque steps are larger than $2 \text{ N}\cdot\text{m}$, the optimal d-axis current is approximated by SLC output directly with fast response and the

output of the integrator is close to zero, which indicates the SLC output approximates the actual MTPA d-axis current accurately.

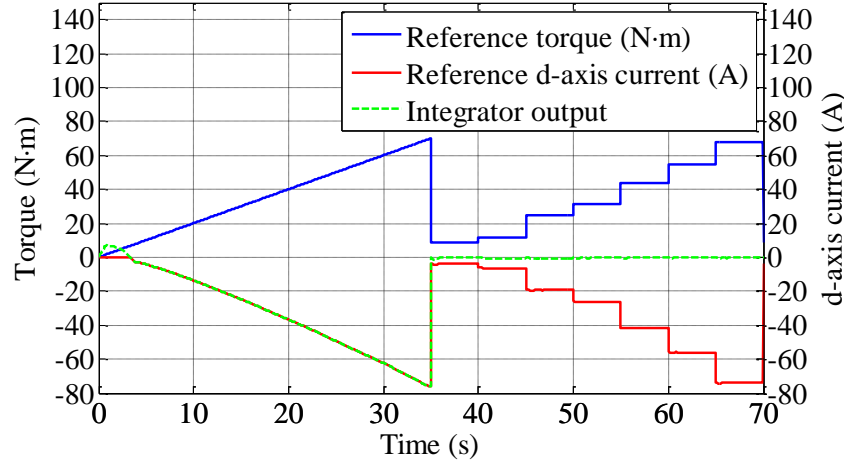


Fig. 4-13. Integrator output when reference torque changes slowly.

4.2.4.4 Reference Torque Fast Changes

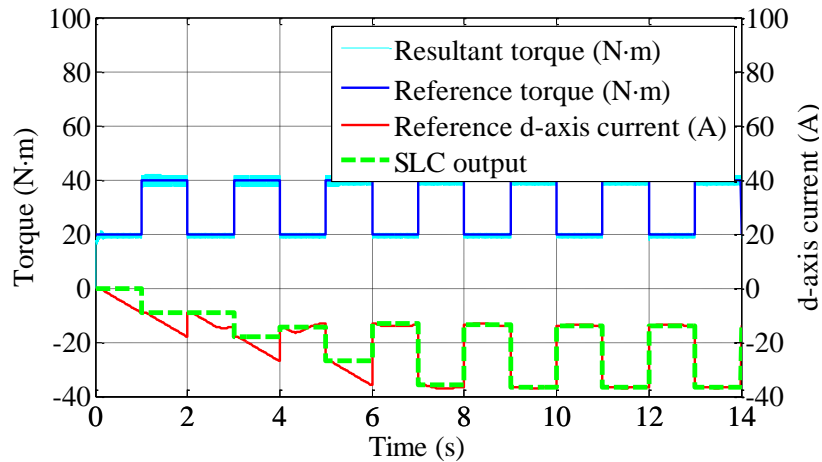


Fig. 4-14. Reference torque fast changes.

Simulations were also performed for the operating condition when the reference torque changes rapidly. As shown in Fig. 4-14, the reference torque steps between 20 N·m and 40 N·m in every 2 s. Before the proposed control scheme is fully trained, i.e., $t < 6$ s, the virtual signal injection drives the d-axis current toward the MTPA d-axis current and the corresponding reference torque and d-axis current are recorded in \mathbf{T}_{MTPA} and \mathbf{i}_{dMTPA} , respectively. At each torque step, the integrator is reset; meanwhile the SLC output is updated based on the data recorded in \mathbf{T}_{MTPA} and \mathbf{i}_{dMTPA} , simultaneously. As can be seen in Fig. 4-14, the accuracy of the SLC output continuously improves and eventually

becomes equal to the optimal values. The tracking speed of the proposed control has been significantly increased when the SLC is fully trained.

The simulated integrator output and reference torque under the same operating conditions as Fig. 4-14 are shown in Fig. 4-15. When $t < 6$ s, the proposed control scheme is not fully trained and the output of the integrator is relatively large. The reference d-axis current is generated from the combination of the integrator output and the SLC output. After $t = 6$ s, the proposed control scheme is fully trained and the reference d-axis current is approximated by SLC output directly with fast response while the integrator output approximates to zero.

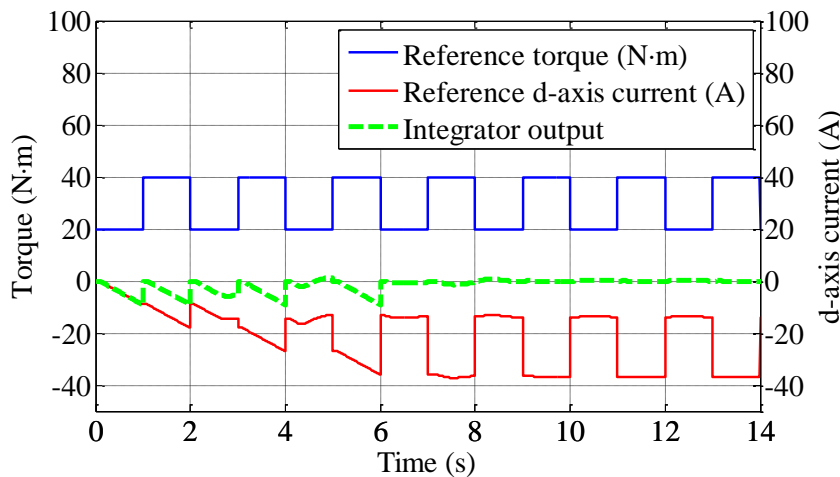


Fig. 4-15. Integrator output when reference torque changes fast.

4.2.5 Experimental Results

To verify the proposed self-learning control scheme, experiments were performed on the IPMSM drive whose specification is given in Table 2-1. The test rig for the experiments is shown in Fig. 2-10. The applicable reference torque range of the machine was divided into 35 sections as those in the simulations.

4.2.5.1 MTPA Points Tracking Performance

The proposed SLC has been implemented with the same training process as described in section 4.2.4.1. The MTPA points tracking performances in steady state are illustrated

in Fig. 4-16. As shown in Fig. 4-16, the payload torque is increased from 10 N·m to 45 N·m in steps of 5 N·m at 1000 r/min. To determine MTPA points experimentally, torque variation with current angle when the current amplitude is kept constant is measured for each payload torque. The actual MTPA points are obtained through curve fitting of the measured torque data and they are represented in Fig. 4-16 by squares. Meanwhile, the MTPA points are also tracked by the proposed self-learning control scheme and they are indeed tracked by the virtual signal injection control scheme through the training. The q-axis currents were generated according to (2-15). The MTPA points tracked by the virtual signal injection based SLC are represented by circles.

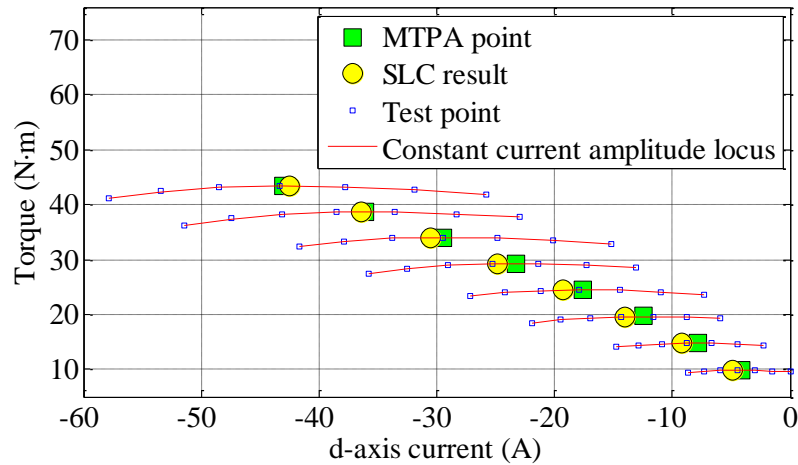


Fig. 4-16. Experimental result of the MTPA tracking performance at 1000 r/min

Table 4-1

Comparison between Resultant Torque of VSIC based SLC and Torque of MTPA Points at 1000r/min				
Reference torque	Current amplitude	Torque generated by VSIC based SLC	MTPA torque	Torque error
10 N·m	17.26 A	9.85 N·m	9.86 N·m	0.10%
15 N·m	25.67 A	14.74 N·m	14.77 N·m	0.20%
20 N·m	34.00 A	19.60 N·m	19.64 N·m	0.20%
25 N·m	42.28 A	24.43 N·m	24.47 N·m	0.16%
30 N·m	50.55 A	29.25 N·m	29.27 N·m	0.07%
35 N·m	58.87 A	34.02 N·m	34.04 N·m	0.06%
40 N·m	67.10 A	38.72 N·m	38.72 N·m	0.00%
45 N·m	75.47 A	43.42 N·m	43.42 N·m	0.00%

Table 4-1 compares the resultant torques of the virtual signal injection based self-learning control and the measured torques at the MTPA points. It can be seen from Fig. 4-16 and Table 4-1 that the proposed self-learning control can always track the MTPA points with high accuracy and the torque errors between the measured MTPA points and the tracked MTPA points are less than 0.2%. It is also evident that the measured output

torque under the proposed control scheme is slightly lower than the reference torque. This is because the parameters in (2-15) may be not accurate and the presence of friction torque in the real machine reduces the net output torque.

4.2.5.2 Performance of Proposed Control Scheme during Payload Torque Changes

To validate the performance of the proposed self-learning control scheme during payload torque changes, the proposed control scheme was firstly tested with reference torque variations from 0 N·m to 35 N·m in steps of 5 N·m at 1000 r/min. The proposed scheme was trained during this process. Subsequently, the reference torque was decreased from 35 N·m to 0 N·m in steps of 5 N·m and the i_{dSLC} was generated from the tracked MTPA points which were recorded in \mathbf{T}_{MTPA} and \mathbf{i}_{dMTPA} . Finally, the reference torque was increased from 3 N·m to 28 N·m in steps of 5 N·m at 1000 r/min so that the references did not coincide with the training data in order to validate the SLC performance at the operation conditions which the drive had not experienced previously.

Fig. 4-17 shows the measured d-axis current together with measured and estimated torques when the reference torque is stepped from 20 N·m to 35 N·m in steps of 5 N·m and back to 20 N·m in the same steps. The estimated torque is based on the high fidelity machine model and measured d- and q-axis currents.

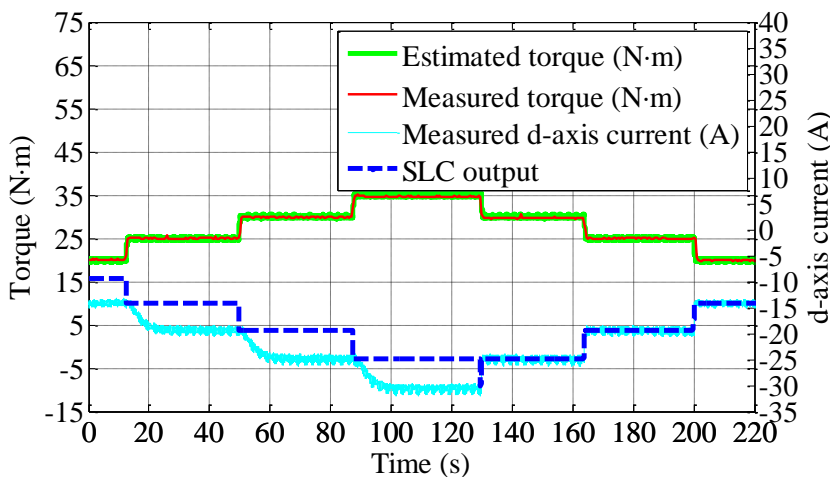


Fig. 4-17. d-axis current and measured/estimated torque response to torque command steps from 20 N·m to 35 N·m then steps back to 20 N·m.

As shown in Fig. 4-17, when reference torque steps from 25 N·m to 30 N·m during the time $t < 60$ s, the SLC has not been trained at 30 N·m reference torque but has been trained at the 25 N·m reference torque. The output of the SLC is equal to the element in \mathbf{i}_{dMTPA}

which corresponds to the maximum reference torque in T_{MTPA} , e.g., the MTPA d-axis current of 25 N·m. The error between the SLC output and the MTPA d-axis current for 30 N·m reference torque is compensated by the virtual signal injection albeit the d-axis current responds to the torque step slowly. Similar result can be observed when the reference torque steps from 30 N·m to 35 N·m.

When the reference torque steps from 35 N·m to 30 N·m, since the SLC has been trained at 30 N·m reference torque previously, the output of the SLC approximated to the optimal d-axis current for the MTPA operation. As shown in Fig. 4-17, the speed of tracking response of the proposed control is significantly increased and similar results can be observed when the reference torque steps from 30 N·m to 25 N·m.

Fig. 4-18 shows the variations of the measured torque and the measured q-axis current which corresponds to the measured d-axis current variations shown in Fig. 4-17. Before the SLC is trained, the q-axis current always has large overshoot due to the slow d-axis current response. However, after the SLC is trained, the overshoot is significantly reduced.

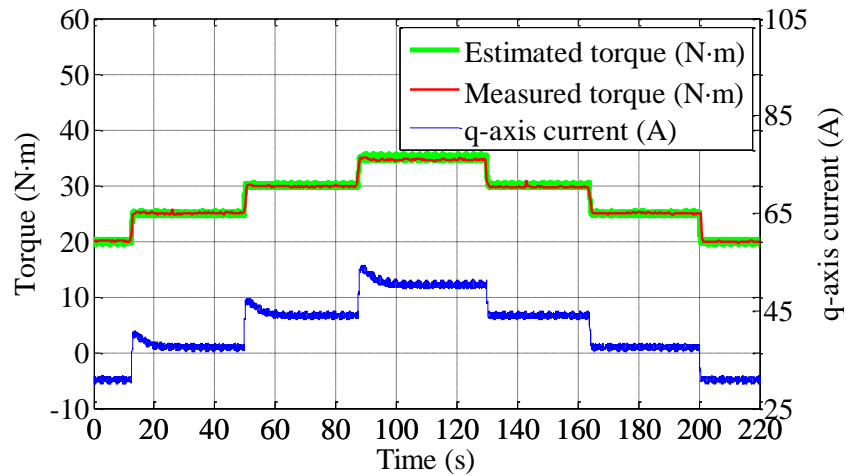


Fig. 4-18. The measured/estimated torque and the measured q-axis current.

The signal processing block output, SLC output and measured d-axis current under the same operation conditions of Fig. 4-17 are shown in Fig. 4-19. As can be seen, the signal processing block output always converges to zero, which means the MTPA operation can always be guaranteed. Moreover, before the proposed control scheme is trained, for each torque step, the signal processing block output is initially large and then converges to zero gradually. However after the proposed control scheme is trained, the output of the signal processing block becomes small and the d-axis reference current responds quickly to the torque change.

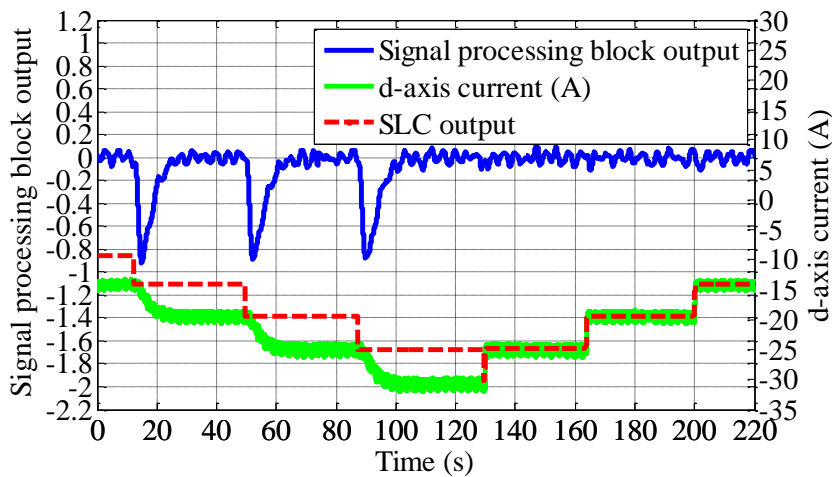


Fig. 4-19. Signal processing block output, SLC output and measured d-axis current.

The reference torque was also increased from 3 N·m to 28 N·m in steps of 5 N·m at 1000 r/min during the tests. Although the SLC was not trained at these reference torques, since they were located between trained reference torques, the SLC can still generate the reference d-axis currents for MTPA control accurately.

Fig. 4-20 illustrates the d-axis current response and the SLC output when the reference torque steps from 23 N·m to 28 N·m after the SLC has been trained. From Fig. 4-20, a fast d-axis current response can be observed. This illustrates that the proposed SLC can produce the MTPA d-axis current even for the reference torque which it has not experienced before.

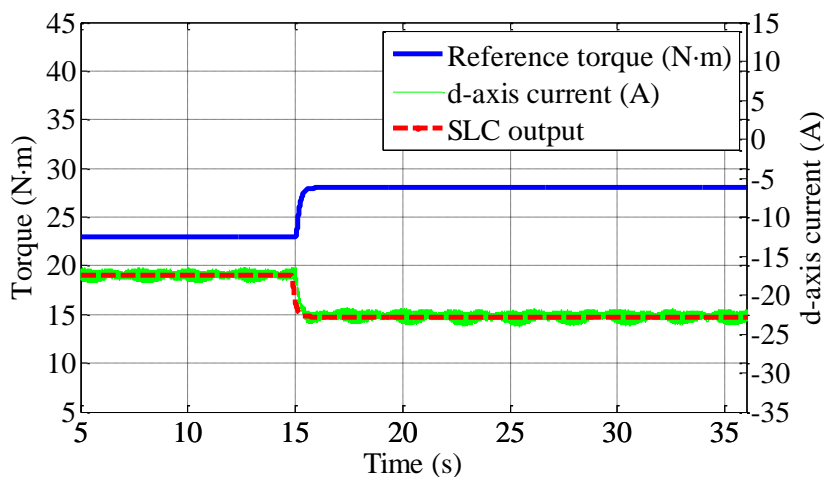


Fig. 4-20. d-axis current, SLC output and reference torque response to torque command step from 23 N·m to 28 N·m.

The comparison between resultant d-axis currents and MTPA d-axis currents is shown in Fig. 4-21. As shown in Fig. 4-21, the errors between the MTPA d-axis currents and

resultant d-axis currents are very small and the proposed control scheme achieves accurate MTPA operation with fast response after training.

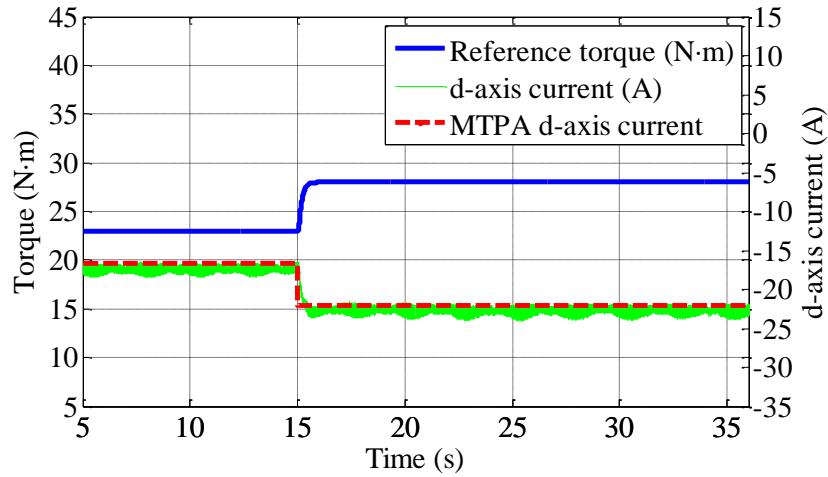


Fig. 4-21. Comparison between resultant d-axis current and MTPA d-axis current.

Fig. 4-22 shows the reference torque and measured q-axis current. Again, the fast response of the measured q-axis current can be observed.

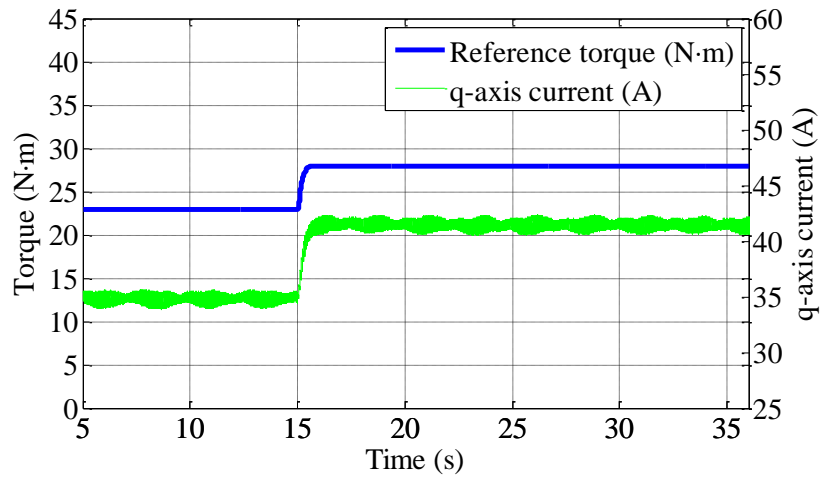


Fig. 4-22. The reference torque and measured q-axis current.

Fig. 4-23 compares the measured torque and reference torque in response to the change in the reference torque at the same operating condition as Fig. 4-20. From Fig. 4-23, a fast torque response can be observed.

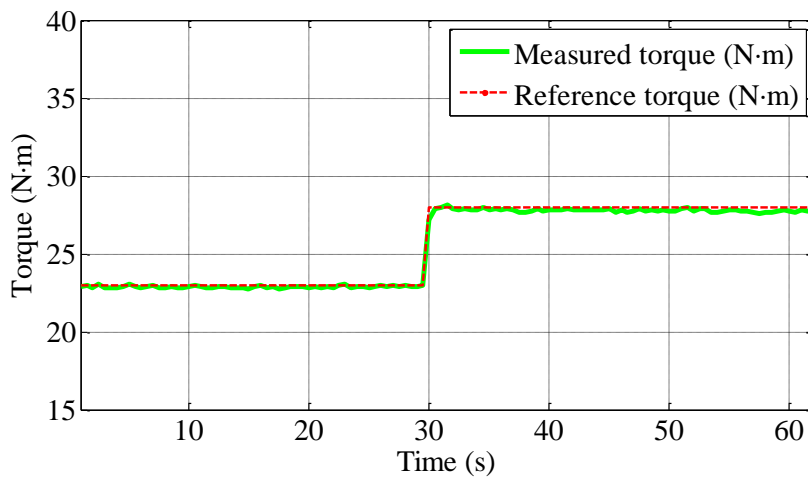


Fig. 4-23. Comparison between the measured torque and reference torque in response to a step change in the reference torque.

4.3 Self-learning Control in f-t Frame

Section 4.2 has proposed a novel self-learning control scheme to achieve accurate parameter independent MTPA operation of IPMSMs with fast response in the d-q frame. As the optimal reference d-axis current for MTPA operation in constant torque region is independent of speed, the relationship between optimal d-axis current and reference torque can be represented by online curve fitting as proposed in section 4.2. The simulation results and experiment results in section 4.2 have illustrated effectiveness of the online curve fitting based self-learning control scheme.

Nevertheless, in the field weakening region, the optimal d-axis current for field weakening operation is not only dependent on reference torque, but also on rotor speed. Therefore, the online curve fitting based self-learning control in d-q frame is no longer effective in field weakening region. Although an online 2-dimensional surface fitting whose input are speed and reference torque and the output is the optimal d-axis current may be possible to implement the self-learning control in field weakening region, it needs much more data than the online 1-dimensional curve fitting to train the self-learning control while the control accuracy may deteriorate.

As described in Chapter 3, direct torque control or direct flux vector control in the stator flux linkage synchronous (f-t) frame [20], [21], [23], [24] can also be utilized to control IPMSM drives. Compared with the d-q frame based control, the f-t frame based control can regulate the stator flux amplitude directly and can manage motor voltage in field weakening region without look-up tables of current or flux references [65]. Therefore, the

f-t frame based control scheme can easily cope with voltage saturation and have better controllability and performance in field weakening region [24], [66].

In the rest of this chapter, self-learning control for IPMSM drives is proposed based on virtual signal injection aided direct flux vector control in the f-t frame. The proposed control scheme achieves MTPA operation through on-line self-learning in constant torque region and directly limits stator flux amplitude for VCMTPA operation in field weakening. In this way, the proposed control scheme not only has the advantages of virtual signal injection aided direct flux vector control such as robustness to current and voltage harmonics, high accuracy in tracking the MTPA and VCMTPA points, no additional iron and copper losses, but also has fast dynamic responses in both constant torque and field weakening regions.

4.3.1 Relationship between Optimal Stator Flux Amplitude and Torque

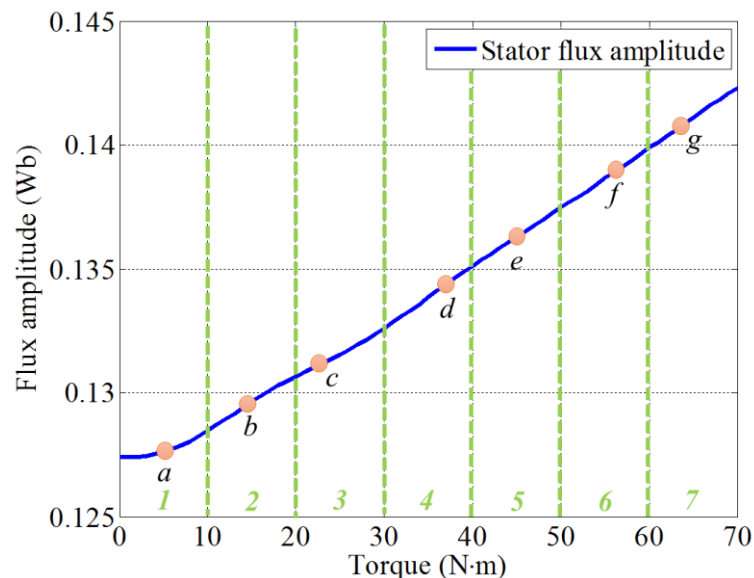


Fig. 4-24. Relationship between torque command and the optimal stator flux for MTPA operation.

For a given torque command, there is a unique optimal stator flux amplitude for the MTPA operation [77] in constant torque region. The relationship between torque command and the optimal stator flux amplitude for MTPA operation is shown in Fig. 4-24. If a sufficient number of MTPA points are tracked online, other points on the curve

can be approximated by interpolations among these tracked points. The proposed self-learning control scheme is based on this simple but effective concept.

When the motor drive is operating in the field weakening region, the stator voltage is constrained by the maximum voltage. Fig. 3-16 shows the variations of torque and reference voltage amplitudes with stator flux amplitude for a given current amplitude when the required voltage for the MTPA operation is larger than the voltage limit. As the flux amplitude increases towards the MTPA point, the resultant torque and reference voltage amplitude, v_a^* , will increase. Therefore, the voltage constrained maximum torque per ampere (VCMTPA) operation is the point at which the voltage amplitude is equal to the voltage limit [77]. At the VCMTPA point, the maximum torque at the intersection is achieved for the given current amplitude and voltage limit.

According to (1-22), the maximum flux amplitude under the voltage constraint is parameter-independent except for the phase resistance. However, the voltage drop across the resistance is relatively small in the field weakening region compared with the voltage limit. Therefore, by assuming the nominal value of the phase resistance at a representative temperature, e.g., 100°C, the optimal flux amplitude for VCMTPA operations can be obtained by (1-22).

4.3.2 Implementation of the Self-learning Control in f-t Frame

In order to generate accurate optimal reference flux amplitudes for MTPA and VCMTPA control with fast response, the proposed self-learning control scheme utilizes curve fitting to approximate the relationship between reference torque and optimal flux amplitude in constant torque region and utilizes (1-22) to limit flux amplitude in field weakening region. The details of the proposed control scheme will be illustrated in this section.

4.3.2.1 Combination of Virtual Signal Injection Aided Direct Flux Vector Control and Self-learning Control

The proposed self-learning control scheme is based on virtual signal injection aided direct flux vector control. The virtual signal injection aided direct flux vector control combines the direct flux vector control scheme [26] and the virtual signal injection

compensation [77] as described in Chapter 3. The direct flux vector control can limit the current amplitude in the f-t frame and easily cope with the voltage limit, and hence has better performance in the field weakening region [26], while the virtual signal injection compensation is parameter independent and insensitive to flux observer error. Therefore, the virtual signal injection aided direct flux vector control inherently has the advantages of both the direct flux vector control and virtual signal injection compensation.

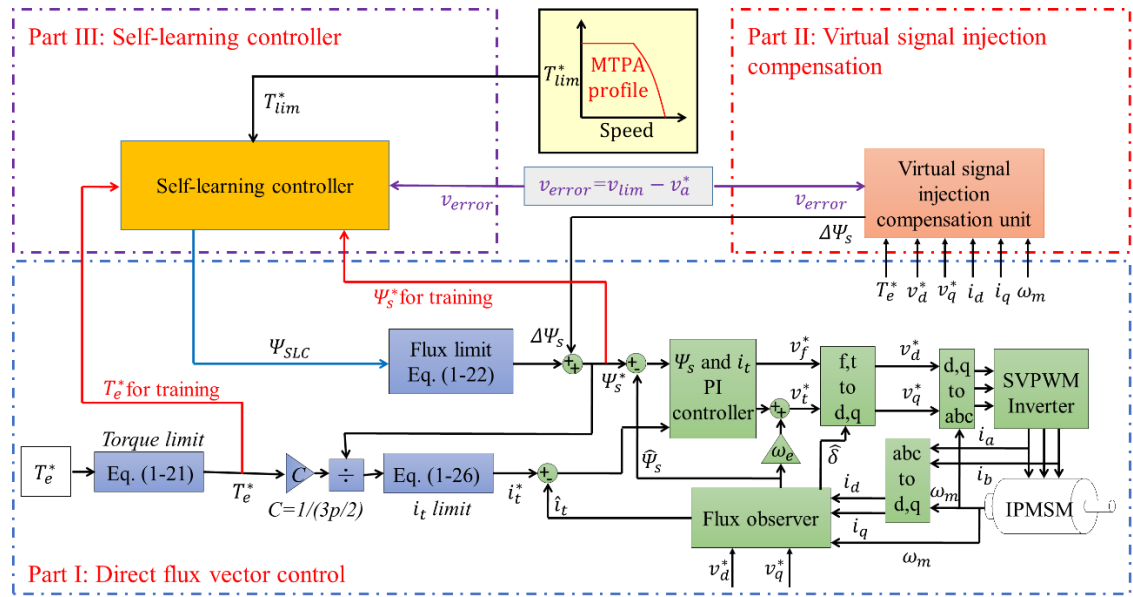


Fig. 4-25. Schematic of the proposed self-learning control scheme in f-t frame.

The schematic of the proposed self-learning control scheme in f-t frame is shown in Fig. 4-25 and the overall flowchart of the proposed control scheme is shown in Fig. 4-28. As it is shown in Fig. 4-25, the flux amplitude command, Ψ_{SLC} , is generated from the proposed self-learning control scheme which will be described in details later. The output of the self-learning control scheme is limited by (1-22) to ensure IPMSM drive operates within the voltage limit. The reference torque is limited by (1-21). The t-axis current is calculated from (1-25) and limited by (1-26) to ensure the IPMSM drive operates within the current limit. As proposed in [26], the stator flux linkage is directly regulated by the f-axis voltage and the t-axis current is regulated by the t-axis voltage through two PI controllers. The flux observer in this paper is the conventional flux observer described in Chapter 3 [111], [75]. However, other observers are also applicable.

In order to generate optimal reference flux amplitude before the self-learning controller is fully trained and to compensate the error of the self-learning output, the reference flux amplitude, Ψ_s^* , is conditioned by the virtual signal injection compensation unit as shown

in Part II of Fig. 4-25, whose details are shown in Fig. 4-26. The inputs of the virtual signal injection compensation unit are d- and q-axis reference voltage (v_d^* , v_q^*), measured d- and q-axis current (i_d , i_q), measured speed (ω_m), reference torque (T_e^*), and voltage error (v_{error}) given in (2-17). The outputs of the virtual signal injection compensation unit are reference flux amplitude error compensation term ($\Delta\Psi_s$).

Similar to the virtual signal injection aided direct flux vector control proposed in Chapter 3, the output of the low-pass filter (LPF) in Fig. 4-26, $LPFO$, is proportional to $\partial T_e / \partial \beta$. In this way, the information of $\partial T_e / \partial \beta$ can be extracted. If $-\partial T_e / \partial \beta$ is present at the input to the integral controller in Fig. 4-26, the output of the integral regulator will change until $\partial T_e / \partial \beta = 0$, i.e., the MTPA points is tracked. Moreover, since $\partial T_e / \partial \beta$ should be equal to zero at the MTPA points, $LPFO$ signal can be defined as a MTPA quality indicator. The integrator output, $\Delta\Psi_s$, will be utilized to compensate the error in reference flux, Ψ_s^* , as shown in Fig. 4-25.

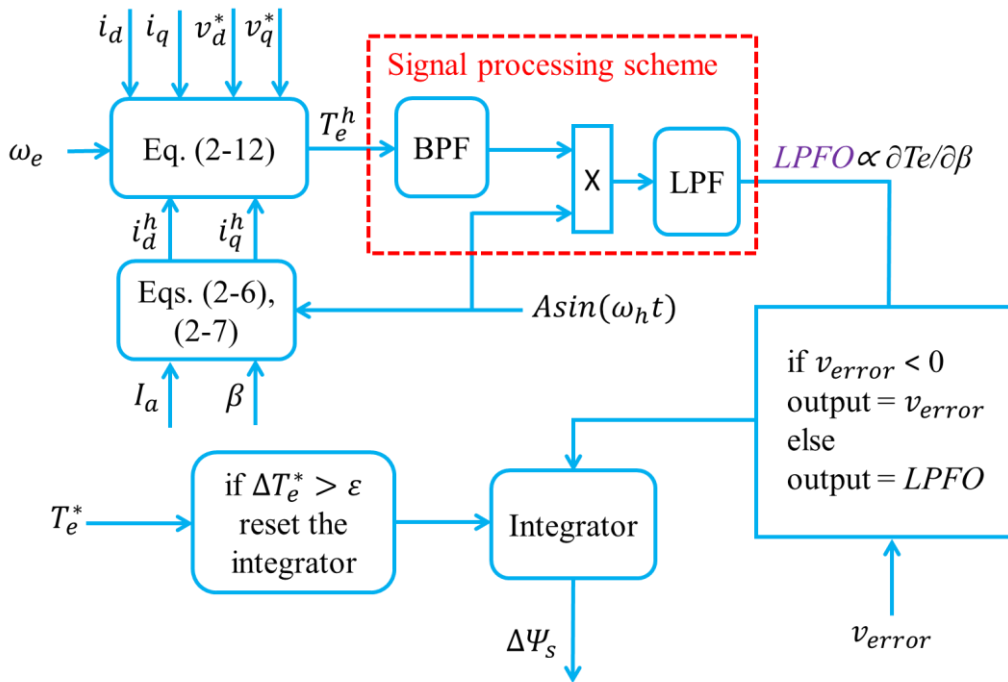


Fig. 4-26. Details of the virtual signal injection compensation unit.

In field weakening region, the stator flux amplitude should be limited by (1-22). However, due to the error of nominal resistance in (1-22) and error in the flux observer, the voltage saturation may still occur. To avoid the voltage saturation, the voltage error, v_{error} , can be fed to the integrator in Fig. 4-26 instead of $LPFO$ to decrease $\Delta\Psi_s$ when v_{error} is negative, i.e., when the voltage reference is greater than the voltage limit. The

sign of v_{error} determines whether $LPFO$ or v_{error} is fed to the integral controller. If the $v_{error} \geq 0$, the drive voltage amplitude is below the voltage limit, the signal $LPFO$ will be fed to the integral controller to adjust $\Delta\Psi_s$ until the MTPA point is reached or voltage amplitude equal to v_{max} , i.e., the VCMTPA point as shown in Fig. 3-16. If the $v_{error} < 0$, v_{error} will be fed to the integral controller and $\Delta\Psi_s$ will decrease until $v_{error} = 0$, i.e., reaching the VCMTPA point. Therefore, the virtual signal injection aided control can always guarantee the motor is operating on MTPA or VCMTPA points.

4.3.2.2 Self-learning Control in Constant Torque Region

As shown in Fig. 4-25, Part III, the inputs of the self-learning controller include the voltage error, v_{error} , the reference stator flux amplitude, Ψ_s^* , the limited reference torque, T_e^* . The output of the self-learning controller is denoted as Ψ_{SLC} . Any error in Ψ_{SLC} due to curve fitting or imperfect learning will be compensated by $\Delta\Psi_s$ to generate an accurate flux amplitude reference Ψ_s^* for MTPA or VCMTPA operation as described previously.

Fig. 4-24 shows the relationship between optimal flux amplitude and corresponding reference torque in constant torque region. If a sufficient number of MTPA points, e.g., a to g in Fig. 4-24, are recorded, other points on the curve can be approximated by interpolations among these recorded points. These optimal flux amplitude and corresponding torque command are recorded in the two column vectors Ψ_{sMTPA} and \mathbf{T}_{MTPA} , respectively. In order to have an even distribution of the recorded MTPA points over an applicable torque range, the torque command range is divided into N sections and each section records one tracked MTPA point. For example, the torque command region in Fig. 4-24 is divided into seven sections. If a new pair of optimal flux amplitude and torque command for MTPA operation is tracked in section M , the M^{th} elements of Ψ_{sMTPA} and \mathbf{T}_{MTPA} will be substituted by the corresponding values of newly tracked MTPA point. This process repeats during the self-learning operation. In this way the proposed control scheme can always adapt itself to machine parameter variations during operation.

The schematic of the proposed self-learning control is shown in Fig. 4-25 and the details of the self-learning controller for MTPA operation are shown in Fig. 4-27. The flowchart of the proposed control scheme is shown in Fig. 4-28. Two column vectors Ψ_{sMTPA} and \mathbf{T}_{MTPA} record the tracked stator flux amplitude, Ψ_s^* , and the corresponding torque reference, T_e^* , respectively.

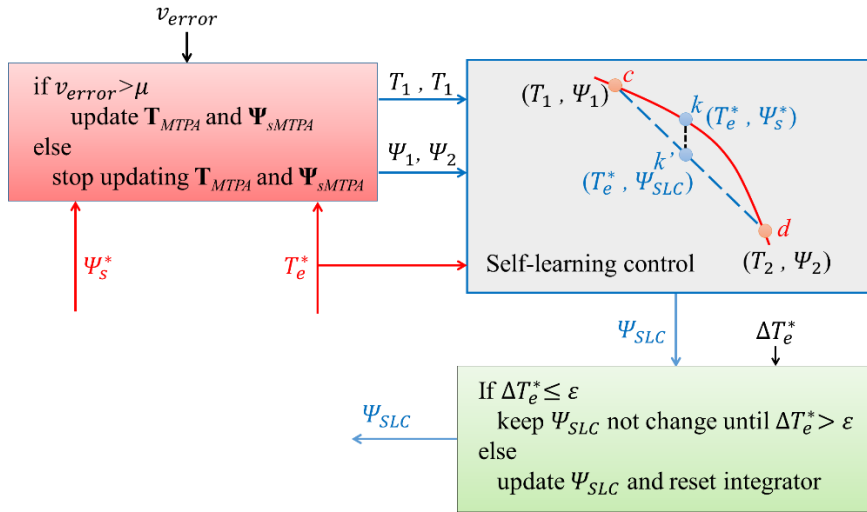


Fig. 4-27. Details of self-learning controller for MTPA and field weakening operations.

Before training, Ψ_{sMTPA} and \mathbf{T}_{MTPA} are nominal values or data for MTPA operation generated off-line. If a torque demand, T_e^* , is located between two elements of \mathbf{T}_{MTPA} , e.g., T_1 and T_2 in Fig. 4-27, the corresponding MTPA point k can be approximated by k' through (4-2). The error between Ψ_{SLC} and Ψ_s^* can be compensated by $\Delta\Psi_s$.

$$\Psi_{SLC} = \frac{T_e^* - T_2}{T_1 - T_2} (\Psi_1 - \Psi_2) + \Psi_2 \quad (4-2)$$

If T_e^* is larger than any recorded torque reference in \mathbf{T}_{MTPA} , the output of the proposed self-learning control scheme will be equal to the element in Ψ_{sMTPA} which corresponds to the reference flux amplitude associated with the maximum torque reference in \mathbf{T}_{MTPA} , $\text{Max}(\mathbf{T}_{MTPA})$. The error between Ψ_{SLC} and optimal Ψ_s^* can be compensated by $\Delta\Psi_s$.

Because the integrator in Fig. 4-26 will accumulate value, in order to increase reference flux response, at each time when the absolute value of torque step, ΔT_e^* , is larger than a pre-defined threshold, ε , the integrator will be reset. Meanwhile the Ψ_{SLC} will update according to the new reference torque based on data recorded in \mathbf{T}_{MTPA} and Ψ_{sMTPA} at the same time when the integrator is reset. When the torque step is smaller than the threshold, because the corresponding change in reference flux amplitude should be small too, the Ψ_{SLC} will not update and the small error will be compensated by the virtual signal injection in short time. In both conditions \mathbf{T}_{MTPA} and Ψ_{sMTPA} will be updated continuously by the reference torque and resultant reference flux amplitude.

When a torque step is larger than the threshold, *LPFO* signal will be masked for a small period of time, e.g., 3 times of the t-axis current loop time constant. After *LPFO* is masked, virtual signal injection will drive the resultant reference flux amplitude toward the MTPA

point, while \mathbf{T}_{MTPA} and Ψ_{sMTPA} will be updated continuously by the reference torque and resultant reference flux amplitude. As virtual signal injection tends to drive the reference flux amplitude towards the MTPA points, the newly recorded reference flux amplitude in Ψ_{sMTPA} should be closer to actual MTPA point than the one which is previously recorded in Ψ_{sMTPA} . Therefore, the accuracy of the SLC output will continuously increase. Moreover, a more accurate SLC output will also accelerate the convergence speed of the reference flux amplitude to the actual MTPA point. Therefore, although the reference flux amplitudes recorded in Ψ_{sMTPA} may initially have large errors, they will eventually approximate the ideal MTPA flux amplitudes. Consequently, the proposed SLC can be trained on-line, and the training of the SLC will not affect the MTPA operation.

4.3.2.3 Self-learning Control in Field Weakening Region

In the field weakening region, the stator flux amplitude should be limited in order to avoid voltage saturation as explained in section 4.3.1. The reference flux amplitude is limited by (1-22) directly and it is independent of machine parameters except for stator resistance R . The error between the reference flux amplitude generated from (1-22) and the optimal flux amplitude for VCMTA operation is compensated by $\Delta\Psi_s$ as illustrated in section 4.3.2.1. Since the flux amplitude for the field weakening control is not only depend on reference torque but also depends on speed, the curve fitting based self-learning is not effective in field weakening region. Therefore, in the field weakening region, the reference flux amplitude should be generated from (1-22) directly and the online training of the self-learning control scheme should be suspended when v_{error} is smaller than a pre-defined threshold μ or if the motor speed and reference torque exceed a pre-defined region, i.e., the MTPA profile. The overall flowchart of the proposed control scheme is shown in Fig. 4-28; the T_{lim}^* is the maximum reference torque to update \mathbf{T}_{MTPA} and Ψ_{sMTPA} .

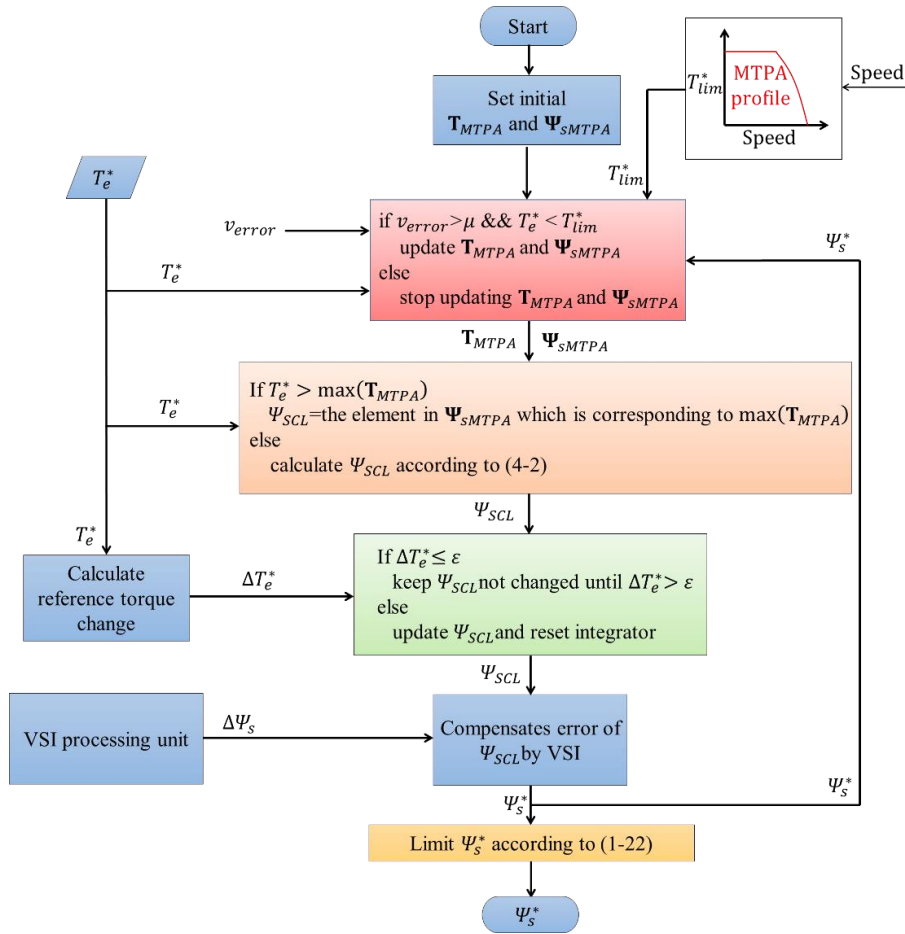


Fig. 4-28. Flowchart of the proposed self-learning control scheme based on virtual signal injection aided direct flux vector control.

4.3.3 Simulation Results

4.3.3.1 Reference Torque Step Larger than the Threshold

Simulations of the self-learning control based on virtual signal injection aided direct flux vector control for both MTPA operation and field weakening operation were performed based on a prototype IPMSM drive system. The motor model in the drive system is same as the one used in section 4.2.4. The applicable reference torque range of the machine is divided into 35 sections. The threshold, μ , to suspend the online training of the self-learning control scheme is set to 2 V. The threshold of torque step, ϵ , is set to 2 N·m. Before training, \mathbf{T}_{MTPA} is set to zero vector and all elements in Ψ_{sMTPA} are set to a nominal value, i.e., 0.1 Wb.

Fig. 4-29 shows the resultant torque, the output of proposed self-learning control and the reference flux amplitude when the reference torque varied between 9 N·m and 68 N·m in steps at 1000 r/min, periodically. Each torque step is larger than the threshold ε . When $t < 35$ s, the SLC output is equal to the reference flux amplitude recorded in Ψ_{sMTPA} which is corresponding to the maximum reference torque in T_{MTPA} . The error between actual MTPA flux amplitude and SLC output is compensated by the virtual signal injection control, albeit its response is relatively slow. When the proposed self-learning control scheme is trained, i.e., when $t > 35$ s, the output of SLC approximates the actual MTPA flux amplitude and the approximation error is small. This error is still compensated by the virtual signal injection control in short time. The speed of tracking response of the proposed control has been significantly increased.

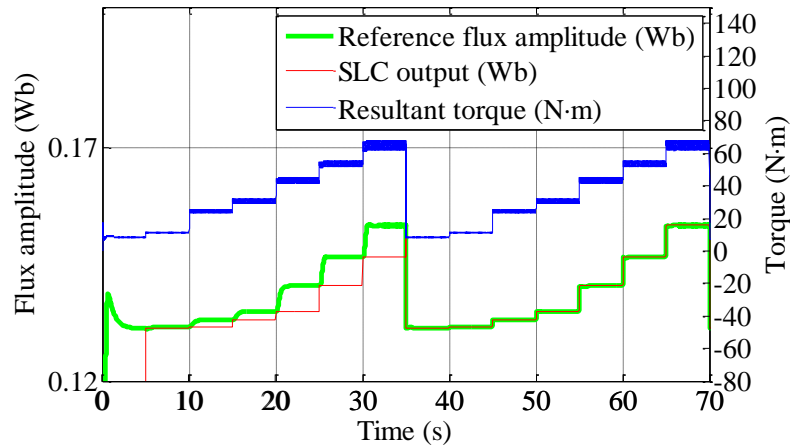


Fig. 4-29. Reference torque, output of proposed self-learning control and the reference flux amplitude at 1000 r/min.

The simulation results of the reference flux amplitude, the output of the signal processing block, *LPFO*, and the output of self-learning control under the same operating conditions as Fig. 4-29 are shown in Fig. 4-30. It can be seen from Fig. 4-30, before the proposed self-learning control scheme is trained, i.e., $t < 35$ s, at each reference torque step, the output of the signal processing block is initially large and then converges to zero gradually. This is because the large error of untrained SLC output and the tracking of the MTPA reference flux amplitude by the virtual signal injection have relatively slow converging rate. After the proposed self-learning control scheme has been trained, the output of the signal processing block becomes small and the reference flux amplitude responds quickly to the torque change. Moreover, *LPFO* always converges to zero, which implies that the flux amplitude converges to the MTPA point and the training of the

proposed self-learning control scheme based on the virtual signal injection control is accurate.

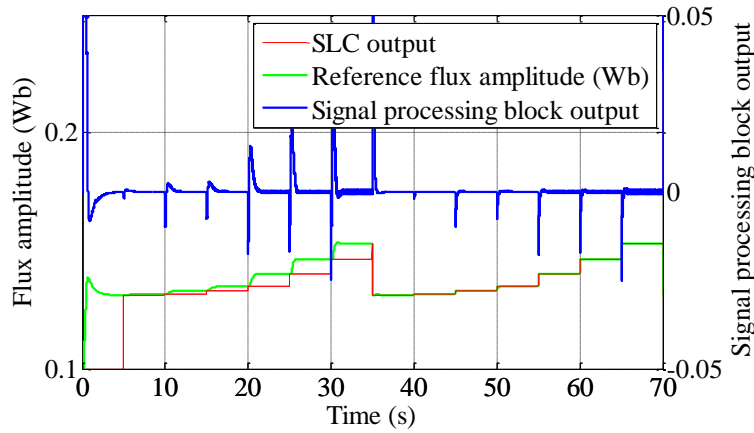


Fig. 4-30. Responses of reference flux amplitude, output of the signal processing block and output of self-learning control.

The simulation results of the resultant d- and q-axis currents under the same operation condition of Fig. 4-29 are shown in Fig. 4-31. As shown in Fig. 4-31, before training, $t < 35$ s, the d- and q-axis currents converge to the optimal values gradually. This is due to the inaccurate SLC output and relatively slow converging rate of the virtual signal injection. However, after training, $t > 35$ s, the response of the proposed control scheme has been significantly improved.

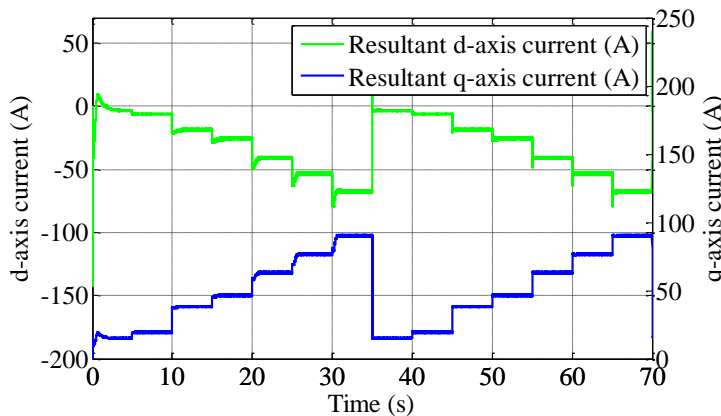


Fig. 4-31. Reference d- and q-axis currents.

4.3.3.2 Automatic Adaptation to Machine Parameter Change

The adaptation of the proposed SLC to significant PM flux change is also investigated by simulation. As it is shown in Fig. 4-32, at $t = 70$ s, the permanent magnet (PM) flux

linkage in the machine model is reduced to 80 percent of its original value while the parameter in flux observer is not changed. This may represent the combined effect of temperature increase and partial demagnetization of the machine. The change in the PM flux linkage causes the new MTPA points to deviate from the original MTPA points and the virtual signal injection compensates the deviation. Meanwhile T_{MTPA} and Ψ_{sMTPA} are updated according to newly tracked MTPA points continuously. It can be seen from Fig. 4-32 that in the first cycle after the parameter changes (from $t=70$ s to $t=105$ s), the reference flux amplitude is obtained from the sum of the SLC output and virtual signal injection with relatively slow response. During this period, the proposed SLC is trained by the newly tracked MTPA reference flux amplitude.

In the second cycle after the machine parameter changes ($t > 105$ s), the proposed SLC has adapted itself to the new machine parameters and the outputs of the SLC reach the new MTPA reference flux amplitudes with fast response. The training of the SLC does not affect MTPA operation of the IPMSM drive, albeit the torque control error increases due to inaccurate machine parameters in flux observer.

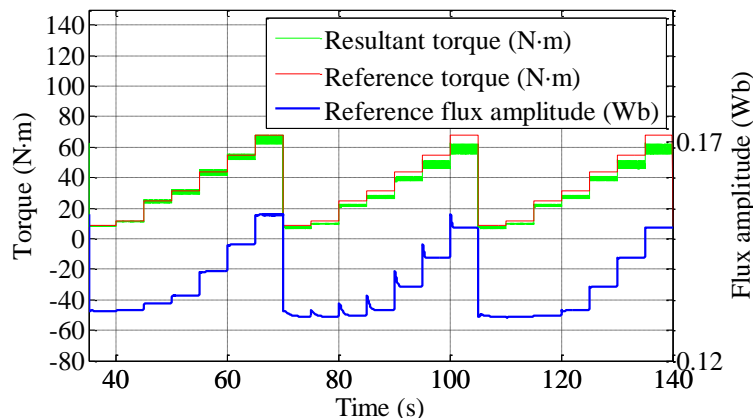


Fig. 4-32. Resultant torque, reference torque and reference flux amplitude after machine parameter changes.

The simulation results of the signal processing block output, i.e., *LPFO* signal, and the reference flux amplitude generated from the proposed self-learning control scheme under the same operating conditions as Fig. 4-32 are shown in Fig. 4-33. It can be seen from Fig. 4-33, before the machine parameters change, i.e., $t < 70$ s, at each reference torque step, the output of the signal processing block is almost zero. This is because the SLC output is close to the actual MTPA reference flux amplitude. However, in the first cycle after the machine parameters change (from $t=70$ s to $t=105$ s), at each reference torque

step, the output of the signal processing block is initially large and then converges to zero gradually. This is due to the large error between the actual MTPA points corresponding to the new machine parameters and the SLC output based on previous training. After $t=105$ s, the proposed SLC has adapted itself to the new machine parameters and the output of the signal processing block becomes small and the reference flux amplitude responds quickly to the torque change.

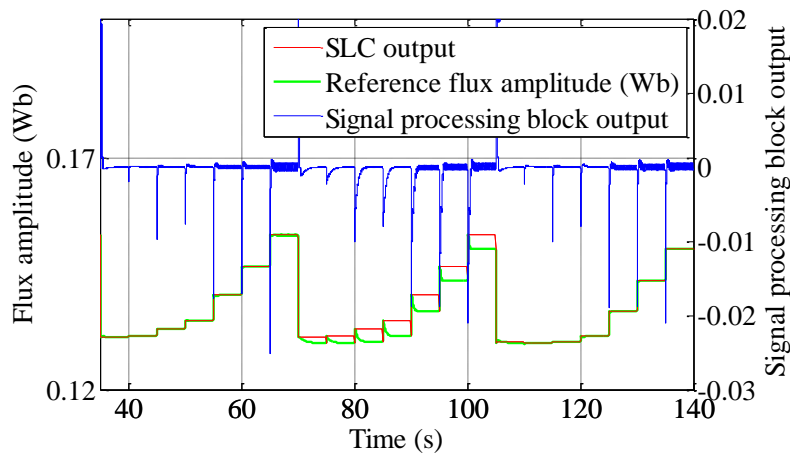


Fig. 4-33. The simulation result of *LPFO*, reference flux amplitude and SLC output after machine parameter changes.

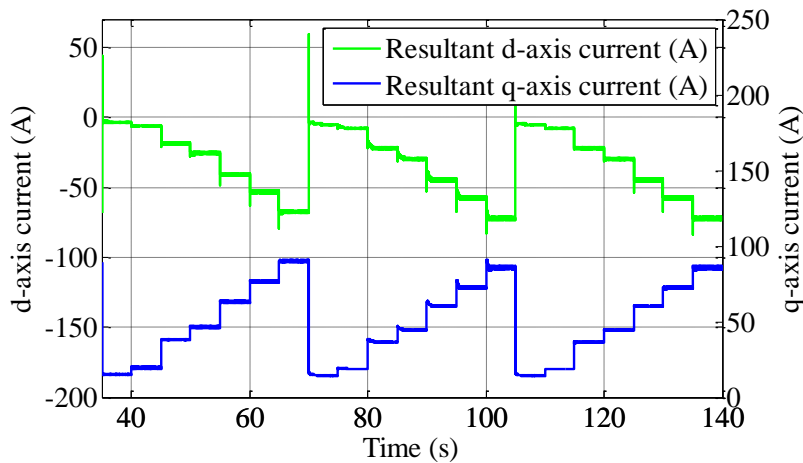


Fig. 4-34. Simulation results of reference torque, resultant torque as well as q-axis current.

The simulated d- and q-axis currents responses under the same operating conditions as Fig. 4-32 are shown in Fig. 4-34. Again, the fast responses of the d- and q-axis currents can be seen after the proposed control scheme has adapted itself to the new machine parameters.

4.3.3.3 Reference Torque Step Smaller than the Threshold

Fig. 4-35 shows the simulation results when the reference torque step is smaller than the threshold, ε . As shown in Fig. 4-35, when $t < 35$ s, the proposed control scheme is not trained, and the reference torque is slowly increased with a 2 N·m/s gradient. Under this condition, the integrator in Fig. 4-26 will not be reset and Ψ_{SLC} will not update. The reference flux amplitude is generated from the combination of Ψ_{SLC} and integrator output based on the virtual signal injection. However, the proposed control scheme is still trained from the VISC output. When $t > 35$ s, the SLC generates the optimal reference flux amplitude directly with fast response.

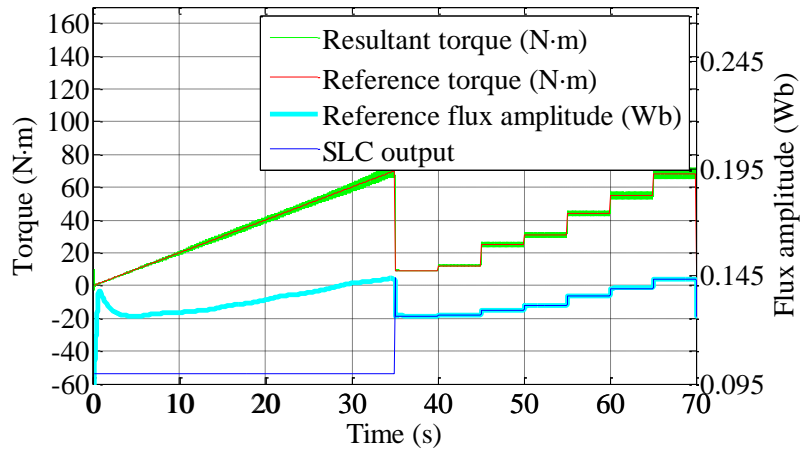


Fig. 4-35. Responses of reference flux amplitude and SLC outputs when reference torque changes slowly.

The simulation results of the integrator output, SLC output and reference flux amplitude under the same operating conditions as Fig. 4-35 are shown in Fig. 4-36. As shown in Fig. 4-36, when $t < 35$ s, the proposed control scheme is not trained. The reference flux amplitude is corrected by the output of the integrator shown in Fig. 4-26 and the SLC output is kept at its initial value, i.e., 0.1 Wb. However, the proposed control scheme is trained during operation. After $t = 35$ s, the reference torque steps are larger than 2 N·m, the reference flux amplitude is approximated by the SLC output directly with fast response and the output of the integrator is close to zero.

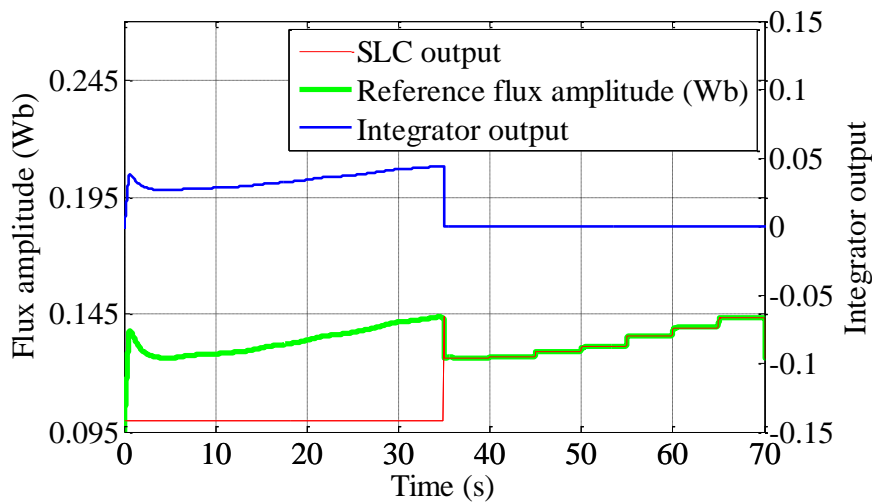


Fig. 4-36. Integrator output when reference torque changes slowly.

The MTPA d-axis current and the resultant d- and q-axis currents under the same operating conditions as Fig. 4-35 are shown in Fig. 4-37. As seen in Fig. 4-37, the resultant d-axis current always follows the MTPA d-axis current accurately because the VSIC is capable of responding to a slow torque change when $t < 35$ s and the trained SLC can respond to fast torque changes quickly.

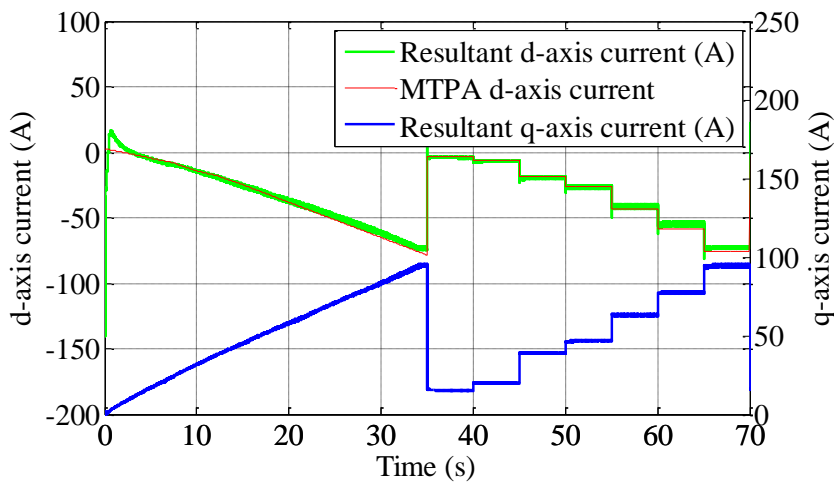


Fig. 4-37. Resultant d- and q-axis currents.

4.3.3.4 Reference Torque Fast Changes

Simulations were also performed for the operating conditions when reference torque changed rapidly. As shown in Fig. 4-38, the reference torque steps between 20 N·m and 40 N·m in every 2 s. Before the proposed control scheme is fully trained, i.e., $t < 6$ s, the virtual signal injection drives the reference flux amplitude toward the MTPA point and

the corresponding reference torque and reference flux amplitude are recorded in \mathbf{T}_{MTPA} and Ψ_{MTPA} , respectively. At each torque step, the integrator is reset meanwhile the SLC output is updated based on the data recorded in \mathbf{T}_{MTPA} and Ψ_{MTPA} , simultaneously. As it can be seen in Fig. 4-38, the accuracy of the SLC output continuously increases and the SLC outputs eventually become equal to the optimal values. The speed of tracking response of the proposed control has been significantly increased.

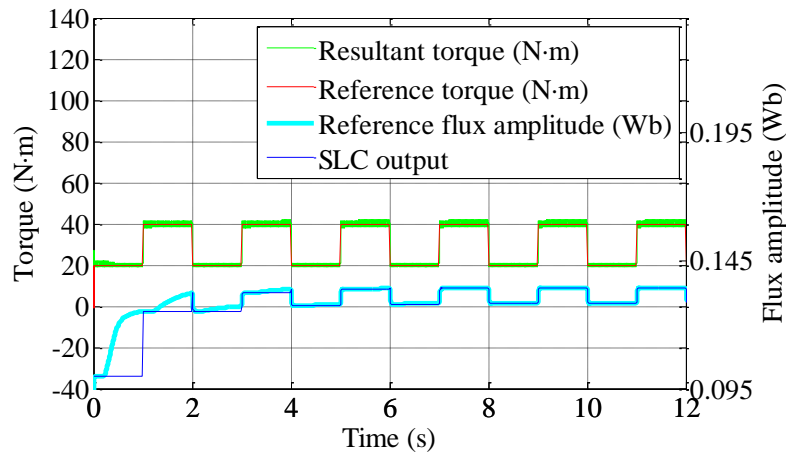


Fig. 4-38. Responses of torque and stator flux amplitude to rapid reference torque changes.

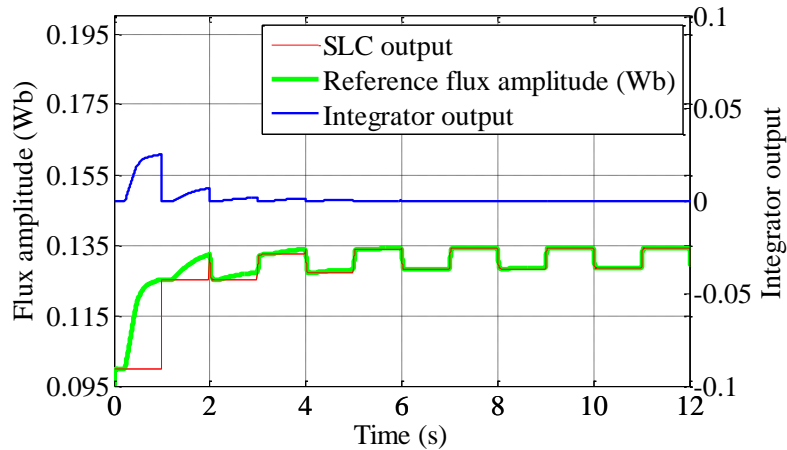


Fig. 4-39. Integrator output when reference torque changes fast.

The simulation results of the integrator output, the SLC output and the reference flux amplitude under the same operating conditions as Fig. 4-38 are shown in Fig. 4-39. As can be seen, before the proposed control scheme is fully trained, the output of the integrator is relative large. The reference flux amplitude is generated from the combination of the integrator output and the SLC output, and the integrator will be reset at each torque step. After $t=6$ s, the proposed control scheme is fully trained and the reference flux amplitude is generated from the SLC output directly with fast response.

The resultant d- and q-axis currents are shown in Fig. 4-40. It is evident that, after the proposed control scheme is fully trained, the speed of tracking response of the proposed control is significantly increased.

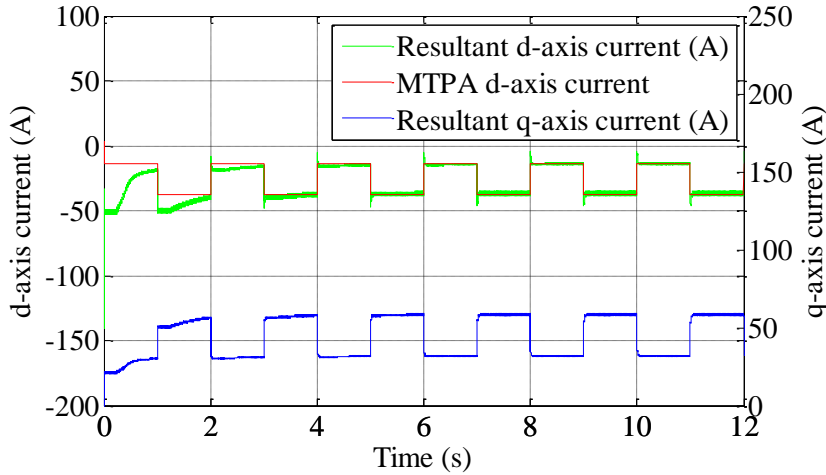


Fig. 4-40. Resultant d- and q-axis currents.

4.3.3.5 Switching between Constant Torque Region and Field Weakening Region

The performances of the proposed control scheme switched between constant torque region and field weakening region when speed varied were also simulated.

As shown in Fig. 4-41, the reference torque varied between 9 N·m and 68 N·m in steps, periodically. When $t < 35$ s, the proposed control scheme is not fully trained, the reference flux amplitude is generated from the combination of Ψ_{SLC} and $\Delta\Psi_s$ with relatively slow tracking speed. Between $t = 35$ s and $t = 70$ s, the proposed control is trained and the speed of tracking optimal reference flux amplitude is significantly increased.

At $t = 70$ s, the rotor speed steps from 1000 r/min to 3000 r/min and the motor enters field weakening region. Under this condition, the self-learning control is suspended and T_{MTPA} and Ψ_{sMTPA} stop updating. The reference flux amplitude is directly limited by (1-22) and compensated by $\Delta\Psi_s$ with fast response. The reference torque, resultant torque and reference flux amplitude are shown in Fig. 4-41, where the maximum torque is limited by the peak torque profile in the field weakening region. Therefore, between $t = 95$ s and $t = 105$ s, the resultant torque is limited at 35 N·m.

At $t = 105$ s, the speed steps from 3000 r/min to 1000 r/min and the self-learning control is activated. The accurate reference flux amplitude is directly approximated by the SLC with fast response.

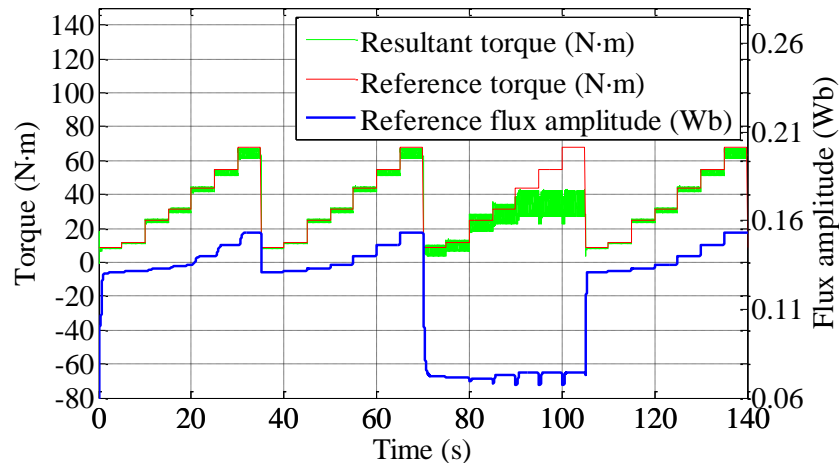


Fig. 4-41. Responses of reference torque and resultant torque when speed steps between 1000 r/min and 3000 r/min.

The SLC output, the reference flux amplitude and the signal processing block output are shown in Fig. 4-42. Before the proposed control scheme is fully trained, i.e., $t < 35$ s, the error between the actual MTPA flux amplitude and the SLC output is compensated by the virtual signal injection control, albeit its response is slow. However, when the proposed self-learning control scheme is trained, i.e., between $t = 35$ s and $t = 70$ s, the SLC output approximates the actual MTPA flux amplitude and the approximation error is small. This error is still compensated by the virtual signal injection control in short time. The speed of tracking response of the proposed control has been significantly increased.

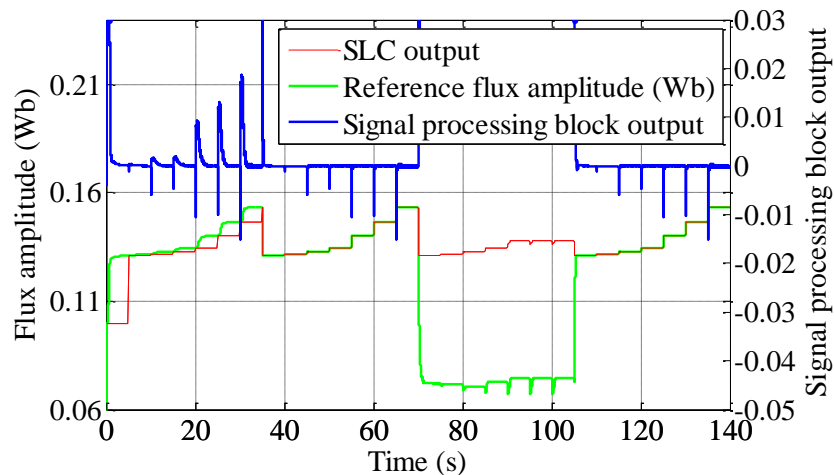


Fig. 4-42. Responses of signal processing block output, reference flux amplitude and SLC output to step changes in torque reference and step change in speed from 1000 r/min to 3000 r/min.

In the field weakening operation between $t = 70$ s and $t = 105$ s, the signal processing block output is relatively large since the operation point is derived from the actual MTPA point. Although the SLC output still approximates the MTPA flux amplitudes of the

corresponding limited reference torque, the reference flux amplitude is limited by (1-22) directly with fast response.

Therefore, whether in constant torque region or field weakening region, the proposed self-learning control based on virtual signal injection aided direct flux vector control can always achieve accurate optimal control with fast response.

The resultant d- and q-axis currents under the same operation condition of Fig. 4-41 are shown in Fig. 4-43. The fast response of the d- and q-axis currents in both constant torque region and field weakening region can be observed after the proposed control scheme is trained, i.e., $t > 35$ s.

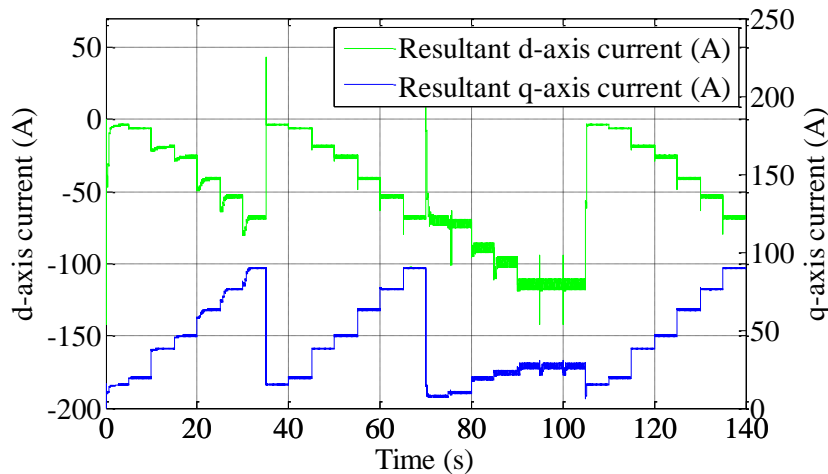


Fig. 4-43. Resultant d- and q-axis current at 1000 r/min and 3000 r/min.

It should be noted that step change in speed in the foregoing simulation is exaggerated to illustrate the robustness of the proposed control in response to rapid change between constant torque and field weakening regions. In reality, step change in speed is not possible due to mechanical inertia and finite torque.

4.3.4 Experimental Result

The proposed self-learning virtual signal injection aided direct flux vector control scheme was implemented in the same IPMSM drive as before. The applicable torque range of the IPMSM was divided into 35 sections. Before training, \mathbf{T}_{MTPA} is set to zero vector and all elements in Ψ_{sMTPA} are set to a nominal value, i.e., 0.1 Wb. The training of

self-learning will be suspended when v_{error} is smaller than 2 V. The torque step threshold, ε , is defined as 2 N·m.

4.3.4.1 Self-learning Performance

The motor drive was first tested by increasing reference torque from 10 N·m to 35 N·m in steps of 5 N·m at 1000 r/min. During this period, the self-learning control scheme was trained. After the training, the reference torque decreased from 35 N·m to 10 N·m in steps of 5 N·m to verify the performance of the proposed self-learning control scheme. During this period, the SLC output, Ψ_{SLC} , of the proposed self-learning was generated from (4-2) based on data in Ψ_{sMTPA} and \mathbf{T}_{MTPA} recorded in training.

Since the actual flux amplitude is difficult to measure, the measured d-axis current is utilized instead of flux amplitude to illustrate the self-learning performance of the proposed control scheme. Fig. 4-44 illustrates the measured d-axis current, the ideal MTPA d-axis current when reference torque increases from 20 N·m to 35 N·m and decreases from 35 N·m to 20 N·m in steps of 5 N·m.

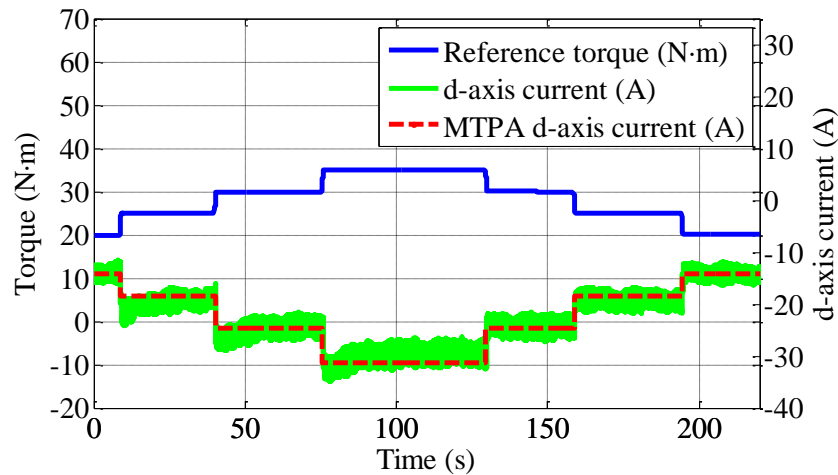


Fig. 4-44. Responses of resultant d-axis current and ideal MTPA d-axis current to reference torque changes.

As shown in Fig. 4-44, when the reference torque steps from 20 N·m to 35 N·m during the time $t < 100$ s, the proposed self-learning control has not been trained and Ψ_{SLC} is set to the flux amplitude associated with the maximum torque reference in \mathbf{T}_{MTPA} . The d-axis current slowly converges to the optimal d-axis current with the compensation of $\Delta\Psi_s$. However, after the proposed control scheme is trained, i.e., when $t > 100$ s, the optimal

reference flux amplitude is directly approximated by (4-2) and the small error of the approximation is compensated by $\Delta\Psi_s$ instantly. The speed of tracking response of the proposed control has been significantly increased. As a result, the d-axis current can reach the optimal value with fast response.

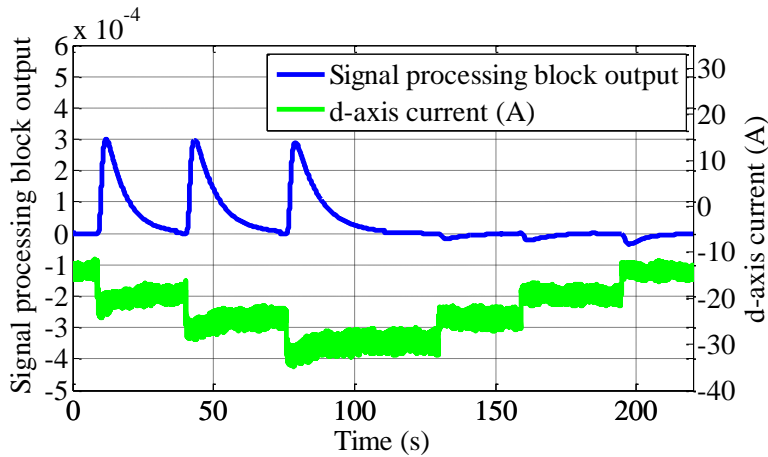


Fig. 4-45. MTPA quality indicator $LPFO$ and resultant d-axis current.

The resultant MTPA quality indicator $LPFO$ and the resultant d-axis current under the same operation conditions of Fig. 4-44 are shown in Fig. 4-45. It can be seen from Fig. 4-45, before the proposed control scheme is trained, i.e., $t < 100$ s, at each torque step, $LPFO$ is initially large and then converges to zero gradually. This is because of the large error between Ψ_{SLC} and the optimal flux amplitude as well as the slow convergence of $\Delta\Psi_s$. However, after the proposed control scheme was trained, $LPFO$ converges to zero fast. The improvement in d-axis current response due to the proposed self-learning control scheme can be clearly seen in Fig. 4-45.

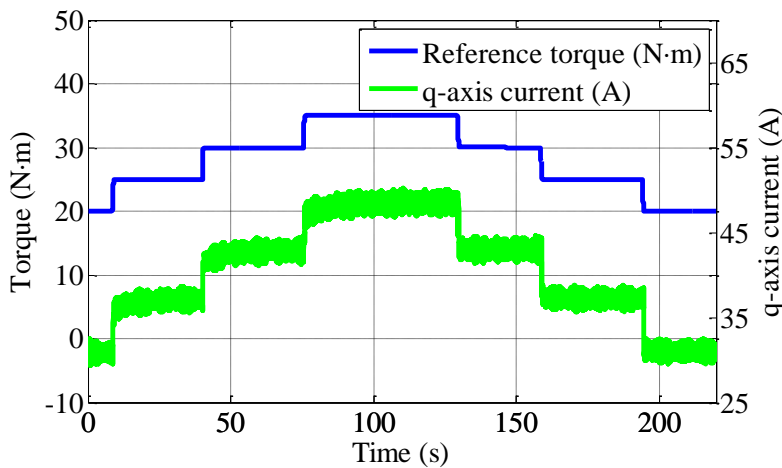


Fig. 4-46. Resultant q-axis current and reference torque.

The measured q-axis current and reference torque under the same operation conditions are shown in Fig. 4-46. Similar improvement in the q-axis current response can also be observed after the proposed control scheme has been trained.

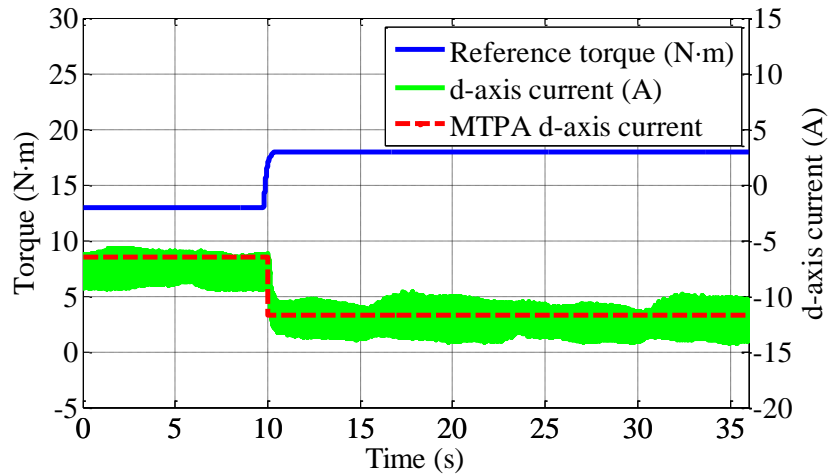


Fig. 4-47. MTPA d-axis current and responses of resultant d-axis current to reference torque change from 13 N·m to 18 N·m.

Further tests were performed by increase in the reference torque from 8 N·m to 28 N·m in a step of 5 N·m at 1000 r/min. Although the control scheme was not trained at these torque commands, Ψ_{SLC} can still be generated accurately according to (4-2).

Fig. 4-47 shows the resultant d-axis current and reference torque when torque command increases from 13 N·m to 18 N·m. As shown in Fig. 4-47, the resultant d-axis current can track the ideal MTPA d-axis currents accurately with fast response although the proposed control scheme has not been trained at 18 N·m torque command previously.

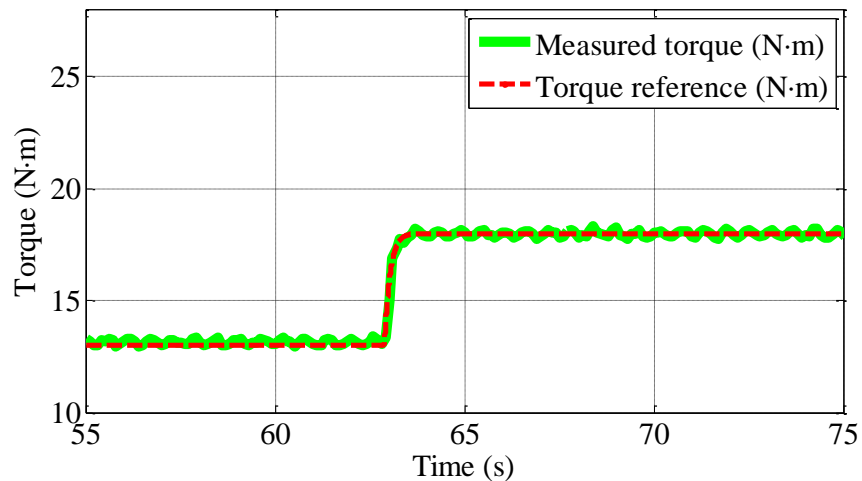


Fig. 4-48. Measured torque in response to reference torque change.

The measured torque and reference torque under the same operation conditions as Fig. 4-47 are compared in Fig. 4-48.

4.3.4.2 Transition between Constant Torque Region and Field Weakening Region

Seamless transition from the constant torque region to field weakening region was also tested. In the field weakening region when v_{error} is smaller than the pre-defined threshold μ , Ψ_{sMTPA} and \mathbf{T}_{MTPA} updates will be stopped. Ψ_{SLC} is still generated from the data recorded in Ψ_{sMTPA} and \mathbf{T}_{MTPA} according to (4-2), however, it will be limited by (1-22) in field weakening region.

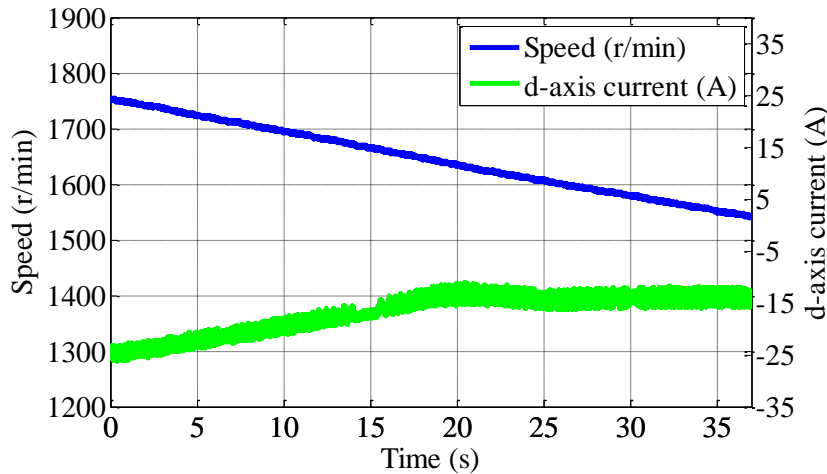


Fig. 4-49. Speed and measured d-axis current during transition from field-weakening region to constant torque region.

Fig. 4-49 illustrates the transition from field weakening region to constant torque region when the reference torque is 20 N·m and speed decreases from 1750 r/min to 1550 r/min. When speed is 1750 r/min, the motor is running in the field weakening. In this condition, Ψ_{SLC} generated from (4-2) is limited by (1-22). As the speed decreases, the resultant d-axis current increases. When the motor enters the constant torque region at the speed of 1640 r/min, the stator flux amplitude or measured d-axis becomes a constant with further reduction in speed. This implies that the transition from the field weakening operation to the constant torque region takes place at 1640 r/min.

Similarly, Fig. 4-50 illustrates the transition from the MTPA operation to the field weakening operation when the reference torque is 20 N·m and the speed is increased from 1550 r/min to 1790 r/min. At the speed of 1550 r/min, the motor operates in the constant

torque region. The d-axis current for the given 20 N·m torque is constant in this region when the speed increases. When the motor enters the field weakening region at 1640 r/min, the resultant d-axis current decreases as the speed is further increased. This indicates that the field weakening control is activated.

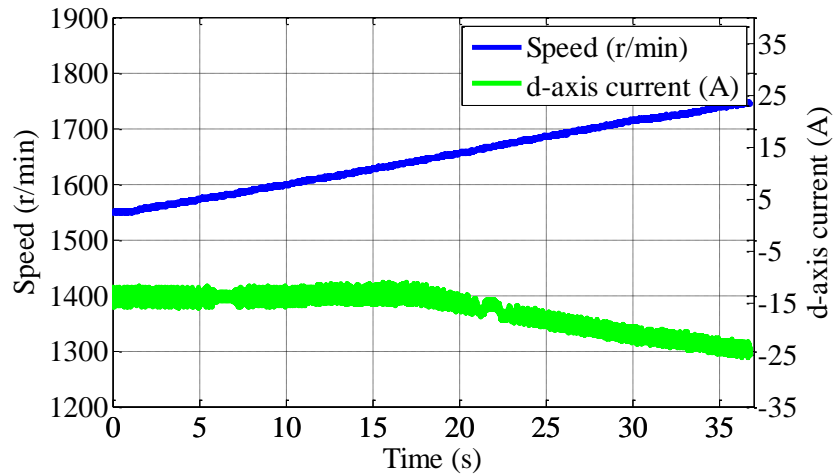


Fig. 4-50. Speed and measured d-axis current during transition from constant torque region to field-weakening region.

4.3.4.3 Performance of Proposed Control Scheme in Deep Field Weakening Region

In the field weakening region, the fast dynamic response of the reference flux amplitude can be achieved by (1-22) directly instead of Ψ_{SLC} . The small error of the reference flux amplitude due to inaccurately observed t- and f-axis currents or the inaccurate nominal stator resistance can be compensated by $\Delta\Psi_s$ as discussed in Chapter 3.

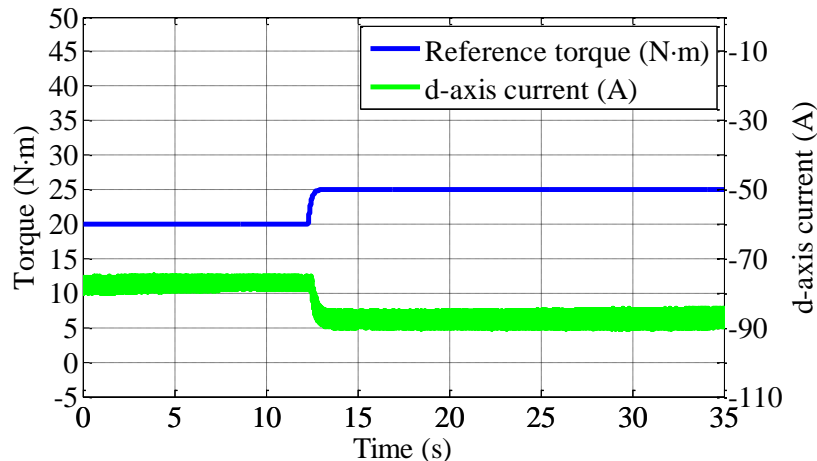


Fig. 4-51. Measured d-axis current and reference torque when torque reference steps from 20 N·m to 25 N·m at 3000 r/min.

Fig. 4-51 shows the measured d-axis current when the reference torque steps from 20 N·m to 25 N·m at 3000 r/min (more than two times base speed). As shown in Fig. 4-51, the fast responses of d-axis current can be observed.

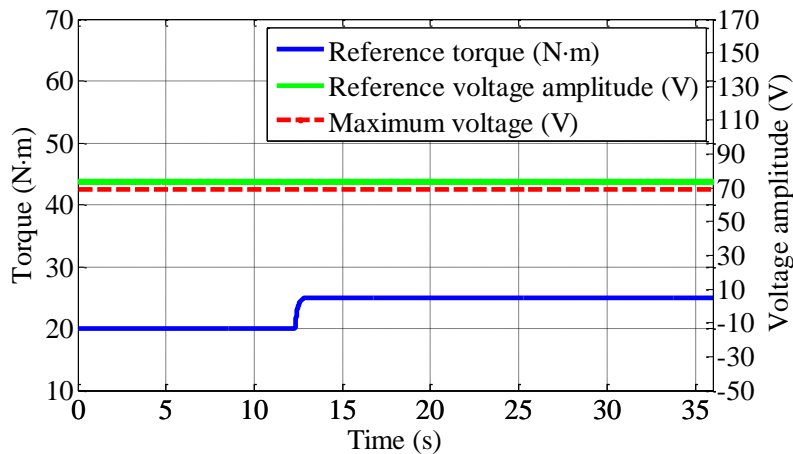


Fig. 4-52. Reference voltage amplitude and reference torque when reference torque steps from 20 N·m to 25 N·m at 3000 r/min.

The reference voltage amplitude and reference torque under the same operation conditions as Fig. 4-51 are shown in Fig. 4-52. As can be seen, the reference voltage amplitude generated from the proposed control is essentially equal to the maximum voltage even during the reference torque change, which illustrates that the motor is controlled on the VCMTPA point. The small error between the reference voltage amplitude and the maximum voltage amplitude is due to the combined effect of flux observer error and voltage drop in the inverter.

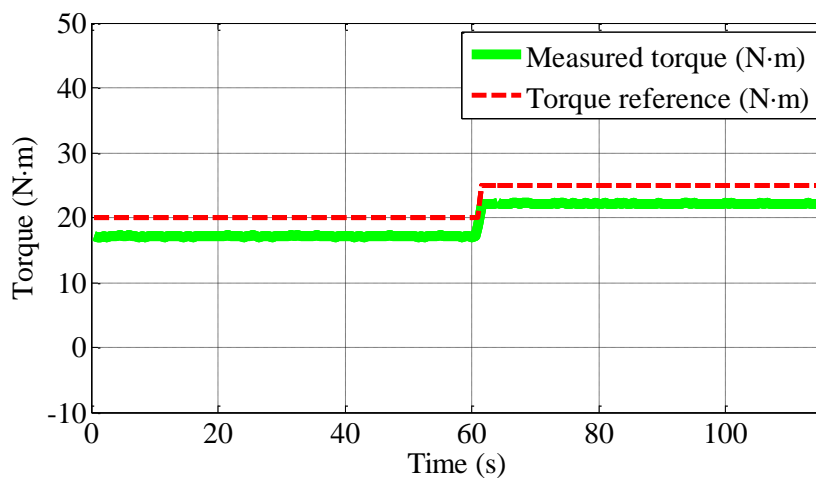


Fig. 4-53. Comparison between reference torque and measured torque when reference torque increased from 20 N·m to 25 N·m at 3000 r/min.

The comparison between the reference torque and the measured torque when the reference torque increased from 20 N·m to 25 N·m at 3000 r/min is shown in Fig. 4-53. The resultant torque response is fast and the gap between the reference and measured torque is due to the flux observer inaccuracy and the frictional torque of the motor.

4.4 Summary

In this chapter, two self-learning control schemes have been proposed in the d-q frame and in the f-t frame, respectively.

The proposed self-learning field orientated control scheme in the d-q frame employs curve fitting to establish the relationship between the torque and the d-axis current for MTPA operation. The proposed control scheme is trained based on the MTPA points tracked by the virtual signal injection control scheme during drive operation. After the proposed control scheme has been trained, the d-axis current command for MTPA operation is directly approximated by the self-learning control scheme for a given reference torque. Meanwhile, the virtual signal injection control scheme can still be utilized to compensate any error between the d-axis current command generated by the SLC and the ideal d-axis current for MTPA operation. The simulation and experiment results show that the proposed SLC scheme can generate accurate d-axis current command to ensure MTPA operation with fast response. The proposed control technique offers accurate MTPA tracking with fast torque response while being independent of machine parameter variations, and hence provides an effective mean for efficient operation of IPMSM drives.

On the other hand, the proposed self-learning direct flux vector control in the f-t frame not only generates accurate optimal reference flux amplitudes for MTPA operation with fast response in constant torque region after training, but also directly limits the flux amplitude for VCMTPA operation in field weakening region with fast response. The proposed control scheme facilitates efficient operation of IPMSM drives without accurate prior knowledge of machine parameters and can adapt to the machine parameter changes based on online training. The performance of the proposed control scheme is verified by simulations and experiments. It has been shown that the transition between the constant torque and field weakening operations is smooth and automatic.

CHAPTER 5 Hybrid Control Scheme

5.1 Introduction

In the previous chapters, control schemes based on the d-q frame and the f-t frame, known as field oriented control (FOC) and direct torque or direct flux vector control (DFVC), respectively, are proposed. In FOC, the d- and q-axis currents are regulated by the d- and q-axis voltages through PI controllers [33], [48], [49]. Since the d- and q-axis currents can be obtained from measured phase currents and rotor positional angle, the FOC can track the d- and q-axis current commands accurately in constant torque region. In field weakening region, due to the voltage limit, the stator flux amplitude should be limited, and this limit is indirectly imposed by setting d-axis current demand as functions of torque and speed based on the machine model. As the machine parameters of an IPMSM are highly nonlinear and uncertain due to cross-coupling effects, material property variation, magnetic saturation and temperature variation [50], [51], it is difficult to model IPMSMs accurately. Hence the limit on the voltage or on the stator flux amplitude for field weakening control cannot be accurately imposed by the d-axis current demand. Moreover, dc-link voltage variations, which could be quite significant in electric vehicle traction drive supplied from batteries, also cause great difficulties in controlling IPMSM in field weakening region. Consequently, the performance of the FOC is compromised in field weakening operation.

On the other hand, f-t frame based DFVC directly regulates the stator flux amplitude by the f-axis voltage and controls the torque by the t-axis voltage through PI controllers [25]–[27]. At high speeds, the flux amplitude can be estimated by a voltage model based flux observer with relative high accuracy [74]. Moreover, in the field weakening region, the maximum reference flux amplitude under voltage constraint can be calculated without machine parameters except for stator resistance [65]. Since the voltage drop across phase resistance is small compared with the maximum voltage, the stator resistance can be assumed as its nominal value. Therefore, the DFVC is not only robust to dc-link voltage variations in field weakening region, but also can directly impose the stator flux amplitude

limit and will have a better performance than the FOC in field weakening region [24], [66]. The performance of DFVC is dependent on the quality of a flux observer. At low speeds, however, due to the inverter nonlinearity, dead time and relatively small voltage amplitude, the voltage model based observer is no longer accurate and a current model based observer is often employed [111], [75]. Since current model based observers rely on the machine model for stator flux estimation, the nonlinearity of the machine model and inaccuracy of its parameters greatly affect the quality of current model based flux observers. Thus, in constant torque region when speed is relatively low, the DFVC scheme is more vulnerable to command and flux observer errors compared with the FOC scheme. Therefore, at low speeds FOC scheme is more desirable than DFVC.

In order to utilize the advantages of the FOC at low speeds and the advantages of DFVC at high speeds, a hybrid control scheme which combines the two control schemes is proposed in this chapter. At low speeds the FOC is adopted, whereas at high speeds, the DFVC is employed. In this way, the proposed control scheme not only inherits the advantages of both the FOC scheme and the DFVC scheme, but also avoids the disadvantages of the two control schemes.

5.2 Principle of the Proposed Hybrid Control Scheme

In this section, the sensitivity of f-t frame based control to errors in the reference flux amplitude and the relationship between (Ψ_s, i_t) and (i_d, i_q) are investigated and discussed.

5.2.1 Sensitivity of f-t Frame Based Control Schemes to Errors in Reference Flux Amplitude

The relationship between d- and q-axis currents, i_d, i_q , and d- and q-axis flux amplitudes, Ψ_d, Ψ_q , is given in (5-1) and (5-2), where L_d, L_q and Ψ_m are the d- and q axis inductances and the flux linkage due to permanent magnets, respectively.

$$\Psi_d = L_d i_d + \Psi_m \quad (5-1)$$

$$\Psi_q = L_q i_q \quad (5-2)$$

According to (5-1) and (5-2), the reference flux amplitude, Ψ_s^* , for MTPA operation can be expressed in (5-3), where Ψ_d^* and Ψ_q^* are the reference d- and q-axis flux amplitudes, respectively. i_d^* and i_q^* are the reference d- and q-axis currents, respectively.

$$\Psi_s^* = \sqrt{(\Psi_d^*)^2 + (\Psi_q^*)^2} = \sqrt{(\Psi_m + L_d i_d^*)^2 + (L_q i_q^*)^2} \quad (5-3)$$

If the reference d-axis current in (5-3) contains a small error, Δi_d^* , the corresponding reference flux amplitude error, $\Delta \Psi_s^*$, can be expressed as:

$$\Psi_s^* + \Delta \Psi_s^* = \sqrt{[\Psi_m + L_d (i_d^* + \Delta i_d^*)]^2 + (L_q i_q^*)^2} \quad (5-4)$$

(5-3) from (5-4) leads to:

$$2(\Psi_s^* + 0.5\Delta \Psi_s^*)\Delta \Psi_s^* = 2[\Psi_m + L_d (i_d^* + 0.5\Delta i_d^*)]L_d \Delta i_d^* \quad (5-5)$$

Since Δi_d^* is small compared with i_d^* and $\Delta \Psi_s^*$ is small compared with Ψ_s^* , (5-5) can be approximated by (5-6).

$$\Psi_s^* \Delta \Psi_s^* \approx [\Psi_m + L_d i_d^*]L_d \Delta i_d^* = \Psi_d^* L_d \Delta i_d^* \quad (5-6)$$

(5-6) can be expressed as:

$$\frac{\Delta \Psi_s^*}{\Psi_s^*} \approx \frac{\Psi_d^*}{\Psi_s^*} \frac{L_d i_d^*}{\Psi_s^*} \frac{\Delta i_d^*}{i_d^*} \quad (5-7)$$

Since $\Psi_s^* > \Psi_d^*$ and $\Psi_s^* \gg (L_d i_d^*)$, $\Delta i_d^*/i_d^*$ will be much larger than $\Delta \Psi_s^*/\Psi_s^*$, which means a relatively small error in the reference flux amplitude would lead to a relative large error in the reference d-axis current and vice versa. Therefore, the MTPA operation is robust to errors in the reference d-axis current but sensitive to errors in the reference flux amplitude. Since the reference flux amplitude and the observed flux always contain errors, the accurate MTPA operations are always difficult to be guaranteed. The relationship between errors in the reference d-axis currents and the corresponding errors in the reference flux amplitudes will be simulated in section 5.4 based on a prototype machine drive described in the previous chapters.

5.2.2 Relationship between d-q Frame Based Control and f-t Frame Based Control

The main idea of the proposed hybrid control scheme is to take the advantages of FOC and DFVC, i.e., employ FOC to achieve MTPA operation and adopt DFVC to achieve

field weakening operation. In order to combine the two control schemes formulated in the d-q and f-t reference frames, discussion of the relationship between the d-q frame based control and the f-t frame based control is insightful. This relationship is expressed in (5-1) to (5-3) and (5-8) to (5-10). δ is the angular displacements of the f-axis with respected to the d-axis. i_t and i_f are the t- and f-axis currents, respectively.

$$\delta = \text{actan}\left(\frac{\Psi_q}{\Psi_d}\right) \quad (5-8)$$

$$i_t = i_q \cos \delta - i_d \sin \delta \quad (5-9)$$

$$i_f = i_d \cos \delta + i_q \sin \delta \quad (5-10)$$

$$T_e = \frac{3}{2}p(\Psi_d i_q - \Psi_q i_d) = \frac{3}{2}p\Psi_s i_t \quad (5-11)$$

In steady state when the voltage drop in the phase resistance is neglected, the d- and q-axis voltages, v_d , v_q , can be simplified as (5-12) and (5-13) where ω_m is the rotor speed and p is the number of pole pairs.

$$v_q = p\omega_m L_d i_d + p\omega_m \Psi_m \quad (5-12)$$

$$v_d = -p\omega_m L_q i_q \quad (5-13)$$

Based on (5-12) and (5-13), the relationship between voltage amplitude, v_a , and d- and q-axis currents can be expressed in (5-14).

$$v_a^2 = (p\omega_m L_q i_q)^2 + (p\omega_m L_d i_d + p\omega_m \Psi_m)^2 \quad (5-14)$$

The relationship between voltage amplitude and flux amplitude, Ψ_s , can be expressed in (5-15).

$$v_a = p\omega_m \Psi_s \quad (5-15)$$

As expressed in (5-14), in the d-q frame, for given speed and voltage amplitudes, the d- and q-axis current locus is an ellipse. By substitution of (5-15) into (5-14), the ellipse also can be expressed in a standard form of (5-16). As can be seen from (5-16), if Ψ_m , L_d and L_q are assumed to be constant, the shape and location of the ellipse in the d-q frame actually only depends on flux amplitude, therefore, the ellipse is the constant flux amplitude locus.

$$\frac{\left(i_d + \frac{\Psi_m}{L_d}\right)^2}{\left(\frac{\Psi_s}{L_d}\right)^2} + \frac{i_q^2}{\left(\frac{\Psi_s}{L_q}\right)^2} = 1 \quad (5-16)$$

The diagram of constant flux amplitude locus and constant torque locus are shown in Fig. 5-1. The center of the constant flux amplitude locus is at the point given by $(-\Psi_m/L_d,$

0). The tangential point between a constant torque locus and a constant flux amplitude locus, e.g., point A, is the maximum torque per voltage (MTPV) point [26]. The MTPV locus, A-C-E, is also shown in Fig. 5-1.

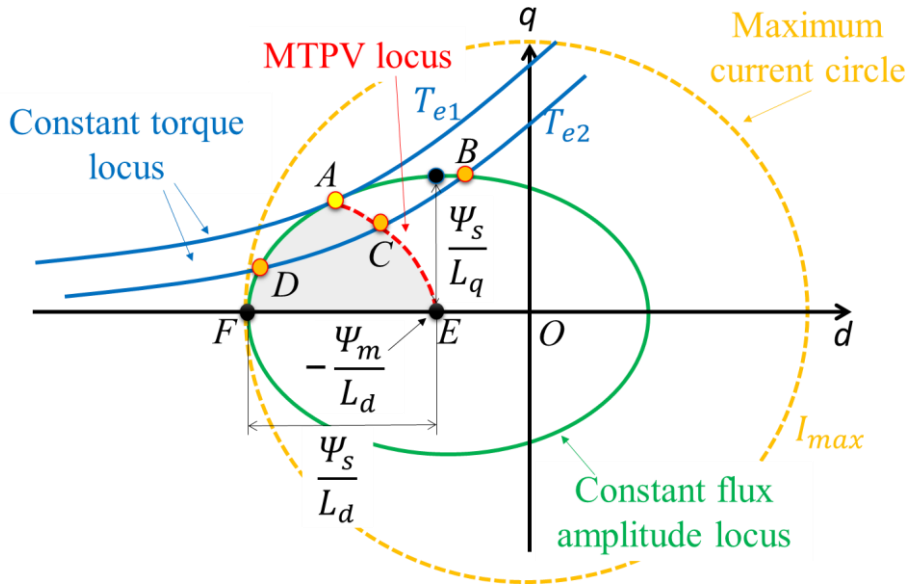


Fig. 5-1. Voltage ellipse, current limit circle, MTPV locus and constant torque locus.

As shown in Fig. 5-1, there are, in general, at most two intersections between a constant torque locus and a constant flux amplitude locus. One intersection is on the left hand side of the MTPV locus and the other one is on the right hand side of the MTPV locus. However, the operation point which is on the left hand side of the MTPV locus should be avoided through limiting the t-axis current [25]–[27]. Since the motor should be controlled either on the right hand side of the MTPV locus or on the MTPV locus, the relationship between Ψ_s , i_t and i_d , i_q under the direct flux vector control is unique.

In direct flux vector control, as mentioned in [25]–[27], the motor’s flux amplitude and t-axis current are controlled through the f- and t-axis voltages. The observed flux amplitude, $\hat{\Psi}_s$, and t-axis current, \hat{i}_t , can be expressed in (5-17) and (5-18) with measured i_d and i_q , respectively.

$$\hat{\Psi}_s^2 = (L_d i_d + \Psi_m)^2 + (L_q i_q)^2 \tag{5-17}$$

$$\hat{i}_t = \frac{\frac{3p}{2} [\Psi_m i_{qm} + (L_d - L_q) i_q i_d]}{\hat{\Psi}_s} \tag{5-18}$$

In steady state, the observed flux amplitude and t-axis current should equal the reference flux amplitude and t-axis current as expressed in (5-19) and (5-20).

transitions between the two control strategies are realized by adopting a unified control structure in the form of the DFVC.

As shown in Fig. 5-2, the proposed control scheme consists of two main control loops, the stator flux control loop and the t-axis current control loop. Limits on the reference flux amplitude, Ψ_s^* , and the reference t-axis current, i_t^* , are imposed in the same manner as described in [26]. However, Ψ_s^* and i_t^* can either be generated from reference d- and q-axis currents via Look-up table I for FOC or from Look-up table II for DFVC, depending on rotor speeds. The details of the proposed control scheme will be discussed below.

5.3.1 FOC at Low Speed

When the motor operates at low speeds, the FOC can be achieved through the DFVC structure due to the unique mapping between (Ψ_s, i_t) and (i_d, i_q) discussed in section 5.2.2. As shown in Fig. 5-2, when ω_m is below a pre-defined value ω_1 , (Ψ_s^*, i_t^*) is equal to $(\Psi_{sFOC}^*, i_{tFOC}^*)$ and $(\hat{\Psi}_m, \hat{i}_t)$ is equal to $(\hat{\Psi}_{sFOC}, \hat{i}_{tFOC})$, where Ψ_s^* and i_t^* are the reference flux amplitude and reference t-axis current, respectively. Ψ_{sFOC}^* and i_{tFOC}^* are the reference flux amplitude and reference t-axis current calculated from (5-1) to (5-3) and (5-8), (5-9) based on the reference d- and q-axis currents, i_d^* and i_q^* , respectively. $\hat{\Psi}_m$ and \hat{i}_t are the observed flux amplitude and t-axis current, respectively. $\hat{\Psi}_{sFOC}$ and \hat{i}_{tFOC} are the flux amplitude and t-axis current calculated from (5-1) to (5-3) and (5-8), (5-9) based on measured d- and q-axis currents, i_d and i_q , respectively. $\hat{\delta}_{FOC}$ is the observed angle between d-axis and f-axis based on current based flux observer through (5-8).

For a given torque command, T_e^* , the Look-up table I generates the optimal reference d- and q-axis current commands, i_d^* and i_q^* , for MTPA operation. The resultant optimal i_d^* and i_q^* will be further converted into Ψ_{sFOC}^* and i_{tFOC}^* through (5-1) to (5-3), (5-8) and (5-9) based on the nominal machine parameters, L_d, L_q, Ψ_m of the machine. In steady state, $(\Psi_{sFOC}^*, i_{tFOC}^*)$ will be equal to $(\hat{\Psi}_{sFOC}, \hat{i}_{tFOC})$. Due to the unique relationship between $(\Psi_{sFOC}^*, i_{tFOC}^*)$ and (i_d^*, i_q^*) as well as the unique relationship between $(\hat{\Psi}_{sFOC}, \hat{i}_{tFOC})$ and the measured d- and q-axis currents, (i_d, i_q) , when $(\Psi_{sFOC}^*, i_{tFOC}^*)$ equals to $(\hat{\Psi}_{sFOC}, \hat{i}_{tFOC})$, the actual d- and q-axis currents (i_d, i_q) will be equal to the reference d-

and q-axis currents, (i_d^*, i_q^*) . It is worth noting that due to modelling error, Ψ_{sFOC}^* and i_{tFOC}^* calculated from the nominal machine parameters may deviate from the optimal flux amplitude and t-axis current for MTPA operation. However, the deviations will be compensated by the current model based flux observer in which $\hat{\Psi}_{sFOC}$ and \hat{i}_{tFOC} are also generated according to (5-1) to (5-3) and (5-8), (5-9) based on the same nominal machine parameters as those used in the generation of Ψ_{sFOC}^* and i_{tFOC}^* . As a result, (i_d, i_q) will always follow (i_d^*, i_q^*) .

It follows that the d- and q-axis currents can be controlled through calculated flux amplitude and t-axis current, Ψ_{sFOC}^* and i_{tFOC}^* . This control scheme essentially controls the d- and q-axis currents and is equivalent to the FOC. In this way, the sensitiveness of MTPA operation to the reference flux amplitude and flux observer errors of the f-t frame based control scheme can be avoided.

However, in field weakening region, the stator flux amplitude cannot be limited accurately due to the flux estimation errors based on the nominal machine parameters, and the reference d- and q-axis currents generated from Look-up table I are difficult to cope with dc-link voltage variations. This will deteriorate field weakening performance. Therefore, at high speed, especially for field weakening control, DFVC is preferable.

5.3.2 DFVC at High Speed

In order to overcome the problems associated to the FOC, the DFVC is adopted at high speeds. However, other kinds of f-t frame based control schemes are also possible. When the motor operates at high speeds, the voltage drops on the stator resistance and inverter are relatively small compared with the voltage amplitude, and the stator resistance can be assumed as its nominal value. In this case, as shown in Fig. 5-2, when ω_m is above a pre-defined value ω_2 , the proposed control scheme switches to the conventional DFVC proposed in [25]–[27]. The optimal reference flux amplitude, Ψ_{sDFVC}^* , for MTPA control is generated from Look-up table II with the reference torque as its input. The reference t-axis current, i_{tDFVC}^* , is calculated from (1-25) based on Ψ_{sDFVC}^* . (Ψ_s^*, i_t^*) is equal to $(\Psi_{sDFVC}^*, i_{tDFVC}^*)$ while $(\hat{\Psi}_s, \hat{i}_t)$ is equal to $(\hat{\Psi}_{sDFVC}, \hat{i}_{tDFVC})$, where, the $\hat{\Psi}_{sDFVC}$ and \hat{i}_{tDFVC} are the observed flux amplitude and t-axis current by conventional flux observer described in section 0. $\hat{\delta}_{DFVC}$ is the observed angle between d-axis and f-axis by

conventional flux observer based on (5-8). The stator flux vector and t-axis current can be observed by the flux observer with higher accuracy since the voltage amplitude is relatively large [75]. In this way, accurate DFVC can be achieved. Since the field weakening control can be directly achieved by limiting the reference flux amplitude through (1-22) in Chapter 1, the proposed control scheme inherits the advantages of the f-t frame based control schemes in field weakening region.

5.3.3 Transition between FOC and DFVC

As described previously, for a given reference torque, two pairs of reference flux amplitudes, $(\Psi_{sFOC}^*, \Psi_{sDFVC}^*)$, and reference t-axis currents, $(i_{tFOC}^*, i_{tDFVC}^*)$, are generated for the FOC and the DFVC, respectively. In order to have a smooth transition between the two control schemes, a transition region, from ω_1 to ω_2 , or vice versa, is defined as shown in Fig. 5-3.

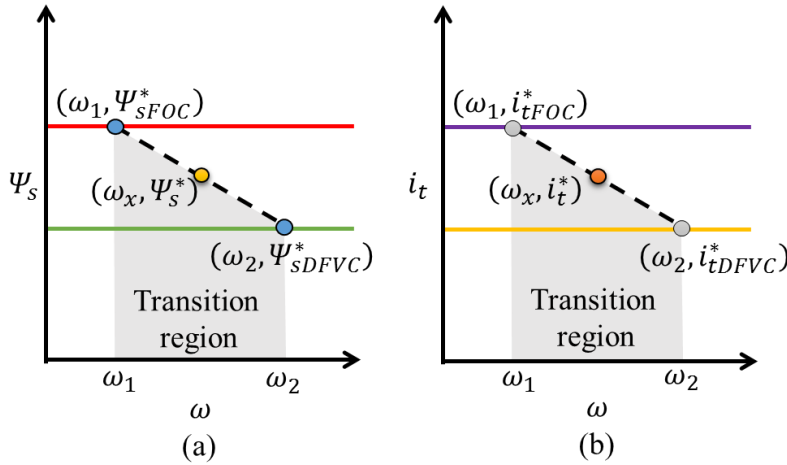


Fig. 5-3. Linear interpolation in transition region.

When the speed is below ω_1 , Ψ_{sFOC}^* and i_{tFOC}^* generated for the FOC are adopted as the reference flux amplitude and t-axis current, respectively. When the speed is above ω_2 , Ψ_{sDFVC}^* and i_{tDFVC}^* generated for the DFVC are adopted. For a given speed ω_x between the two, i.e., $\omega_1 < \omega_x < \omega_2$, the reference flux amplitude and t-axis current can be generated from the linear interpolation given in (5-21) and (5-22), respectively.

$$\Psi_s^* = \frac{\omega_2 - \omega_x}{\omega_2 - \omega_1} \Psi_{sFOC}^* + \frac{\omega_x - \omega_1}{\omega_2 - \omega_1} \Psi_{sDFVC}^* \quad (5-21)$$

$$\hat{i}_t^* = \frac{\omega_2 - \omega_x}{\omega_2 - \omega_1} \hat{i}_{tFOC}^* + \frac{\omega_x - \omega_1}{\omega_2 - \omega_1} \hat{i}_{tDFVC}^* \quad (5-22)$$

Similarly, two different observers, i.e., current model based flux observer and conventional flux observer shown in Fig. 1-19, are employed in the feedback loops of the proposed control scheme. When the speed is below ω_1 , the observed $\hat{\Psi}_s$ and \hat{i}_t are equal to the outputs of the current model based observer, $\hat{\Psi}_{sFOC}$ and \hat{i}_{tFOC} , respectively. When the speed is above ω_2 , $\hat{\Psi}_s$ and \hat{i}_t are equal to the outputs of the conventional observer, $\hat{\Psi}_{sDFVC}$ and \hat{i}_{tDFVC} , respectively. If the speed is between the two, $\hat{\Psi}_s$ and \hat{i}_t are generated from the linear interpolation given in (5-23) and (5-24).

$$\hat{\Psi}_s = \frac{\omega_2 - \omega_x}{\omega_2 - \omega_1} \hat{\Psi}_{sFOC} + \frac{\omega_x - \omega_1}{\omega_2 - \omega_1} \hat{\Psi}_{sDFVC} \quad (5-23)$$

$$\hat{i}_t = \frac{\omega_2 - \omega_x}{\omega_2 - \omega_1} \hat{i}_{tFOC} + \frac{\omega_x - \omega_1}{\omega_2 - \omega_1} \hat{i}_{tDFVC} \quad (5-24)$$

Therefore, a smooth transition between the two control schemes can be achieved.

5.4 Simulation Results

The d- and q-axis inductances and the permanent magnet flux linkage of the machine are highly non-linear and vary significantly with currents because of magnetic saturation. ξ in the conventional flux observer introduced in Chapter 1 is set to 0.707 while ω_0 is set to 50π rad/s which corresponds to 500 r/min rotor speed since the accuracy of the voltage model based observer is satisfactory above this speed. Moreover, given that the upper-limit of the transition speed should be below the based speed, ω_1 and ω_2 in Fig. 5-3 are set to 800 r/min and 900 r/min, respectively. L_d , L_q and Ψ_m in (5-1) and (5-2) are set to their nominal values, i.e., 0.64 mH, 1.84 mH and 0.1132 Wb, respectively. The MTPA look-up table I and II in Fig. 5-2 are obtained from the high fidelity nonlinear IPMSM machine model [13].

5.4.1 FOC Performance in DFVC Frame

In order to verify the FOC performance achieved in DFVC frame when speed is below ω_1 , simulations were performed by varying d- and q-axis reference currents from 0 A to

the maximum current, i.e., 120 A, at 100 r/min, repetitively. The simulation results of the reference and resultant d- and q-axis currents of the proposed control scheme are shown in Fig. 5-4. It can be seen from Fig. 5-4, the resultant d- and q-axis currents always follow the reference d- and q-axis currents accurately, which demonstrates that the reference d- and q-axis current can be controlled through Ψ_s^* and i_t^* .

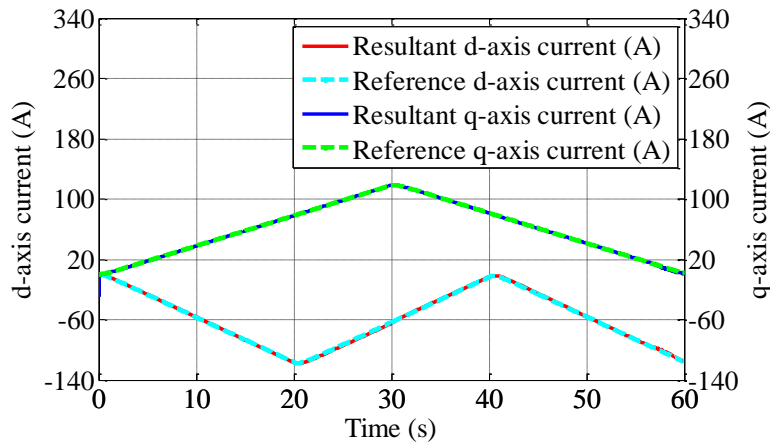


Fig. 5-4. Reference and resultant d- and q-axis currents of the proposed control scheme at 100 r/min.

5.4.2 Performance of the Proposed Control Scheme during Speed and Torque Changing

In order to verify the performance of the proposed hybrid control scheme during speed and torque changes, simulations were performed with the rotor speed stepped from 100 r/min ($<\omega_1$) to 1000 r/min ($>\omega_2$) in every 5 seconds before $t=30$ s. After $t=30$ s, the rotor speed varied between ω_1 and ω_2 , i.e., from 810 r/min to 890 r/min in every 5 seconds. In this way, the proposed control scheme switched between FOC mode and DFVC mode repeatedly before $t=30$ s and the rotor speed stepped continuously in the transition region after $t=30$ s. Moreover, the reference torque stepped from 10 N·m to 50 N·m in every 10 s. The resultant torque, reference torque and rotor speed are shown in Fig. 5-5. As shown in Fig. 5-5, the resultant torque always follows the reference torque regardless of whether the control mode is switched or the rotor speed varies in the transition region. It is worth noting that for most applications, electric vehicle traction in particular, a step change in speed cannot occur due to drive system inertia or large mass. Therefore, conditions which are worse than that illustrated in Fig. 5-5 will not occur practically.

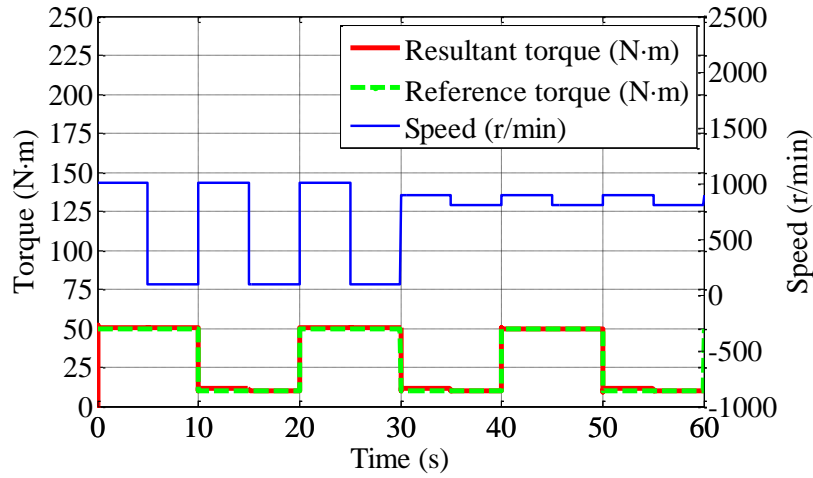


Fig. 5-5. The resultant torque, reference torque and rotor speed when rotor speed and torque varies.

5.4.3 Control Performance in Transition Region

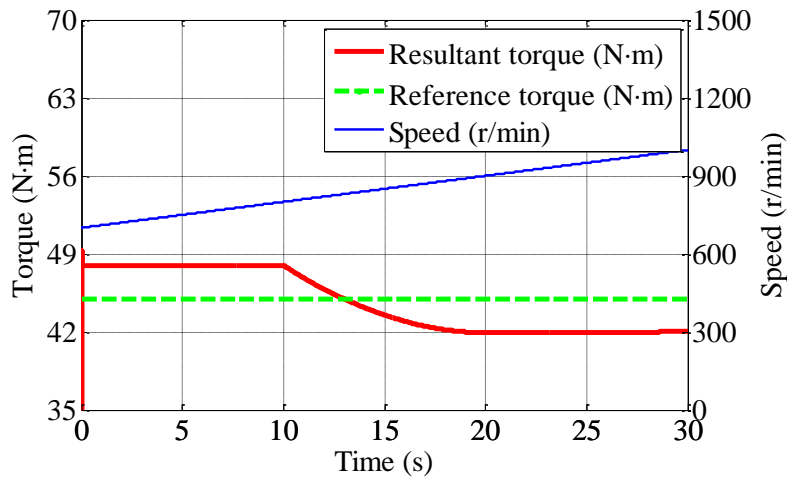


Fig. 5-6. Control performance of the proposed hybrid control scheme in transition region.

The control performance of the proposed hybrid control scheme in the transition region was also studied by simulations. The reference torque was set to 45 N·m and rotor speed varied from 700 r/min ($<\omega_1$) to 1000 r/min ($>\omega_2$) gradually. Errors were deliberately injected in i_q^* and i_{DFVC}^* of Fig. 5-2 so that when the motor was controlled in the FOC mode, the resultant torque was 48 N·m. Whereas when the motor was controlled in the DFVC mode, the resultant torque was 42 N·m. The simulation result of the proposed control scheme is shown in Fig. 5-6. As can be seen, when the rotor speed is below ω_1 , the motor is controlled in the FOC mode, the resultant torque is 48 N·m. When the rotor speed is above ω_2 , the motor is controlled in DFVC mode and the resultant torque is 42

N·m. When the rotor speed is between ω_1 and ω_2 , i.e., in the transition region, the resultant torque is between 48 N·m and 42 N·m.

5.4.4 Comparison between Proposed Control and DFVC

In the literature, the MTPA operation of FOC is mainly achieved by controlling the reference d-axis current [49] while the MTPA operation of the f-t frame based control is achieved by controlling reference flux amplitude [25]–[27]. According to the analysis described in section 5.2.1, even a small deviation in Ψ_s^* will cause a relatively large deviation in i_d^* and vice versa. Thus, the d-q frame based control is more robust for MTPA operations than f-t frame based schemes and the FOC is preferable than f-t frame based control in constant torque region. To illustrate this, simulations were performed by initially setting i_d^* in Fig. 5-2 to the optimal value for MTPA operation when the reference torque and the speed were set to 45 N·m and 400 r/min ($<\omega_1$), respectively. The resultant Ψ_s^* was calculated through (5-1) to (5-3). Therefore, Ψ_s^* was the optimal flux amplitude for the MTPA operation. Then, deviations were injected into the optimal i_d^* and the corresponding deviations in Ψ_s^* were calculated. In order to eliminate other factors which may affect the comparison, L_d , L_q and Ψ_m in (5-1) to (5-3) were set to the same values as the corresponding machine parameters in the motor model and i_d^* in Fig. 5-2 was obtained from (2-15). In this way, the resultant torque was kept constant.

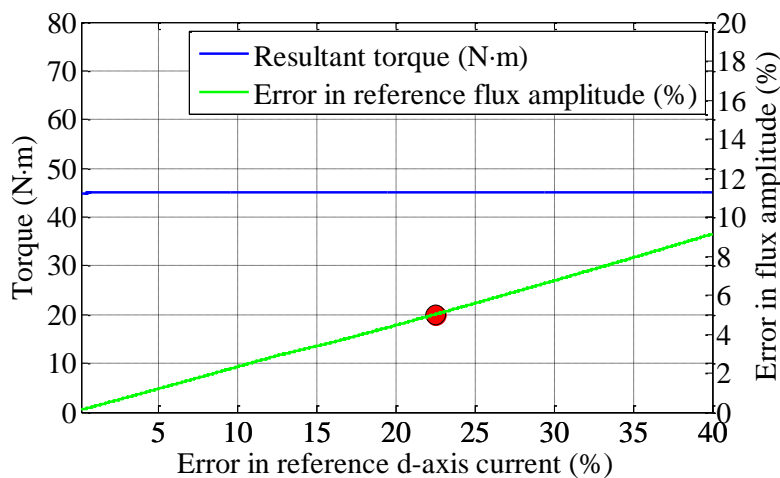


Fig. 5-7 Comparison between the percentage errors in i_d^* and the corresponding percentage errors in Ψ_s^* when speed is 400 r/min and reference torque is 45 N·m.

The comparison between the percentages of deviation in i_d^* and the corresponding percentages of deviation in Ψ_s^* and the resultant torque are shown in Fig. 5-7. As can be seen from Fig. 5-7, a 5% deviation in Ψ_s^* corresponds to the 22.5% deviation in i_d^* . Since f-t frame based control schemes always suffer from sensitiveness to errors in both Ψ_s^* and $\hat{\Psi}_s$, the proposed hybrid control is more suitable than DFVC for IPMSM drives in constant torque region.

The motor efficiencies with different percentage errors in the reference d-axis currents and in the reference flux amplitudes at 1200 r/min and 50 N·m are listed in Table 5-1.

Table 5-1
Motor efficiency with different errors in reference flux amplitude and reference d-axis currents

Reference d-axis current	Error in reference d-axis current	Reference flux amplitude	Error in reference flux amplitude	Efficiency
-50.39 A	0 %	0.1416 Wb	0 %	91.87 %
-45.35 A	10 %	0.1451 Wb	2.46 %	91.82 %
-40.31 A	20 %	0.1485 Wb	4.83 %	91.65 %
-35.27 A	30 %	0.1511 Wb	6.71 %	91.41 %
-30.23 A	40 %	0.1543 Wb	8.91 %	91.06 %
-28.05 A	44.3 %	0.1558 Wb	10.00 %	90.87 %

As can be seen from Table 5-1, the motor efficiency is very sensitive to the reference flux amplitude error. A 10 % error in the reference flux amplitude causes the motor efficiency drop by 1 %, while a 10 % error in reference d-axis current only causes motor efficiency drop by 0.05 %. Similarly, the motor efficiency is also very sensitive to errors in the observed flux amplitude. Therefore, in constant torque region, accurate MTPA operation is very difficult to be guaranteed with DFVC schemes.

5.5 Experimental Results

Experiments were performed based on the test rig adopted in Chapter 2. The L_d , L_q and Ψ_m in (5-1), (5-2) and in the flux observer introduced in Chapter 1 were again set to their nominal values, i.e., 0.64 mH, 1.84 mH and 0.1132 Wb, respectively. The MTPA look-up table I and II in Fig. 5-2 were the same as those used in the simulations. ξ and ω_0 in the conventional closed loop flux observer shown in Fig. 1-19 were set to 0.707 and 50π rad/s, respectively. ω_1 and ω_2 in Fig. 5-3 were set to 800 r/min and 900 r/min, respectively.

5.5.1 FOC at Low Speed

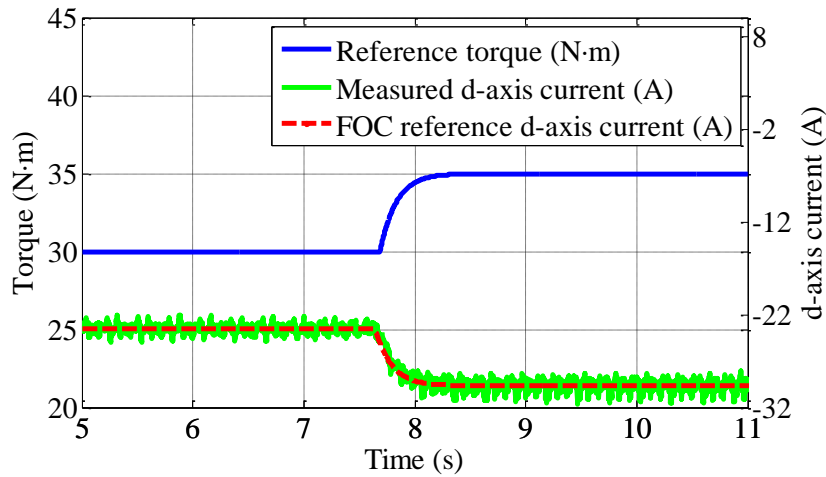


Fig. 5-8. Reference torque, FOC reference d-axis current and measured d-axis current at 400 r/min.

The test was first carried out when the speed was below 800 r/min, and the motor was effectively controlled by the FOC scheme through the f-t frame based DFVC. To illustrate the performance of the proposed control scheme, the motor drive was tested at 400 r/min with step changes in reference torque. Fig. 5-8 shows the reference d-axis current and measured d-axis current when the reference torque steps from 30 N·m to 35 N·m at 400 r/min. As can be seen, the measured d-axis current follows the reference d-axis current generated under the FOC accurately.

The reference and measured q-axis currents under the same operating conditions as Fig. 5-8 are compared in Fig. 5-9. The accurate q-axis current control can also be observed. The measured torque is shown in Fig. 5-14.

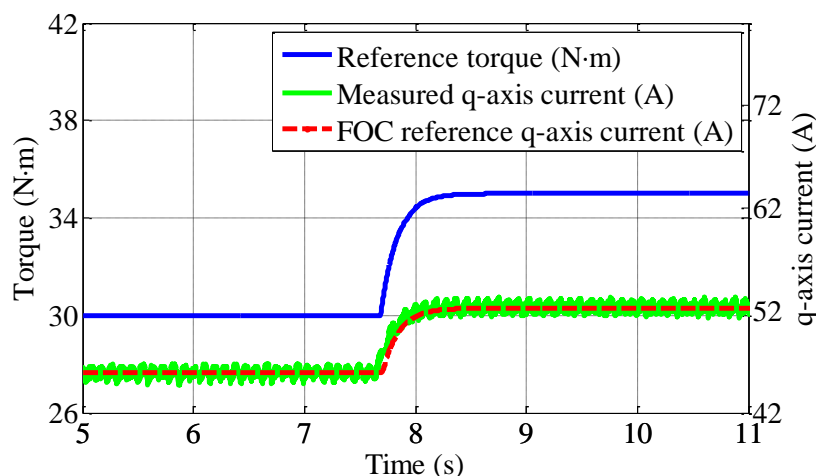


Fig. 5-9. FOC reference q-axis current, measured q-axis current and reference torque at 400 r/min.

5.5.2 Transition between FOC and DFVC

When the motor is operating in the transition region, i.e., between 800 r/min and 900 r/min, the proposed control scheme is a linear combination of the FOC scheme and the DFVC scheme through (5-21)-(5-24).

To verify the performance of the proposed control scheme in the transition region, the motor drive was tested at 850 r/min. Fig. 5-10 shows the reference d-axis current, i_d^* , generated by the look-up table I in Fig. 5-2 and the measured d-axis current when the reference torque changes in a step from 30 N·m to 35 N·m. Due to the modelling errors, $(\Psi_{sFOC}^*, i_{tFOC}^*)$ is not equal to $(\Psi_{DFVC}^*, i_{tDFVC}^*)$. According to (5-21) and (5-22) the reference d-axis current corresponding to $(\Psi_{sFOC}^*, i_{tFOC}^*)$ is different from that corresponding to (Ψ_s^*, i_t^*) . Hence, the resultant d-axis current of the proposed control scheme in transition region is not equal to i_d^* generated by look-up table I as shown in Fig. 5-10. However, in transition region, since the proposed hybrid control scheme directly controls (Ψ_s^*, i_t^*) which are calculated from (5-21) and (5-22), and therefore, even (Ψ_s^*, i_t^*) is different from $(\Psi_{sFOC}^*, i_{tFOC}^*)$ or $(\Psi_{sDFVC}^*, i_{tDFVC}^*)$, the motor's flux amplitude and t-axis current can be still controlled through (Ψ_s^*, i_t^*) . The relatively large d-axis current ripple in Fig. 5-10 is due to the inverter voltage drop which causes additional harmonics to voltage model based flux observer in Fig. 1-19. The measured torque is shown in Fig. 5-14.

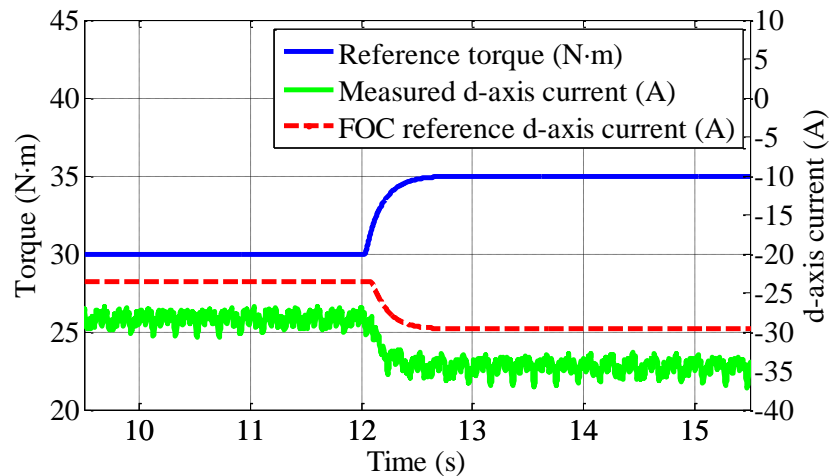


Fig. 5-10. Reference torque, measured d-axis current and FOC reference d-axis current (i_d^*) at 850 r/min.

Fig. 5-11 shows the observed flux amplitude, $\hat{\Psi}_s$, of the proposed control scheme and Ψ_{sDFVC}^* (from look-up table II) under the same operating condition as in Fig. 5-10. Similarly, the observed flux amplitude of the proposed control scheme, in the transition region, is also not equal to Ψ_{sDFVC}^* .

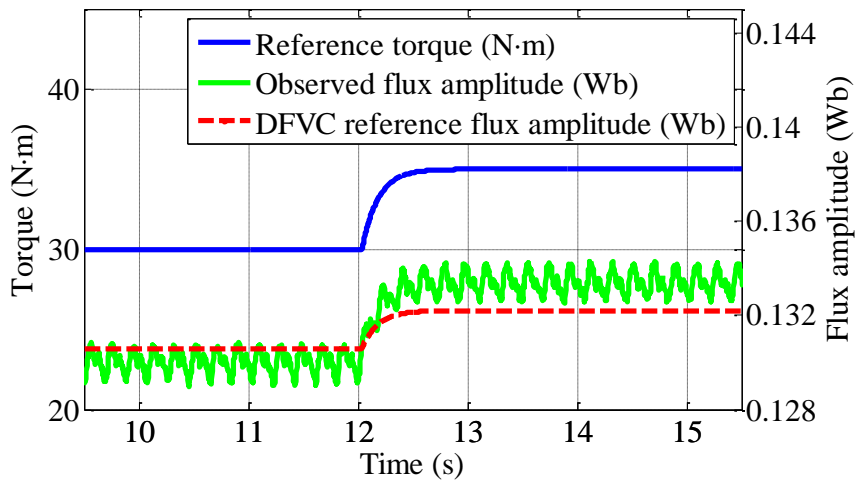


Fig. 5-11. Reference torque, observed flux amplitude and DFVC reference flux amplitude at 850 r/min.

Tests were also performed by varying speed from 1100 r/min to 400 r/min and back to 1100 r/min with 20 N·m reference torque. As shown in Fig. 5-12, smooth transitions from the DFVC to the FOC and vice versa can be observed. During the transitions, the measured torque is kept essentially constant.

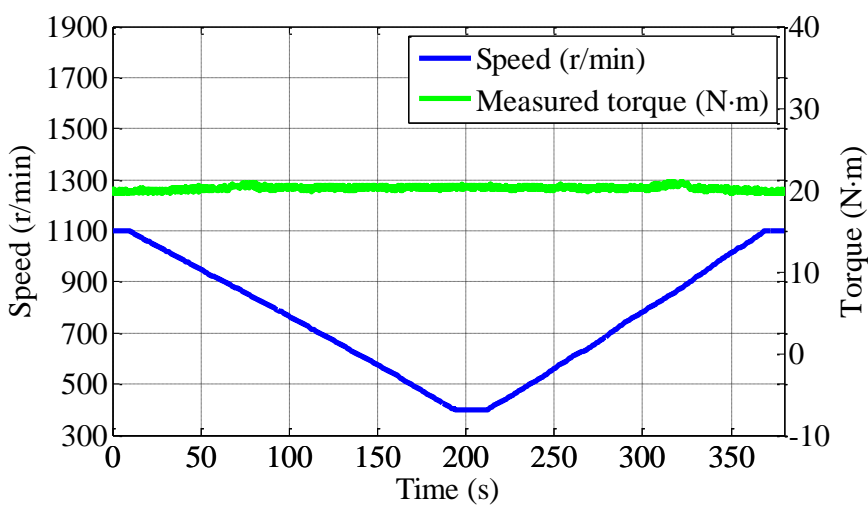


Fig. 5-12. Transitions between DFVC and FOC with 20 N·m reference torque.

5.5.3 DFVC at High Speed

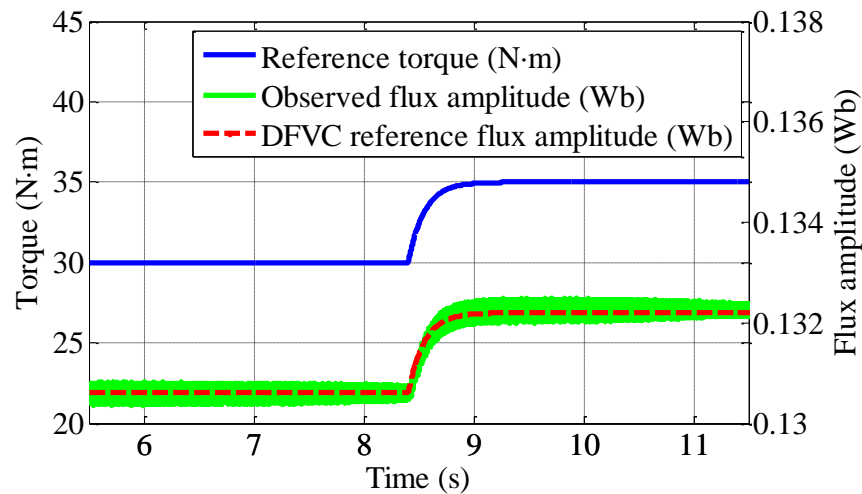


Fig. 5-13. Reference torque, observed flux amplitude and DFVC reference flux amplitude, Ψ_{DFVC}^* , at 1000 r/min.

When speed is above 900 r/min, the proposed control scheme becomes a conventional DFVC as proposed in [25]–[27]. To illustrate the performance of the proposed control scheme, the motor drive was tested at 1000 r/min. Fig. 5-13 shows the observed flux amplitude and reference flux amplitude of the proposed control scheme when the reference torque steps from 30 N·m to 35 N·m. As shown in Fig. 5-13, because the motor drive is only controlled by the DFVC, the observed flux amplitude follows the DFVC reference flux amplitude, Ψ_{DFVC}^* , accurately. The measured torque is shown in Fig. 5-14.

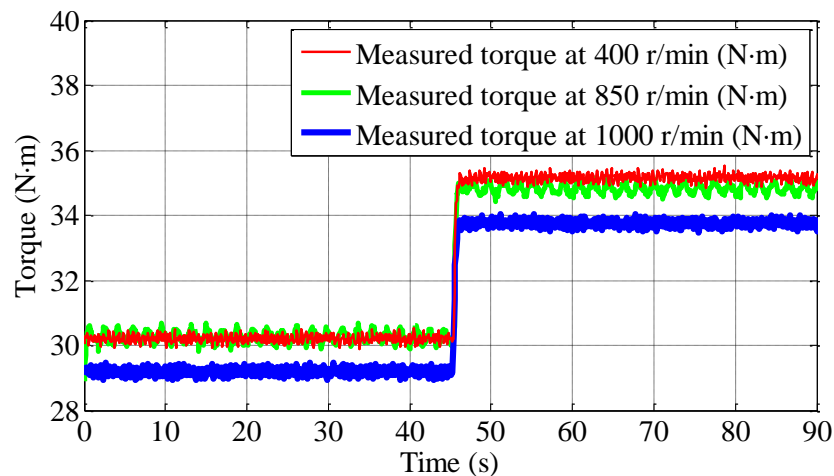


Fig. 5-14. Measured torque at 400 r/min, measured torque at 850 r/min and measured torque at 1000 r/min when torque reference steps from 30 N·m to 35 N·m.

Fig. 5-14 shows the measured torque when reference torque steps from 30 N·m to 35 N·m at 400 r/min, 850 r/min and 1000 r/min, respectively. As shown in Fig. 5-14, the resultant torques in transition region ($\omega_m=850$ r/min) are always between the torques under the FOC and DFVC due to the fact that (Ψ_s^*, i_t^*) and $(\hat{\Psi}_s, \hat{i}_t)$ are calculated from (5-21) to (5-24). The measured torques are slightly lower than the references due to reasons mentioned before.

5.5.4 Field Weakening Control

In the field weakening region, the rotor speed is above ω_2 , conventional DFVC is adopted by the proposed control scheme and the stator flux amplitude is directly limited by (1-22) in Chapter 1. The performance of the proposed control scheme in field weakening region was tested by experiments. Fig. 5-15 shows the reference torque, reference flux amplitude and observed flux amplitude when the reference torque steps from 25 N·m to 30 N·m at 2700 r/min (two times the based speed). As shown in Fig. 5-15, since the motor is controlled by the DFVC, the reference flux amplitude is equal to the observed flux amplitude.

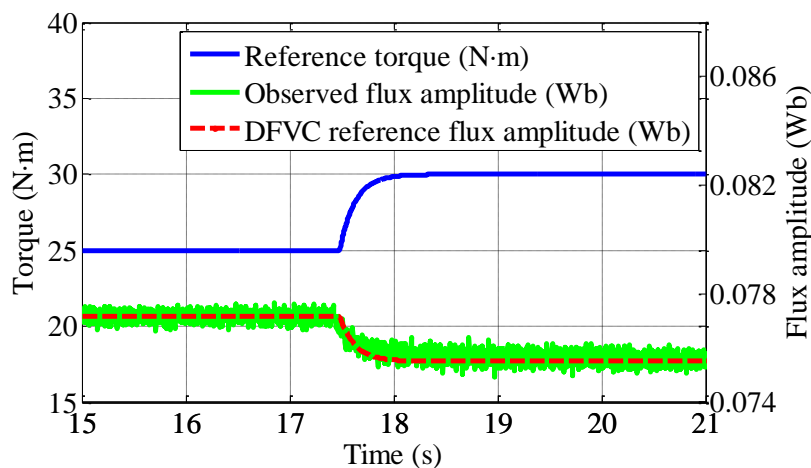


Fig. 5-15. Reference torque, reference flux amplitude and observed flux amplitude at 2700 r/min.

Fig. 5-16 shows the reference torque and measured torque when the reference torque steps from 25 N·m to 30 N·m at 2700 r/min. The gap between the reference and measured torques is due to the reasons mentioned before.

Fig. 5-17 shows the resultant voltage amplitude, the maximum voltage amplitude and the resultant d-axis current under the same operating condition as in Fig. 5-16. According

to Fig. 5-16 and Fig. 5-17, although errors can be observed in the resultant torque, the resultant voltage amplitude is always kept at the maximum voltage amplitude; therefore, the proposed control scheme inherits the advantages of the DFVC in field weakening region.

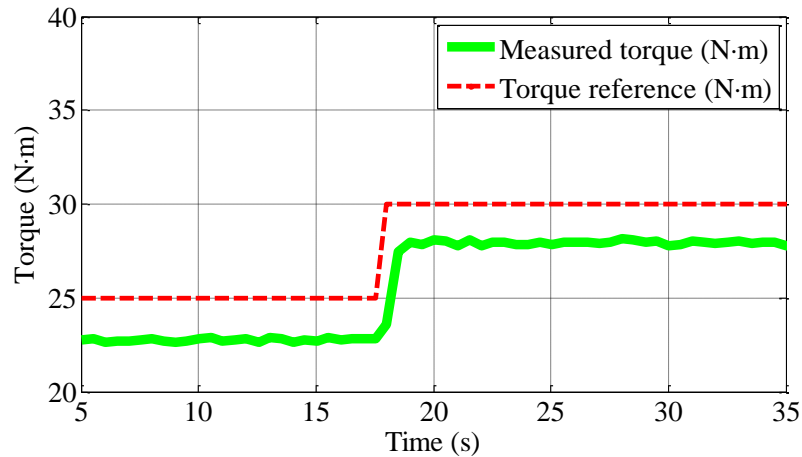


Fig. 5-16. Reference torque and measured torque at 2700 r/min.

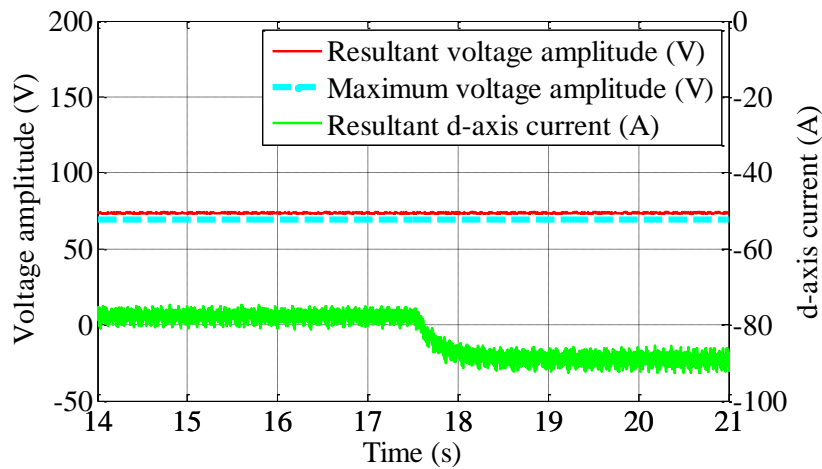


Fig. 5-17. Resultant voltage amplitude, maximum voltage amplitude and resultant d-axis current when reference torque steps from 25 N·m to 30 N·m at 2700 r/min.

5.6 Summary

The proposed novel hybrid control scheme combines the FOC with the DFVC and inherits the advantages of both the FOC and DFVC while avoiding the disadvantages of the two conventional control schemes. The proposed control scheme is verified by simulations and experiments. Simulation and experiment results show that the proposed control scheme not only controls IPMSM drive to follow reference d- and q-axis currents

accurately at low speed, but also limits flux amplitude directly in field weakening region. The smooth transition between FOC and DFVC has also been verified by experiments.

CHAPTER 6 Conclusions and Future Work

6.1 Conclusions

The increasing applications of interior permanent magnet synchronous motor (IPMSM), especially in electric and hybrid electric vehicles demand high efficiency operations. This thesis, therefore, focused on and contributed to the existing body of technology in the area of optimal efficiency control of IPMSMs in both constant torque region and field weakening region. The contributions of the research to the body of knowledge are summarised as follows:

6.1.1 Proposed Virtual Signal Injection Concept

Different from the existing real signal injection based MTPA control schemes which inject real high frequency signals into d- and q-axis currents or flux amplitude, Chapter 2 of this thesis proposes a novel concept that the MTPA points can also be tracked by injecting high frequency signals through mathematical calculations. It has been shown that the proposed virtual signal injection concept has many advantages over the current state-of-the-art real signal injection control schemes and other efficiency optimized control schemes.

First, the virtual signal injection will not incur any additional loss which can be caused by real signal injection control. Since the real signal injection control schemes inject high frequency signals into a motor, the additional iron/copper loss is inevitable. On the contrary, the proposed virtual signal injection control does not inject any high frequency signal into the motor, and no additional iron/copper loss will occur.

Secondly, the selection of the frequency and amplitude of the virtually injected signal is more flexible than that of real signal injection. Due to the bandwidth of control loops and the limitation of hardware, the signal frequency and amplitude of real signal injection should be carefully selected to make a trade-off between accurately tracking the MTPA

points and maintaining a relative good control performance, e.g., no significant torque or speed fluctuations due to the injected signals. However, the signal frequency of the proposed virtual signal injection control is only limited by the sample rate of the controller and the selection of signal frequency and signal amplitude for virtual signal injection control is very flexible and the bandwidth of control loops will not affect the selection.

Thirdly, the virtual signal injection control is robust to current and voltage harmonics. The harmonics in currents and voltages can be easily filtered by low-pass filters. However, the real signal injection control schemes always suffer from harmonics which are always present in measured current and voltages.

In addition, the virtual signal injection control has a wide speed range. Due to the bandwidth of control loops, the signal frequency of real signal injection control cannot be very high. Therefore, the frequency of the injected signal may overlap with the dominant current or voltage harmonics, which will affect the MTPA tracking performance of the real signal injection control significantly and this limits the application of real signal injection at high speed. However, because the signal frequency of the virtual signal injection is only limited by the sample rate of the controller, the virtual signal injection control can be applied to any speed in constant torque region.

Moreover, compared with other model based control schemes, including look-up table based control schemes, the proposed control scheme can achieve accurate MTPA control while being independent of machine parameters. The high MTPA control accuracy of the proposed virtual signal injection has been verified by simulations and experiments under various operation conditions.

6.1.2 Extension of the Virtual Signal Injection Control into Field Weakening Region

In field weakening region, due to voltage saturation, both real signal injection and virtual signal injection control schemes are no longer effective. Chapter 2 of the thesis has developed an innovative control scheme that combines the virtual signal injection control together with voltage feedback based field weakening control. Seamless transition between constant torque region and field weakening region can be achieved by the proposed control scheme. In constant torque region, the proposed control can

automatically track the MTPA points by the virtual signal injection control. In field weakening region at high speeds, if the voltage amplitude of the control output is smaller than the maximum available voltage, the virtual signal injection control will automatically adjust the voltage amplitude to the maximum value, so that the drive operates on the voltage constrained maximum torque per ampere (VCMTPA) operating point. If the voltage amplitude is larger than the maximum value, the voltage feedback based field weakening control will be activated and adjust the voltage amplitude equal to the maximum value. Therefore, the VCMTPA control can always be guaranteed by the proposed control scheme. The performance of the control scheme in both constant torque and field weakening regions has been extensively validated by simulations and experiments.

6.1.3 Applied Virtual Signal Injection Control in f-t Frame

It is well known that IPMSM drive controlled in the stator flux synchronous rotating reference frame (f-t frame) is advantageous in field weakening operation since the voltage constraint can be naturally imposed. In Chapter 3, a novel concept that utilizes d-q frame based searching techniques (including virtual signal injection control schemes) to compensate the MTPA control errors of the f-t frame based control schemes is proposed. The proposed approach implemented in the f-t frame based control will be independent of flux observer errors. Without loss of generality, the direct flux vector control is adopted in the thesis as an example of the f-t frame based control scheme and the virtual signal injection control is adopted as an example of searching schemes in the d-q frame. By using the d-q frame based searching schemes to compensate the errors in the reference and observed flux amplitudes in the f-t frame, the MTPA control accuracy and the robustness of the f-t frame based control scheme can be significantly increased.

Moreover, the f-t frame based control scheme is also extended into field weakening region by limiting the flux amplitude directly. Therefore, the virtual signal injection aided direct flux vector control also inherits the advantage of the f-t frame based control schemes in field weakening region.

6.1.4 Proposed Self-learning Control

While the developed virtual signal injection control techniques can achieve accurate MTPA and VCMTPA operations in wide torque-speed ranges, the response time to torque changes is relatively slow. To improve response time, self-learning control is investigated and developed in this research. Currently, artificial intelligence control is primarily concerned with speed or position tracking rather than MTPA operations of motor drives. In Chapter 4 of this thesis, a novel self-learning control for MTPA operation is proposed. The proposed self-learning control can automatically track the MTPA points with high accuracy and will be self-trained online at the same time. After training, the proposed control scheme can achieve accurate MTPA operation with fast response even for the torque reference which has not been experienced before.

The self-learning control was also integrated into the f-t frame based control to achieve seamless transition between constant torque region and field weakening region. After training, the motor drives with the proposed self-learning control in the f-t frame can achieve accurate optimal efficiency control with fast response in both constant torque region and field weakening region independent of machine parameters. Thus, robust optimal efficiency control of IPMSM drives can be realized with fast dynamic response.

6.1.5 Proposed Hybrid Control Concept

Since d-q frame based control schemes are more robust to parameter variations for MTPA operation than f-t frame based control schemes in constant torque region, while f-t frame based control schemes are preferable for field weakening operation than d-q frame based control schemes, a hybrid control scheme has been proposed in Chapter 5 to utilize the advantages of the d-q frame based control at low speeds and the advantages of f-t frame based control at high speeds. Moreover, a seamless transition between the d-q frame based control and the f-t frame based control is achieved by the adoption of a linear shape function.

The proposed hybrid control inherits the advantages of both d-q frame based control schemes and f-t frame based control schemes, and the performance of the proposed hybrid control scheme has been verified by simulations and experiments.

6.2 Future Work

The novel virtual signal injection concept, self-learning concept and hybrid control concept are proposed in this thesis and verified by simulations and experiments under various operation conditions. These concepts may also be applied to control of other drives and further researches in these are needed.

6.2.1 Utilization of Virtual Signal Injection Control to Control Other Types of Electric Machine Drives

In this thesis, the novel virtual signal injection control has been proposed and developed for control of IPMSM drives. However, the concept of virtual signal injection control may also be utilized to achieve optimal efficiency control of induction machine drives, switched reluctance machine drives and other machine drives.

Moreover, the concept of the virtual signal injection may be employed to replace real signal injection in other applications, such as sensorless control, minimum loss control, etc.

6.2.2 Improvement of Self-learning Control

The self-learning control proposed in the thesis is relatively simple based on curve fitting of the recorded MTPA points. However, other artificial intelligence control schemes such as artificial neural network, fuzzy logic, and least square methods may also be adopted to achieve the self-learning control based on the MTPA points tracked by the virtual signal injection or other parameter independent control schemes. Moreover, since the quality of MTPA control can be indicated by the output of the signal processing block of the virtual signal injection, i.e., the MTPA quality indicator $LPFO$, a more sophisticated and more intelligent self-learning ability may be achieved with the feedback loop of the MTPA quality indicator.

6.2.3 Improvement of Hybrid Control Scheme

The control of d- and q-axis currents in the hybrid control scheme at low speed is achieved through direct flux vector control frame. However, other f-t frame based control schemes are also applicable. A comparative study of the hybrid control scheme with different f-t frame based control schemes would be useful in selection of the best combination. Moreover, because the direct flux vector control controls the flux amplitude and t-axis current directly, this control scheme may suffer from the coupling effect between the d- and q-axis currents and a study on developing decoupling methods for the f-t frame based control schemes may be needed.

Bibliography

- [1] H. C. Righolt and F. G. Rieck, "Energy Chain and Efficiency in Urban Traffic for ICE and EV," in *Proc. IEEE EVS.*, 2013, pp. 1–7.
- [2] Y. Guo, J. Xiong, S. Xu, and W. Su, "Two-Stage Economic Operation of Microgrid-Like Electric Vehicle Parking Deck," *IEEE Trans. Smart Grid.*, vol. PP, no. 99, pp. 1–9, 2015.
- [3] C. Pillot, "Micro Hybrid , HEV , P - HEV and EV Market 2012 - 2025 Impact on the Battery Business," in *Proc. IEEE EVS.*, 2013, pp. 1–6.
- [4] D. Meyer, J. Choi, and J. Wang, "Increasing EV Public Charging with Distributed Generation in the Electric Grid," in *Proc. IEEE ITEC.*, 2015, pp. 1 – 6.
- [5] C. C. Chan, "The State of the Art of Electric and Hybrid Vehicles," *Proc. IEEE*, vol. 90, no. 2, pp. 247–275, 2002.
- [6] M. Zeraoulia, M. E. H. Benbouzid, and D. Diallo, "Electric Motor Drive Selection Issues for HEV Propulsion Systems: A Comparative Study," *IEEE Trans. Veh. Technol.*, vol. 55, no. 6, pp. 1756–1764, 2006.
- [7] Z. Yang, F. Shang, I. P. Brown, and M. Krishnamurthy, "Comparative Study of Interior Permanent Magnet, Induction, and Switched Reluctance Motor Drives for EV and HEV Applications," *IEEE Trans. Trans. Electri.*, vol. 1, no. 3, pp. 245–254, 2015.
- [8] L. Chang, "Comparison of AC Drives for Electric Vehicles - A report on Experts' Opinion Survey," *IEEE Aerosp. Electron. Syst. Mag.*, vol. 9, no. 8, pp. 7–11, 1994.
- [9] A. M. Bazzi and P. T. Krein, "Comparative Evaluation of Machines for Electric and Hybrid Vehicles Based on Dynamic Operation and Loss Minimization," in *Proc. IEEE ECCE.*, 2010, pp. 3345–3351.
- [10] V. T. Buyukdegirmenci, A. M. Bazzi, and P. T. Krein, "Evaluation of Induction and Permanent-Magnet Synchronous Machines Using Drive-Cycle Energy and Loss Minimization in Traction Applications," *IEEE Trans. Ind. Appl.*, vol. 50, no. 1, pp. 395–403, 2014.
- [11] T. Finken, M. Felden, and K. Hameyer, "Comparison and Design of Different Electrical Machine Types Regarding Their Applicability in Hybrid Electrical Vehicles," in *Proc. IEEE ICEM.*, 2008, pp. 1–5.
- [12] T. M. Jahns, G. B. Kliman, and T. W. Neumann, "Interior Permanent-Magnet Synchronous Motors for Adjustable-Speed Drives," *IEEE Trans. Ind. Appl.*, vol. IA-22, no. 4, pp. 738–747, Jul. 1986.

- [13] X. Chen, J. Wang, B. Sen, P. Lazari, and T. Sun, "A High-Fidelity, Computationally Efficient Model for Interior Permanent Magnet Machines Considering the Magnetic Saturation, Spatial Harmonics and Iron Loss Effect," *IEEE Trans. Ind. Electron.*, vol. 62, no. 7, pp. 4044–4055, 2015.
- [14] T. Finken, M. Hombitzer, and K. Hameyer, "Study and Comparison of Several Permanent-Magnet Excited Rotor Types Regarding Their Applicability in Electric Vehicles," in *Proc. Emobility - Elect. Power Train.*, 2010, pp. 1–7.
- [15] A. Vagati, G. Pellegrino, and P. Guglielmi, "Comparison Between SPM and IPM Motor Drives for EV Application," in *Proc. IEEE ICEM.*, 2010, pp. 1–6.
- [16] B. Cheng and T. R. Tesch, "Torque Feedforward Control Technique for Permanent-Magnet Synchronous Motors," *IEEE Trans. Ind. Electron.*, vol. 57, no. 3, pp. 969–974, Mar. 2010.
- [17] C. Cavallaro, A. O. Di Tommaso, R. Miceli, A. Raciti, G. R. Galluzzo, and M. Trapanese, "Efficiency Enhancement of Permanent-Magnet Synchronous Motor Drives by Online Loss Minimization Approaches," *IEEE Trans. Ind. Electron.*, vol. 52, no. 4, pp. 1153–1160, 2005.
- [18] S. Morimoto, Y. Tong, Y. Takeda, and T. Hirasu, "Loss Minimization Control of Permanent Magnet Synchronous Motor Drives," *IEEE Trans. Ind. Electron.*, vol. 41, no. 5, pp. 511–517, 1994.
- [19] R. Nalepa and T. Orłowska-Kowalska, "Optimum Trajectory Control of the Current Vector of a Nonsalient-Pole PMSM in the Field-Weakening Region," *IEEE Trans. Ind. Electron.*, vol. 59, no. 7, pp. 2867–2876, 2012.
- [20] L. Tang, L. Zhong, M. F. Rahman, and Y. Hu, "A Novel Direct Torque Controlled Interior Permanent Magnet Synchronous Machine Drive With Low Ripple in Flux and Torque and Fixed Switching Frequency," *IEEE Trans. Power Electron.*, vol. 19, no. 2, pp. 346–354, 2004.
- [21] Y. Ren, Z. Q. Zhu, and J. Liu, "Direct Torque Control of Permanent-Magnet Synchronous Machine Drives With a Simple Duty Ratio Regulator," *IEEE Trans. Ind. Electron.*, vol. 61, no. 10, pp. 5249–5258, 2014.
- [22] Z. Xu and M. F. Rahman, "Comparison of a Sliding Observer and a Kalman Filter for Direct-Torque-Controlled IPM Synchronous Motor Drives," *IEEE Trans. Ind. Electron.*, vol. 59, no. 11, pp. 4179–4188, 2012.
- [23] Y. Ren and Z. Q. Zhu, "Enhancement of Steady-State Performance in Direct Torque Controlled Dual-three Phase Permanent Magnet Synchronous Machine Drives with Modified Switching Table," *IEEE Trans. Ind. Electron.*, vol. 62, no. 6, pp. 3338–3350, 2015.
- [24] C. Xia, J. Zhao, Y. Yan, and T. Shi, "A Novel Direct Torque Control of Matrix Converter-Fed PMSM Drives Using Duty Cycle Control for Torque Ripple Reduction," *IEEE Trans. Ind. Electron.*, vol. 61, no. 6, pp. 2700–2713, 2014.

- [25] G. Pellegrino, E. Armando, and P. Guglielmi, "Direct Flux Field-Oriented Control of IPM Drives With Variable DC Link in the Field-Weakening Region," *IEEE Trans. Ind. Appl.*, vol. 45, no. 5, pp. 1619–1627, 2009.
- [26] G. Pellegrino, E. Armando, and P. Guglielmi, "Direct-Flux Vector Control of IPM Motor Drives in the Maximum Torque Per Voltage Speed Range," *IEEE Trans. Ind. Electron.*, vol. 59, no. 10, pp. 3780–3788, Oct. 2012.
- [27] G. Pellegrino, R. I. Bojoi, and P. Guglielmi, "Unified Direct-Flux Vector Control for AC Motor Drives," *IEEE Trans. Ind. Appl.*, vol. 47, no. 5, pp. 2093–2102, 2011.
- [28] M. M. I. Chy and M. N. Uddin, "Analysis of Flux Control for Wide Speed Range Operation of IPMSM Drive," in *Proc. IEEE LESCPE.*, 2007, pp. 256–260.
- [29] A. Ahmed, Y. Sozer, and M. Hamdan, "Maximum Torque Per Ampere Control for Interior Permanent Magnet Motors Using DC Link Power Measurement," in *Proc. IEEE APEC.*, 2014, pp. 826–832.
- [30] A. Verl and M. Bodson, "Torque Maximization for Permanent Magnet Synchronous Motors," *IEEE Trans. Control Syst. Technol.*, vol. 6, no. 6, pp. 740–745, 1998.
- [31] S. Morimoto, Y. Takeda, and T. Hirasu, "Current Phase Control Methods for Permanent Magnet Synchronous Motors," *IEEE Trans. Power Electron.*, vol. 5, no. 2, pp. 133–139, Apr. 1990.
- [32] S. Morimoto, K. Hatanaka, Y. Tong, Y. Takeda, and T. Hirasu, "High Performance Servo Drive System of Salient Pole Permanent Magnet Synchronous Motor," in *Proc. IEEE IAS.*, 1991, pp. 463–468.
- [33] S. Morimoto, K. Hatanaka, Y. Tong, Y. Takeda, and T. Hirasu, "Servo Drive System and Control Characteristics of Salient Pole Permanent Magnet Synchronous Motor," *IEEE Trans. Ind. Appl.*, vol. 29, no. 2, pp. 338–343, 1993.
- [34] S. Morimoto, Y. Takeda, T. Hirasu, and K. Taniguchi, "Expansion of Operating Limits for Permanent Magnet Motor by Current Vector Control Considering Inverter Capacity," *IEEE Trans. Ind. Appl.*, vol. 26, no. 5, pp. 866–871, 1990.
- [35] M. N. Uddin, T. S. Radwan, and M. A. Rahman, "Performance of Interior Permanent Magnet Motor Drive Over Wide Speed Range," *IEEE Trans. Energy Convers.*, vol. 17, no. 1, pp. 79–84, 2002.
- [36] Y.-S. Kim and S.-K. Sul, "Torque Control Strategy of an IPMSM Considering the Flux Variation of the Permanent Magnet," in *Proc. IEEE IAS.*, 2007, pp. 1301–1307.
- [37] Z. Lei, W. Xuhui, Z. Feng, K. Liang, and Z. Baocang, "Deep Field-Weakening Control of Pmsms for Both Motion and Generation Operation," in *Proc. IEEE ICEMS.*, 2011, no. 4, pp. 1–5.

- [38] G. Gallegos-López, F. S. Gunawan, and J. E. Walters, "Optimum Torque Control of Permanent-Magnet AC Machines in the Field-Weakened Region," *IEEE Trans. Ind. Appl.*, vol. 41, no. 4, pp. 1020–1028, 2005.
- [39] F. Parasiliti, M. Villani, S. Lucidi, and F. Rinaldi, "Finite-Element-Based Multiobjective Design Optimization Procedure of Interior Permanent Magnet Synchronous Motors for Wide Constant-Power Region Operation," *IEEE Trans. Ind. Electron.*, vol. 59, no. 6, pp. 2503–2514, 2012.
- [40] G. Kang, J. Lim, K. Nam, H.-B. Ihm, and H.-G. Kim, "A MTPA Control Scheme for an IPM Synchronous Motor Considering Magnet Flux Variation Caused by Temperature," in *Proc. IEEE APEC.*, 2004, pp. 1617–1621.
- [41] T. Sun, J. Wang, and X. Chen, "Maximum Torque per Ampere (MTPA) Control for Interior Permanent Magnet Synchronous Machine Drives Based on Virtual Signal Injection," *IEEE Trans. Power Electron.*, vol. 30, no. 9, pp. 5036–5045, 2015.
- [42] S. Morimoto, M. Sanada, and Y. Takeda, "Wide-Speed Operation of Interior Permanent Magnet Synchronous Motors With High-Performance Current Regulator," *IEEE Trans. Ind. Appl.*, vol. 30, no. 4, pp. 920–926, 1994.
- [43] C. T. Pan and S. M. Sue, "A Linear Maximum Torque Per Ampere Control for IPMSM Drives Over Full-Speed Range," *IEEE Trans. Energy Convers.*, vol. 20, no. 2, pp. 359–366, Jun. 2005.
- [44] S. Morimoto, M. Sanada, and Y. Takeda, "Effects and Compensation of Magnetic Saturation in Flux-Weakening Controlled Permanent Magnet Synchronous Motor Drives," *IEEE Trans. Ind. Appl.*, vol. 30, no. 6, pp. 1632–1637, 1994.
- [45] A. H. Wijenayake and P. B. Schmidt, "Modeling and Analysis of Permanent Magnet Synchronous Motor by Taking Saturation and Core Loss into Account," in *Proc. IEEE PEDS.*, 1997, pp. 530–534.
- [46] A. Consoli, G. Scarcella, G. Scelba, and S. Sindoni, "Modeling Control of IPM Synchronous Motors," in *Proc. IEEE PES.*, 2008, pp. 1–6.
- [47] N. Yang, G. Luo, W. Liu, and K. Wang, "Interior Permanent Magnet Synchronous Motor Control for Electric Vehicle Using Look-Up Table," in *Proc. IEEE IPEMC.*, 2012, pp. 1015–1019.
- [48] S.-Y. Jung, J. Hong, and K. Nam, "Current Minimizing Torque Control of the IPMSM Using Ferrari's Method," *IEEE Trans. Power Electron.*, vol. 28, no. 12, pp. 5603–5617, 2013.
- [49] A. Consoli, G. Scarcella, G. Scelba, and A. Testa, "Steady-State and Transient Operation of IPMSMs Under Maximum-Torque-per-Ampere Control," *IEEE Trans. Ind. Appl.*, vol. 46, no. 1, pp. 121–129, 2010.

- [50] K. D. Hoang, J. Wang, M. Cyriacks, A. Melkonyan, and K. Kriegl, "Feed-forward Torque Control of Interior Permanent Magnet Brushless AC Drive for Traction Applications," in *Proc. IEEE IEMDC.*, 2013, pp. 152–159.
- [51] B. Štumberger, G. Štumberger, D. Dolinar, A. Hamler, and M. Trlep, "Evaluation of Saturation and Cross-Magnetization Effects in Interior Permanent-Magnet Synchronous Motor," *IEEE Trans. Ind. Appl.*, vol. 39, no. 5, pp. 1264–1271, Sep. 2003.
- [52] R. S. Colby and D. W. Novotny, "An Efficiency-Optimizing Permanent-Magnet Synchronous Motor Drive," *IEEE Trans. Ind. Appl.*, vol. 24, no. 3, pp. 462–469, 1988.
- [53] A. Dianov, Y. Kk. Kim, S. J. Lee, and S. T. Lee, "Robust Self-Tuning MTPA Algorithm for IPMSM Drives," in *Proc. IEEE IECON.*, 2008, pp. 1355–1360.
- [54] K. W. Lee and S. Bin Lee, "MTPA Operating Point Tracking Control Scheme for Vector Controlled PMSM Drives," in *Proc. IEEE SPEEDAM.*, 2010, pp. 24–28.
- [55] S. Bolognani, R. Petrella, A. Prearo, and L. Sgarbossa, "Automatic Tracking of MTPA Trajectory in IPM Motor Drives Based on AC Current Injection," *IEEE Trans. Ind. Appl.*, vol. 47, no. 1, pp. 105–114, Jan. 2011.
- [56] R. Antonello, M. Carraro, and M. Zigliotto, "Towards the Automatic Tuning of MTPA Algorithms for IPM Motor Drives," in *Proc. IEEE ICEM.*, 2012, pp. 1121–1127.
- [57] R. Antonello, M. Carraro, and M. Zigliotto, "Theory and Implementation of a MTPA Tracking Controller for Anisotropic PM Motor Drives," in *Proc. IEEE IECON.*, 2012, pp. 2061–2066.
- [58] R. Antonello, M. Carraro, and M. Zigliotto, "Maximum-Torque-Per-Ampere Operation of Anisotropic Synchronous Permanent-Magnet Motors Based on Extremum Seeking Control," *IEEE Trans. Ind. Electron.*, vol. 61, no. 9, pp. 5086–5093, Sep. 2014.
- [59] S. Kim, Y.-D. Yoon, S.-K. Sul, and K. Ide, "Maximum Torque per Ampere (MTPA) Control of an IPM Machine Based on Signal Injection Considering Inductance Saturation," *IEEE Trans. Power Electron.*, vol. 28, no. 1, pp. 488–497, 2013.
- [60] S. Bolognani, S. Calligaro, and R. Petrella, "Adaptive Flux-Weakening Controller for Interior Permanent Magnet Synchronous Motor Drives," *IEEE J. Emerg. Sel. Top. Power Electron.*, vol. 2, no. 2, pp. 236–248, Jun. 2014.
- [61] T. M. Jahns, "Flux-Weakening Regime Operation of an Interior Permanent-Magnet Synchronous Motor Drive," *IEEE Trans. Ind. Appl.*, vol. IA-23, no. 4, pp. 681–689, Jul. 1987.

- [62] T. Sun and J. Wang, "Extension of Virtual Signal Injection Based MTPA Control for Interior Permanent Magnet Synchronous Machine Drives into Field Weakening Region," *IEEE Trans. Ind. Electron.*, vol. 62, no. 11, pp. 6809–6817, 2015.
- [63] J.-M. Kim and S.-K. Sul, "Speed Control of Interior Permanent Magnet Synchronous Motor Drive for the Flux Weakening Operation," *IEEE Trans. Ind. Appl.*, vol. 33, no. 1, pp. 43–48, 1997.
- [64] Y. Inoue, S. Morimoto, and M. Sanada, "Comparative Study of PMSM Drive Systems Based on Current Control and Direct Torque Control in Flux-Weakening Control Region," *IEEE Trans. Ind. Appl.*, vol. 48, no. 6, pp. 2382–2389, Nov. 2012.
- [65] G. Pellegrino, E. Armando, and P. Guglielmi, "Direct-Flux Field-Oriented Control of IPM Motor Drives With Robust Exploitation of the Maximum Torque Per Voltage Speed Range," in *Proc. IEEE ISIE*, 2010, pp. 1271–1277.
- [66] X. Xu and D. W. Novotny, "Selection of the Flux Reference for Induction Machine Drives in the Field Weakening Region," *IEEE Trans. Ind. Appl.*, vol. 28, no. 6, pp. 1353–1358, 1992.
- [67] I. Takahashi and T. Noguchi, "A New Quick-Response and High-Efficiency Control Strategy of an Induction Motor," *IEEE Trans. Ind. Appl.*, vol. IA-22, no. 5, pp. 820–827, 1986.
- [68] S. Mathapati and J. Böcker, "Analytical and Offline Approach to Select Optimal Hysteresis Bands of DTC for PMSM," *IEEE Trans. Ind. Electron.*, vol. 60, no. 3, pp. 885–895, 2013.
- [69] V. Ambrozic, G. S. Buja, and R. Menis, "Band-Constrained Technique for Direct Torque Control of Induction Motor," *IEEE Trans. Ind. Electron.*, vol. 51, no. 4, pp. 776–784, 2004.
- [70] J.-K. Kang and S.-K. Sul, "Analysis and Prediction of Inverter Switching Frequency in Direct Torque Control of Induction Machine Based on Hysteresis Bands and Machine Parameters," *IEEE Trans. Ind. Electron.*, vol. 48, no. 3, pp. 545–553, 2001.
- [71] K. R. Jordan, S. B. Dewan, and G. R. Slemon, "General Analysis of Three-Phase Inverters," *IEEE Trans. Ind. Gen. Appl.*, vol. IGA-5, no. 6, pp. 672–679, 1969.
- [72] K. R. Jordan, "Modes of Operation of Three-Phase Inverters," *IEEE Trans. Ind. Gen. Appl.*, vol. IGA-5, no. 6, pp. 680–685, 1969.
- [73] Y. Inoue, S. Morimoto, and M. Sanada, "Control Method Suitable for Direct-Torque-Control-Based Motor Drive System Satisfying Voltage and Current Limitations," *IEEE Trans. Ind. Appl.*, vol. 48, no. 3, pp. 970–976, May 2012.
- [74] P. L. Jansen, R. D. Lorenz, and D. W. Novotny, "Observer-Based Direct Field Orientation: Analysis and Comparison of Alternative Methods," *IEEE Trans. Ind. Appl.*, vol. 30, no. 4, 1994.

- [75] A. Yoo and S.-K. Sul, "Design of Flux Observer Robust to Interior Permanent-Magnet Synchronous Motor Flux Variation," *IEEE Trans. Ind. Appl.*, vol. 45, no. 5, pp. 1670–1677, 2009.
- [76] T. Inoue, Y. Inoue, S. Morimoto, and M. Sanada, "Mathematical Model for MTPA Control of Permanent-Magnet Synchronous Motor in Stator Flux Linkage Synchronous Frame," *IEEE Trans. Ind. Appl.*, vol. 51, no. 5, pp. 3620–3628, 2015.
- [77] T. Sun, J. Wang, and M. Koc, "Virtual Signal Injection Based Direct Flux Vector Control of IPMSM Drives," *IEEE Trans. Ind. Electron.*, vol. in press, 2016.
- [78] A. Shinohara, Y. Inoue, S. Morimoto, and M. Sanada, "Correction of Reference Flux for MTPA Control in Direct Torque Controlled Interior Permanent Magnet Synchronous Motor Drives," in *Proc. IEEE IPEC.*, 2014, no. 1, pp. 324–329.
- [79] S. Bolognani, L. Peretti, and M. Zigliotto, "Online MTPA Control Strategy for DTC Synchronous-Reluctance-Motor Drives," *IEEE Trans. Power Electron.*, vol. 26, no. 1, pp. 20–28, Jan. 2011.
- [80] Y. Tan, W. H. Moase, C. Manzie, D. Nešić, and I. M. Y. Mareels, "Extremum Seeking From 1922 To 2010," in *Proc. IEEE CCC*, 2010, pp. 14–26.
- [81] A. Khlaief, M. Bendjedia, M. Boussak, and M. Gossa, "A Nonlinear Observer for High-Performance Sensorless Speed Control of IPMSM Drive," *IEEE Trans. Power Electron.*, vol. 27, no. 6, pp. 3028–3040, 2012.
- [82] T. Miyajima, H. Fujimoto, and M. Fujitsuna, "A Precise Model-Based Design of Voltage Phase Controller for IPMSM," *IEEE Trans. Power Electron.*, vol. 28, no. 12, pp. 5655–5664, 2013.
- [83] O. Wallmark, S. Lundberg, and M. Bongiorno, "Input Admittance Expressions for Field-Oriented Controlled Salient PMSM Drives," *IEEE Trans. Power Electron.*, vol. 27, no. 3, pp. 1514–1520, Mar. 2012.
- [84] W. L. Soong and T. J. E. Miller, "Field-Weakening Performance of Brushless Synchronous AC Motor Drives," in *Proc. IEE Elect. Power Appl.*, 1994, vol. 141, no. 6, p. 331.
- [85] R. F. Schiferl and T. A. Lipo, "Power Capability of Salient Pole Permanent Magnet Synchronous Motors in Variable Speed Drive Applications," *IEEE Trans. Ind. Appl.*, vol. 26, no. 1, pp. 115–123, 1990.
- [86] W. L. Soong and T. J. E. Miller, "Theoretical Limitations to the Field-Weakening Performance of the Five Classes of Brushless Synchronous AC Motor Drive," in *Proc. IEEE IEMDC.*, 1993, pp. 127–132.
- [87] A. K. Adnanes and T. M. Undeland, "Optimum Torque Performance in PMSM Drives above Rated Speed," in *Proc. IEEE IAS.*, 1991, pp. 169–175.

- [88] C. Mademlis and V. G. Agelidis, "A High-Performance Vector Controlled Interior PM Synchronous Motor Drive with Extended Speed Range Capability," in *Proc. IECON.*, 2001, vol. 00, pp. 1475 – 1482.
- [89] M. Tursini, E. Chiricozzi, and R. Petrella, "Feedforward Flux-Weakening Control of Surface-Mounted Permanent-Magnet Synchronous Motors Accounting for Resistive Voltage Drop," *IEEE Trans. Ind. Electron.*, vol. 57, no. 1, pp. 440–448, 2010.
- [90] L. Zhu, S. Xue, X. Wen, Y. Li, and L. Kong, "A New Deep Field-Weakening Strategy of IPM Machines Based on Single Current Regulator and Voltage Angle Control," in *Proc. IEEE ECCE.*, 2010, pp. 1144–1149.
- [91] B. Cheng and T. R. Tesch, "Torque Feedforward Control Technique for Permanent Magnet Synchronous Motors," in *Proc. IEEE IECON.*, 2007, vol. 2, no. 1, pp. 1055–1060.
- [92] B.-H. Bae, N. Patel, S. Schulz, and S.-K. Sul, "New Field Weakening Technique for High Saliency Interior Permanent Magnet Motor," in *Proc. IEEE IAS.*, 2003, vol. 2, no. 2, pp. 898–905.
- [93] T.-S. Kwon, G.-Y. Choi, M.-S. Kwak, and S.-K. Sul, "Novel Flux-Weakening Control of an IPMSM for Quasi-Six-Step Operation," *IEEE Trans. Ind. Appl.*, vol. 44, no. 6, pp. 1722–1731, 2008.
- [94] Y. S. Chen, Z. Q. Zhu, and D. Howe, "Influence of Inaccuracies In Machine Parameters on Field-Weakening Performance of PM Brushless AC Drives," in *Proc. IEEE IEMDC.*, 1999, pp. 691 – 693.
- [95] Y.-C. Kwon, S. Kim, and S.-K. Sul, "Voltage Feedback Current Control Scheme for Improved Transient Performance of Permanent Magnet Synchronous Machine Drives," *IEEE Trans. Ind. Electron.*, vol. 59, no. 9, pp. 3373–3382, 2012.
- [96] S. Bolognani, S. Calligaro, R. Petrella, and F. Pogni, "Flux-Weakening in IPM motor drives: Comparison of state-Of-Art algorithms and a Novel Proposal for Controller Design," in *Proc. IEEE EPE*, 2011, pp. 1 – 11.
- [97] D. Stojan, D. Drevensek, Z. Plantic, B. Grcar, and G. Stumberger, "Novel Field-Weakening Control Scheme for Permanent-Magnet Synchronous Machines Based on Voltage Angle Control," *IEEE Trans. Ind. Appl.*, vol. 48, no. 6, pp. 2390–2401, 2012.
- [98] J. Goss, P. H. Mellor, R. Wrobel, D. A. Staton, and M. Popescu, "The Design of AC Permanent Magnet Motors for Electric Vehicles: A Computationally Efficient Model of The Operational Envelope," in *Proc. IET PEMD.*, 2012, pp. 1–6.
- [99] P. H. Mellor, R. Wrobel, and D. Holliday, "A Computationally Efficient Iron Loss Model for Brushless AC Machines that Caters for Rated Flux and Field Weakened Operation," in *Proc. IEEE IEMDC.*, 2009, pp. 490–494.

- [100] H. Aorith, J. Wang, and P. Lazari, "A New Loss Minimization Algorithm for Interior Permanent Magnet Synchronous Machine Drives," in *Proc. IEEE IEMDC.*, 2013, pp. 526 – 533.
- [101] M. N. Uddin and J. Khastoo, "Fuzzy Logic-Based Efficiency Optimization and High Dynamic Performance of IPMSM Drive System in Both Transient and Steady-State Conditions," *IEEE Trans. Ind. Appl.*, vol. 50, no. 6, pp. 4251–4259, 2014.
- [102] Y. Yi, D. M. Vilathgamuwa, and M. A. Rahman, "Implementation of an Artificial-Neural-Network-Based Real-Time Adaptive Controller for an Interior Permanent-Magnet Motor Drive," *IEEE Trans. Ind. Appl.*, vol. 39, no. 1, pp. 96–104, 2003.
- [103] C. B. Butt and M. Azizur Rahman, "Untrained Artificial Neuron-Based Speed Control of Interior Permanent-Magnet Motor Drives Over Extended Operating Speed Range," *IEEE Trans. Ind. Appl.*, vol. 49, no. 3, pp. 1146–1153, 2013.
- [104] M. N. Uddin, M. A. Abido, and M. A. Rahman, "Development and Implementation of a Hybrid intelligent Controller for Interior Permanent-Magnet Synchronous Motor Drives," *IEEE Trans. Ind. Appl.*, vol. 40, no. 1, pp. 68–76, 2004.
- [105] A. Rubaai and P. Young, "Hardware/Software Implementation of Fuzzy Neural Network Self-Learning Control Methods for Brushless DC Motor Drives," *IEEE Trans. Ind. Appl.*, vol. in press, 2015.
- [106] A. Rubaai and P. Young, "EKF-Based PI-/PD-Like Fuzzy-Neural-Network Controller for Brushless Drives," *IEEE Trans. Ind. Appl.*, vol. 47, no. 6, pp. 2391–2401, 2011.
- [107] S.-J. Kang, J.-S. Ko, J.-S. Choi, J.-W. Baek, and D.-H. Chung, "Maximum Torque Control of IPMSM Drive With Multi-MFC," in *Proc. IEEE ICCAS.*, 2010, pp. 1242–1247.
- [108] L. Guo and L. Parsa, "Model Reference Adaptive Control of Five-Phase IPM Motors Based on Neural Network," *IEEE Trans. Ind. Electron.*, vol. 59, no. 3, pp. 1500–1508, 2012.
- [109] M. S. Hossain and M. J. Hossain, "Performance Analysis of a Novel Fuzzy Logic and MTPA Based Speed Control for IPMSM Drive with variable d- and q-axis Inductances," in *Proc. ICCIT.*, 2009, no. Iccit, pp. 21–23.
- [110] C. B. Butt, M. A. Hoque, and M. A. Rahman, "Simplified Fuzzy-Logic-Based MTPA Speed Control of IPMSM Drive," *IEEE Trans. Ind. Appl.*, vol. 40, no. 6, pp. 1529–1535, 2004.
- [111] P. L. Jansen and R. D. Lorenz, "A Physically Insightful Approach to the Design and Accuracy Assessment of Flux Observers for Field Oriented Induction Machine Drives," *IEEE Trans. Ind. Appl.*, vol. 30, no. 1, pp. 101–110, 1994.

List of Figures

Fig. 1-1. Efficiency map of: (a) IPMSM. (b) IM. (c) SRM. [7].....	3
Fig. 1-2. Schematic of SPMSM.	5
Fig. 1-3. Schematic of IPMSM.	6
Fig. 1-4. Different IPMSM rotor topologies: (a) I-PMSM. (b) RI-PMSM. (c) VI-PMSM.	6
Fig. 1-5. α - β reference frame, f-t reference frame and d-q reference frame.	7
Fig. 1-6. Schematic of FOC.	9
Fig. 1-7. Constant current loci, constant torque loci, and MTPA trajectory.....	10
Fig. 1-8. Nonlinear IPMSM machine parameters. (a): L_d as a function of d- and q-axis currents. (b): L_q as a function of d- and q-axis currents. (c): Ψ_m as a function of d- and q-axis currents [41]. The results apply to the machine used throughout this thesis and the data will be given in Chapter 2.	11
Fig. 1-9. Maximum current circle, voltage ellipses, constant torque loci, and MTPA trajectory of IPMSM in d-q axes coordinate.....	14
Fig. 1-10. Variations of torque and voltage amplitude with d-axis current for given current amplitude I_d	15
Fig. 1-11. The schematic of feedback field weakening control scheme.	16
Fig. 1-12. Principle of DTC operation.	18
Fig. 1-13. Block diagram of DTC scheme	19
Fig. 1-14. Block diagram of improved DTC.....	20
Fig. 1-15. Block diagram of direct flux vector control.	22
Fig. 1-16. Block diagram of voltage model based flux observer.....	23
Fig. 1-17. Block diagram of voltage model based flux observer.....	23

Fig. 1-18. Simplified block diagram of closed loop flux observers.....	23
Fig. 1-19. Block diagram of flux observer.....	24
Fig. 2-1. The MTPA point, constant current locus and constant torque locus.....	34
Fig. 2-2. The relationship between current angle and torque of fixed current vector amplitude.....	35
Fig. 2-3. The waveform of injected signal and torque fluctuation.....	36
Fig. 2-4. The influence of iron loss on MTPA point at speed of 1000 r/min.....	37
Fig. 2-5. Schematic of signal processing block to extract $\partial T/\partial\beta$	39
Fig. 2-6. IPMSM drive control system with virtual signal injection method.	40
Fig. 2-7. Schematic of virtual signal injection block of Fig. 2-6.	40
Fig. 2-8. The MTPA points and virtual signal injection MTPA tracking simulation result.....	43
Fig. 2-9. d-axis current tracking response to step change in torque at speed of 1 r/min.	43
Fig. 2-10. Experimental test-rig. (a): IPMSM, torque transducer, dynamometer. (b): controller and inverter.....	44
Fig. 2-11. The exact MTPA points and virtual signal injection MTPA tracking experimental result at speed of 400 r/min.....	45
Fig. 2-12. The exact MTPA points and virtual signal injection MTPA tracking experimental result at speed of 1000 r/min.....	46
Fig. 2-13. Measured results of proposed VSIC method for IPMSM control under MTPA operation. (a): Voltage and current waveform at 400 r/min speed and 45 N·m torque. (b): Voltage and current waveform at 1000 r/min speed and 45 N·m torque.	47
Fig. 2-14. Experimental result of MTPA tracking performance during torque changing.....	48

Fig. 2-15. Experimental result of torque step response at speed of 1000 r/min.....	48
Fig. 2-16. Measured torque, estimated torque, reference torque of a step change in torque from 40 N·m to 45 N·m at 1000 r/min.	49
Fig. 2-17. Theoretical MTPA current angle and VSIC tracking current angle in response to a step load torque change.	49
Fig. 2-18. Measured current amplitude and torque responses to a step load torque change.	50
Fig. 2-19. Experimental result of torque step response at speed of 15 r/min.....	50
Fig. 2-20. Variations of torque and voltage amplitude with d-axis current for given current amplitude.	52
Fig. 2-21. The diagram of virtual signal injection aided field weakening control.	53
Fig. 2-22. The reference voltage amplitude and <i>LPFO</i> signal without field weakening control (from constant torque region to field weakening region).	56
Fig. 2-23. The reference voltage amplitude and <i>LPFO</i> signal with proposed field weakening control (from constant torque region to field weakening region).	57
Fig. 2-24. The reference voltage amplitude and <i>LPFO</i> signal output with proposed field weakening control (from field weakening region to constant torque region).	58
Fig. 2-25. d-axis current responses of proposed field weakening control.	59
Fig. 2-26. Fast transition of the motor operation from constant torque region to field weakening region through a 500 r/min speed step.	59
Fig. 2-27. Reference voltage amplitude for different speed with and without virtual signal injection.	61
Fig. 2-28. Reference torque and d-axis currents.	61
Fig. 2-29. Reference torque and q-axis currents.	62
Fig. 2-30. Peak torque profile and resultant torques against the speed.	62

Fig. 2-31. d-axis current responses to step change in torque from 40 N·m to 45 N·m at 1000 r/min.	63
Fig. 2-32. The comparison between the measured torques and torque reference. .	64
Fig. 2-33. Variation of measured drive system efficiency with d-axis current for a given current amplitude (75.5 A, 1000 r/min, 45 N·m).	65
Fig. 2-34. d-axis current and estimated torque response to step changes in torque demand from 20 N·m to 25 N·m and back to 20 N·m at 3000 r/min.	65
Fig. 2-35. Measured torque and reference torque at 3000 r/min.	66
Fig. 2-36. Reference voltage amplitude and estimated torque responses during step change in torque demand.	66
Fig. 2-37. The current angle variation during torque step.	67
Fig. 2-38. Voltage and current waveform at 3000 r/min speed and 20 N·m torque.	67
Fig. 2-39. Variations of speed and d-axis current during transition from field weakening region to constant torque region.	68
Fig. 2-40. Variations of speed and d-axis current during transition from constant torque region to field weakening region.	69
Fig. 2-41. Reference torque and reference voltage amplitude when reference torque varies from 0 N·m to 30 N·m at 1600 r/min.	69
Fig. 2-42. Measured d- and q-axis currents when reference torque was varied from 0 to 30 N·m in steps of 5 N·m.	70
Fig. 2-43. Reference torque and reference voltage amplitude when reference torque varies from 30 N·m to 0 N·m at 1600 r/min.	70
Fig. 2-44. Measured d- and q-axis currents when reference torque was varied from 30 to 0 N·m in steps of 5 N·m.	71

Fig. 2-45. Measured torque and reference torque when reference torque was varied from 0 N·m to 30 N·m in a step of 5 N·m and from 30 N·m back to 0 N·m in the same step.	71
Fig. 3-1. (a) Relationship between flux amplitude and current angle. (b) Relationship between flux amplitude and resultant torque.	78
Fig. 3-2. Schematic of the proposed control scheme.	79
Fig. 3-3. Influence of observed flux amplitude error on MTPA tracking of proposed and conventional direct flux vector control schemes.	82
Fig. 3-4. Influence of observed flux vector angle error on MTPA tracking of proposed and conventional direct flux vector control schemes.	84
Fig. 3-5. MTPA point tracking performance when temperature changes.	84
Fig. 3-6. Measured d-axis current, MTPA d-axis current, and reference torque ...	86
Fig. 3-7. The output of LPF 1 and measured d-axis current.	86
Fig. 3-8. Comparison between proposed control scheme and conventional control scheme at 400 r/min when reference torque steps from 0 N·m to 5 N·m.	87
Fig. 3-9. Comparison of MTPA tracking performances of proposed and conventional control scheme at 400 r/min.	88
Fig. 3-10. Comparison of MTPA tracking performances of proposed and conventional control schemes at 1000 r/min.	88
Fig. 3-11. Comparison of torque per ampere variations of proposed and conventional control schemes at 1000 r/min.	89
Fig. 3-12. MTPA tracking response of proposed control scheme to step change in reference torque at speed of 1000 r/min.	90
Fig. 3-13. Response of LPF 1 output to torque step change at 1000 r/min.	91
Fig. 3-14. Measured torque and reference torque at 1000 r/min.	91

Fig. 3-15. MTPA tracking response of proposed control scheme to step change in reference torque at 15 r/min.	92
Fig. 3-16. Torque and voltage amplitude variations according to flux amplitude variation for a given current amplitude.	94
Fig. 3-17. Schematic of the proposed control scheme.	95
Fig. 3-18. Reference flux responses of proposed field weakening control.	97
Fig. 3-19. Resultant voltage amplitude and reference flux amplitude under same operation conditions of Fig. 3-18.	98
Fig. 3-20. Fast transition of motor operation from constant torque region to field weakening region and large speed step in field weakening region.	98
Fig. 3-21. Resultant voltage amplitude during speed step.	99
Fig. 3-22. Reference flux and voltage amplitude response to observer error in field weakening region.	100
Fig. 3-23. Variations of speed and d-axis current during transition from field weakening region to constant torque region.	101
Fig. 3-24. Reference voltage amplitude and d-axis current during transition from field weakening region to constant torque region.	101
Fig. 3-25. Variations of speed and d-axis current during transition from constant torque region to field weakening region.	102
Fig. 3-26. Reference voltage amplitude and motor speed during transition from constant torque region to field weakening region.	102
Fig. 3-27. Measured d-axis current and reference torque when reference torque steps from 10 N·m to 15 N·m at 3000 r/min.	103
Fig. 3-28. Reference voltage amplitude and reference torque when reference torque steps from 20 N·m to 25 N·m at 3000 r/min.	104
Fig. 3-29. Comparison between reference torque and measured torque when reference torque increased from 20 N·m to 25 N·m at 3000 r/min.	104

Fig. 4-1. d-axis current vs. torque for MTPA operation.	108
Fig. 4-2 Schematic of the proposed self-learning control scheme.	109
Fig. 4-3. Schematic of proposed self-learning MTPA control for IPMSM drives.	110
Fig. 4-4. Flowchart of proposed self-learning MTPA control for IPMSM drives	112
Fig. 4-5. Variations of resultant torque, reference d-axis current and output of SLC.	113
Fig. 4-6. Signal processing block output and reference d-axis current generation.	114
Fig. 4-7. The simulation result of resultant torque and reference q-axis current.	115
Fig. 4-8. SLC behavior after machine parameter changes.	116
Fig. 4-9. The simulation result of <i>LPFO</i> , reference d-axis current generation and SLC output after machine parameter changes.	116
Fig. 4-10. Simulation results of reference torque, resultant torque as well as q-axis current.	117
Fig. 4-11. Constant current amplitude loci and the control performance of the proposed control scheme with inaccurate q-axis current.	117
Fig. 4-12. Reference torque slowly changes.	118
Fig. 4-13. Integrator output when reference torque changes slowly.	119
Fig. 4-14. Reference torque fast changes.	119
Fig. 4-15. Integrator output when reference torque changes fast.	120
Fig. 4-16. Experimental result of the MTPA tracking performance at 1000 r/min	121
Fig. 4-17. d-axis current and measured/estimated torque response to torque command steps from 20 N·m to 35 N·m then steps back to 20 N·m.	122

Fig. 4-18. The measured/estimated torque and the measured q-axis current.....	123
Fig. 4-19. Signal processing block output, SLC output and measured d-axis current.	124
Fig. 4-20. d-axis current, SLC output and reference torque response to torque command step from 23 N·m to 28 N·m.....	124
Fig. 4-21. Comparison between resultant d-axis current and MTPA d-axis current.	125
Fig. 4-22. The reference torque and measured q-axis current.	125
Fig. 4-23. Comparison between the measured torque and reference torque in response to a step change in the reference torque.	126
Fig. 4-24. Relationship between torque command and the optimal stator flux for MTPA operation.	127
Fig. 4-25. Schematic of the proposed self-learning control scheme in f-t frame.	129
Fig. 4-26. Details of the virtual signal injection compensation unit.	130
Fig. 4-27. Details of self-learning controller for MTPA and field weakening operations.	132
Fig. 4-28. Flowchart of the proposed self-learning control scheme based on virtual signal injection aided direct flux vector control.....	134
Fig. 4-29. Reference torque, output of proposed self-learning control and the reference flux amplitude at 1000 r/min.....	135
Fig. 4-30. Responses of reference flux amplitude, output of the signal processing block and output of self-learning control.	136
Fig. 4-31. Reference d- and q-axis currents.	136
Fig. 4-32. Resultant torque, reference torque and reference flux amplitude after machine parameter changes.	137

Fig. 4-33. The simulation result of <i>LPFO</i> , reference flux amplitude and SLC output after machine parameter changes.	138
Fig. 4-34. Simulation results of reference torque, resultant torque as well as q-axis current.	138
Fig. 4-35. Responses of reference flux amplitude and SLC outputs when reference torque changes slowly.	139
Fig. 4-36. Integrator output when reference torque changes slowly.	140
Fig. 4-37. Resultant d- and q-axis currents.	140
Fig. 4-38. Responses of torque and stator flux amplitude to rapid reference torque changes.	141
Fig. 4-39. Integrator output when reference torque changes fast.	141
Fig. 4-40. Resultant d- and q-axis currents.	142
Fig. 4-41. Responses of reference torque and resultant torque when speed steps between 1000 r/min and 3000 r/min.	143
Fig. 4-42. Responses of signal processing block output, reference flux amplitude and SLC output to step changes in torque reference and step change in speed from 1000 r/min to 3000 r/min.	143
Fig. 4-43. Resultant d- and q-axis current at 1000 r/min and 3000 r/min.	144
Fig. 4-44. Responses of resultant d-axis current and ideal MTPA d-axis current to reference torque changes.	145
Fig. 4-45. MTPA quality indicator <i>LPFO</i> and resultant d-axis current.	146
Fig. 4-46. Resultant q-axis current and reference torque.	146
Fig. 4-47. MTPA d-axis current and responses of resultant d-axis current to reference torque change from 13 N·m to 18 N·m.	147
Fig. 4-48. Measured torque in response to reference torque change.	147

Fig. 4-49. Speed and measured d-axis current during transition from field-weakening region to constant torque region.	148
Fig. 4-50. Speed and measured d-axis current during transition from constant torque region to field-weakening region.	149
Fig. 4-51. Measured d-axis current and reference torque when torque reference steps from 20 N·m to 25 N·m at 3000 r/min.	149
Fig. 4-52. Reference voltage amplitude and reference torque when reference torque steps from 20 N·m to 25 N·m at 3000 r/min.	150
Fig. 4-53. Comparison between reference torque and measured torque when reference torque increased from 20 N·m to 25 N·m at 3000 r/min.	150
Fig. 5-1. Voltage ellipse, current limit circle, MTPV locus and constant torque locus.	156
Fig. 5-2. Block diagram of hybrid control scheme.	157
Fig. 5-3. Linear interpolation in transition region.	160
Fig. 5-4. Reference and resultant d- and q-axis currents of the proposed control scheme at 100 r/min.	162
Fig. 5-5. The resultant torque, reference torque and rotor speed when rotor speed and torque varies.	163
Fig. 5-6. Control performance of the proposed hybrid control scheme in transition region.	163
Fig. 5-7. Comparison between the percentage errors in i_d^* and the corresponding percentage errors in Ψ_s^* when speed is 400 r/min and reference torque is 45 N·m.	164
Fig. 5-8. Reference torque, FOC reference d-axis current and measured d-axis current at 400 r/min.	166
Fig. 5-9. FOC reference q-axis current, measured q-axis current and reference torque at 400 r/min.	166

Fig. 5-10. Reference torque, measured d-axis current and FOC reference d-axis current (i_d^*) at 850 r/min.	167
Fig. 5-11. Reference torque, observed flux amplitude and DFVC reference flux amplitude at 850 r/min.	168
Fig. 5-12. Transitions between DFVC and FOC with 20 N·m reference torque.	168
Fig. 5-13. Reference torque, observed flux amplitude and DFVC reference flux amplitude, Ψ_{sDFVC}^* , at 1000 r/min.	169
Fig. 5-14. Measured torque at 400 r/min, measured torque at 850 r/min and measured torque at 1000 r/min when torque reference steps from 30 N·m to 35 N·m.	169
Fig. 5-15. Reference torque, reference flux amplitude and observed flux amplitude at 2700 r/min.	170
Fig. 5-16. Reference torque and measured torque at 2700 r/min.	171
Fig. 5-17. Resultant voltage amplitude, maximum voltage amplitude and resultant d-axis current when reference torque steps from 25 N·m to 30 N·m at 2700 r/min.	171
Fig. A-1. Block diagram of inverter drive system.	203
Fig. A-2. Controller topology.	204
Fig. A-3. Set Path.	204
Fig. A-4. Simulink model of motor drive system.	205
Fig. A-5. Generation of C code.	205
Fig. A-6. Logic interfaces.	206
Fig. A-7. Check Ethernet connection.	206
Fig. B-1. Simulink model of motor drive system for virtual signal injection based FOC.	208
Fig. B-2. Subsystem of maximum voltage limit block.	209

Fig. B-3. Subsystem of current controller.....	209
Fig. B-4. Subsystem of reference currents generator.....	210
Fig. B-5. Subsystem of q-axis current calculation block in reference currents generator.....	211
Fig. B-6. Subsystem of virtual signal injection block.....	211
Fig. B-7. Subsystem of T_e^h calculator.	212
Fig. B-8. Simulink model of motor drive system for virtual signal injection based DFVC.....	212
Fig. B-9. Subsystem of Ψ_s^* generation block.	213
Fig. B-10. Subsystem of flux observer block.....	215
Fig. B-11. Simulink model of motor drive system for self-learning control in d-q frame.	217
Fig. B-12. Subsystem of reference currents generator.....	218
Fig. B-13. Subsystem of d-axis current generator.	218
Fig. B-14. Simulink model of motor drive system of self-learning control in f-t frame.	223
Fig. B-15. Subsystem of reference flux amplitude generator.	224
Fig. B-16. Overall Simulink model of hybrid control scheme.....	231
Fig. B-17. Subsystem of flux observer.	231
Fig. B-18. Subsystem of Ψ_s^* generator.....	233
Fig.C-1. Subsystem of Ψ_s^* generator.Constant current amplitude locus of different machine parameters and nonlinear machine model with $I_a = 77$ A.	241
Fig. C-2. $ i_d^2 \partial L_q / \partial i_q $, $ L_d i_q $ and $ \partial \Psi_d / \partial \beta $ when $I_a = 77$ A.....	242
Fig. C-3. $ i_d^2 \partial L_q / \partial i_q $, $ L_d i_q $ and $ \partial \Psi_d / \partial \beta $ when $I_a = 120$ A.	242

Fig. C-4. The MTPA points and the MTPA tracking simulation results of virtual signal injection control based on (2-12) and (C-8).243

Fig. C-5. Comparison of $|\partial L_q/\partial i_q|$, $|L_d i_q|$, $|\partial \Psi_d/\partial \beta|$ and $|\partial T_e/\partial \beta|$ when $I_a = 77$ A.244

Fig. D-1. Schematic of proposed electromagnetic model of IPM machines.....248

List of Tables

Table 1-1 2

Table 1-2 2

Table 1-3 13

Table 1-4 19

Table 2-1 42

Table 2-2 46

Table 2-3 47

Table 4-1 121

Table 5-1 165

Appendix A

A.1 Inverter Configuration

A 3-phase prototype IGBT inverter produced by SIEMENS for electric vehicle is adopted to test the proposed control schemes. The inverter topology is shown in Fig. A-1. The inverter is designed to operate at a 120 V nominal DC link voltage. However, a DC link voltage within the range of 80 V to 150 V is acceptable. The motor has to be connected to the inverter's 3-phase high voltage power output. Rotor position and winding temperature information are obtained by a resolver and temperature sensors in the motor, respectively, and are transmitted to inverter. The communication between computer and inverter is achieved through Ethernet.

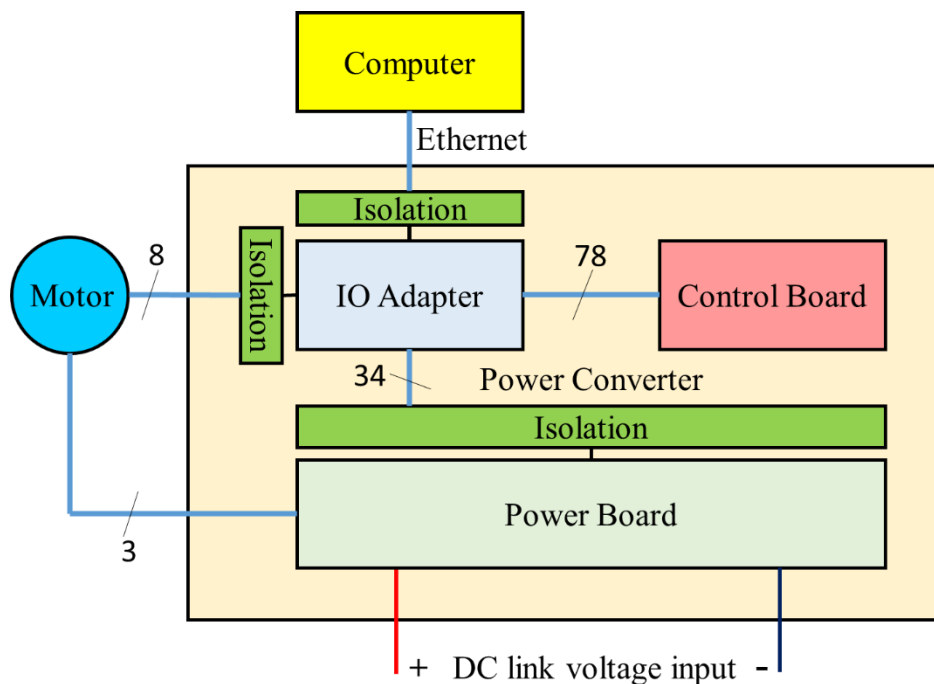


Fig. A-1. Block diagram of inverter drive system.

The schematic of controller platform is shown in Fig. A-2. The inverter is controlled by TigerSHARC ADSP-TS201S from Analog Devices. The controller code is built by the Visual DSP++ tool and transmitted to flash memory on the control board through NiOS embedded CPU in FPGA. The embedded CPU also enables a Matlab Graphical User Interface (GUI) which is developed to control and monitor the inverter operation on

a supervisory computer (Laptop or PC). During tests, the reference torque or currents are inputted into the Matlab GUI and the measured inverter and motor information such as speed, d- and q-axis currents, reference d- and q-axis voltages, etc., is displayed on the Matlab GUI.

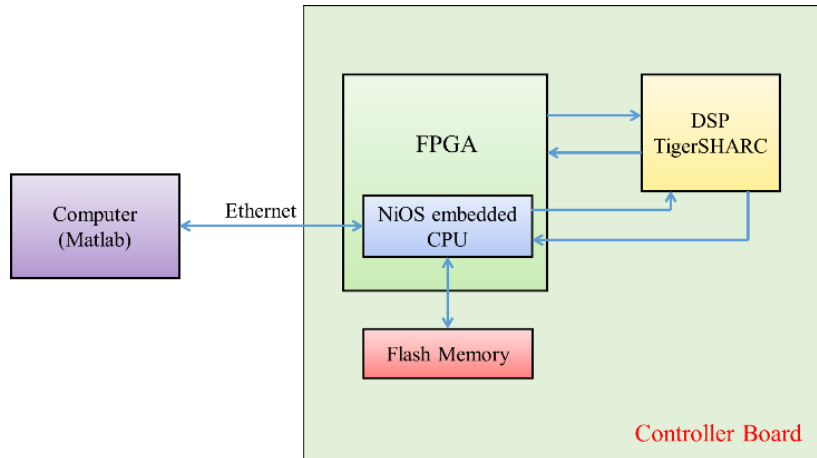


Fig. A-2. Controller topology.

A.2 Programming the Inverter

The controller code is generated and flashed according to the following procedure:

1. Add the library folder 'Simulation' (provide by SIEMENS) to the Matlab path by 'Set Path', as shown in Fig. A-3.

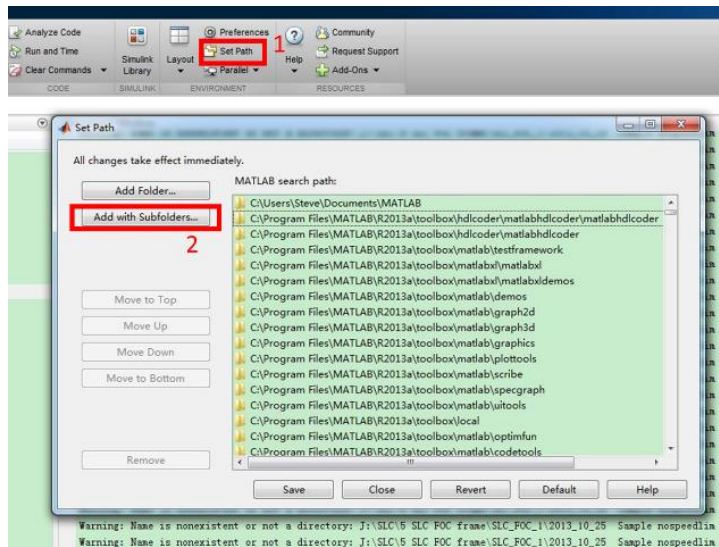


Fig. A-3. Set Path.

- Build Simulink blocks of the proposed control schemes in the motor drive system model configured for the inverter and feedback signals in Simulink (Fig. A-4) and simulate the drive system model to make sure if everything works as expected. The motor drive system model has defined all the low level interfaces such as data acquisitions, PWM generation, and communication with the supervisory computer and inverter controller when the drive is operational.

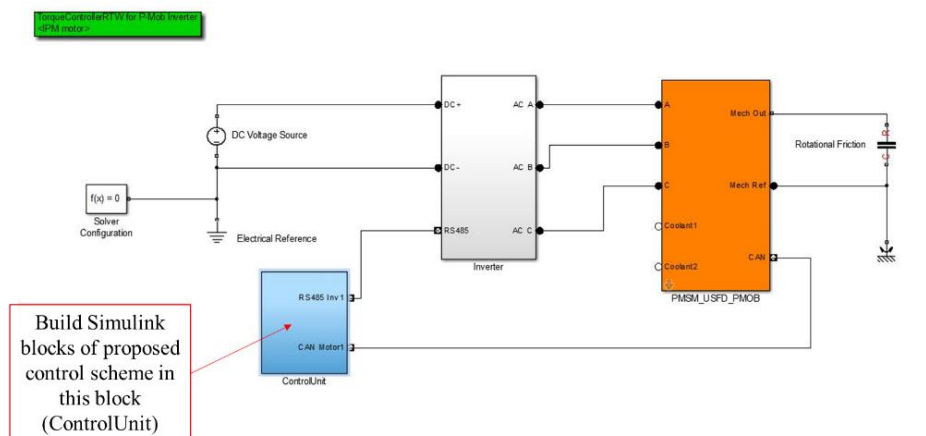


Fig. A-4. Simulink model of motor drive system.

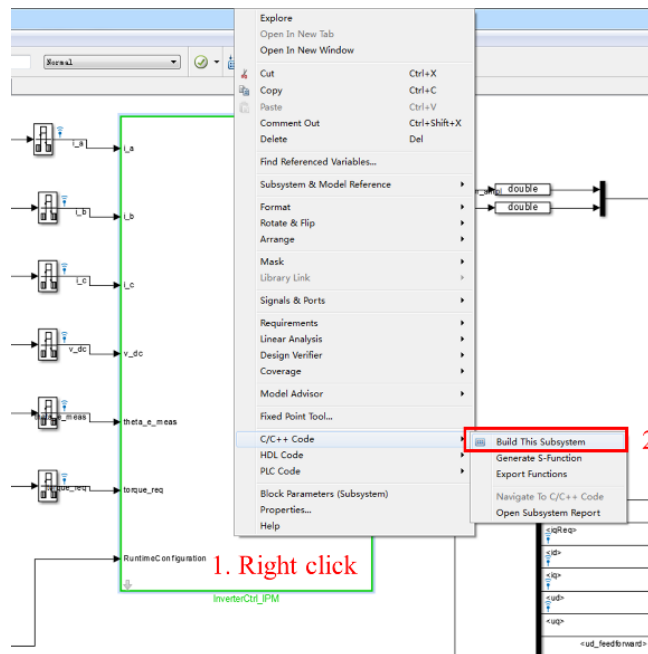


Fig. A-5. Generation of C code.

- To convert the control blocks/algorithms in the Control Unit, Fig. A-4, open the context menu by right clicking on the controller block. Choose the bottom: C/C++ code, click on "Build this Subsystem" (generating code only for the controller block).

As shown in Fig. A-5.

4. Update the resultant C code for Visual DSP++ by double clicking “UpdateCode.bat” in folder ‘Tigersharc’ which is provided by SIEMENS (Tigersharc→ RealtimeCode→ UpdatCode.bat”).
5. Run the “PMOB_Inverter.dpg” in the “Tigersharc” folder (provided by SIEMENS)
6. Recompile the C code by pressing F7. The control code is ready to be downloaded to the flash memory of the controller.
7. Connect the inverter interface ports shown in Fig. A-6 to appropriate signals and 12V logic power supply.

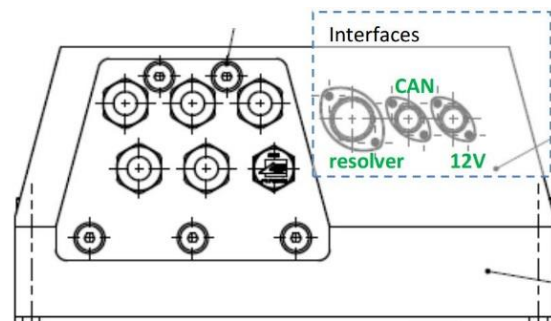


Fig. A-6. Logic interfaces.

8. Switch on the 12 V logic power supply of the inverter.
9. Connect the inverter to the PC via LAN port using Ethernet cable. Set the network IP address in the PC: Control Panel→Network and Internet→ Change adapter settings → Internet Protocol Version4 (TCP/IPV4)→Properties (set IP:192.168.32.1 Subnet mask:225.255.255.0)

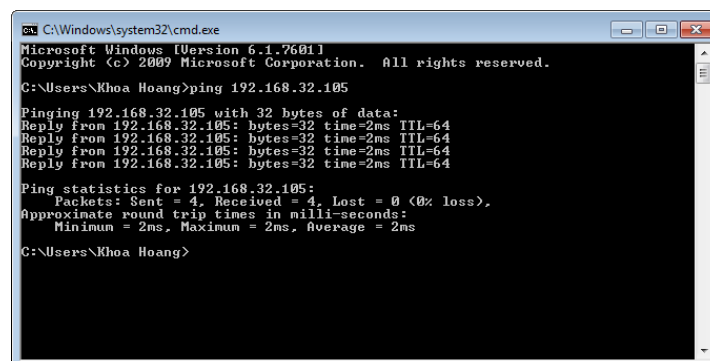


Fig. A-7. Check Ethernet connection.

10. Check Ethernet connection as shown in Fig. A-7. (Run →cmd → C: \User \User_Name \ping 192. 168. 32. 105) and make sure the ‘Lost=0’.

11. Use 'Tigersharc → RealtimeCode → Release → FlashTigersharcCodeViaEthernet.bat' (provided by SIEMENS) to flash the code.
12. Power cycle (turn on and off) the 12 V logic supply after the programming and code downloading.

Appendix B

Key blocks in Simulink models of the proposed control schemes are shown below.

B.1 Simulink Model of Virtual Signal Injection Control in d-q Frame

The overall Simulink model of virtual signal injection control in d-q frame is shown in Fig. B- 1. The Simulink blocks in Fig. B- 1 are numbered from 1 to 6. The No. 6 block is motor model.

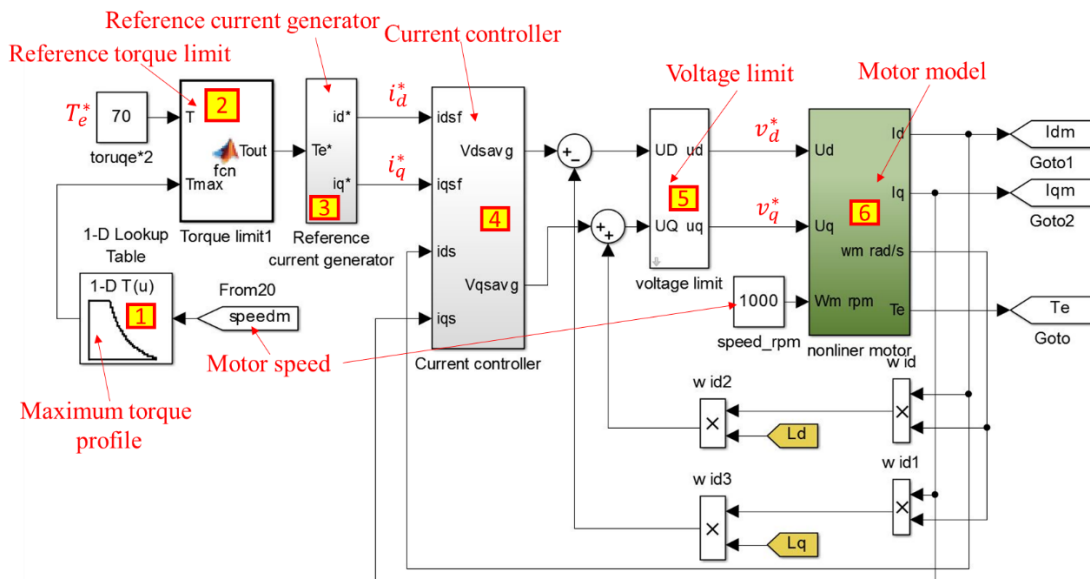


Fig. B- 1. Simulink model of motor drive system for virtual signal injection based FOC.

The No. 1 block in Fig. B- 1 is the maximum torque profile in a one dimensional look-up table whose input is motor speed and output is the maximum torque that corresponds to the speed. The No. 2 block in Fig. B- 1 is torque limit block. The code in No. 2 block is given below:

%%%%%%%%%% Code in No. 2 block in Fig. B- 1 %%%%%%%%%%

function Tout = fcn(T, Tmax)

%#codegen

% Tout is limited reference torque.

% T is reference torque, Tmax is output of No. 1 block

Tout=T;

if T>=Tmax

 Tout=Tmax;

end

%%%

The No. 5 block in Fig. B- 1 is voltage limit block. The subsystem of No. 5 block is given in Fig. B- 2.

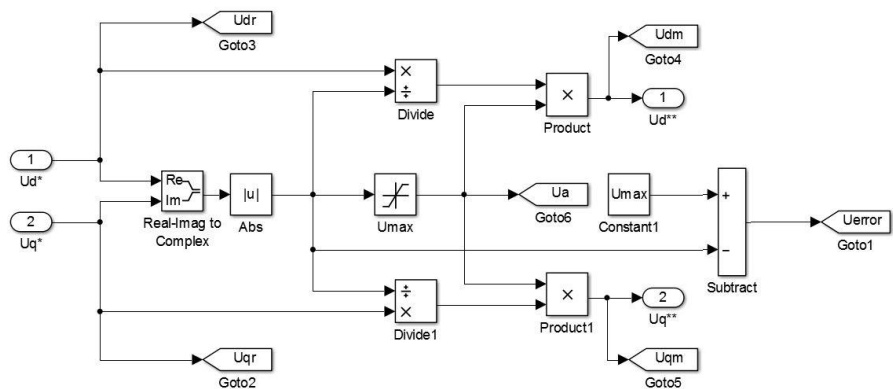


Fig. B- 2. Subsystem of maximum voltage limit block.

The No. 4 block in Fig. B- 1 is current controller. The subsystem of No. 4 block is shown in Fig. B- 3.

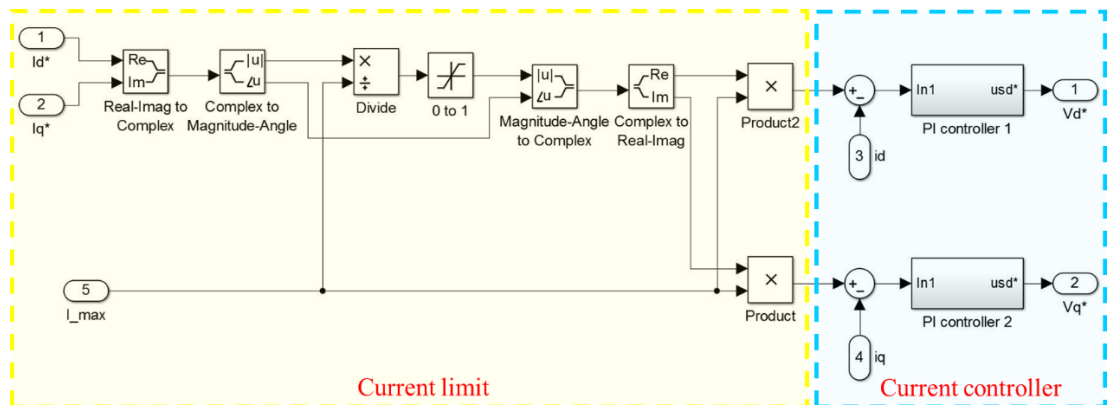


Fig. B- 3. Subsystem of current controller.

The No. 3 block in Fig. B- 1 is the reference current generator and the subsystem of No. 3 block is shown in Fig. B- 4.

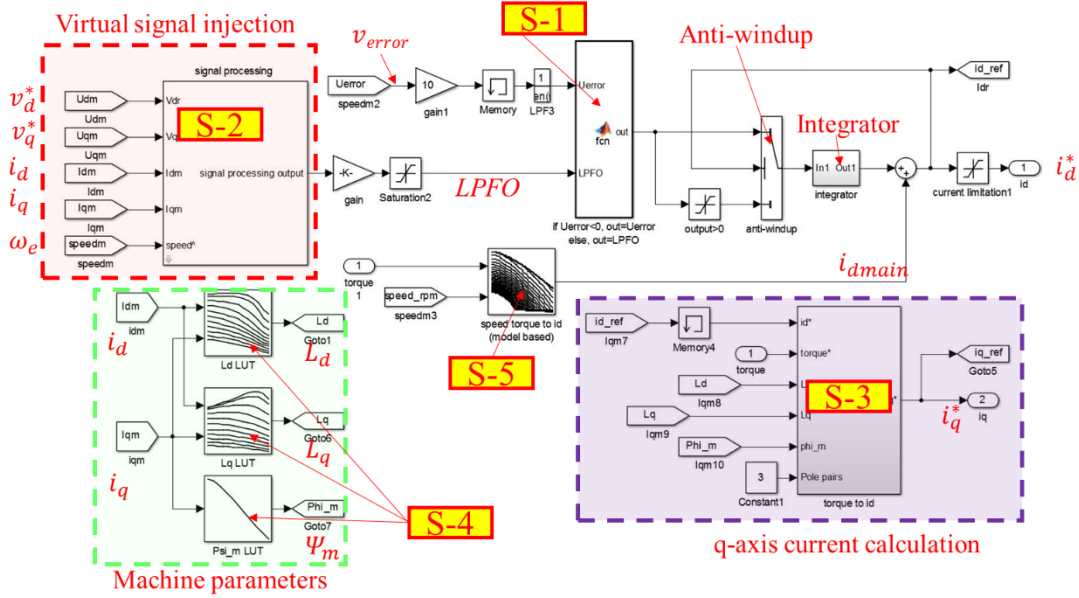


Fig. B- 4. Subsystem of reference currents generator.

The No. S-1 block in Fig. B- 4 is to identify whether the *LPFO* signal or v_{error} should be input into the integrator in Fig. B- 4. The code in No. S-1 block is given below.

```

%% Code in No. S-1 block in Fig. B- 4
function out= fcn(Uerror, LPFO)
%#codegen
% Uerror is  $v_{error}$  and LPFO is LPFO signal.
y=0;
if Uerror>5
    y=LPFO;
end
if Uerror>0&&Uerror<=5
    y=Uerror*LPFO/5;
end
if Uerror<=0
    y=-abs(Uerror);
end
    
```

out=y;

%%%

The No. S-4 blocks in Fig. B- 4 are look-up tables to obtain machine parameters for reference q-axis current calculation. The subsystem of q-axis current calculation block, No. S-3 block, in Fig. B- 4 is shown in Fig. B- 5.

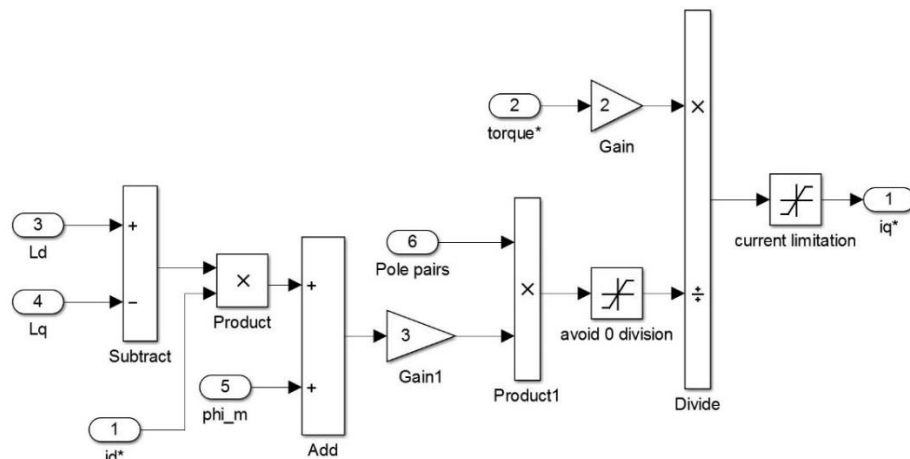


Fig. B- 5. Subsystem of q-axis current calculation block in reference currents generator.

The No. S-2 block in Fig. B- 4 is the virtual signal injection block. The subsystem of the virtual signal injection block is shown in Fig. B- 6.

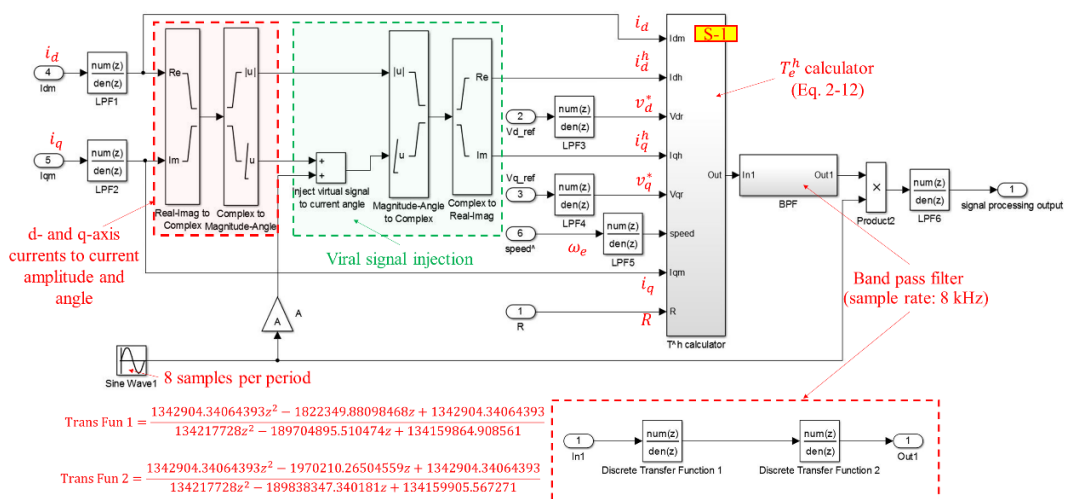


Fig. B- 6. Subsystem of virtual signal injection block.

The subsystem of the T_e^h calculator, i.e., the No. S-1 block in Fig. B- 6 is shown in Fig. B- 7.

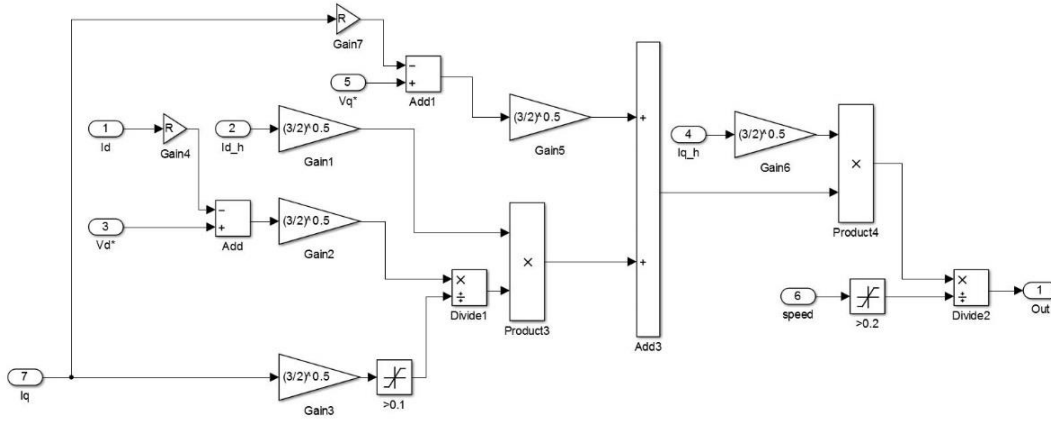


Fig. B- 7. Subsystem of T_e^h calculator.

B.2 Simulink Model of Virtual Signal Injection Control in f-t Frame

The Simulink model of motor drive system of virtual signal injection based DFVC is shown in Fig. B- 8. The blocks in Fig. B- 8 are numbered from 1 to 7. The No. 1 and No. 2 blocks are the torque profile look-up table and torque limit block which are the same as the No. 1 and No. 2 block in Fig. B- 1. The No. 7 block is motor model.

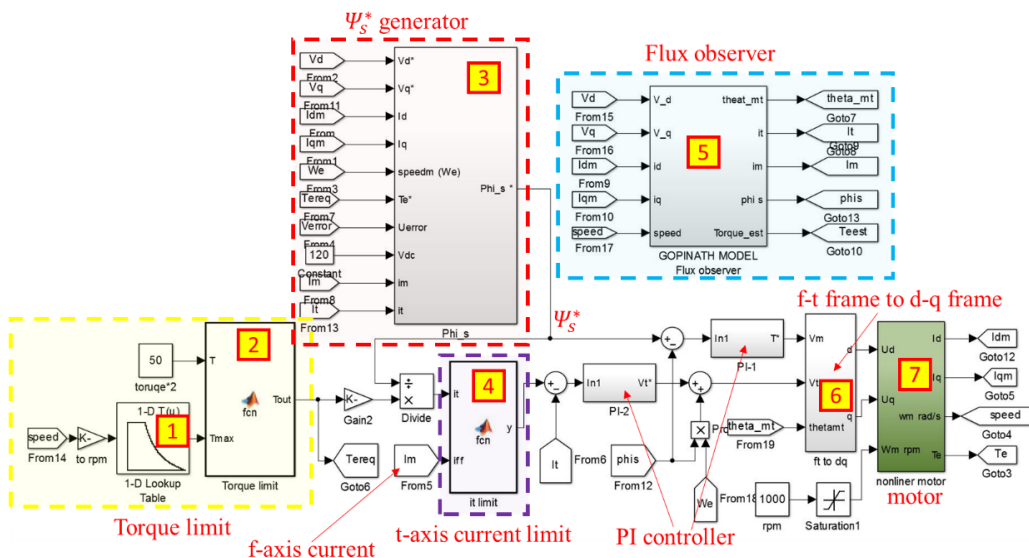


Fig. B- 8. Simulink model of motor drive system for virtual signal injection based DFVC.

The No. 3 block in Fig. B- 8 is the Ψ_s^* generation block and its subsystem is shown in Fig. B- 9. The No. S-1 block in Fig. B- 9 is the virtual signal injection block whose subsystem is the same as the one shown in Fig. B- 6. The No. S-2 blocks in Fig. B- 9 are two look-up tables to generate Ψ_{main} .

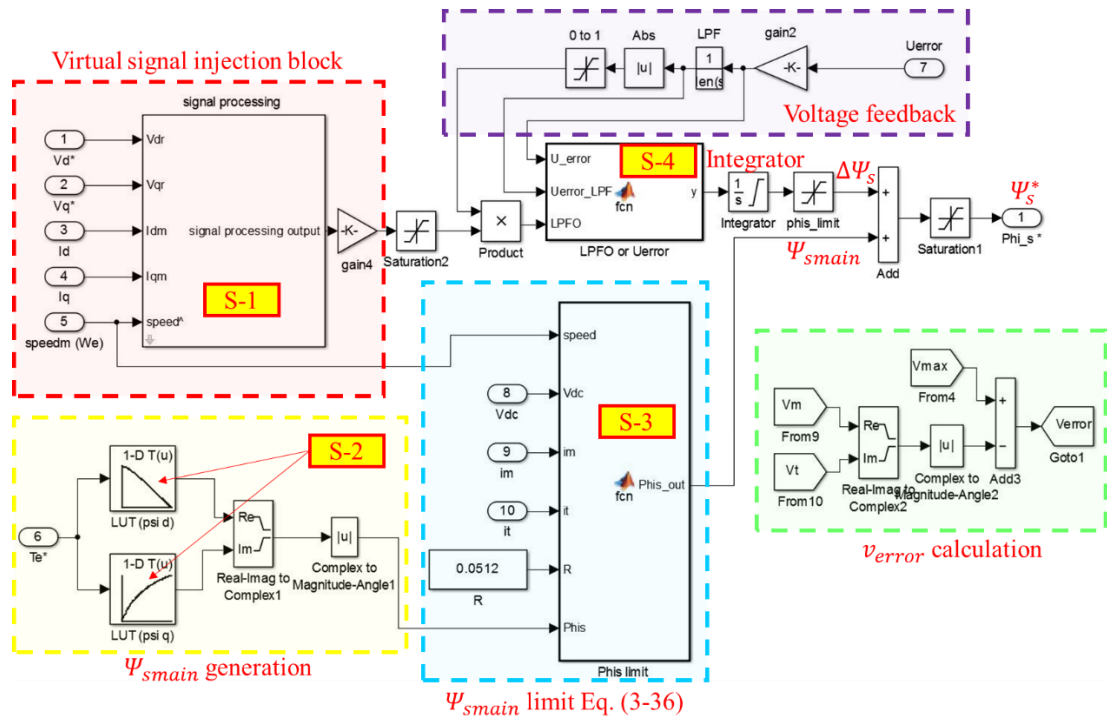


Fig. B- 9. Subsystem of Ψ_s^* generation block.

The No. S-4 block in Fig. B- 9 is to identify whether the *LPFO* signal or v_{error} should be input into the integrator in Fig. B- 9. The code in the No. S-4 block is given below.

```

%%%%%%%%%%%%%%%%%%%%%%%%%%%%%%%%%%%%%%%%%%%%%%%%%%%%%%%%%%%%%%%%%%%%%%%% Code in No. S-4 block in Fig. B- 9 %%%%%%%%%
function y = fcn(U_error,Uerror_LPF,LPFO)
% U_error is v_error, Uerror_LPF is the v_error filtered by low-pass filter.
% LPFO is LPFO signal.
% y is output
%#codegen
if Uerror_LPF<0
    y=U_error;
else

```

```
y=LPFO;
end
%%%%%%%%%%%%%%%%%%%%%%%%%%%%%%%%%%%%%%%%%%%%%%%%%%%%%%%%%%%%%%%%%%%%%%%%%
```

The No. S-3 block in Fig. B- 9 is flux amplitude limit block. The code in the block is shown below.

%%% Code in No. S-3 block in Fig. B- 9 %%

```
function Phis_out = fcn(Vdc,im,i_t,R,Phis)
%#codegen
% Phis_out is limited reference flux amplitude.
% Vdc=DC link voltage, im=f-axis current, i_t=t-axis current, R=stator resistance,
% Phis=reference flux amplitude
Vm=Vdc/(3)^0.5;
a=Vm^2-(R*im)^2;

if a<=0 % avoid dividing by zero
    a=0;
end

Phis_limit=1/speed*((a)^0.5-abs(R*i_t)); % Phis_limit is the maximum flux

if Phis_limit<=0
    Phis_limit=0;
end
Phis_out=Phis;

if Phis_out>=Phis_limit
    Phis_out=Phis_limit;
end

if Phis_out<=0
    Phis_out=0;
```

end

%%%%%%%%%

The No. 5 block in Fig. B- 8 is a closed loop flux observer, the subsystem of the flux observer is shown in Fig. B- 10. As is shown in Fig. B- 10, the closed loop flux observer consists of a current model based flux observer and a voltage model based flux observer. The voltage model based flux observer and the current model based flux observer are combined by a PI controller.

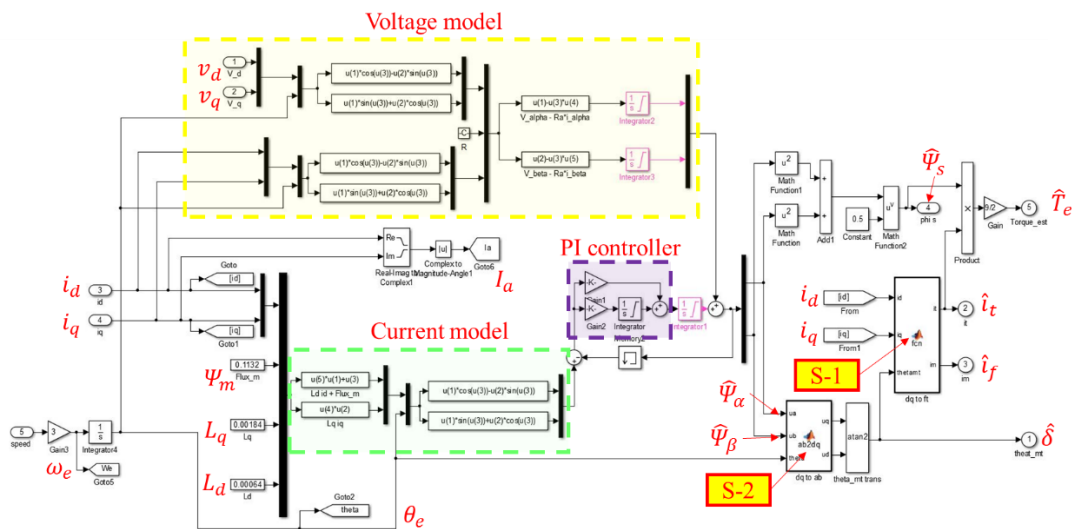


Fig. B- 10. Subsystem of flux observer block.

The codes in No. S-1 block and No. S-2 blocks in Fig. B- 10 are given below.

%%%%%%%%% Code in No. S-1 block in Fig. B- 10 %%%%%%%%%

function [i_t,im] = fcn(id,iq,thetamt)

##codegen

% i_t, im are t- and f-axis currents, respectively.

% id, iq are d- and q-axis currents, respectively.

% thetamt is $\hat{\delta}$.

im=cos(thetamt)*id+sin(thetamt)*iq;

i_t=-sin(thetamt)*id+cos(thetamt)*iq;

%%%%%%%%%

Code in No. S-2 block in Fig. B- 10

```
function [Phi_q,Phi_d] = ab2dq(Phi_a,Phi_b,theta)
%#codegen
% Phi_q, Phi_d are q- and d-axis flux amplitudes.
% Phi_a, Phi_b are  $\alpha$  and  $\beta$ -axis flux amplitudes.
% theta is  $\theta_e$ .
Phi_d =cos(theta)* Phi_a+sin(theta)* Phi_b;
Phi_q =-sin(theta)* Phi_a+cos(theta)* Phi_b;

```

The No. 4 block in Fig. B- 8 is t-axis current limit block. The code in it is given below.

Code in No.4 block in Fig. B- 8

```
function y = fcn(i_t,im)
%#codegen
% y is limited t-axis current.
% i_t and im are t- and f-axis currents, respectively.
y = i_t;
a=120^2-im^2;

if a<0 % avoid square root of negative
    a=0;
end

itmax=a^0.5; % itmax= maximum t-axis current

if it>=itmax
    y=itmax;
end

```

The code in No. 6 block in Fig. B- 8 is given below.

```

%%%%%%%%%%%%%% Code in No. 6 block in Fig. B- 8 %%%%%%%%%%%%%%%
function [Vd,Vq] = fcn(Vm,Vt,thetamt)
%#codegen
% Vd, Vq are the reference d- and q-axis voltages, respectively.
% Vm, Vt are the reference f- and t-axis voltages, respectively.
% thetamt is  $\hat{\delta}$ 
Vd=cos(thetamt)*Vm-sin(thetamt)*Vt;
Vq=sin(thetamt)*Vm+cos(thetamt)*Vt;
%%%%%%%%%%%%%%

```

B.3 Simulink Model of Self-learning Control in d-q Frame

The overall Simulink model of self-learning control in d-q frame is shown in Fig. B-11. The Simulink blocks in Fig. B- 11 are numbered from 1 to 6. The No. 1, No. 2, No. 4, No. 5, No. 6 blocks in Fig. B- 11 are the same as corresponding blocks in Fig. B- 1.

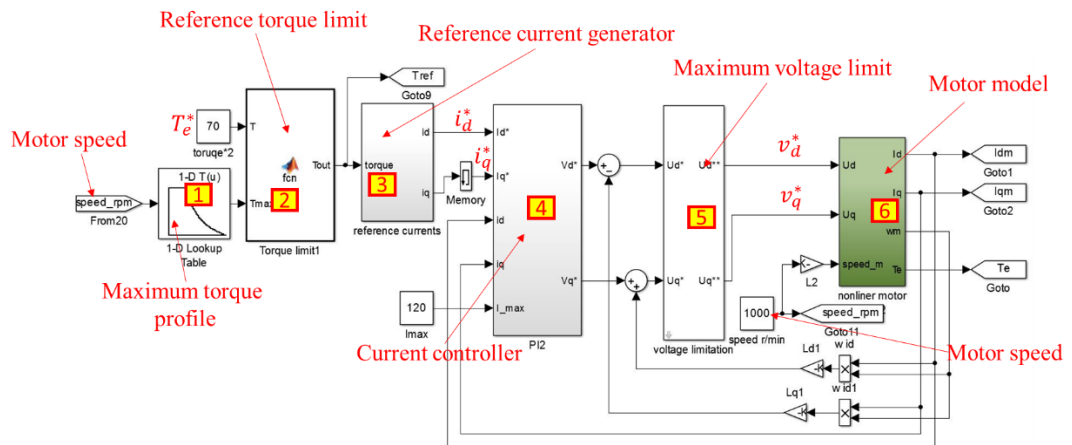


Fig. B- 11. Simulink model of motor drive system for self-learning control in d-q frame.

The subsystem of the No. 3 block in Fig. B- 11 is shown in Fig. B- 12.

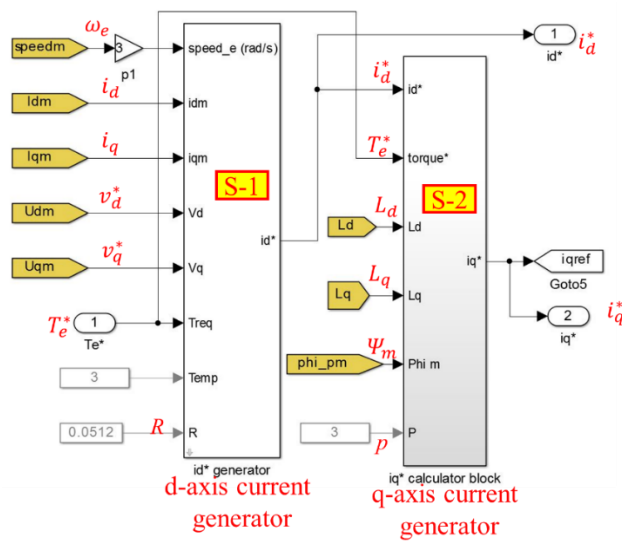


Fig. B- 12. Subsystem of reference currents generator.

The No. S-2 block in Fig. B- 12 is the q-axis current generator, and its subsystem is shown in Fig. B- 5. The No. S-1 block in Fig. B- 12 is the d-axis current generator and its subsystem is shown in Fig. B- 13.

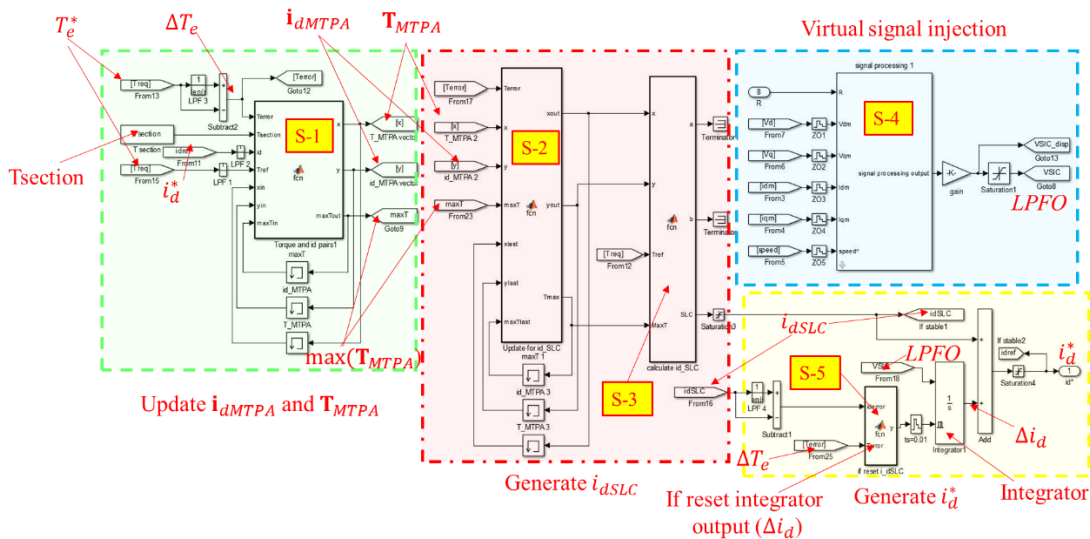


Fig. B- 13. Subsystem of d-axis current generator.

The No. S-4 in Fig. B- 13 is the virtual signal injection block. The subsystem of virtual signal injection block is shown in Fig. B- 6. The No. S-1 block in Fig. B- 13 is to update i_{dMTPA} and T_{MTPA} . The code in No. S-1 block is given below.

```

%% Code in block No. S-1 in Fig. B- 13 (Update  $i_{dMTPA}$  and  $T_{MTPA}$ )

```

Appendix

```
function [x,y,maxTout]= fcn(Terror,Tsection,id,Tref,xin,yin,maxTin)
%#codegen
% x is the updated  $\mathbf{T}_{MTPA}$  vector, y is the updated  $\mathbf{i}_{dMTPA}$  vector.
% maxTout is the updated  $\max(\mathbf{T}_{MTPA})$ .
% Terror is  $\Delta T_e^*$ .
% Tsection is a vector which records the boundary of torque sections.
% id is reference d-axis current.
% Tref is reference torque.
% xin and yin are the  $\mathbf{T}_{MTPA}$  vector and  $\mathbf{i}_{dMTPA}$  vector of the last time step, respectively.
% maxTin is the  $\max(\mathbf{T}_{MTPA})$  of the last time step.

s=36; % s-1=torque section number.
x=xin; % Set  $\mathbf{T}_{MTPA}$  equals to its value of last time step.
y=yin; % Set  $\mathbf{i}_{dMTPA}$  equals to its value of last time step.
maxTout=maxTin; % Set  $\max(\mathbf{T}_{MTPA})$  equals to its value of last time step.

if abs(Terror)<2 % Update  $\mathbf{T}_{MTPA}$  and  $\mathbf{i}_{dMTPA}$  if Terror < threshold
for i=1:1:s-1 % s-1=torque section number
% determine which torque section does Tref belong to.
if Tsection(i)<=Tref&&Tref<Tsection(i+1)

    x(i)=Tref; % update the  $i^{\text{th}}$  element in  $\mathbf{T}_{MTPA}$ 
    y(i)=id; % update the  $i^{\text{th}}$  element in  $\mathbf{i}_{dMTPA}$ 

% in block No.S-1,  $\mathbf{T}_{MTPA}$  vector,  $\mathbf{i}_{dMTPA}$  and  $\max(\mathbf{T}_{MTPA})$  are updated continuously.

    if maxTout<=Tref % update the  $\max(\mathbf{T}_{MTPA})$ 
        maxTout=Tref;
    end

end

end

end
```

end

%%%

The i_{dSLC} is generated by No. S-2 and No. S-3 blocks in Fig. B- 13. The codes in No. S-2 and No. S-3 blocks are given below.

%%% Code in block No. S-2 in Fig. B- 13 %%

function [xout,yout,Tmax] = fcn(Terror,x,y,maxT,xlast,ylast,maxTlast)

%#codegen

% xout,yout,Tmax are the \mathbf{T}_{MTPA} , \mathbf{i}_{dMTPA} and $\max(\mathbf{T}_{MTPA})$ for i_{dSLC} calculation.

% Terror is ΔT_e^* .

% x is the updated \mathbf{T}_{MTPA} vector from No. S-1 block output.

% y is the updated \mathbf{i}_{dMTPA} vector from No. S-1 block output.

% maxT is the updated $\max(\mathbf{T}_{MTPA})$ from No. S-1 block output.

% xlast and ylast are the \mathbf{T}_{MTPA} vector and \mathbf{i}_{dMTPA} vector in last time step, respectively.

% maxTlast is the $\max(\mathbf{T}_{MTPA})$ in last time step.

xout=xlast; %Set \mathbf{T}_{MTPA} equals to its value of last time step.

yout=ylast; % Set \mathbf{i}_{dMTPA} equals to its value of last time step.

Tmax=maxTlast; % Set $\max(\mathbf{T}_{MTPA})$ equals to its value of last time step.

if abs(Terror)>2

% if $\Delta T_e^* > \text{threshold}$, update \mathbf{T}_{MTPA} vector, \mathbf{i}_{dMTPA} and $\max(\mathbf{T}_{MTPA})$ for i_{dSLC} calculation.

 xout=x;

 yout=y;

 Tmax=maxT;

end

%%%

%%% Code in block No. S-3 in Fig. B- 13 %%

function [a,b,SLC] = fcn(x,y,Tref,MaxT)

Appendix

```
%#codegen
% a and b are the numbers of two adjacent torque sections of  $T_e^*$ .
% SLC is  $i_{dSLC}$ .
% x is the  $\mathbf{T}_{MTPA}$  vector, y is the  $\mathbf{i}_{dMTPA}$  vector generated by No. S-2 block.
% Tref is reference torque.
% maxTin is the  $\max(\mathbf{T}_{MTPA})$ .

s=36; % torque section number = s-1
a=1;
b=1;

if abs(Tref)>=abs(MaxT)
    Tref=MaxT;
end

for j=1:1:s-1

    if x(j)>=Tref % find the left adjacently recorded MTPA point of Tref.
        b=j;
        break;
    end

end

for i=s-1:-1:1 % find the right adjacently recorded MTPA point of Tref.

    if x(i)~=0;
        if x(i)<=Tref
            a=i;
            break;
        end
    end

end
```

```

end

if x(a)==x(b) % calculate  $i_{dSLC}$ .
    SLC=y(a);
else
    SLC=y(a)+(y(b)-y(a))*(Tref-x(a))/(x(b)-x(a)); % calculate  $i_{dSLC}$ .
end

if x(1)~=0

if 0<=Tref&&Tref<=x(1) % if  $T_e^*$  is in the first section.
    SLC=Tref/x(1)*y(1);
end

end

%%%%%%%%%%%%%%%%%%%%%%%%%%%%%%%%%%%%%%%%%%%%%%%%%%%%%%%%%%%%%%%%%%%%%%%%%
```

The block No. S-5 in Fig. B- 13 is to determine whether the integrator in Fig. B- 13 should be reset. The code in Fig. B- 13 is given below.

```

%%%%%%%%%%%%%%%%%%%%%%%%%%%%%%%%%%%%%%%%%%%%%%%%%%%%%%%%%%%%%%%%%%%%%%%%% Code in block No. S-5 in Fig. B- 13 %%%%%%%%%%%%%%%
function y = fcn(iderror,Terror)
%#codegen
% y is the signal to reset the integrator.
% iderror is the change of  $\Delta i_d$ .
% Terror is  $\Delta T_e^*$ .
y=0;
if abs(iderror)>1 % if the speed of the change in  $\Delta i_d$  is larger than a threshold.
    y=1; % rest integrator.
end

if abs(Terror)>2 % if  $\Delta T_e^*$  > threshold, rest integrator.
```

```

y=1;
end

```

%%%

B.4 Simulink Model of Self-learning Control in f-t Frame

The Simulink model of motor drive system of self-learning control in f-t frame is shown in Fig. B- 14. The blocks in Fig. B- 14 are numbered from 1 to 7. The No. 1, No. 2, No. 4, No. 5, No. 6 blocks in Fig. B- 14 are the same as corresponding blocks in Fig. B- 8.

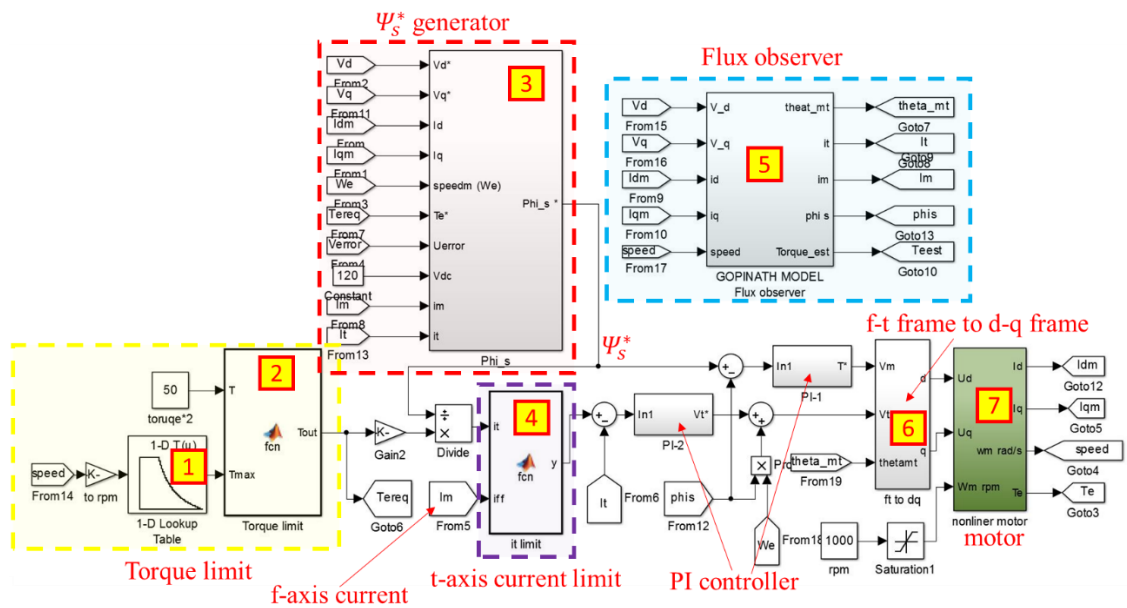


Fig. B- 14. Simulink model of motor drive system of self-learning control in f-t frame.

The No. 3 block in Fig. B- 14 is reference flux amplitude generator. The subsystem of the No. 3 block is shown in Fig. B- 15.

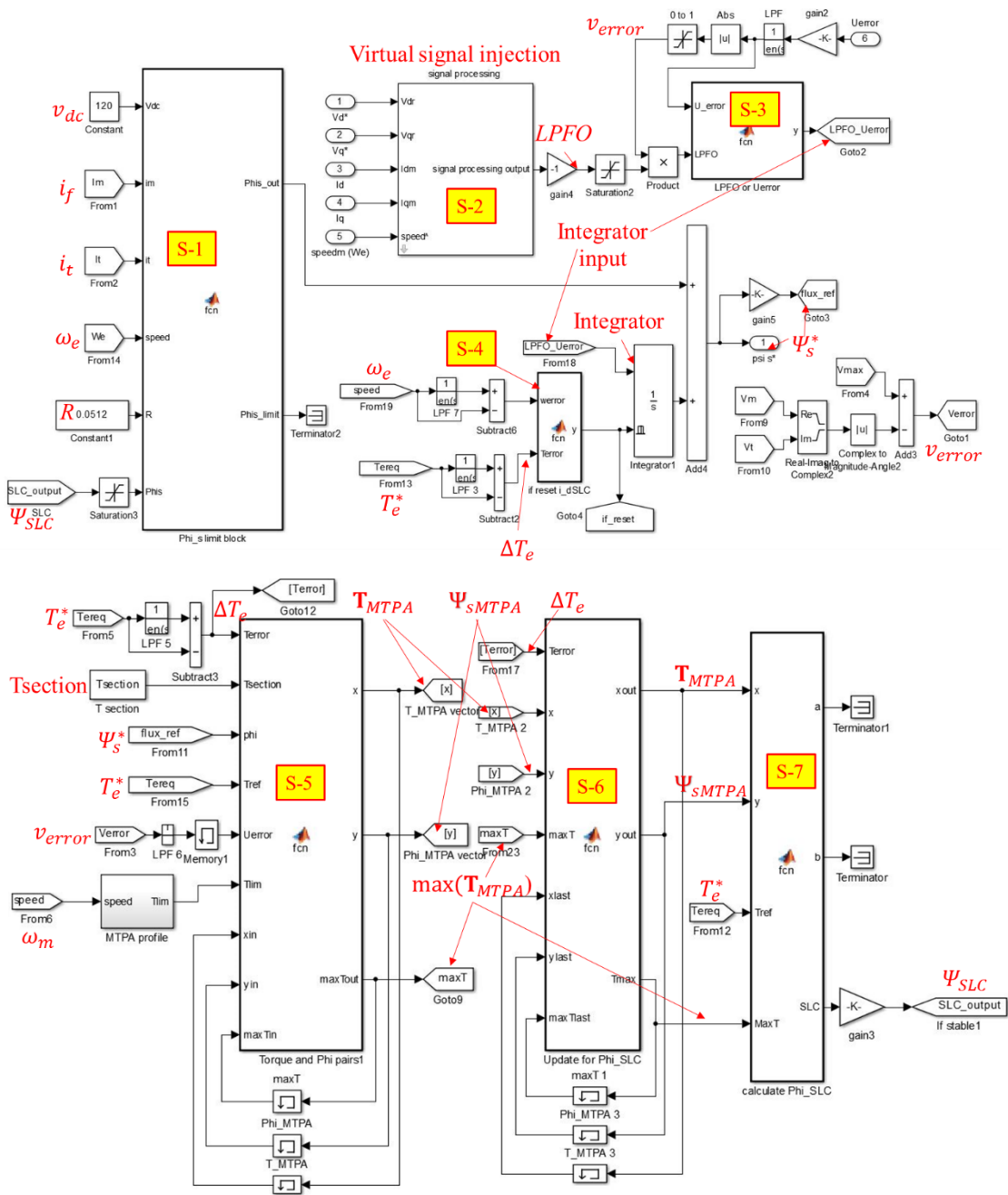


Fig. B- 15. Subsystem of reference flux amplitude generator.

The No. S-1 block in Fig. B- 15 is the reference flux amplitude limit block. The code in No. S-1 block is given below.

```

%% Code in No. S-1 block in Fig. B- 15
function [Phi_s_out,Phi_s_limit] = fcn(Vdc,im,i_t,speed,R,Phi)
%#codegen
% Phi_s_out is limited reference flux amplitude, Phi_s_limit is the maximum flux amplitude.
    
```

Appendix

```
% Vdc is DC link voltage, im is f-axis current, i_t is t-axis current.
% speed is rotor speed, R is stator resistance, Phis is reference flux amplitude.
Vm=Vdc/(3)^0.5;

if speed<1 % avoid dividing by zero.
    speed=1;
end

a=Vm^2-(R*im)^2;

if a<=0 % square root of negative
    a=0;
end

Phis_limit=1/speed*((a)^0.5-abs(R*i_t));

if Phis_limit<=0
    Phis_limit=0;
end

Phis_out=Phis;

if Phis_out>=Phis_limit
    Phis_out=Phis_limit;
end

if Phis_out<=0
    Phis_out=0;
end

%%%%%%%%%%%%%%%%%%%%%%%%%%%%%%%%%%%%%%%%%%%%%%%%%%%%%%%%%%%%%%%%%%%%%%%%%
```

The No. S-2 block in Fig. B- 15 is virtual signal injection block whose subsystem is the same as the one shown in Fig. B- 6. The No. S-3 block in Fig. B- 15 is to identify

whether the *LPFO* signal or v_{error} should be input into the integrator in Fig. B- 15. The code in No. S-3 block is given below.

%%%%%%%%%%%%%% Code in No. S-3 block in Fig. B- 15 %%%%%%%%%%%%%%

```
function y = fcn(U_error,LPFO)
%#codegen
% U_error is  $v_{error}$ 
% LPFO is the LPFO signal.
```

```
if U_error<0
    y=U_error;
else
    y=LPFO;
end
```

%%%%%%%%%%%%%%

The No. S-4 block in Fig. B- 15 is to identify whether the integrator in Fig. B- 15 should be reset. The code in No. S-4 is given below.

%%%%%%%%%%%%%% Code in No. S-4 block in Fig. B- 15 %%%%%%%%%%%%%%

```
function y = fcn(werror,Terror)
%#codegen
% y=0, do not reset integrator. y=1, reset integrator.
% werror is the change in speed. Terror is the change in reference torque, i.e.,  $\Delta T_e^*$  .
```

```
y=0;
if abs(Terror)>2 % if  $\Delta T_e^*$  is larger than the threshold.
    y=1;
end
```

```
if abs(werror)>2 % if speed change is larger than a threshold, reset the integrator.
    y=1;
end
```

%%%

The No. S-5 block in Fig. B- 15 is to update Ψ_{SMTPA} and \mathbf{T}_{MTPA} . The code in No. S-5 block is given below.

%%% Code in No. S-5 block in Fig. B- 15 %%

function [x,y,maxTout]= fcn(Terror,Tsection,phi,Tref,Uerror,Tlim,xin,yin,maxTin)

%#codegen

% x is the updated \mathbf{T}_{MTPA} vector, y is the updated Ψ_{SMTPA} vector.

% maxTout is the updated $\max(\mathbf{T}_{MTPA})$.

% Terror is ΔT_e^* . Tsection is a vector which records the boundary of torque sections.

% phi is reference flux amplitude.

%Tref is reference torque.

% Uerror is v_{error}

% Tlim is the T_{lim}^* .

% xin and yin are the \mathbf{T}_{MTPA} vector and Ψ_{SMTPA} vector of last time step, respectively.

% maxTin is the $\max(\mathbf{T}_{MTPA})$ of last time step.

s=36; % s-1 is torque section number

x=xin; % Set \mathbf{T}_{MTPA} equals to its value of last time step.

y=yin; % Set Ψ_{SMTPA} equals to its value of last time step.

maxTout=maxTin; % Set $\max(\mathbf{T}_{MTPA})$ equals to its value of last time step.

if abs(Terror)<2 % if Terror < threshold, update \mathbf{T}_{MTPA} and Ψ_{SMTPA}

for i=1:1:s-1 % s-1 is the last torque section number

if Tsection(i)<=Tref&&Tref<Tsection(i+1)

% determine which torque section does Tref belong to.

x(i)=Tref; % update the i^{th} element in \mathbf{T}_{MTPA}

y(i)=phi; % update the i^{th} element in Ψ_{SMTPA}

% \mathbf{T}_{MTPA} vector, Ψ_{SMTPA} vector and $\max(\mathbf{T}_{MTPA})$ are updated continuously.

if maxTout<=Tref % update the $\max(\mathbf{T}_{MTPA})$

maxTout=Tref;

end

```

end

end

end

if Uerror<2 % if  $v_{error} < \text{threshold}$ , stop updating  $\mathbf{T}_{MTPA}$  vector and  $\Psi_{SMTPA}$  vector.
    x=xin;
    y=yin;
    maxTout=maxTin;
end

if Tref>=Tlim
% if reference torque is larger than  $T_{lim}^*$ , stop updating  $\mathbf{T}_{MTPA}$  vector
% and  $\Psi_{SMTPA}$  vector.
    x=xin;
    y=yin;
    maxTout=maxTin;
end

%%%%%%%%%%%%%%%%%%%%%%%%%%%%%%%%%%%%%%%%%%%%%%%%%%%%%%%%%%%%%%%%%%%%%%%%

```

The No. S-6 and No. S-7 blocks in Fig. B- 15 are to update Ψ_{SLC} . The code in No. S-6 and No. S-7 blocks are given below.

```

%%%%%%%%%%%%%%%%%%%%%%%%%%%%%%%%%%%%%%%%%%%%%%%%%%%%%%%%%%%%%%%%%%%%%%%% Code in No. S-6 block in Fig. B- 15 %%%%%%%%%
function [xout,yout,Tmax] = fcn(Terror,x,y,maxT,xlast,ylast,maxTlast)
%#codegen
% xout, yout, Tmax are the  $\mathbf{T}_{MTPA}$ ,  $\Psi_{SMTPA}$  and  $\max(\mathbf{T}_{MTPA})$  for  $\Psi_{SLC}$  calculation.
% Terror is  $\Delta T_e^*$ .
% x is the updated  $\mathbf{T}_{MTPA}$ , y is the updated  $\Psi_{SMTPA}$  generated by No. S-5 block.
% maxT is the updated  $\max(\mathbf{T}_{MTPA})$  from No. S-5 block output.
% xlast is the  $\mathbf{T}_{MTPA}$  vector of last time step, ylast is the  $\Psi_{SMTPA}$  vector of last time step.
% maxTlast is the  $\max(\mathbf{T}_{MTPA})$  in last time step.

```

```

xout=xlast;
yout=ylast;
Tmax=maxTlast;

if abs(Terror)>2
% if  $\Delta T_e^*$ >threshold, update  $\mathbf{T}_{MTPA}$ ,  $\Psi_{sMTPA}$  and  $\max(\mathbf{T}_{MTPA})$  for  $\Psi_{SLC}$  calculation.
    xout=x;
    yout=y;
    Tmax=maxT;
end

%%%%%%%%%%%%%%%%%%%%%%%%%%%%%%%%%%%%%%%%%%%%%%%%%%%%%%%%%%%%%%%%%%%%%%%%

%%%%%%%%%%%%%%%%%%%%%%%%%%%%%%%%%%%%%%%%%%%%%%%%%%%%%%%%%%%%%%%%%%%%%%%% Code in No. S-7 block in Fig. B- 15 %%%%%%%%%
function [a,b,SLC] = fcn(x,y,Tref,MaxT)
%#codegen
% a, b are the element numbers of two torque sections.
% The two torque sections are adjacent to the torque section which  $T_e^*$  is inside.
% SLC is  $\Psi_{SLC}$ .
% x, y are the  $\mathbf{T}_{MTPA}$  and  $\Psi_{sMTPA}$  from block No. S-6 for  $\Psi_{SLC}$  calculation.
% Tref is reference torque.
% maxT is the  $\max(\mathbf{T}_{MTPA})$ .
s=36; % torque section number = s-1
a=1;
b=1;
if abs(Tref)>=abs(MaxT)
    Tref=MaxT;
end

for j=1:1:s-1
    if x(j)>=Tref % find the left adjacently recorded MTPA point of Tref.
        b=j;
        break;
    end
end

```

```

end
end

for i=s-1:-1:1 % find the right adjacently recorded MTPA point of Tref.
    if x(i)~=0;
        if x(i)<=Tref
            a=i;
            break;
        end
    end
end

if x(a)==x(b) % calculate  $\Psi_{SLC}$ .
    SLC=y(a);
else
    SLC=y(a)+(y(b)-y(a))*(Tref-x(a))/(x(b)-x(a));
end

if x(1)~=0
    if 0<=Tref&&Tref<=x(1) % if  $T_e^*$  is in the first section
        SLC=Tref/x(1)*y(1);
    end
end

%%%%%%%%%%

```

B.5 Simulink Model of Hybrid Control Scheme

The overall Simulink model of motor drive system of hybrid control scheme is shown in Fig. B- 16. The blocks in Fig. B- 16 are numbered from 1 to 7. The No. 1, No. 2, No. 4, No. 6, No. 7 blocks in Fig. B- 16 are the same as corresponding blocks in Fig. B- 8.

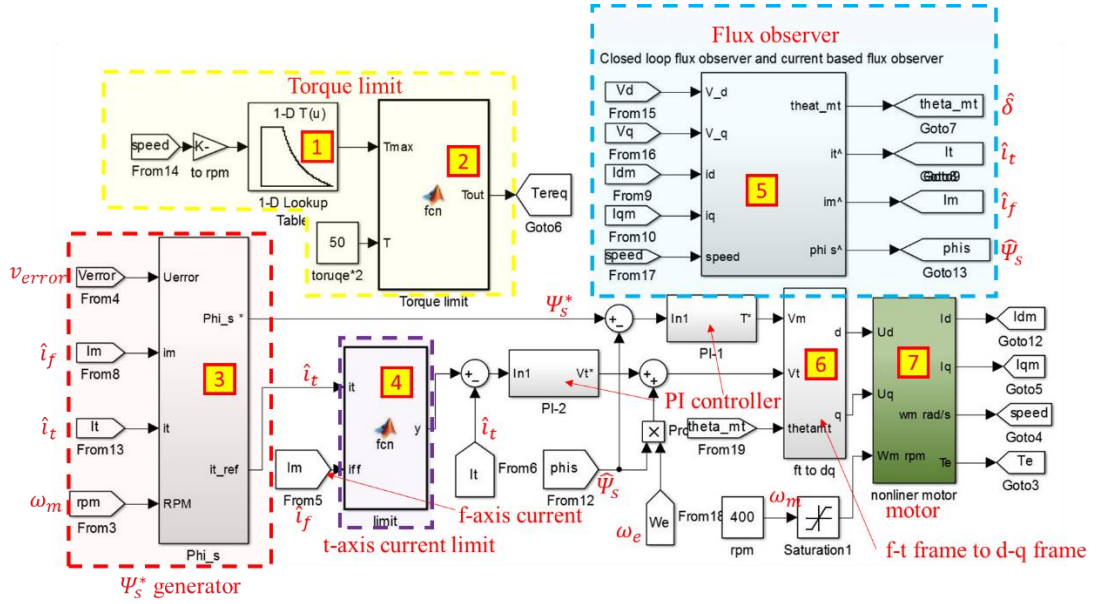


Fig. B- 16. Overall Simulink model of hybrid control scheme.

The No. 5 block in Fig. B- 16 is a flux observer whose subsystem is given in Fig. B- 17. The No. S-1 and No. S-2 blocks in Fig. B- 17 are the same as the corresponding blocks in Fig. B- 17.

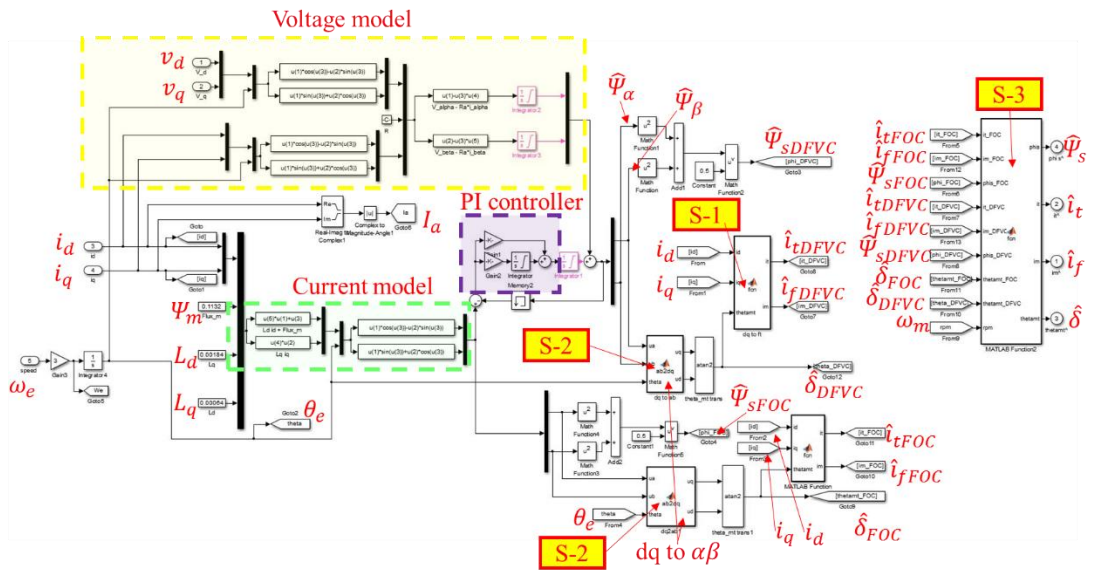


Fig. B- 17. Subsystem of flux observer.

The No. S-3 block in Fig. B- 17 is to calculate $\hat{\Psi}_s$ and \hat{i}_t based on $\hat{\Psi}_{SFOC}$, \hat{i}_{tFOC} , $\hat{\Psi}_{SDFVC}$, \hat{i}_{tDFVC} and rotor speed. The code in No. S-3 block is given below.

```

%%%%%%%%%%%%%%%%%%%%%%%%%%%%%%%%%%%%%%%%%%%%%%%%%%%%%%%%%%%%%%%%%%%%%%%% Code in No. S-3 block in Fig. B- 17 %%%%%%%%%
function [phis,it,im,thetamt] = fcn(it_FOC, im_FOC, phis_FOC, it_DFVC, im_DFVC,
phis_DFVC, thetamt_FOC, thetamt_DFVC, rpm)
%#codegen
% phis is  $\hat{\Psi}_s$ , i_t is  $\hat{i}_t$ , im is  $\hat{i}_f$ , thetamt is  $\hat{\delta}$ .
% it_FOC is  $\hat{i}_{tFOC}$ , im_FOC is  $\hat{i}_{mFOC}$ , phis_FOC is  $\hat{\Psi}_{sFOC}$ ,
% it_DFVC is  $\hat{i}_{tDFVC}$ , im_DFVC is  $\hat{i}_{mDFVC}$ , phis_DFVC is  $\hat{\Psi}_{sDFVC}$ .
% thetamt_FOC is  $\hat{\delta}_{FOC}$ , thetamt_DFVC is  $\hat{\delta}_{DFVC}$ , rpm is rotor speed in r/min.

a=800; %  $\omega_1$ , i.e., lower boundary of transition region.
b=900; %  $\omega_2$ , i.e., upper boundary of transition region.
L=b-a;

% in transition region
phis=phis_FOC*(b-rpm)/L+phis_DFVC*(rpm-a)/L;
i_t=it_FOC*(b-rpm)/L+it_DFVC*(rpm-a)/L;
im=im_FOC*(b-rpm)/L+im_DFVC*(rpm-a)/L;
thetamt=thetamt_FOC*(b-rpm)/L+thetamt_DFVC*(rpm-a)/L;
% in FOC control mode
if rpm<=a
    phis=phis_FOC;
    i_t=it_FOC;
    im=im_FOC;
    thetamt=thetamt_FOC;
end
% in DFVC control mode
if rpm>=b
    phis=phis_DFVC;
    i_t=it_DFVC;
    im=im_DFVC;
    thetamt=thetamt_DFVC;
end
%%%%%%%%%%%%%%%%%%%%%%%%%%%%%%%%%%%%%%%%%%%%%%%%%%%%%%%%%%%%%%%%%%%%%%%%

```

The No. 3 block in Fig. B- 16 is Ψ_s^* generator. The subsystem of the Ψ_s^* generator is given in Fig. B- 18.

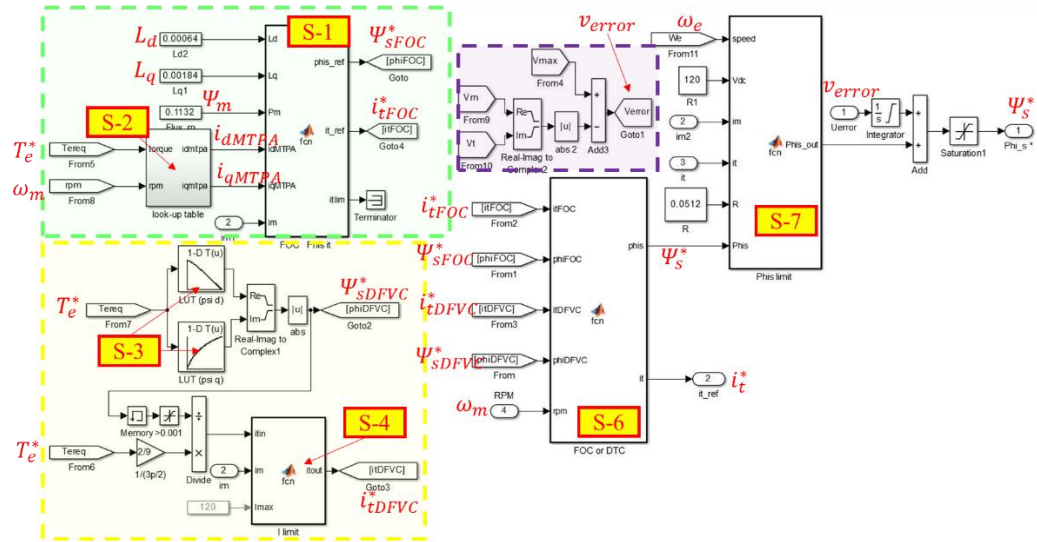


Fig. B- 18. Subsystem of Ψ_s^* generator.

As it is shown in Fig. B- 18, look-up tables for generating the optimal d- and q-axis currents are inside the No. S-2 block. The output of No. S-2 are i_{dMTPA} and i_{qMTPA} . The resultant i_{dMTPA} and i_{qMTPA} are input into No.S-1 block. The code inside the No. S-1 block is given below.

```

%%%%%%%%%% Code in No. S-1 block in Fig. B- 18 %%%%%%%%%%
function [phis_ref, it_ref, itlim] = fcn(Ld, Lq, Pm, idMTPA, iqMTPA, im)
%#codegen
% phis_ref is  $\Psi_{sFOC}^*$ , it_ref is  $i_{tFOC}^*$ , itlim is the maximum t-axis current.
% Ld is d-axis inductance, Lq is q-axis inductance
% Pm is flux linkage due to permanent magnet
% idMTPA is the optimal d-axis current for MTPA operation.
% iqMTPA is the optimal q-axis current for MTPA operation.
% im is the estimated f-axis current.
a=(Ld*idMTPA+Pm)^2+(Lq*iqMTPA)^2;
if a>=0 % avoid dividing by zero
    phis_ref=a^0.5;

```

```

else
    phis_ref=0;
end

thetamt=atan2(Lq*iqMTPA,Ld*idMTPA+Pm); % calculate  $\delta$ .

it_ref=-sin(thetamt)*idMTPA+cos(thetamt)*iqMTPA; % calculate  $i_{tFOC}^*$ .

Imax=idMTPA^2+iqMTPA^2;

b=Imax-(im)^2;

if b<=0 % avoid squire root of negative.
    b=0;
end

itlim=(b)^0.5;

if it_ref>=itlim
    it_ref=itlim;
end

%%%%%%%%%%%%%%%%%%%%%%%%%%%%%%%%%%%%%%%%%%%%%%%%%%%%%%%%%%%%%%%%%%%%%%%%

```

The No. S-3 blocks in Fig. B- 18 are look-up tables for generating Ψ_{SDFVC}^* . The No. S-4 block in Fig. B- 18 is a t-axis current limit block. The code in the No. S-4 block is given below.

```

%%%%%%%%%%%%%%%%%%%%%%%%%%%%%%%%%%%%%%%%%%%%%%%%%%%%%%%%%%%%%%%%%%%%%%%% Code in No. S-4 block in Fig. B- 18 %%%%%%%%%
function itout = fcn(itin,im,Imax)
%#codegen
% itout is the limited t-axis current. itin is the refercne t-axis current.
% im is the estimated f-axis current. Imax is the maximum current amplitude.
itout=itn;

```

```

aa=(Imax)^2-(im)^2;
if aa<=0 % avoid square root of negative.
    aa=0;
end

itlim=(aa)^0.5;

if abs(itout)>=itlim
    itout=itlim;
end

%%%%%%%%%%%%%%%%%%%%%%%%%%%%%%%%%%%%%%%%%%%%%%%%%%%%%%%%%%%%%%%%%%%%%%%%

```

The No. S-6 block in Fig. B- 18 is to determine whether the FOC or DFVC should be adopted by the hybrid control scheme. The code in No. S-6 block is given below.

```

%%%%%%%%%%%%%%%%%%%%%%%%%%%%%%%%%%%%%%%%%%%%%%%%%%%%%%%%%%%%%%%%%%%%%%%% Code in No.S-6 block in Fig. B- 18 %%%%%%%%%
function [phis,it] = fcn(itFOC,phiFOC,itDFVC,phiDFVC,rpm)
%#codegen
% phis is  $\Psi_s^*$ , i_t is  $i_t^*$ .
% itFOC is  $i_{tFOC}^*$ , phiFOC is  $\Psi_{sFOC}^*$ , itDFVC is  $i_{tDFVC}^*$ , phiDFVC is  $\Psi_{sDFVC}^*$ , rpm is speed.

a=800; % a is  $\omega_1$ 
b=900; % b is  $\omega_2$ 
L=b-a;

phis=phiFOC*(b-rpm)/L+phiDFVC*(rpm-a)/L;
i_t=itFOC*(b-rpm)/L+itDFVC*(rpm-a)/L;

if rpm<=a % if speed is smaller than  $\omega_1$ , FOC is adopted
    phis=phiFOC;
    i_t=itFOC;
end

```

```

if rpm>=b % if speed is larger than  $\omega_2$ , FOC is adopted
    phis=phiDFVC;
    i_t=itDFVC;
end
%%%%%%%%%%%%%%%%%%%%%%%%%%%%%%%%%%%%%%%%%%%%%%%%%%%%%%%%%%%%%%%%%%%%%%%%

```

The No. S-7 block in Fig. B- 18 is flux amplitude limit block. The code in the No. S-7 block is given below.

```

%%%%%%%%%%%%%%%%%%%%%%%%%%%%%%%%%%%%%%%%%%%%%%%%%%%%%%%%%%%%%%%%%%%%%%%% Code No. S-7 block in Fig. B- 18 %%%%%%%%%
function Phis_out = fcn(speed,Vdc,im,i_t,R,Phis)
%#codegen
% Phis_out is  $\Psi_s^*$  after limit.
% speed is rotor speed, Vdc is DC link voltage, im is estimated f-axis current.
% i_t is estimated t-axis current, R is stator resistance, Phis is reference flux amplitude.

Vm=Vdc/(3)^0.5;

if speed<1 % avoid dividing by zero
    speed=1;
end

a=Vm^2-(R*im)^2;

if a<=0 % avoid square root of negative.
    a=0;
end

Phis_limit=1/speed*((a)^0.5-abs(R*i_t));

if Phis_limit<=0
    Phis_limit=0;

```

end

Phis_out=Phis;

if Phis_out>=Phis_limit

 Phis_out=Phis_limit;

end

if Phis_out<=0

 Phis_out=0;

end

%%%%%%%%%

Appendix C

Virtual signal injection error analysis

The electromagnetic torque can be expressed as in (1-3) and (1-3) is repeated in (C-1) for convenience.

$$T_e = \frac{3p}{2} [\Psi_m i_q + (L_d - L_q) i_d i_q] \quad (C-1)$$

according to (1-1) and (1-2), in steady state:

$$\Psi_m = \Psi_d - L_d i_d = \frac{v_q - R i_q}{p \omega_m} - L_d i_d \quad (C-2)$$

$$(L_d - L_q) = \frac{v_d - R i_d}{p \omega_m i_q} + L_d \quad (C-3)$$

Substituting (C-2), (C-3) into (C-1) leads to:

$$T_{e-1} = \frac{3p}{2} \left[\left(\frac{v_q - R i_q}{p \omega_m} - L_d i_d \right) + \left(L_d + \frac{v_d - R i_d}{p \omega_m i_q} \right) i_d \right] i_q \quad (C-4)$$

As can be seen from (C-1), the torque is contributed by the alignment torque component, $\Psi_m i_q$, and the reluctance torque component due to the difference in the d- and q-axis inductances, $L_d - L_q$. As discussed in Chapter 2, the machine parameters such as Ψ_m , L_d and L_q vary with operating conditions, however, since the variation of current angle, β , and machine parameters are small over the very short period of the injected signals, the machine parameters can be considered as constants in one period of injected signal and according to (C-1) the relationship between torque and d- and q-axis currents can be approximated by a polynomial in form of (C-5):

$$T_{e-1} = (a + b i_d) i_q \quad (C-5)$$

$$a = \Psi_m \quad (C-6)$$

$$b = (L_d - L_q) \quad (C-7)$$

Substituting (2-6), (2-7), (C-2) and (C-3) into (C-5):

$$\begin{aligned} T_{e-1}^h &= \frac{3p}{2} \left[\frac{v_q - R i_q}{p \omega_m} - L_d i_d + \left(L_d + \frac{v_d - R i_d}{p \omega_m i_q} \right) i_d^h \right] i_q^h \\ &= \frac{3p}{2} \left[\frac{v_q - R i_q}{p \omega_m} - L_d (i_d - i_d^h) + \frac{v_d - R i_d}{p \omega_m i_q} i_d^h \right] i_q^h \end{aligned} \quad (C-8)$$

Since the $L_d(i_d - i_d^h)$ is small compared with other terms in (C-8) and the L_d of IPMSM is always relatively small, L_d can be assumed as its nominal value or even be ignored. If the $L_d(i_d - i_d^h)$ is ignored, (C-8) becomes (2-12) and (C-4) becomes (C-9):

$$T_{e_2} = \frac{3}{2} \left[\frac{(v_q - Ri_q)}{\omega_m} + \frac{(v_d - Ri_d)}{i_q \omega_m} i_d \right] i_q \quad (\text{C-9})$$

The (C-9) also can be approximated by a polynomial in form of (C-10).

$$T_{e_2} = (c + di_d)i_q \quad (\text{C-10})$$

As discussed in Chapter 2, according to Taylor's series expansion, the signal processing of virtual signal injection is based on (2-12), it is essentially tracks $\partial T_{e_2}/\partial \beta = 0$ for a given operating point under the assumption that c and d are constant.

Similarly if $T_{e_1}^h$ in (C-8) is processed by the same signal processing scheme described in Chapter 2, the output of the signal processing block will be proportional to $\partial T_{e_1}/\partial \beta$ assuming that a and b in (C-5) are constant and the scheme will track $\partial T_{e_1}/\partial \beta = 0$.

Since:

$$i_d = -I_a \sin(\beta) \quad (\text{C-11})$$

$$i_q = I_a \cos(\beta) \quad (\text{C-12})$$

Substituting (C-2), (C-3), (C-11), (C-12) into (C-9) leads to:

$$\begin{aligned} T_{e_2} &= \frac{3p}{2} [\Psi_d I_a \cos(\beta) + L_q I_a^2 \sin(\beta) \cos(\beta)] \\ &= \frac{3p}{2} \left[\Psi_d I_a \cos(\beta) + \frac{1}{2} L_q I_a^2 \sin(2\beta) \right] \end{aligned} \quad (\text{C-13})$$

Substituting (C-2), (C-3), (C-11), (C-12) into (C-4) leads to:

$$T_{e_1} = \frac{3p}{2} [\Psi_m I_a \cos(\beta) - \frac{1}{2} (L_d - L_q) I_a^2 \sin(2\beta)] \quad (\text{C-14})$$

According to (C-13) and (C-14), the $\partial T_{e_2}/\partial \beta$ and $\partial T_{e_1}/\partial \beta$ based on estimated machine parameters at a given operating point are given in (C-15) and (C-16), respectively.

$$\frac{\partial T_{e_2}}{\partial \beta} = \frac{3p}{2} [-\Psi_d I_a \sin \beta + L_q I_a^2 \cos 2\beta] \quad (\text{C-15})$$

$$\frac{\partial T_{e_1}}{\partial \beta} = \frac{3p}{2} [-\Psi_m I_a \sin \beta - L_d I_a^2 \cos 2\beta + L_q I_a^2 \cos 2\beta] \quad (\text{C-16})$$

It worth to be noticed that the (C-15) and (C-16) is also valid when accurate machine parameters are obtained from look-up tables.

However, if the machine parameter variations due to the current angle change are fully considered, according to (C-1), the actual derivative of torque with respect to current angle should be expressed in (C-17) and (C-18):

$$\begin{aligned} \frac{\partial T_e}{\partial \beta} = \frac{3p}{2} & \left[-\Psi_d I_a \sin \beta + \frac{\partial \Psi_m}{\partial \beta} I_a \cos \beta - \frac{\partial L_d}{\partial \beta} \frac{I_a^2}{2} \sin 2\beta - L_d I_a^2 \cos^2 \beta \right. \\ & \left. + L_q I_a^2 \cos 2\beta + \frac{\partial L_q}{\partial \beta} \frac{I_a^2}{2} \sin 2\beta \right] \end{aligned} \quad (C-17)$$

$$\begin{aligned} \frac{\partial T_e}{\partial \beta} = \frac{3p}{2} & \left[-\Psi_m I_a \sin \beta + \frac{\partial \Psi_m}{\partial \beta} I_a \cos \beta - L_d I_a^2 \cos 2\beta + L_q I_a^2 \cos 2\beta \right. \\ & \left. - \frac{\partial L_d}{\partial \beta} \frac{I_a^2}{2} \sin 2\beta + \frac{\partial L_q}{\partial \beta} \frac{I_a^2}{2} \sin 2\beta \right] \end{aligned} \quad (C-18)$$

Comparison of (C-15) with (C-17) leads to:

$$\begin{aligned} \frac{\partial T_{e,2}}{\partial \beta} = \frac{\partial T_e}{\partial \beta} - \frac{3p}{2} & \left[\frac{\partial \Psi_m}{\partial \beta} I_a \cos \beta - \frac{\partial L_d}{\partial \beta} \frac{I_a^2}{2} \sin 2\beta - L_d I_a^2 \cos^2 \beta \right. \\ & \left. + \frac{\partial L_q}{\partial \beta} \frac{I_a^2}{2} \sin 2\beta \right] \end{aligned} \quad (C-19)$$

Comparison of (C-16) with (C-18) leads to:

$$\frac{\partial T_{e,1}}{\partial \beta} = \frac{\partial T_e}{\partial \beta} - \frac{3p}{2} \left[\frac{\partial \Psi_m}{\partial \beta} I_a \cos \beta - \frac{\partial L_d}{\partial \beta} \frac{I_a^2}{2} \sin 2\beta + \frac{\partial L_q}{\partial \beta} \frac{I_a^2}{2} \sin 2\beta \right] \quad (C-20)$$

The (C-19) and (C-20) can also be expressed as (C-21) and (C-22), respectively.

$$\frac{\partial T_{e,2}}{\partial \beta} = \frac{\partial T_e}{\partial \beta} - \frac{3p}{2} \left[\frac{\partial \Psi_m}{\partial \beta} + \frac{\partial L_d}{\partial \beta} i_d - \frac{\partial L_q}{\partial \beta} i_d - L_d i_q \right] i_q = \frac{\partial T_e}{\partial \beta} - error_2 \quad (C-21)$$

$$\frac{\partial T_{e,1}}{\partial \beta} = \frac{\partial T_e}{\partial \beta} - \frac{3p}{2} \left[\frac{\partial \Psi_m}{\partial \beta} + \frac{\partial L_d}{\partial \beta} i_d - \frac{\partial L_q}{\partial \beta} i_d \right] i_q = \frac{\partial T_e}{\partial \beta} - error_1 \quad (C-22)$$

As can be seen from (C-21) and (C-22) even use accurate machine parameters to calculate the MTPA points by letting $\partial T_{e,1}/\partial \beta = 0$ or $\partial T_{e,2}/\partial \beta = 0$, the errors are still inevitable.

In order to verify the above discussion, simulations were first performed based on the nonlinear IPMSM model adopted in this thesis and the resultant constant current amplitude locus is denoted as locus 1 in Fig. C-1. The machine parameters at the point A, B and C on locus 1 are also recorded, respectively. Simulations are then performed based on (C-1) with the machine parameters of points A, B and C, respectively. The resultant constant current amplitude loci are denoted as locus 2, 3, and 4, respectively. As can be seen from Fig. C-1, the $\partial T_A/\partial \beta$, $\partial T_B/\partial \beta$, $\partial T_C/\partial \beta$ in Fig. C-1 are always smaller than $\partial T_e/\partial \beta$. This is due to the $error_1 > 0$. Moreover, the constant current amplitude locus

of the nonlinear machine model in the vicinity of the MTPA point is flatter than those of loci 2, 3 and 4 around their MTPA points. The machine parameter variations with β cause the true MTPA point to shift toward the right.

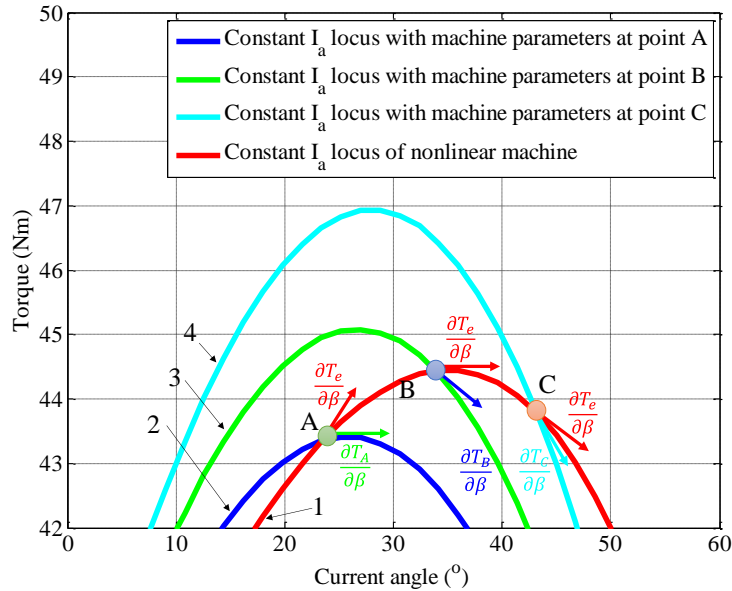


Fig. C-1. Torque variations with β obtained from different machine parameters and nonlinear machine model when $I_a = 77$ A.

Due to:

$$\frac{\partial \Psi_d}{\partial \beta} = \frac{\partial \Psi_m}{\partial \beta} - \frac{\partial L_d}{\partial \beta} I_a \sin \beta - L_d I_a \cos \beta = \frac{\partial \Psi_m}{\partial \beta} + \frac{\partial L_d}{\partial \beta} i_d - L_d i_d \quad (C-23)$$

$$\frac{\partial L_q}{\partial \beta} = \frac{\partial L_q}{\partial i_q} \times \frac{\partial i_q}{\partial \beta} = \frac{\partial L_q}{\partial i_q} \times \frac{\partial I_a \cos \beta}{\partial \beta} = -\frac{\partial L_q}{\partial i_q} I_a \sin \beta = \frac{\partial L_q}{\partial i_q} i_d \quad (C-24)$$

According to (C-23) and (C-24):

$$error_2 = \frac{3p}{2} \left[\frac{\partial \Psi_m}{\partial \beta} + \frac{\partial L_d}{\partial \beta} i_d - \frac{\partial L_q}{\partial \beta} i_d - L_d i_q \right] i_q = \frac{3p}{2} \left[\frac{\partial \Psi_d}{\partial \beta} - \frac{\partial L_q}{\partial i_q} i_d^2 \right] i_q \quad (C-25)$$

$$error_1 = \frac{3p}{2} \left[\frac{\partial \Psi_m}{\partial \beta} + \frac{\partial L_d}{\partial \beta} i_d - \frac{\partial L_q}{\partial \beta} i_d \right] i_q = \frac{3p}{2} \left[\frac{\partial \Psi_d}{\partial \beta} - \frac{\partial L_q}{\partial i_q} i_d^2 + L_d i_q \right] i_q \quad (C-26)$$

Due to the $\partial \Psi_d / \partial \beta$ is negative. $\partial L_q / \partial i_q$ is negative and $L_d i_q$ is positive. The (C-25) and (C-26) can also be written as:

$$error_2 = \frac{3p}{2} \left[\left| \frac{\partial L_q}{\partial i_q} i_d^2 \right| - \left| \frac{\partial \Psi_d}{\partial \beta} \right| \right] i_q \quad (C-27)$$

$$error_1 = \frac{3p}{2} \left[\left| \frac{\partial L_q}{\partial i_q} i_d^2 \right| + |L_d i_q| - \left| \frac{\partial \Psi_d}{\partial \beta} \right| \right] i_q \quad (C-28)$$

In order to study the relationship between $|i_d^2 \partial L_q / \partial i_q|$, $|L_d i_q|$ and $|\partial \Psi_d / \partial \beta|$, simulations are performed based on the nonlinear IPMSM model as shown in Fig. C-2 and Fig. C-3. The simulated $|i_d^2 \partial L_q / \partial i_q|$, $|L_d i_q|$ and $|\partial \Psi_d / \partial \beta|$ when $I_a = 77$ A are shown in Fig. C-2 and the simulated $|i_d^2 \partial L_q / \partial i_q|$, $|L_d i_q|$ and $|\partial \Psi_d / \partial \beta|$ when $I_a = 120$ A are shown in Fig. C-3.

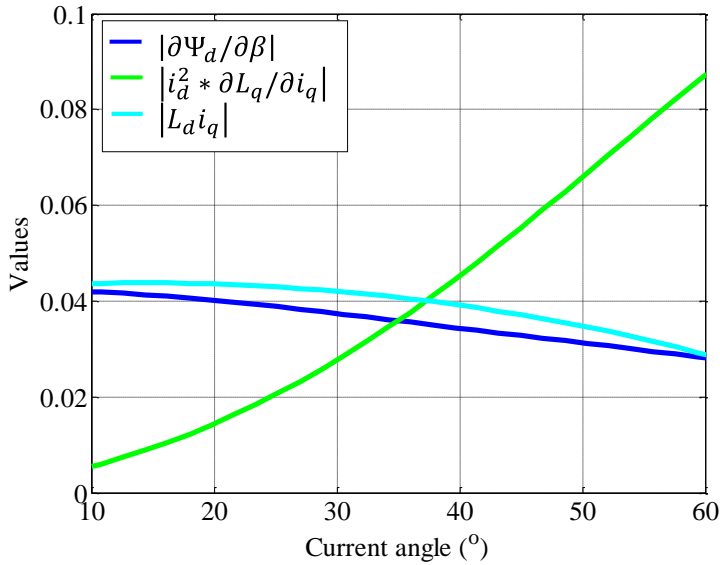


Fig. C-2. Variations of $|i_d^2 \partial L_q / \partial i_q|$, $|L_d i_q|$ and $|\partial \Psi_d / \partial \beta|$ with β when $I_a = 77$ A.

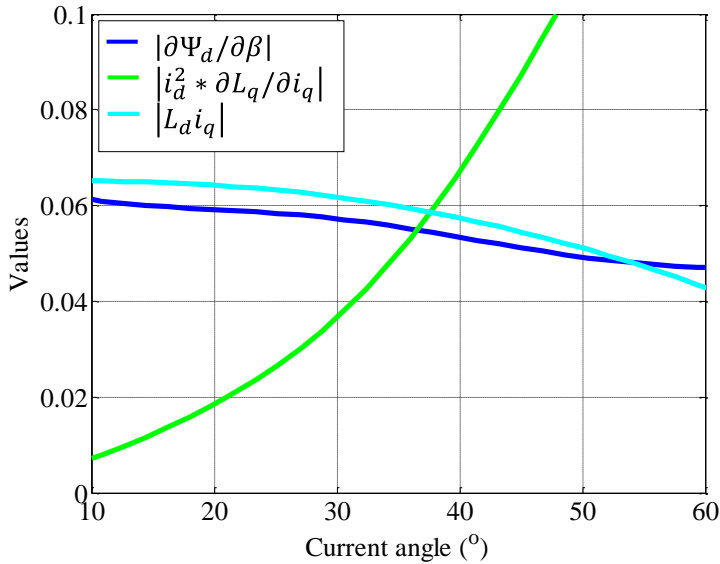


Fig. C-3. Variations of $|i_d^2 \partial L_q / \partial i_q|$, $|L_d i_q|$ and $|\partial \Psi_d / \partial \beta|$ with β when $I_a = 120$ A.

As can be seen from Fig. C-2 and Fig. C-3, $|i_d^2 \partial L_q / \partial i_q|$ increases from zero while the $|L_d i_q|$ and $|\partial \Psi_d / \partial \beta|$ are almost equal. Therefore, for the machine whose MTPA current

angle is around 30° to 45° , i.e., IPMSM, the $|i_d^2 \partial L_q / \partial i_q|$ and $|\partial \Psi_d / \partial \beta|$ in (C-27) can cancel each other partly, therefore, the virtual signal injection based on (2-12) may have higher accuracy. However, for the machine who has relatively small reluctance torque, i.e., SPMSM, due to $|i_d^2 \partial L_q / \partial i_q|$ is small around $\beta = 0$, the virtual signal injection based on (C-8) is preferred and the L_d in (C-8) can be defined as its nominal value of obtained from a look-up table.

To verify the above conclusions, the MTPA tracking results of virtual signal injections based on (2-12) and (C-8) are shown in Fig. C-4. As shown in Fig. C-4, the VSIC based on (2-12) has higher accuracy than (C-8) due to $|i_d^2 \partial L_q / \partial i_q|$ and $|\partial \Psi_d / \partial \beta|$ in (C-27) can partly cancel each other.

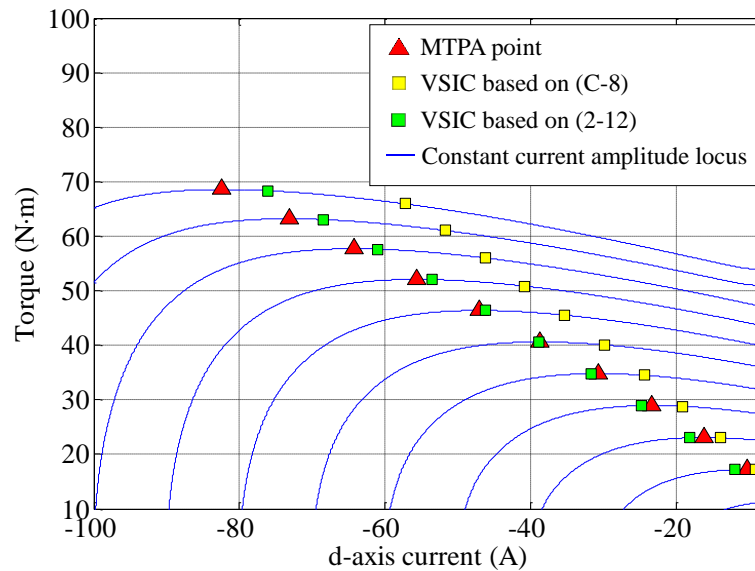


Fig. C-4. The MTPA points and the MTPA tracking simulation results of virtual signal injection control based on (2-12) and (C-8).

The comparison of $error_1$, $error_2$ and $\partial T_e / \partial \beta$ when $I_a = 77$ A is shown in Fig. C-5. As can be seen in Fig. C-5, the $error_1$ and $error_2$ are not negligible compared with $\partial T_e / \partial \beta$. As current angle increases, the $error_1$ keeps increasing and always larger than zero. While the $error_2$ increases from negative to positive. If $\beta < 22^\circ$, the $|error_2| > |error_1|$, the virtual signal injection based on (C-8) has relative small error. If $\beta > 22^\circ$, the $|error_2| < |error_1|$, the virtual signal injection based on (2-12) has relative small error. Since $|i_d^2 \partial L_q / \partial i_q|$ and $|\partial \Psi_d / \partial \beta|$ in (C-27) can partly cancel each other, $error_2$ is very small around the MTPA points, i.e., the point where $\partial T_e / \partial \beta = 0$. Therefore, the virtual signal injection based on (2-12) can track the MTPA point accurately.

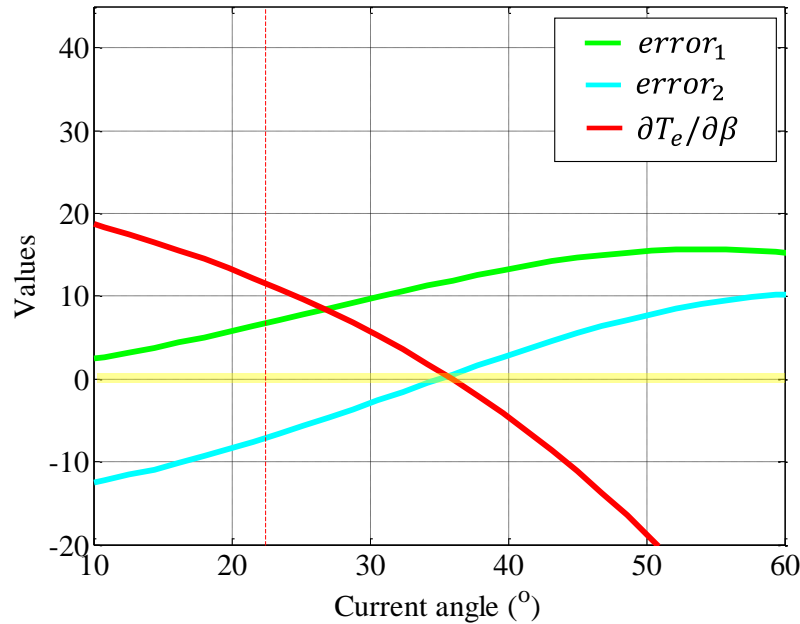


Fig. C-5. Comparison of $error_1$, $error_2$ and $\partial T_e / \partial \beta$ when $I_a = 77$ A.

It has been shown that due to parameter variations with stator currents in IPMSMs, any technique that determines MTPA operating condition by assuming piece constant parameters will result in tracking errors. These include online calculation of optimal d-axis current using machine parameters obtained from look-up tables or through online parameter estimations. For IPMSMs with relatively low reluctance torque contribution, including surface mounted permanent magnet machines, VSIC based on (C-8) would yield more accurate results. For most IPMSMs in which the optimal current angle is between 30° to 45° degrees, VSIC based (2-12) gives the better tracking accuracy. These findings provide fundamental understanding and clarification for achieving MTPA operation of IPMSM drives.

Appendix D

A High-Fidelity, Computationally Efficient Model for Interior Permanent Magnet Machines Considering the Magnetic Saturation, Spatial Harmonics and Iron Loss Effect

In the simulation parts of this thesis, a high-fidelity, computationally efficient model for interior permanent magnet machines proposed in [13] was adopted. The modelling of the high-fidelity model will be briefly introduced below.

Since the conventional voltage model based machine model only considers the effect of fundamental components but does not consider the harmonics fields caused by combination effect of magnetic saturation, slotting effect and permeance variation with rotor position, to take the harmonics into account, a novel modelling scheme was derived from the flux linkage based machine model of an IPMSM. The mathematical model is expressed as in (D- 1) to (D- 4).

$$v_d = \frac{d\Psi_d}{dt} + Ri_d - \omega_e \Psi_q \quad (\text{D- 1})$$

$$v_q = \frac{d\Psi_q}{dt} + Ri_q + \omega_e \Psi_d \quad (\text{D- 2})$$

$$\Psi_d = f(i_d, i_q, \theta) \quad (\text{D- 3})$$

$$\Psi_q = g(i_d, i_q, \theta) \quad (\text{D- 4})$$

where θ is the rotor position. According to (D- 3) and (D- 4):

$$i_d = f^{-1}(\Psi_d, \Psi_q, \theta) \quad (\text{D- 5})$$

$$i_q = g^{-1}(\Psi_d, \Psi_q, \theta) \quad (\text{D- 6})$$

According to (D- 1) and (D- 2), the d- and q-axis flux linkages can be obtained by integrals:

$$\Psi_d = \int (v_d - Ri_d + \omega_e \Psi_q) \quad (\text{D- 7})$$

$$\Psi_q = \int (v_q - Ri_q - \omega_e \Psi_d) \quad (\text{D- 8})$$

To capture all the torque components, including cogging torque, the electromagnetic torque computed from finite element analysis (FEA) can be written as a function of d- and q-axis currents with rotor position:

$$T_e = T(i_d, i_q, \theta) \tag{D- 9}$$

Based on the above equations, the schematic of the high-fidelity machine model is given in Fig. D- 1.

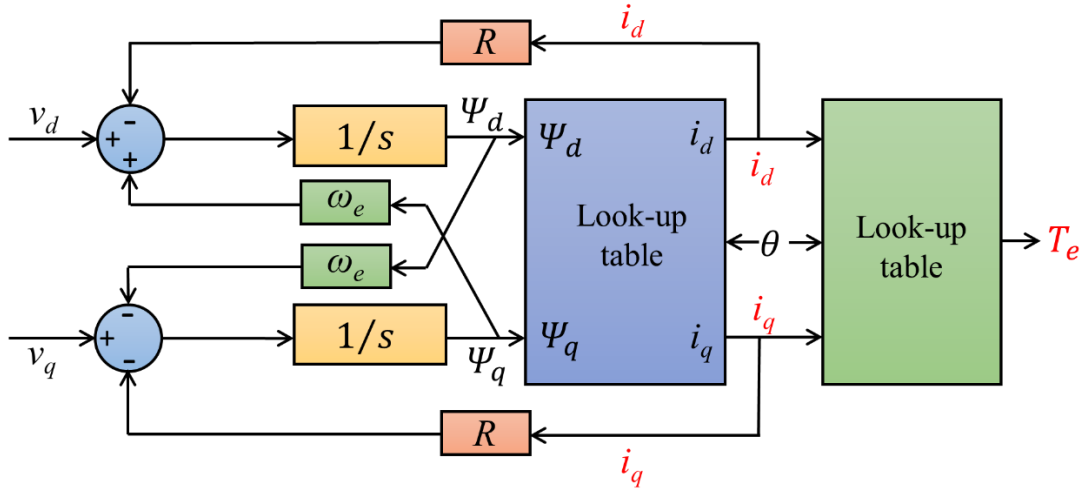


Fig. D- 1. Schematic of proposed electromagnetic model of IPM machines.

As shown in Fig. D- 1, for a given voltage vector, the d- and q-axis flux linkages can be calculated by the integrals in (D- 7) and (D- 8). Subsequently, the d- and q-axis current are obtained from pre-defined 3-dimensional look-up tables whose inputs are Ψ_d , Ψ_q and θ while the outputs of the look-up tables are i_d and i_q respectively. The resultant electromagnetic torque, T_e , can be acquired from another 3-dimensional look-up table whose inputs are i_d , i_q and θ . All of the data in look-up tables is obtained from FEA.